Notes on Numerical Fluid Mechanics
and Multidisciplinary Design 125

Michel O. Deville · Jean-Luc Estivalezes
Vincent Gleize · Thien-Hiep Lê
Marc Terracol · Stéphane Vincent *Editors*

Turbulence and Interactions

Proceedings of the TI 2012 conference

Springer

Notes on Numerical Fluid Mechanics and Multidisciplinary Design

Volume 125

About this Series

Notes on Numerical Fluid Mechanics and Multidisciplinary Design publishes state-of-art methods (including high performance methods) for numerical fluid mechanics, numerical simulation and multidisciplinary design optimization. The series includes proceedings of specialized conferences and workshops, as well as relevant project reports and monographs.

Michel O. Deville · Jean-Luc Estivalezes
Vincent Gleize · Thien-Hiep Lê
Marc Terracol · Stéphane Vincent
Editors

Turbulence and Interactions

Proceedings of the TI 2012 Conference

Springer

Editors
Michel O. Deville
Ecole Polytechnique Fédérale de Lausanne
Lausanne
Switzerland

Jean-Luc Estivalezes
ONERA Toulouse
France

Vincent Gleize
ONERA
Chatillon
France

Thien-Hiep Lê
ONERA
Chatillon
France

Marc Terracol
ONERA
Chatillon
France

Stéphane Vincent
ENSCBP
Pessac
France

ISSN 1612-2909 ISSN 1860-0824 (electronic)
ISBN 978-3-662-43488-8 ISBN 978-3-662-43489-5 (eBook)
DOI 10.1007/978-3-662-43489-5
Springer Heidelberg New York Dordrecht London

Library of Congress Control Number: 2014940791

Printed on acid-free paper

Springer is part of Springer Science+Business Media (www.springer.com)

Preface

The "Turbulence and Interactions 2012" (TI2012) conference was held in La Saline-les-Bains on the island of La Réunion, France, on June 11th–14th, 2012. The scientific sponsors of the conference were

- Ecole Polytechnique Fédérale de Lausanne (EPFL),
- ERCOFTAC : European Research Community on Flow, Turbulence and Combustion,
- Institut de Mécanique et d'Ingénierie (I2M), Bordeaux,
- ONERA - The French Aerospace Lab,
- Université de La Réunion.

This third TI conference was very successful as it attracted 35 researchers from 6 countries. The magnificent venue and the beautiful weather helped the participants to discuss freely and casually, share ideas and projects, and spend very good times all together.

The organisers were fortunate in obtaining the presence of the following invited speakers: J.H. Chen (Sandia National Laboratories), B. Geurts (University of Twente), C. Wagner (The German Aerospace Center -DLR). The topics covered by the 23 contributed papers ranged from experimental results through theory to computations. They represent a snapshot of the state-of-the-art in turbulence research. The papers of the conference went through the usual reviewing process and the result is given in this book of Proceedings.

In the present volume, the reader will find the keynote lectures followed by the contributed talks given in alphabetical order of the first author.

The organisers of the conference would like to acknowledge the support of EPFL, I2M and ONERA.

Bordeaux, Lausanne, Paris, Toulouse
January 23rd, 2014.

Michel O. Deville
Jean-Luc Estivalezes
Vincent Gleize
Thien-Hiep Lê
Marc Terracol
Stéphane Vincent

Contents

Keynote Lectures

Regular Papers

Theory and Application of Regularization Modeling of Turbulence

Bernard J. Geurts

Abstract. Turbulence readily arises in numerous flows in nature and technology. The large number of degrees of freedom of turbulence poses serious challenges to numerical approaches aimed at simulating and controlling such flows. While the Navier-Stokes equations are commonly accepted to precisely describe fluid turbulence, alternative coarsened descriptions need to be developed to cope with the wide range of length and time scales. These coarsened descriptions are known as large-eddy simulations in which one aims to capture only the primary features of a flow, at considerably reduced computational effort. Such coarsening introduces a closure problem that requires additional phenomenological modeling. A systematic approach to the closure problem, known as regularization modeling, will be reviewed. Its application to turbulent mixing will be illustrated. Leray and LANS-alpha regularization are discussed in some detail.

1 Introduction

A new modeling approach for large-eddy simulation (LES) is obtained by combining a 'regularization principle' with an explicit filter and its inversion. This regularization approach allows a systematic derivation of the implied subgrid-model, which resolves the closure problem. The central role of the filter in LES is fully restored, i.e., both the interpretation of LES predictions in terms of direct simulation results as well as the corresponding subgrid closure are specified by the filter (Geurts & Holm, 2003). The regularization approach is illustrated with 'Leray-smoothing' of the nonlinear convective terms. In turbulent mixing the new, implied

Bernard J. Geurts
Multiscale Modeling and Simulation, Faculty EEMCS, University of Twente,
P.O. Box 217, 7500 AE Enschede, The Netherlands
Anisotropic Turbulence, Laboratory for Fluid Dynamic, Faculty Applied Physics,
Eindhoven University of Technology, P.O. 513, 5300 MB Eindhoven, The Netherlands
e-mail: b.j.geurts@utwente.nl

M.O. Deville et al. (eds.), *Turbulence and Interactions*,
Notes on Numerical Fluid Mechanics and Multidisciplinary Design 125,
DOI: 10.1007/978-3-662-43489-5_1,

subgrid model performs favorably compared to the dynamic eddy-viscosity procedure (Geurts & Holm, 2006; Kuczaj & Geurts , 2007). The model is robust at arbitrarily high Reynolds numbers and correctly predicts self-similar turbulent flow development.

Accurate modeling and simulation of turbulent flow is a topic of intense ongoing research (Meneveau & Katz, 2000). Modern strategies for turbulent flow are aimed at reducing the dynamical complexity of the underlying system of partial differential equations while reliably predicting the primary flow phenomena. In large-eddy simulation (LES) these conflicting requirements are expressed by coarsening the description on the one hand and subgrid modeling on the other hand. The coarsening is achieved by spatial filtering (Germano, 1992) which externally specifies the physical detail that will ideally be retained in the LES solution. Maintaining the dynamical properties of the resolved large scales is approached by introducing subgrid modeling to deal with the closure problem that arises from filtering the nonlinear terms.

In the filtering approach to incompressible flow the specification of the basic convolution filter L is all that is required to uniquely define the relation between the unfiltered and filtered flow field as well as the closure problem for the so-called turbulent stress-tensor τ_{ij}. This situation is in sharp contrast with actual present-day large-eddy modeling in which the specification of the subgrid model for τ_{ij} as well as the comparison with reference direct numerical simulation (DNS) results is performed largely independent of the specific choice of the filter L.

In this paper we will formulate an alternative approach to large-eddy simulations which completely restores the two central roles of the basic filter L, i.e., providing an interpretation of LES predictions in terms of filtered DNS results as well as fully specifying all details of the subgrid model. The key elements in this new formulation are a 'regularization principle', a filter L and its (formal) inverse operator denoted by L^{-1} (Geurts, 1997).

The organization of this paper is as follows. In Section 2 we introduce the concept of regularization. Section 3 is devoted to the derivation of sub-filter models for large-eddy simulation from regularization principles. The assessment of the Leray model is presented in Section 4 and concluding remarks are collected in Section 5.

2 Turbulence Regularization

A regularization principle expresses the smoothing of the dynamics of the Navier-Stokes equations through a specific proposal for direct alteration of the nonlinear convective terms. This modeling differs significantly from traditional, less direct approaches, e.g., involving the introduction of additional eddy-viscosity contributions (Smagorinsky, 1963). The latter are clearly of a different physical nature and do not fully do justice to the intricate nonlinear transport structure of the filtered Navier-Stokes equations. The regularization principle gives rise to a basic mixed formulation involving both the filtered and unfiltered solution. Application of L and L^{-1} then allows to derive an equivalent representation solely in terms of the filtered

solution. This provides a unique identification of the implied subgrid model without any further external (ad hoc) input or mathematical-physical considerations of the closure problem. The regularization modeling approach is not only theoretically transparent and elegant, but it also gives rise to accurate LES predictions. In particular, we consider the implied subgrid model that arises from Leray's regularization principle (Leray, 1934). A comparison between the Leray model and dynamic subgrid modeling (e.g., (Vreman, Geurts & Kuerten, 1997)) will be made for turbulent mixing flow, both at moderate and at high Reynolds numbers.

In the filtering approach one assumes any normalized convolution filter $L : u_i \rightarrow \overline{u}_i$ where $\overline{u}_i$ (u_i) denotes the filtered (unfiltered) component of the velocity field in the x_i direction. Filtering the Navier-Stokes equations yields

$$\partial_t \overline{u}_i + \partial_j(\overline{u}_j \overline{u}_i) + \partial_i \overline{p} - \frac{1}{Re}\partial_{jj}\overline{u}_k = -\partial_j \tau_{ij} \tag{1}$$

where the turbulent stress tensor $\tau_{ij} = \overline{u_i u_j} - \overline{u}_i \overline{u}_j$ represents the closure problem and Re denotes the Reynolds number. Both the relation between u_i and $\overline{u}_i$ as well as the properties of τ_{ij} are fully specified by L. In actual subgrid modeling for LES, the next step is to introduce a subgrid model $m_{ij}(\overline{\mathbf{u}})$ to approximate τ_{ij}. A variety of subgrid models has been proposed to capture dissipative, dispersive or similarity properties of τ_{ij}.

Many subgrid models are arrived at through a physical or mathematical reasoning which is only loosely connected to a specific filter L. As an example, the well-known Smagorinsky model (Smagorinsky, 1963) is given by $m_{ij}^S = -(C_S\Delta)^2|S_{ij}(\overline{\mathbf{u}})|S_{ij}(\overline{\mathbf{u}})$ where the rate of strain tensor $S_{ij} = \partial_i \overline{u}_j + \partial_j \overline{u}_i$ and $|S_{ij}|^2 = S_{ij}S_{ij}/2$. The only explicit reference to the filter, made in this model, is through the filter-width Δ. In actual simulations Δ is specified in terms of the grid-spacing h rather than in terms of L. Furthermore, the Smagorinsky constant C_S is determined independent of L, which further reduces any principal role for the filter. The situation is comparable for the 'tensor-diffusivity' model $m_{ij}^{TD} = C_{TD}\Delta_k^2 \partial_k \overline{u}_i \partial_k \overline{u}_j$, with Δ_k the filter-width in the x_k-direction (Clark, Ferziger & Ferziger, 1979). The coefficient C_{TD} is usually related to the normalized second moment $(L(x^2) - x^2)/\Delta^2$ of the filter L. For various popular filters such as the top-hat or the Gaussian filter one finds $C_{TD} = 1/12$, i.e., independent of the actual filter used. The role of the filter is in principle fully explicit in Bardina's similarity model $m_{ij}^B = \overline{\overline{u}_i \overline{u}_j} - \overline{\overline{u}}_i \overline{\overline{u}}_j$ (Bardina, Ferziger, & Reynolds, 1984). In actual simulations, however, one frequently adopts a wider explicit filter or a filter of a different type, to enhance smoothing properties of this model (Meneveau & Katz, 2000). Moreover, the model is sometimes multiplied by a constant C_B which is specified independently of any presumed filter (Salvetti & Banerjee, 1995). Finally, the successful dynamic subgrid modeling requires only the explicit specification of the so-called test-filter (Germano, Piomelli, Moin & Cabot, 1991). To retain the central Germano identity the test-filter can in principle be chosen independent of L, mainly requiring the specification of the filterwidth of the test-filter relative to Δ. Additional averaging over homogeneous directions, 'clipping' steps to stabilize actual simulations, and the fact

that the assumed base-models are themselves only loosely connected to L, also make the dynamic procedure rather insensitive to the specific assumed filter.

In contrast to these popular LES models, the regularization approach involves the introduction of a pair $(L,\ L^{-1})$ to fully specify the implied subgrid model as well as the interpretation of LES predictions in terms of reference DNS results. The selection of any other pair $(\mathscr{L},\ \mathscr{L}^{-1})$ directly leads to its corresponding DNS interpretation and the associated subgrid model consistent with the regularization principle. This modeling strategy has a number of important benefits, addressing directly the nonlinear convective contributions and requiring no additional 'external' information such as model coefficients or the width of the test-filter. The regularization principle allows a transparent modeling in which the modeled system of equations can be made to share a number of fundamental properties with the Navier-Stokes equations, such as transformation symmetries, Kelvin's circulation theorem, etc.. The implied subgrid model is quite simple to implement, with some technical complications arising from the construction of an accurate inverse operator L^{-1}.

3 Regularization to Derive Sub-filter Models

In this section we present two regularization principles and their translation to the corresponding sub-filter model for Large-Eddy Simulation. We begin with the Leray model and subsequently extend this to the LANS$-\alpha$ model.

Leray Modeling

To illustrate the regularization approach we consider the intuitively appealing and particularly simple Leray regularization in which the convective fluxes are replaced by $\overline{u}_j\partial_j u_i$, i.e., the solution $\mathbf{u}$ is convected with a smoothed velocity $\overline{\mathbf{u}}$. Consequently, the nonlinear effects are reduced by an amount governed by the smoothing properties of L. The governing equations in the Leray formulation can be written as (Leray, 1934)

$$\partial_j\overline{u}_j = 0\ \ ;\ \ \partial_t u_i + \overline{u}_j\partial_j u_i + \partial_i p - \frac{1}{Re}\partial_{jj}u_i = 0 \tag{2}$$

Uniqueness and regularity of the solution to these equations have been established rigorously (Leray, 1934). The Leray formulation contains the unfiltered Navier-Stokes equations in the limiting case $L \to Id$, e.g., as $\Delta \to 0$ (Id denotes the identity). The unfiltered solution can readily be eliminated from (2) by using the inversion operator $u_j = L^{-1}(\overline{u}_j)$. After some calculation (2) can be written in the same way as the LES 'template' (1) in which τ_{ij} on the right hand side is replaced by the asymmetric, filtered similarity-type Leray model m^L_{ij} given by:

$$m^L_{ij} = L\Big(\overline{u}_j L^{-1}(\overline{u}_i)\Big) - \overline{u}_j\overline{u}_i = \overline{\overline{u}_j u_i} - \overline{u}_j\overline{u}_i \tag{3}$$

This model requires the explicit application of both L and L^{-1}. The tensor m^L_{ij} is not symmetric. However, the flow is governed by the divergence $\partial_j m^L_{ij}$ which

can be shown to transform covariantly under Galilean transformations and under a change to a uniformly rotating reference frame, as does $\partial_j \tau_{ij}$. For properly chosen filter, Leray solutions of the regularized Navier-Stokes equations behave better with respect to smoothness and boundedness. Correspondingly, the subgrid model (3) can be expected to yield similar benefits in a large-eddy context. The straightforward model $m_{ij} = L(L^{-1}(\overline{u}_i)L^{-1}(\overline{u}_j)) - \overline{u}_i\overline{u}_j$ does not provide sufficient smoothing and leads to unstable LES on coarse grids, at high Re.

LANS$-\alpha$ Regularisation by Kelvin Filtering

A regularisation principle which additionally possesses correct circulation properties may be obtained by starting from the following Kelvin theorem:

$$\frac{d}{dt}\oint_{\Gamma(\mathbf{u})} u_j\, dx_j - \frac{1}{Re}\oint_{\Gamma(\mathbf{u})} \Delta u_j\, dx_j = 0 \tag{4}$$

where $\Gamma(\mathbf{u})$ is a closed fluid loop moving with the Eulerian velocity $\mathbf{u}$. The unfiltered Navier-Stokes equations may be derived from (4) (Foias, Holm & Titi, 2001). This provides some of the inspiration to arrive at an alternative regularisation principle for Navier-Stokes turbulence (Foias, Holm & Titi, 2001). In fact, the basic regularisation principle was originally derived by applying Taylor's hypothesis of frozen-in turbulence in a Lagrangian averaging framework. In this framework, the fluid loop is considered to move with the smoothed transport velocity $\overline{\mathbf{u}}$, although the circulation velocity is still the unsmoothed velocity, $\mathbf{u}$. That is, in (4) we replace $\Gamma(\mathbf{u})$ by $\Gamma(\overline{\mathbf{u}})$; so the material loop Γ moves with the filtered transport velocity. From this filtered Kelvin principle, we may obtain the Euler-Poincaré equations governing the smoothed solenoidal fluid dynamics, with $\partial_j \overline{u}_j = 0$

$$\partial_t u_j + \overline{u}_k \partial_k u_j + u_k \partial_j \overline{u}_k + \partial_j p - \partial_j(\frac{1}{2}\overline{u}_k u_k) - \frac{1}{Re}\Delta u_j = 0 \tag{5}$$

Comparison with the Leray regularisation principle reveals two additional terms in (5). These terms guarantee the regularised flow to be consistent with the modified Kelvin circulation theorem in which $\Gamma(\mathbf{u}) \to \Gamma(\overline{\mathbf{u}})$. For LANS$-\alpha$ the analytical properties of the regularised solution are based on the energy balance for $\int \mathbf{u}\cdot L(\mathbf{u})\, d^3x$.

The Euler-Poincaré equations (5) can also be rewritten in the form of the LES template. The extra terms that arise in (5) give rise to additional terms in the implied subgrid model:

$$\partial_t \overline{u}_i + \partial_j(\overline{u}_j\overline{u}_i) + \partial_i \overline{p} - \frac{1}{Re}\Delta \overline{u}_i = -\partial_j\left(\overline{\overline{u}_j u_i} - \overline{u}_j\overline{u}_i\right) - \frac{1}{2}\left(\overline{u_j \partial_i \overline{u}_j - \overline{u}_j \partial_i u_j}\right) \tag{6}$$

We observe that the Leray model reappears as part of the implied LANS$-\alpha$ subgrid model on the right-hand side of (6). Compared to the Leray model, the additional second term in the LANS$-\alpha$ model takes care of recovering the Kelvin circulation theorem for the smoothed solution. This formulation is given in terms of a general

filter L and its inverse. After some further rewriting it may be shown that this model can be formulated in conservative form, i.e., a tensor m_{ij}^{α} can be found such that the right hand side of (6) can be written as $-\partial_j m_{ij}^{\alpha}$. We illustrate this next for a particular filter.

The subgrid model presented in (6) can be specified further in case the filter L has the Helmholtz operator as its inverse, i.e., $u_i = L^{-1}(\overline{u}_i) = (1-\alpha^2\partial_{jj})\overline{u}_i = \mathrm{He}_{\alpha}(\overline{u}_i)$. Then we recover the original LANS$-\alpha$ equations (Foias, Holm & Titi, 2001). The LANS$-\alpha$ model derives its name from the length-scale parameter $\alpha \approx \Delta/5$. After some rewriting, the following parameterisation for the turbulent stress tensor is obtained:

$$m_{ij}^{\alpha} = \alpha^2 \mathrm{He}_{\alpha}^{-1}\Big(\partial_k\overline{u}_i\,\partial_k\overline{u}_j + \partial_k\overline{u}_i\,\partial_j\overline{u}_k - \partial_i\overline{u}_k\,\partial_j\overline{u}_k\Big) \tag{7}$$

The first term on the right-hand side is the *Helmholtz-filtered* tensor-diffusivity model. The second term combined with the first term, corresponds to Leray regularisation using Helmholtz inversion as filter. The third term completes the LANS$-\alpha$ model and maintains Kelvin's circulation theorem. In (7) an inversion of the Helmholtz operator He_{α} is required which implies application of the exponential filter. However, since the Taylor expansion of the exponential filter is identical at quadratic order to that of the top-hat or the Gaussian filters, one may approximate $\mathrm{He}_{\alpha}^{-1}$, e.g., by an application of the explicit top-hat filter, for reasons of computational efficiency.

Spectral Consequences of Regularization Modeling

The different regularisation models are known to have different effects on the tail of the resolved kinetic energy spectrum $E(k)$. In the Kolmogorov picture of homogeneous, isotropic turbulence an inertial range in which $E(k) \sim k^{-5/3}$ develops over an extended range of wavenumbers k up to a Kolmogorov wavenumber $k_{\eta} \sim 1/\eta$ where η is the viscous dissipation length-scale. This entire dynamic range needs to be properly captured in order to arrive at a reliable DNS. The Leray and LANS$-\alpha$ models give rise to a spectrum in which there is a smooth transition from a $-5/3$ power law to a much steeper algebraic decay, beyond wavenumbers $\sim 1/\Delta$. The sharper decrease of kinetic energy with wavenumber implies a corresponding strong reduction in required computational effort needed for the simulation of the relevant dynamic range. The LANS$-\alpha$ model displays a tail of the spectrum $\sim k^{-3}$ while the Leray model decays even more steeply, as $\sim k^{-13/3}$ (Foias, Holm & Titi, 2001). The steeper decay using the Leray model is directly reflected in the smoother impression of instantaneous solutions. Hence, through the selection of Δ a direct external control is achieved over the computational costs associated with the regularisation models. This is illustrated in figure 1. In case an energy range of, say, m decades is desired then all wavenumbers up to $k_L(m)$, $k_{\alpha}(m)$ and $k_{DNS}(m)$ need to be resolved for the Leray, LANS$-\alpha$ and DNS approaches respectively. This corresponds to a significant difference in the associated computational expense, while all three simulations would provide excellent accuracy at least for all wavenumbers up to $\sim 1/\Delta$.

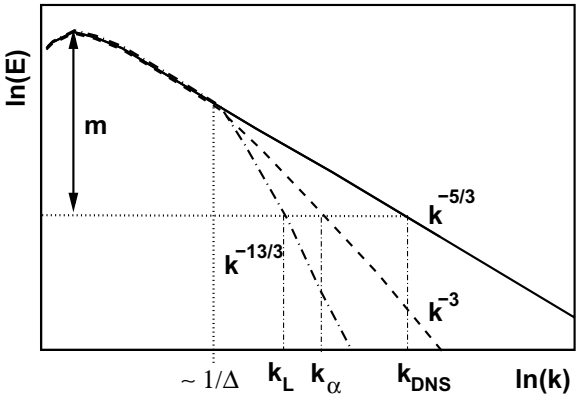

Fig. 1 Sketch of resolved kinetic energy spectrum in a homogeneous, isotropic turbulence, displaying a $-5/3$ tail in DNS (solid), a -3 tail in LES using the LANS$-\alpha$ model (dashed) and a $-13/3$ tail in LES using the Leray model (dash-dotted)

In the sequel we consider invertible numerical quadrature approximating the top-hat filter. In one dimension the numerical convolution filtering $\overline{u} = G * u$ corresponds to kernels

$$G(z) = \sum a_j \delta(z - z_j) \;\; ; \;\; |z_j| \leq \Delta/2 \tag{8}$$

In particular, we consider three-point filters with $a_0 = 1-\alpha$, $a_1 = a_{-1} = \alpha/2$ and $z_0 = 0$, $z_1 = -z_{-1} = \Delta/2$. Here we use $\alpha = 1/3$ which corresponds to Simpson quadrature of the top-hat filter. In actual simulations the resolved fields are known only on a set of grid points $\{x_m\}_{m=0}^N$. The application of L^{-1} to a general discrete solution $\{\overline{u}(x_m)\}$ can be specified using discrete Fourier transformation as (Kuerten, Geurts, Vreman & Germano, 1999)

$$L^{-1}(\overline{u}_m) = \sum_{j=-n}^{n} \Big(\frac{\alpha - 1 + \sqrt{1-2\alpha}}{\alpha} \Big)^{|j|} \frac{\overline{u}_{m+rj/2}}{(1-2\alpha)^{1/2}} \tag{9}$$

where the subgrid resolution $r = \Delta/h$ is assumed to be even. An accurate and efficient inversion can be obtained with only a few terms, recovering the original signal to within machine accuracy with $n \approx 10$. The invertibility of L only refers to invertibility on the LES grid. Injection from a fine DNS grid to a coarse LES grid is not invertible. At fixed Δ, variation of the subgrid resolution r allows an independent control over flow-smoothing and numerical representation (Geurts & Fröhlich, 2002). Simulation results obtained in this way are properly smoothed for $k\Delta < 2\pi$. At constant Δ the inclusion of modes with higher wavenumber k in case $r > 1$ allows to approach the grid-independent solution to the 'fixed-Δ' problem. However, the modes with $k > 2\pi/\Delta$ are not properly smoothed in the sense of Leray; the Fourier transform of the kernel G does not reduce in amplitude for large $k\Delta$ but rather, it oscillates between fixed limits. To achieve a genuine PDE result, Leray analysis

requires correct smoothing by the filter also at high wavenumber. The present results are limited to the modes with $k\Delta < 2\pi$ and in subsequent illustrations we restrict ourselves to this range.

4 Assessment of Leray Model

To assess the Leray model the turbulent mixing layer is simulated in a volume ℓ^3 at various *Re* adopting a fourth order accurate finite volume discretization and explicit four-stage, second-order accurate Runge-Kutta time-stepping. We compare predictions with those obtained using the dynamic subgrid model, which was shown to be among the most accurate models in a comparative study of the same turbulent mixing layer reported in (Vreman, Geurts & Kuerten, 1997).

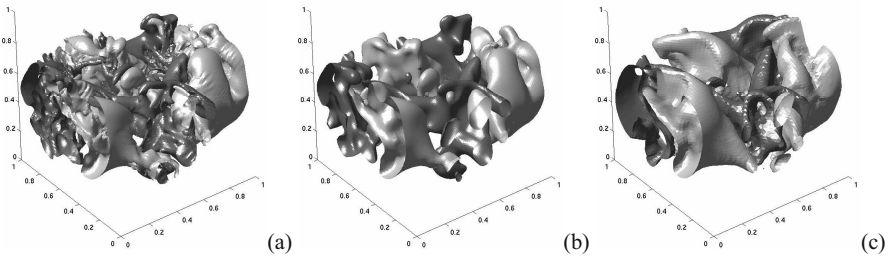

Fig. 2 Normal velocity component u_2 at time $t = 80$, (a): DNS, (b): filtered DNS, (c): Leray on 64^3; using a filterwidth $\Delta = \ell/16$. The light (dark) isosurfaces correspond to $u_2 = 0.3$ (-0.3).

A first introductory test of the Leray model is obtained by studying instantaneous solutions. As a typical illustration of the mixing layer the DNS prediction of the normal velocity u_2, obtained at a spatial resolution of 256^3, is shown in the turbulent regime in Fig. 2(a). We used $Re = 50$ based on the initial momentum thickness and free-stream flow properties. The filtered u_2 can be seen in Fig. 2(b) establishing a significant smoothing due to the 'Simpson' filter at $\Delta = \ell/16$. The Leray prediction (Fig. 2(c)) appears to capture the main 'character' as well as some of the details of the filtered DNS solution. A slight underprediction of the influence of the small scales is, however, apparent. Further visualization showed that the instantaneous Leray predictions display much better overall agreement with filtered DNS than the dynamic model, which relative to the Leray model significantly overpredicts the smoothing (Vreman, Geurts & Kuerten, 1997). Of course, assessing the quality of LES predictions in this way is difficult to quantify and we consider more specific measures next.

The evolution of a crucial mean-flow property such as the momentum thickness is shown in Fig. 3. The Leray results compare significantly better with filtered DNS results than those obtained with the dynamic model on 32^3 grid-cells. We observe

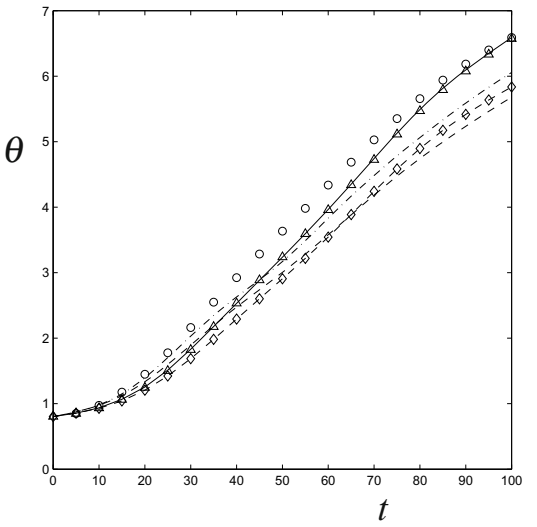

Fig. 3 Momentum thickness θ: filtered DNS ($\circ$), Leray-model (32^3: dash-dotted, 64^3: solid, 96^3: $\triangle$), dynamic model (32^3: dashed, 64^3: dashed with $\diamond$). A fixed filterwidth of $\ell/16$ was used.

that some of the discrepancies between Leray and filtered DNS results are due to numerical contamination. By increasing the resolution at fixed Δ, a good impression of the grid-independent solution to the modeled equations can be inferred using 64^3 – 96^3 grid-cells, i.e., $\Delta/h = 4$ to 6 (Geurts & Fröhlich, 2002). Numerical contamination also plays a role in the dynamic model. The grid-independent solution corresponding to the dynamic model appears less accurate than the corresponding Leray result.

A more detailed assessment is obtained from the streamwise kinetic energy spectrum shown in Fig. 4. The dynamic model yields a significant underprediction of the intermediate and smaller retained scales, particularly for the approximately grid-independent solution. The Leray predictions are much better. On coarse grids, an overprediction of the smaller scales is apparent due to interaction with the spatial discretization method (Vreman, Geurts & Kuerten , 1994). At proper numerical subgrid resolution the situation is considerably improved and the Leray model is seen to capture all scales with high accuracy. A slight, systematic underprediction of the smaller scales remains, consistent with the impression obtained from Figs. 2(b)-(c).

A particularly appealing property of Leray modeling is the robustness at very high Reynolds numbers, cf. Fig. 5. This is quite unique for a subgrid model without an explicit eddy-viscosity contribution. Although comparison with filtered DNS data is impossible here, we observe that the smoothed Leray dynamics is essentially captured as $r = \Delta/h \geq 4$ (Geurts & Fröhlich, 2002). The tail of the spectrum increases with *Re*, indicating a greater importance of small scale flow features.

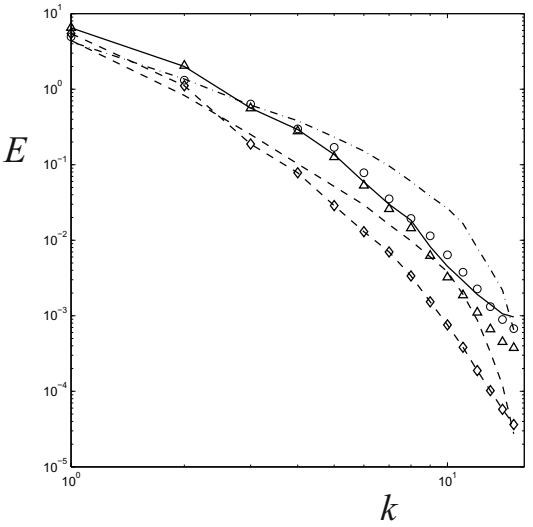

Fig. 4 Streamwise kinetic energy spectrum E at $t = 75$: filtered DNS ($\circ$), Leray-model (32^3: dash-dotted, 64^3: solid, 96^3: $\triangle$), dynamic model (32^3: dashed, 64^3: dashed with $\diamond$). A fixed filterwidth of $\ell/16$ was used.

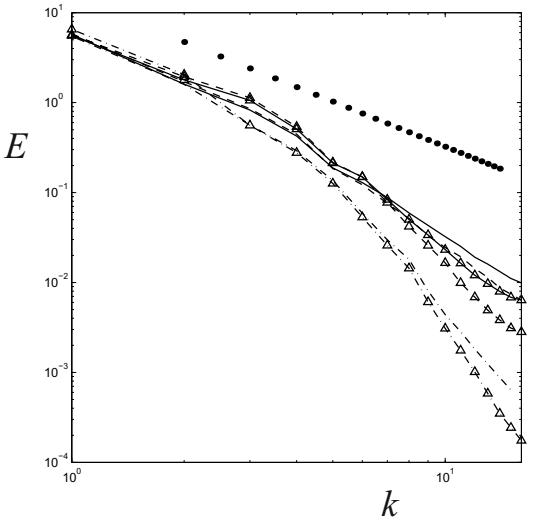

Fig. 5 Streamwise kinetic energy spectrum E at $t = 75$ predicted by the Leray model: $Re = 50$ (64^3: dash-dotted, 96^3: dash-dotted, $\triangle$), $Re = 500$ (64^3: dashed, 96^3: dashed, $\triangle$), $Re = 5000$ (64^3: solid, 96^3: solid, $\triangle$). A fixed filterwidth of $\ell/16$ was used. The dotted line represents $k^{-5/3}$.

Improved subgrid resolution shows a reduction of these smallest scales, consistent with the reduced numerical error. At high *Re* the spectrum corresponding to the Leray model tends to contain a region with approximately $k^{-5/3}$ behavior, which is absent at $Re = 50$. Further analysis showed that the solution develops self-similarly at high *Re*.

5 Concluding Remarks

The Leray model displays excellent robustness with increasing Reynolds number. This feature allows one to apply the Leray model accurately at reasonable computational costs and under flow-conditions that are well outside current DNS capabilities. However, the LANS$-\alpha$ model yields solutions with more realistic variability, corresponding better to the filtered DNS results than for the Leray model. Thus, a trade-off emerges between these two models. The solutions of the LANS$-\alpha$ model may more accurately represent the effects of intermittency in turbulence than the less-variable solutions of the Leray model. However, the LANS$-\alpha$ model is less robust and its application to flow at high Reynolds numbers is not as straightforward as with the Leray model. Further investigation of this trade-off may lead to interesting developments in the comparison of the time-dependent solutions of these two models.

A convenient benefit of the regularisation approach to turbulence modelling is that it enables one to derive the implied small-scale treatment from the underlying regularisation principle. This yields a systematic closure of the equations whose analysis allows an extension in which the filter width Δ is determined dynamically by the evolving flow. The evolving filter-width may even be anisotropic. The application of this self-adaptive modelling approach in a spatially developing mixing layer and, more importantly, in near wall turbulence is a topic of current research.

References

Bardina, J., Ferziger, J.H., Reynolds, W.C.: Improved turbulence models based on LES of homogeneous incompressible turbulent flows. Department of Mechanical Engineering. Report No. TF-19, Stanford (1984)

Clark, R.A., Ferziger, J.H., Reynolds, W.C.: Evaluation of subgrid-scale models using an accurately simulated turbulent flow. J. Fluid Mech. 91, 1–16 (1979)

Foias, C., Holm, D.D., Titi, E.S.: The Navier-Stokes-alpha model of fluid turbulence. Physica D 152, 505–519 (2001)

Germano, M., Piomelli, U., Moin, P., Cabot, W.H.: A dynamic subgrid-scale eddy viscosity model. Phys. Fluids A 3, 1760–1765 (1991)

Germano, M.: Turbulence: the filtering approach. J. Fluid Mech. 238, 325–336 (1992)

Geurts, B.J.: Inverse Modeling for Large-Eddy Simulation. Phys. of Fluids 9, 3585–3588 (1997)

Geurts, B.J., Fröhlich, J.: A framework for predicting accuracy limitations in large-eddy simulation. Phys. Fluids 14, 17–22 (2002)

Geurts, B.J., Holm, D.D.: Regularization modeling for large-eddy simulation. Phys. of Fluids 15, L13 (2003)
Geurts, B.J., Holm, D.D.: Leray and NS-α modeling of turbulent mixing. J. of Turbulence 7, 1–33 (2006)
Kuczaj, A.K., Geurts, B.J.: Mixing in manipulated turbulence. J. of Turbulence 7, 1–28 (2007)
Kuerten, J.G.M., Geurts, B.J., Vreman, A.W., Germano, M.: Dynamic inverse modeling and its testing in large-eddy simulations of the mixing layer. Phys. Fluids 11, 3778–3785 (1999)
Leray, J.: Sur les mouvements d'un fluide visqueux remplissant l'espace. Acta Mathematica 63, 193–248 (1934)
Meneveau, C., Katz, J.: Scale-invariance and turbulence models for large-eddy simulation. Annu. Rev. Fluid Mech. 32, 1–32 (2000)
Salvetti, M.V., Banerjee, S.: A priori tests of a new dynamic subgrid-scale model for finite-difference large-eddy simulations. Phys. of Fluids 7, 2831–2847 (1995)
Smagorinsky, J.: General circulation experiments with the primitive equations. Mon. Weather Rev. 91, 99–164 (1963)
Vreman, A.W., Geurts, B.J., Kuerten, J.G.M.: Discretization error dominance over subgrid-terms in large eddy simulations of compressible shear layers. Comm. Num. Meth. Eng. Math. 10, 785 (1994)
Vreman, A.W., Geurts, B.J., Kuerten, J.G.M.: Large-eddy simulation of the turbulent mixing layer. J. Fluid Mech. 339, 357 (1997)

Penalty Methods for Turbulent Flows Interacting with Obstacles

W. Bizid, A. Etcheverlepo, S. Vincent, J.-P. Caltagirone,
D. Monfort, and M. Hassine

Abstract. The objective is to evaluate the applicability of the penalty method for practically high-Re flows and to investigate the influence of wall model on the quality of the predicted results. This penalty method is introduced at first time on staggered Cartesian grid and then using unstructured mesh. For validation, due to faster convergence, 2D finite volume method in a cartesian grid is used to numerically investigate the incompressible unsteady laminar ($Re = 100$) and turbulent ($Re = 3900$) flow around a circular cylinder and the turbulent flow in a channel at $Re_{u_\tau} = 395$. 3D simulation is performed on an unstructured grid to simulate the turbulent flow behind a circular cylinder at $Re = 3900$ without the use of a wall model.

1 Modelling and Numerical Background

Incompressible turbulent flows at high Reynolds number in complex geometries are simulated in the framework of immersed boundary methods (IBM). Industrial applications such as turbulent flow in a rod bundle or around a wind turbine are the goals of this work. Our approach is based on a penalty method which allows the computation of flows around complex objects without requiring a body-fitted mesh. The incompressible Navier-Stokes equations are solved by a finite volume method on a non conformal grid and the boundary conditions on the immersed boundary are

W. Bizid · S. Vincent · J.-P. Caltagirone
Universit de Bordeaux, Institut de Mécanique et Ingénierie (I2M) - UMR 5295,
F-33400 Talence, France
e-mail: wided.bizid@etu.u-bordeaux1.fr, {vincent,calta}@enscbp.fr

A. Etcheverlepo · D. Monfort
EDF R&D, Chatou, France
e-mail: adrien.etcheverlepo@gmail.com, david.monfort@edf.fr

M. Hassine
Universit Tunis El Manar, ENIT, LAMSIN, 1002, Tunis, Tunisie
e-mail: maatoug.hassine@enit.rnu.tn

M.O. Deville et al. (eds.), *Turbulence and Interactions*,
Notes on Numerical Fluid Mechanics and Multidisciplinary Design 125,
DOI: 10.1007/978-3-662-43489-5_2,

enforced adding a penalty term in the governing equations. The following equations are solved in the fictitious domain which contains both the physical domain and the immersed object.

$$\begin{cases} \rho(\partial_t \mathbf{u} + \nabla \cdot (\mathbf{u} \otimes \mathbf{u})) + \frac{\chi_{\Omega_e}}{\varepsilon}(\mathbf{u} - \mathbf{u}_D) = -\nabla p + \nabla \cdot ((\mu + \mu_t)(\nabla \mathbf{u} + \nabla^t \mathbf{u})) \\ \nabla \cdot \mathbf{u} = 0 \end{cases} \quad (1)$$

Here $\mathbf{u}$ denotes the velocity, p the pressure, ρ the density and μ the viscosity of the fluid. Velocity and pressure are the Reynolds average quantities in RANS and spatially filtered quantities in LES. The turbulent viscosity μ_t depends on the turbulence model used in the simulation (LES or RANS simulations). χ_{Ω_e} denotes the Heavyside function, ε is the penalty parameter which tends to zero and $\mathbf{u}_D$ is the value of the boundary condition for the velocity.

This penalty method was first introduced on staggered Cartesian grid and has been successfully applied to many applications at moderate Reynolds numbers [8][6]. In the present work, in order to deal with high Reynolds numbers, the very near wall is modeled for the first time with two set of transient-RANS type equations. In addition the second order penalty method, called the sub-mesh penalty method[1] is extended to unstructured grid with a special treatment of the wall boundary condition. All the computational simulations have been performed with Thetis [7] and Code_Saturne [5] based respectively on a staggered finite volume method and a collocated finite volume method on unstructured grid.

2 Penalty Method

Until now, all the applications of the penalty method have been carried out in the moderate Reynolds number on staggered grid. For those applications, linear interpolation provided good results. So it was not necessary to pay attention to the near wall resolution. Recently, the direct forcing method (an other IBM) has been adapted in the framework of the Reynolds-Averaged Navier-Stokes equation [4] to be applied to industrial turbulent flows at high Reynolds number. At the same time, a simple near-wall model has been applied in the framework of fictitious domain method for LES simulations [3].

Let us describe the modifications of the second order sub mesh penalty method [1] to use it in a collocated finite volume method. The penalty methods are techniques for solving flow problems with irregular boundaries without using a body fitted mesh. Thus, the computational grid of the domain is not conformed with the immersed boundary which simplifies the mesh's creation. In our case, the immersed surface of the object is represented in STL format. Since this format is widely used in computer graphic, specific algorithm such like the Ray Tracing algorithm is adapted for our needs. This algorithm consists of shooting a ray from each cell of the mesh and counting the number of intersection between the ray and the STL mesh. Finally, each cell of the grid is tagged according to the position (fluid or solid).

For each node $\mathbf{x}_K$ in the immersed domain near the interface, the $\{\frac{\chi_{\Omega_e}}{\varepsilon}(\mathbf{u}-\mathbf{u}_D)\}_K$ is replaced by $\frac{\chi_{\Omega_e}(\mathbf{x}_K)}{\varepsilon}(\phi_K(\mathbf{x}_{ib})\mathbf{u}_K+\sum\phi_L(\mathbf{x}_{ib})\mathbf{u}_L-\mathbf{u}_D)$.

Practically, the nodes $\mathbf{x}_L$ are in the discrete neighborhood of $\mathbf{x}_K$.

The equation solved for the velocity variable near the immersed boundary is:

$$\phi_K(\mathbf{x}_{ib})\mathbf{u}_K+\sum\phi_L(\mathbf{x}_{ib})\mathbf{u}_L=\mathbf{u}_D|_\Sigma \tag{2}$$

where ϕ_K and ϕ_L are the interpolation coefficients. These coefficients depend on the position of the local immersed boundary and the grid, the computation is made once at the beginning of the calculation and stored. The interpolation method is based on a moving least square method using a linear approximation. Similar interpolation method has been successfully applied to a direct forcing method [9] for the simulation of laminar flow on a staggered grid.

3 Wall Force Calculation

In the case of non-boundary-conforming grid the numerical computation of the local forces on the surface of the body is a non-trivial problem.

For viscous flows, the fluid force F_i^f exerted on the complex body arises from two sources: surface pressure distribution and shear stress along the body.
This force can be written as :

$$\mathbf{F}_i^f=\int_{\partial\Omega_i}(2\mu\mathbf{D}-pId).\mathbf{n}dS \tag{3}$$

In general, the immersed boundary surface does not coincide with the boundary of the computational cell. As a consequence, a quantity has to be extrapolated from the fluid domain to the interface.

In this work we propose a method to compute the local force distribution. Starting from the knowledge of the body discretization Σ_h, we define the barycenter X_i of each element σ_i of Σ_h. From this point the outward normal is drawn and the probe point is identified along the normal direction located at a distance δ from the immersed boundary.

$$P=X_i+\delta.\mathbf{n} \text{ with } \delta=2(\frac{\Delta x+\Delta y+\Delta z}{3}) \tag{4}$$

This ensures that the probe point is always surrounded by fluid points. The discrete values of a given field Φ (pressure, derivative ...) are then interpolated at the probe point using the technique described in [10]. The algorithm uses the fluid field at the cell node nearest to the particle, $N(x,y,z)$, to estimate the local fluid field at the probe point $P(X,Y,Z)$.

In cartesian coordinates the equation can be written as follows:

$$\Phi_i|_P\approx\Phi_i|_N+\frac{\partial\Phi_i}{\partial x}|_N(X-x)+\frac{\partial\Phi_i}{\partial y}|_N(Y-y)+\frac{\partial\Phi_i}{\partial z}|_N(Z-z) \tag{5}$$

Following the idea given in [11], the following advection equation will be employed to transport the values along the direction that is normal to the immersed boundary.

$$\frac{\partial \Phi_i}{\partial \tau} + \mathbf{n}.\nabla \Phi_i = 0 \tag{6}$$

In the above, τ is the artificial time. Like that, the extrapolation of the field Φ is done as a constant along the normal $\mathbf{n}$.

4 Immersed Boundary Method for LES of High Reynolds Number Flow

Immersed boundary method greatly simplifies the grid generation process for computing flows with complex and moving boundaries, by avoiding the need for a body-fitted mesh. However, the application of Cartesian grid methods can become prohibitive for high Reynolds number flows due to the demanding resolution requirement near the wall boundary(DNS or wall-resolving LES). Another key point of the IB method is that the linear interpolation required for the reconstruction of the velocity field at the interface region can be used only if the first computational node is placed inside the linear region of the boundary layer.

To avoid the placement of a large number of grid points near a wall, the use of wall-layer model is considered as a promising alternative to render the (IB) method effective for high Reynolds number.

In order to reduce the computational cost of the LES, a technique based on the idea that using RANS to simulate the near-wall region and LES in the exterior region on a single mesh was examined. A well-known approach in this category is the Detached Eddy Simulation (DES) which was designed to simulate massively separated aerodynamic flows. When the standard DES of Spalart is used, the turbulent eddy viscosity is obtained by solving a transport equation for an auxiliary variable as proposed by Spalart and Allmaras (SA) [12]:

$$\frac{D\tilde{\nu}}{Dt} = Production + Diffusion - Destruction \tag{7}$$

$$= C_{b1}\tilde{S}\tilde{\nu} + \frac{1}{\sigma}[\frac{\partial}{\partial x_j}((\nu+\tilde{\nu})\frac{\partial \tilde{\nu}}{\partial x_j}) + C_{b2}\frac{\partial \tilde{\nu}}{\partial x_j}.\frac{\partial \tilde{\nu}}{\partial x_j}] - C_{w1}f_w(\frac{\tilde{\nu}}{d})^2 \tag{8}$$

The DES formulation is obtained by replacing the distance to the nearest wall d by d_{des} in the production/destruction terms and model parameters. The distance d_{des} is defined as:

$$d_{des} = min(d_{rans}, C_{des}\Delta) \text{ with } \Delta = max(\Delta x, \Delta y, \Delta z) \text{ and } C_{des} = 0.65 \tag{9}$$

Unfortunately, this approach is not grid spacing independent and the grid has significant effects on the results of the DES. In order to capture the effects of viscous

boundary layers within the framework of a Cartesian grid solver, a simple near-wall model based on the local equilibrium hypothesis is used.

Following Balaras et *al.* [2] and Tessicini et *al.* [3] simplified turbulent boundary-layer equations are solved using a one-dimensional discretization embedded within the flow field between the wall and an outer point chosen at a distance δ from the wall. This boundary layer grid, attached to the solid surface grid and not part of the fluid (LES) grid, is used to penalize the value of the last (LES) flow grid points to physically pertinent values near the wall.

The boundary layer equations have the following general form:

$$\frac{\partial}{\partial n}[(\nu+\nu_t)\frac{\partial u}{\partial n}] = \frac{\partial u}{\partial t} + u\frac{\partial u}{\partial s} + \frac{1}{\rho}\frac{dp}{ds} = F_i, \tag{10}$$

$$\nu_t = \kappa u_\tau n[1-exp(-\frac{u_\tau}{\nu A}n)]^2 \ , \ u_\tau = \sqrt{\frac{\tau_{wall}}{\rho}} \ , \ \tau_{wall} = \mu\frac{\partial u}{\partial n}|_0 \tag{11}$$

This model has to use some information from exterior LES and feed back some information to the exterior flow simulation. In the present study only the equilibrium stress balance model obtained by setting $F_i = 0$, was used.

In the framework of penalty method, we propose also another wall function [14] capable of switching smoothly between sub-, buffer- and log- layers to penalize velocity at the first computational node.

$$\frac{u}{u_\tau} = \begin{cases} y^+ & y^+ \leq 5 \\ \Sigma_{i=}^4 a_i (y^+)^i & 5 < y^+ \leq 30 \\ \kappa^{-1} ln(y^+) + 5.1 & y^+ \geq 30 \end{cases} \tag{12}$$

with a_i are the model constants.

To summarize the model works as follows:

- The first fluid point off the immersed surface *IB* is detected.
- Over the line normal to the surface and passing through *IB* the probe node *P* is placed.
- The velocity components are interpolated at the probe node *P*
- Starting from the knowledge of the cartesian velocity and through a rotation of the coordinate system we calculate the tangential and wall-normal velocity.
- This velocity is used in conjunction with wall function or the simple near wall resolved equation, to compute the tangential and normal velocity at *IB* point.
- Moving back the local frame to the cartesian frame reference, we can compute the wall velocity components at *IB* point.
- The physical computed velocity are then penalized at the IB node

5 Results

Channel flow and flow around a circular cylinder are a fundamental fluid mechanics problem and they are well understood by both Direct Numerical Simulation (DNS)

and Large Eddy Simulation (LES). Hence, we propose to simulate the incompressible unsteady laminar ($Re = 100$) and turbulent ($Re = 3900$) flow around a circular cylinder and the turbulent flow in a channel at $Re_{u_\tau} = 395$. It is known that for the latest turbulent case the vortex shedding occurs in cells and therefore the flow is generally simulated in $3D$. But the $3D$ simulation is very much complicated and treated as a numerically costly procedure. Therefore, in order to evaluate the capability of the penalty method in conjunction with the DES approach and wall modeling technique, a two-dimensional LES and DES of the quasi-two-dimensional turbulent flows around a cylinder and inside a channel is investigated on a structured Cartesian grid. In addition, for the sake of comparison to 2D penalty approach and LES/DES results, $3D$ simulation is performed on an unstructured grid to simulate the turbulent flow behind a circular cylinder at $Re = 3900$ without the use of a wall model.

Flow Past a Cylinder

The main goal of the present study is consequently to compute the drag coefficient C_D and visualize the laminar and turbulent unsteady flow field for different Reynolds numbers. The drag coefficient defined as a global average of a normalized drag force on the cylinder from the flow

$$C_D = \frac{D}{0.5\rho U_\infty A}$$

where U_∞ is the inflow velocity and A is the projected area of the cylinder.

We consider the cases of $Re = 100$ and $Re = 3900$ with the Reynolds numbers being based on the cylinder diameter D.

The Laminar Flow (Re = 100)

Computations are presented at a Reynolds number based on the freestream velocity and cylinder diameter D of 0.1. The simulation is performed on a $2D$ grid. The computational domain equals $[0,10] \times [-4.05, 4.05]$ which is discretised using a 572×296 grid. Uniform free stream condition with velocity $U_\infty = 1.0m/s$ are applied at the inlet boundary. $Figure1$ shows the lift and drag coefficient for $Re = 100$.

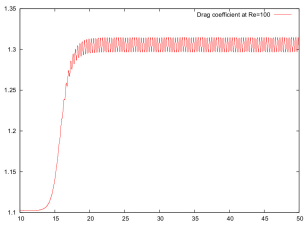

(a) Drag coefficient

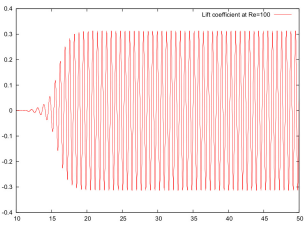

(b) Lift coefficient

Fig. 1 Time History of (a) Lift coefficient and (b) Drag coefficient at Re = 100

The drag coefficient is compared with experimental and other numerical results in *Table*1

Table 1 Comparison with other simulations and experiments

		C_D	C_L	S_t
$Re = 100$	Experiment [15]	$1.24 - 1.26$	–	0.164-0.165
	Kim et al. [13]	1.33	± 0.32	0.165
	Le et al. [16]	1.37 ± 0.009	± 0.323	0.16
	present	1.306	± 0.314	0.1617

The Turbulent Flow (Re = 3900)

In this section we focus on Reynolds numbers $Re = 3900$. The turbulent flow around a circular cylinder is studied using $2D$ finite volume method. The turbulent flow is simulated using the LES approach with 1100×580 grid and then using the DES97 approach with 219×120 grid. For each case the physical velocity in the boundary layer is computed and penalized using the two method previously presented in section 4.

Figure 2 shows the drag coefficient for LES approach in conjunction with wall function (a) and with thin boundary layer equation (TBLE) (b). Figure 3 shows the drag coefficient for DES approach in conjunction with wall function (a) and with thin boundary layer equation (TBLE) (b).

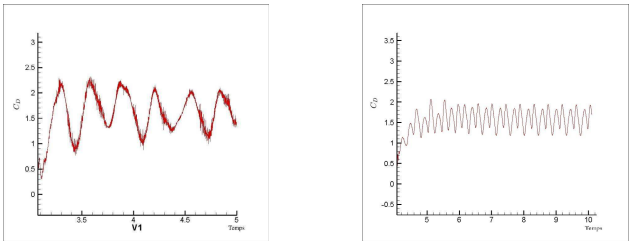

(a) LES + wall function (b) LES + TBLE

Fig. 2 Time History of the Drag coefficient at Re = 3900 using the LES approach with wall function (a) and with TBLE equation (b)

LES simulations for the flow around a circular cylinder at Reynolds 3900 is also performed with Code_Saturne. Results are compared with numerical simulations and experiments performed by other authors. The computational domain is 20 diameters long in both streamwise and normal directions. The spanwise domain is chosen to be πD and the center of the cylinder is located at $5D$ from the inlet boundary. The non-orthogonal mesh has $2.4 \cdot 10^6$ cells and the unstructured mesh used for the simulation without penalty method has $2.5 \cdot 10^6$ cells. The boundary conditions are a

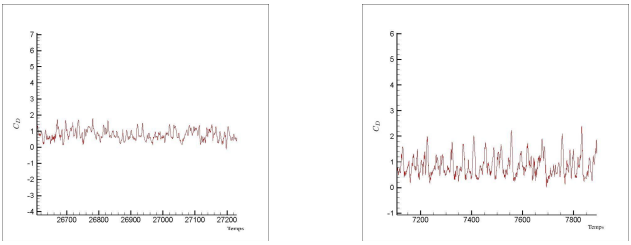

(a) DES + wall function (b) DES + TBLE

Fig. 3 Time History of the Drag coefficient at Re = 3900 using the DES approach with wall function (a) and with TBLE equation (b)

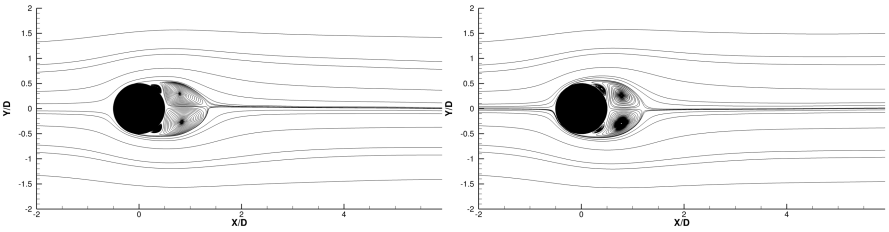

(a) unstructured mesh without penalty method (b) non-orthogonal mesh with penalty method

Fig. 4 Mean streamlines of the flow around the cylinder. Left: without penalty method, Right: with penalty method.

Table 2 Strouhal, length recirculation and separation angle

	L_r/D	θ_{sep}	S_t
Lourenko, Cardell (Experimental)	1.4 ± 0.1	86 ± 2	0.215 ± 0.005
Kravchenko (LES)	1.35	88	0.210
unstructured mesh (without penalty method)	1.33	86.11	0.207
non-orthogonal structured mesh (with penalty method)	1.19	90	0.185

uniform inflow velocity for the inlet boundary and periodic velocity component in other directions. We wait 100 characteristic times before starting statistics. The flow statistics have been accumulated over 300 characteristic times defined as tU_∞/D.

Figure 4 shows the streamlines of the mean velocity field. Similar recirculation behaviour is observed with both an unstructured conform mesh without using a penalty method and with a penalty method. The secondary recirculation observed for the two simulations have been reported in precedent LES studies. In Table 2, we compare the flow parameters such as the separation angle θ_{sep}, the length of the mean recirculation and the Strouhal frequency shedding St. The non-orthogonal

mesh together with the penalty method provides the poorest results with an underestimated recirculation length and Strouhal number.

Turbulent Flow in a Channel at $Re_{u_\tau} = 395$

The flow field simulated is a fully developed two-dimensional turbulent flow in a channel. The flow is statistically homogeneous both in the streamwise and spanwise directions and the statistics depend only upon the distance from the wall. The simulations of channel flows is performed at first time using the eddy detached simulation (DES) on fine grids, then the near-wall treatments is tested on a coarse grid. The simulation results is compared to the direct numerical simulation (DNS) data of Moser et al. [17] obtained for $Re_{u_\tau} = 395$ based on the friction velocity u_τ and the channel half-width.

Results for the channel simulation using (DES) model are presented in Figure 3 and is compared to the Moser et al. [17] simulation.

The results is obtained with 100×130 grid points. Also, the eddy viscosity of the (DES) model is compared with Medic et al. [18] RANS/LES simulation. Corresponding to the two wall approaches, a coarse mesh 100×50 is used for wall functions. While for the enhanced wall treatment a $1D$ finer mesh with 27 grid cells is used in the viscous sublayer.

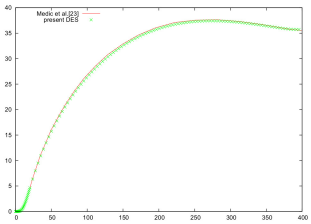

(a) Comparison between the eddy viscosity profile at $Re_\tau = 395$

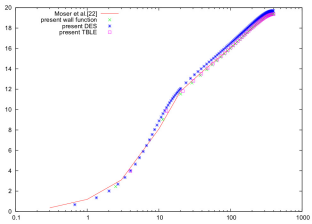

(b) Comparison between the mean velocity profile in wall units at $Re_\tau = 395$

Fig. 5 Turbulent flow in a channel at $Re_{u_\tau} = 395$

Conclusion

The drag and lift coefficients are evaluated for the unsteady laminar flow around a cylinder at $Re = 100$. The DES approach in conjunction with the penalty method and two versions of a wall model is used to study the 2D flow around a circular cylinder at $Re = 3900$ and the turbulent flow in a channel at $Re_{u_\tau} = 395$. The result is in reasonable agreement with the literature results. In the future work the application of the wall model in conjunction with the penalty method will be used in 3D domain and then extended to unstructured grid.

References

1. Sarthou, A., Vincent, S., Angot, P., Caltagirone, J.P.: The sub-mesh penalty method. Finite Volumes for Complex Applications V, 633–640 (2008)
2. Balaras, E., Benocci, C., Piomelli, U.: Two-Layer Approximate Boundary Conditions for Large Eddy Simulations. AIAA J. 34, 1111–1119 (1996)
3. Tessicini, F., Iaccarino, G., Fatica, M., Wang, M., Verzicco, R.: CTR, Ann. Res. Briefs, 349 (2005)
4. Kalitzin, G., Iaccarino, G.: CTR, Ann. Res. Briefs, 415 (2002)
5. Archambeau, F., Méchitoua, N., Sakiz, M.: Code Saturne: A Finite Volume Code for Turbulent flows - Industrial applications. Int. J. Finite Vol. 1, 1–62 (2004)
6. Khadra, K., Angot, P., Parneix, S., Caltagirone, J.-P.: Fictitious domain approach for numerical modelling of Navier-Stokes equations. Int. J. Numer. Meth. Fluids 34, 651–684 (2000)
7. Vincent, S., Caltagirone, J.-P.: A one-cell local multigrid method for solving unsteady incompressible multiphase flows. J. Comput. Phys. 163, 172–215 (2000)
8. Arquis, E.: Transferts en milieu poreux et á l'interface: de l'échelle microscopique à l'échelle macroscopique. PhD thesis, Université Bordeaux I (1984)
9. Vanella, M., Balaras, E.: A moving-least-squares reconstruction for embedded-boundary formulations. J. Comput. Phys. 228, 6617–6628 (2009)
10. Marchioli, C., Armanio, V., Soldati, A.: Simple and accurate scheme for fluid velocity interpolation for Eulerian–Lagrangian computation of dispersed flows in 3D curvilinear grids. Comput. Fluids 36, 1187–1198 (2007)
11. Aslam, T.D.: A partial differential equation approach to multidimensional extrapolation. J. Comput. Phys. 193, 349–355 (2004)
12. Spalart, P.R., Allmaras, S.R.: A One-Equation Turbulence Model for Aerodynamic Flows. La Recherche Aérospatiale 1, 5–21 (1994)
13. Kim, J., Kim, D., Choi, H.: An immersed-boundary finite-volume method for simulations of flow in complex geometries. J. Comput. Phys. 171, 132–150 (2001)
14. Yang, J., Bhushan, S., Suh, J.S., Wang, Z., Koo, B., Sakamoto, N., Xing, T., Stern, F.: Large-Eddy Simulation of Ship Flows with Wall-Layer Models on Cartesian Grids. In: 27th Symposium on Naval Hydrodynamics Seoul, Korea (2008)
15. Tritton, D.J.: Note on the effect of a nearby obstacle on turbulence intensity in a boundary layer. J. Fluid Mech. 6, 547–567 (1959)
16. Le, D.V., Khoo, B.C., Peraire, J.: An immersed interface method for viscous incompressible flows involving rigid and flexible boundaries. J. Comput. Phys. 220, 109–138 (2006)
17. Moser, R.D., Kim, J., Mansour, N.N.: Direct numerical simulation of turbulent channel flow up to Re= 590. Phys. Fluids 11, 943500 (1999)
18. Medic, G., Daenincky, G., Templeton, J.A.: A framework for near-wall RANS/LES coupling. Center for Turbulence Research, Annual Research Briefs (2005)

Direct Numerical Simulation of Particle Turbulence Interaction in Forced Turbulence

J.C. Brändle de Motta, J.-L. Estivalezes, E. Climent, and S. Vincent

Abstract. Usually, numerical simulations of two-phase particle dispersed flow both with Eulerian or Lagrangian approaches assume particle size to be smaller than the smallest scales of the carrier fluid, which is not the case for most two-phase dispersed flows. The present work aims at giving a detailed analysis of particle behaviour by performing fully resolved of finite size particle simulations in the case of forced homogeneous isotropic turbulence

1 Introduction

Turbulent particle-laden flows in nature and industrial applications are ubiquitous like spray combustion, liquid atomization, fluidized bed combustion or aerosol transport. Hence, it is of major importance to clearly understand the effect of particles on turbulence. Recently Balachandar et al [1] has given an exhaustive review on that topic. Experimentally, it is often difficult to obtain some relevant data concerning the local particle and flow characteristics, so the numerical simulation becomes mandatory. Moreover, in numerical methods, it is possible to perform either Large Eddy Simulation (LES) or Direct Numerical Simulation (DNS). DNS can be seen as a real numerical experiment. However, in order to be fully resolved for turbulent flows, the spatial resolution must be lower than the Kolmogorov scale. A lot of works have been published about DNS of two-phases flow with particles smaller than this scale with point particle approximation [2, 3] for example. In this work,

J.C. Brändle de Motta · J.-L. Estivalezes
ONERA, The French Aerospace Lab, 2, avn Edouard Belin, 31055 Toulouse, France
e-mail: {jorge-cesar.brandle_de_motta,
jean-luc.estivalezes}@onera.fr

S. Vincent
Université de Bordeaux, Institut de Mécanique et Ingénierie (I2M) - UMR 5295,
F-33400 Talence, France
e-mail: vincent@enscpb.fr

E. Climent
IMFT, 1, Allée du Professeur Camille Soula - 31400 Toulouse - France
e-mail: eric.climent@imft.fr

M.O. Deville et al. (eds.), *Turbulence and Interactions*,
Notes on Numerical Fluid Mechanics and Multidisciplinary Design 125,
DOI: 10.1007/978-3-662-43489-5_3,

we are interested in particles larger than the Kolmogorov scales, typically thirty times the initial Kolmogorov scale. Simulations performed are four way coupling, this means that the presence of particles influences the carrier fluid and vice versa, and furthermore the interaction particle-particle is taken into account by a repulsive force. Moreover, the turbulence is isotropic and so the computational domain is a periodic cubic box.

2 Numerical Method

The present approach is based on one fluid formulation for particulate disperse two-phase flows. A fictitious domain approach on a Cartesian fixed grid has been chosen as a computational framework. An implicit tensorial penalty method allows to account for solid behavior, while, the incompressibility constraint is tackled with an augmented Lagrangian method [4]. The originality of this method is to split the stress tensor in order to increase the space order. The solid constraint is enforced by high viscosity. The resolved particles are tracked in a Lagrangian way. To avoid deformations, the solid fraction in each cell are updated taking into account the analytical spherical shape. This solid fraction indicator is introduced in the fictitious domain model similarly as in the Volume of Fluid method. Particle-particle collision or wall-particle collision are taken into account thanks to an improved model [5]. A detailed presentation of the finite size particle simulations and their validations are presented in [6].

3 Parameters of the Simulation

3.1 Turbulence Forcing

Numerical simulations of forced isotropic turbulence are most often formulated in Fourier space, where a forcing is applied to low wave number modes. As we use finite volume method and to avoid extra cpu time consuming by the Fast Fourier Transform calling, we implement linear forcing in physical space as proposed by Lundgren [7]. Rosales [8] has shown that linear forcing is a useful alternative method and can be easily integrated into finite volume based codes. The forcing is insured by keeping constant total kinetic energy in the computational domain.

3.2 Parameters

The non dimensional domain is a square box of $L_b = 2\pi$, the ratio of box size over Taylor micro-scale is $L_b/\lambda = 27$ the ratio of Taylor micro-scale over Kolgomorov scale is $\lambda/\eta = 17$, $\eta/\Delta x = 0.56$, and finally the ratio of particle diameter over Kolmogorov scale is $D_p/\eta = 20$. The Taylor micro-scale Reynolds number is $Re_\lambda = \lambda u'/\nu_f = 73$. Three density ratio (particle density over fluid density) have been simulated $\rho_p/\rho_f = \{1,2,4\}$. With these parameters, we can define particle Stokes

number based on eddy turnover time, which can be written as a function of density ratio: $St_E = 1.5\rho_p/\rho_f$ giving the following Stokes numbers $St_E = \{1.5, 3, 6\}$. The particle volume fraction is $\phi_v = 0.03$ which corresponds to $N_p = 512$ particles. The simulations have been done on 256^3 grid points with 512 processors. The cpu time is about 10 hours per processor for one eddy turnover time. In figure 1 is plotted the initial kinetic energy spectrum. The vertical dotted line gives the particle radius.

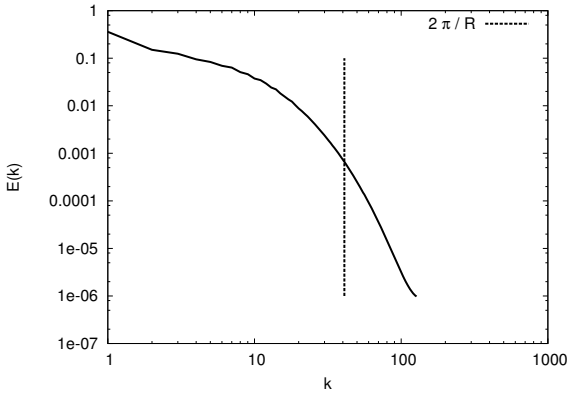

Fig. 1 Initial kinetic energy spectrum

4 Results

We present influence of particles on turbulent kinetic energy spectra in figure 2. The first comment that can be drawn for this figure, is the quite weak influence of particle phase on the spectra except for high wave numbers. We can see that this difference, which seems to increase the energy at the high wave numbers, increase as density ratio does. The small oscillations at high wave numbers are due to Fourier Transform through the particule, see [9].

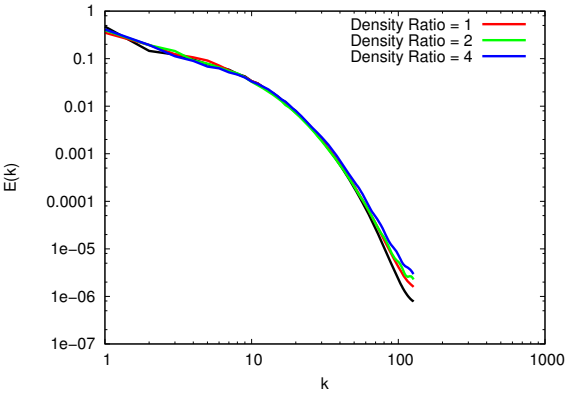

Fig. 2 Comparison of energy kinetic spectra, black line is single phase flow

A more significant modification by increasing particle volume fraction should be expected, which is here quite low. Next figure 3 depicts Lagrangian autocorrelation coefficients for both single and two-phase flows. In this figure time variable is made non dimensional by using the carrier fluid integral Lagrangian time scale. Single phase Lagrangian autocorrelation has been obtained by seeding the fluid with 20000 massless point tracers and following their trajectory. The same procedure has been applied for finite size particles. As in the previous figure, increase of density ratio causes deviation from single phase case. However, one would expect a more important difference at least for $T/T_l < 1$. One explanation is that even for quite low particle volume fraction collisions are quite frequent, whatever the density ratio is.

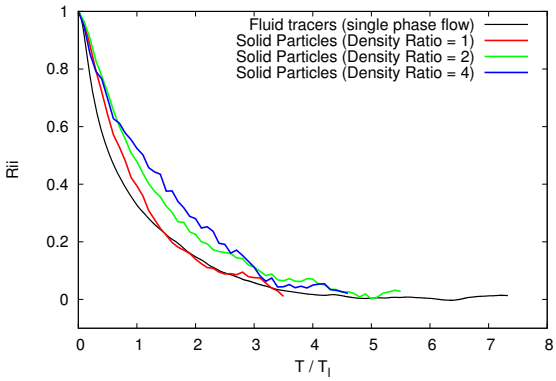

Fig. 3 Comparison of autocorrelation coefficients

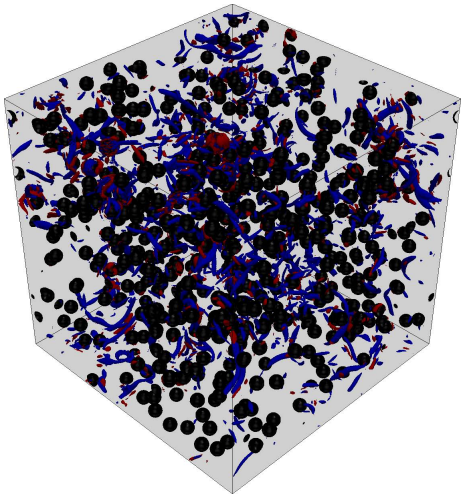

Fig. 4 Snapshot of particules and Q criterium - blue value corresponds to negative value and red to positive

Figure 4 gives an overview of the flow field with the particles at a selected time step. It can be seen in this figure although the volume fraction is low, particle-particle collision could occur relatively often.

In order to get more insight in the particles motion, we try to extract averaged property over the whole particle phase. To do that, we define a local mesh around each particle as depicted in figure 5.

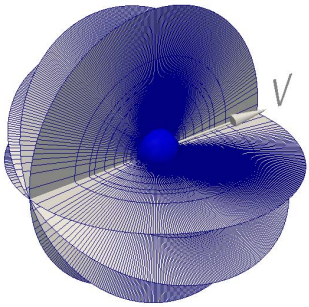

Fig. 5 Local mesh around a particle

For each particle, its center of mass velocity is subtracted and then average is performed for all particles and all time step. Finally one obtains the mean carrier fluid velocity seen by the particle which by symmetry is contained in a particle diametral plane. Figure 6 shows the mean streamlines around the particles superimposed on the carrier fluid pressure field.

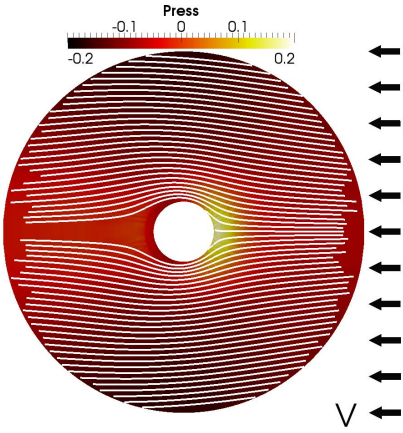

Fig. 6 Mean streamlines around particles and pressure field

From the streamlines, one can deduce that the flow seen by the particle seems to correspond to a low Reynolds number flow as the wake is very thin, and close to a Stokes flow as can be compared with the next figure 7, where are plotted the streamlines and the pressure field for a Stokes flow.

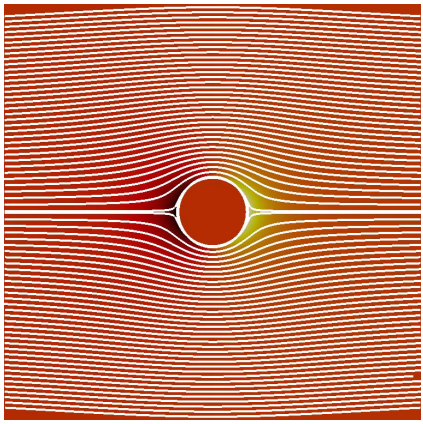

Fig. 7 Mean streamlines around particles and pressure field for a Stokes flow

In figure 8 is plotted the mean vorticity field around the particle. This figure emphasizes the fact that field is quite close to the vorticity field induced by a Stokes flow where the vorticity maxima appear to the top and the bottom of the particle whereas mimina are located upstream and downstream.

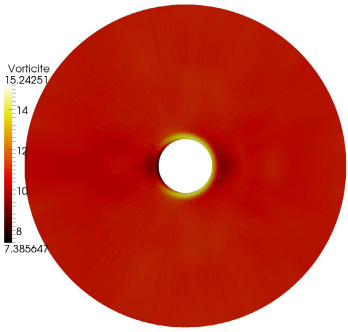

Fig. 8 Mean vorticity field around particles

5 Conclusion

Finite size resolved particle simulations in forced homogeneous turbulence have been performed for low volume fraction value. Parametric study on Stokes numbers based on eddy turnover time has been conducted. Analysis on kinetic energy spectrum have shown that Stokes number increase raises energy density at high wave numbers compared to single phase flow. However this increase stays moderate, most probably due to low volume fraction. Temporal evolution of Lagrangian autocorrelation coefficient have demonstrated Stokes number effect, but early time behaviours seem to indicate collision effect. That has to be more deeply investigated. Finally, mean pressure, vorticity and streamlines values seen by particle show nearly Stokes flow behaviour. This fact demonstrates the the particle phase experiences nearly equilibrium with carrier fluid.

References

1. Balachandar, S., Eaton, J.K.: Turbulent dispersed multiphase flows. Annual Review of Fluid Mechanics 42, 111–133 (2010)
2. Ferrante, A., Elghobashi, S.: On the physical mechanisms of two-way coupling in particle-laden isotropic turbulence. Physics of Fluids 15, 315–329 (2003)
3. Fede, P., Simonin, O.: Numerical study of the subgrid fluid turbulence effects on the statistics of heavy colliding particles. Physics of Fluids 18, 045103–045120 (2006)
4. Randrianarivelo, T.N., Pianet, G., Vincent, S., Caltagirone, J.-P.: Numerical modelling of the solid particle motion using a new penalty method. International Journal for Numerical Methods in Fluids 47, 1245–1251 (2005)
5. Brändle de Motta, J.C., Breugem, W.-P., Gazanion, B., Estivalezes, J.-L., Vincent, S., Climent, E.: Numerical modelling of finite-size particle collisions in a viscous fluid. Physics of Fluids (2013) (in press)
6. Vincent, S., Brändle de Motta, J.C., Sarthou, A., Estivalezes, J.-L., Simonin, O., Climent, E.: A Lagrangian VOF tensorial penalty method for the DNS of resolved particle-laden flows. Submitted to Journal of Computational Physics (2013)
7. Lundgren, T.: Linearly forced isotropic turbulence, annual research briefs. Center for Turbulence Research Stanford (2003)
8. Rosales, C., Meneveau, C.: Linear forcing in numerical simulations of isotropic turbulence: physical space implementations and convergence properties. Physics of Fluids 17, 509–529 (2005)
9. Lucci, F., Ferrante, A., Elghobash, S.: Modulation of isotropic turbulence by particles of Taylor length-scale size. Journal of Fluid Mechanics 650, 555 (2011)

Wake Instabilities behind an Axisymmetric Bluff Body at Low Reynolds Numbers

Yannick Bury and Thierry Jardin

Abstract. This paper aims at understanding the dynamical process that leads to the onset of chaos in the flow past a blunt based axisymmetric bluff body. On the basis of direct numerical simulations, conducted for Reynolds numbers ranging from 100 to 800, we show that the flow undergoes multiple transitions, successively giving rise to the Steady State SS and to the Reflectional Symmetry Preserving RSP_a, RSP_b and RSP_c wake states. In particular, the RSP_c state, revealed in this work *via* long-term computations, is characterized by intermittent vortex stretching denoting the onset of chaos and the potential occurence of a third instability that superimposes to the first and second instability associated with state RSP_a and RSP_b respectively. Interestingly, the reflectional symmetry plane that characterizes the RSP states is still retained. Hence, chaos is triggered before the symmetry breaking and the occurence of the Reflectional Symmetry Breaking RSB state observed at higher Reynolds numbers.

1 Introduction

The thorough analysis of bluff body wakes is essentially twofold. First, it advances the knowledge of fundamental mechanisms driving the destabilization of massively separated flows, *i.e.* the transition between dominant flow instabilities. Second, as an ultimate goal, it serves the definition of optimal flow control strategies through the manipulation of such flow instabilities. As such, it has been proven, for low Reynolds number flows, that forcing the flow at specific forcing frequencies/wavelengths can drastically modify the wake topology and the drag experienced by the bluff body [1] [2] [3]. Moreover it is reasonable to assume that instabilities observed at low Reynolds numbers still persist at much higher Reynolds numbers. An evident but still fascinating example is the clear occurence of the von

Yannick Bury · Thierry Jardin
Université de Toulouse, ISAE, 10, avenue Edouard Belin, 31055 Toulouse, France
e-mail: {yannick.bury,thierry.jardin}@isae.fr

M.O. Deville et al. (eds.), *Turbulence and Interactions*,
Notes on Numerical Fluid Mechanics and Multidisciplinary Design 125,
DOI: 10.1007/978-3-662-43489-5_4,

Kármán vortex shedding in the wake of geological obstacles, for Reynolds numbers $\mathcal{O}(10^9)$. Therefore one can expect a flow control strategy, primarily optimized at low Reynolds number, to be efficient at higher Reynolds number. In this sense the effort to enhance knowledge of the flow destabilization towards chaotic states is a prerequisite for the potential definition of optimal flow control strategies at higher Reynolds numbers.

In this paper, the wake instabilities behind a blunt-based axisymmetric bluff body at various Reynolds numbers, ranging from 100 to 800, are analysed. Wakes of axisymmetric bluff bodies at low Reynolds number have gained interest due to the variety of instabilities that develop as the Reynolds number is increased, eventually leading to chaotic state. Numerous studies focused on spheres, revealing transitions of the wake structure from 1) an axisymmetric steady state (corresponding to the base flow) to 2) a reflectional symmetry steady state (SS), 3) a reflectional symmetry preserving (RSP) oscillatory state, and 4) a reflectional symmetry breaking (RSB) oscillatory state [4] [5]. Such transitions and resulting wake structures exhibit similarities with wakes that develop downstream blunt-based axisymmetric bluff bodies [6] [7]. However this geometry is still poorly documented despite its practical interest and a lack of comprehension subsists regarding the scenario that leads to a chaotic state.

In order to decipher this scenario, we have conducted 3D direct numerical simulations of the flow past a blunt-based axisymmetric bluff body of length-to-diameter ratio $L/D = 7$ for Reynolds numbers $100 < Re < 800$, spanning the transitions up to chaos.

2 Numerical Methods

The three-dimensional time-dependent incompressible Navier-Stokes equations around a blunt-based axisymmetric bluff body of diameter D and length L are directly solved using an Eulerian finite volume method [8]. The Reynolds number Re, based on D and on the free stream velocity U_∞, is varied from 100 to 800.

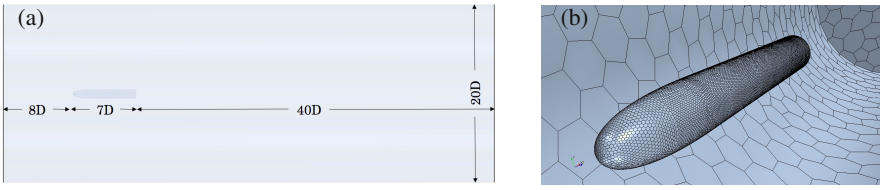

Fig. 1 Computational domain (a) and illustration of the surfacic polyhedral mesh (b)

The geometry consists of a 4:1 semi-elliptic nose and a cylindrical aft section. It is enclosed in a cylindrical computational domain of diameter $20D$ and length $55D$ aligned with the free stream direction **x** (figure 1a). The coordinates' origin is

located at the nose tip of the body, corresponding to the stagnation point. The inlet boundary is located at $x/D = -8$ and is subjected to a uniform velocity Dirichlet condition. A similar condition is imposed on the tubular surface of the computational domain. A zero diffusion flux condition is prescribed at the outlet boundary located at $x/D = 47$. The surface of the blunt-based axisymmetric bluff body is modelled as non-slip surface. The domain is composed of 2.3×10^6 polyhedral cells (figure 1b).

The spatial and temporal discretizations are achieved using second-order upwind schemes and second-order implicit time-stepping method respectively [8]. The pressure-velocity coupling is obtained using a SIMPLE algorithm. Time step is fixed in order to satisfy the CFL condition (Courant Number close to unity) for each Reynolds number. As an example non dimensional time step $\Delta t^+ = \Delta t U_\infty / D = 0.06$ at $Re = 800$.

3 Results

3.1 Steady States

Figure 2 illustrates a sequence of the flow topology obtained for *Re* numbers ranging from 100 to 450, in terms of iso-surfaces of normalized λ_2^+ [9] (normalization is based on the minimum value of λ_2 for each Reynolds number considered).

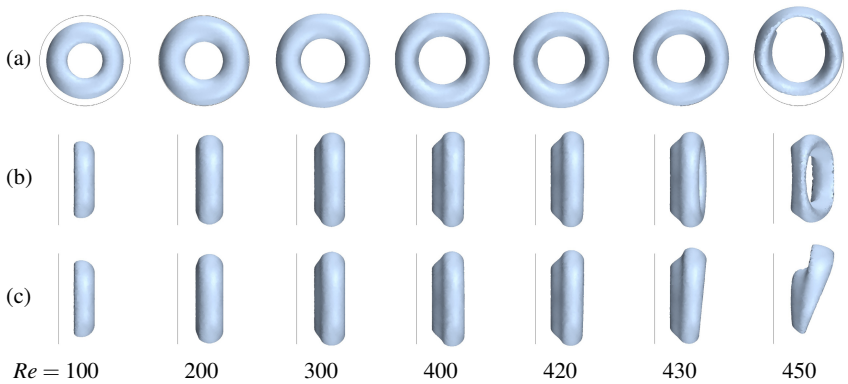

Fig. 2 Iso-surfaces of $\lambda_2^+ = 0.02$ obtained for *Re* numbers ranging from 100 to 450. Solid line depicts the base of the bluff body. (a), (b) and (c) correspond to rear, lower and side views respectively.

At $Re = 100$, figure 2 depicts an opened torus of revolution at the base of the body. The associated recirculation region is axisymmetric. Between $Re = 100$ and $Re = 400$ the torus radially expands towards the external flow and progressively stretches along the streamwise direction. This scenario results from the concomitant

influence of strong shear and suction effects on the torus. While the low-pressure region maintains the opened torus close to the bluff body base, the external flow tends to stretch the periphery of the opened torus.

As the Reynolds number is increased up to $Re \approx 450$ the torus progressively shifts away from the bluff body axis of revolution. Hence, the upper part of the torus is subjected to stronger shear than the lower part, such that it distorts into a pelvis-like structure. This is associated with the loss of axisymmetry of the torus, corresponding to the destabilization of the wake towards the reflectional symmetry steady state (SS). At this stage only a single streamwise planar symmetry is retained whose azimuthal position fixes randomly.

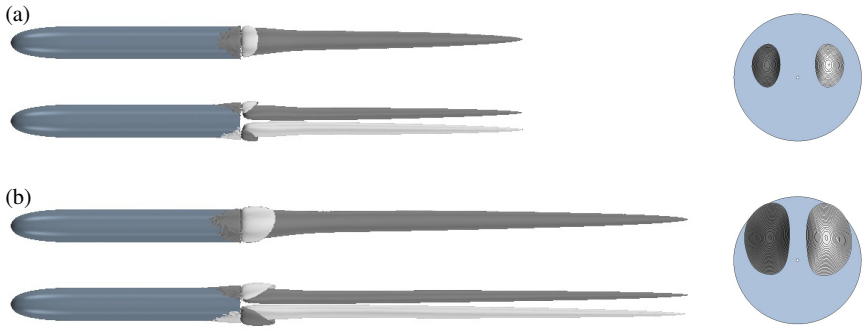

Fig. 3 Normalized streamwise vorticity $\omega^+ = \omega D/U_\infty$ obtained for *Re* numbers 450 (a) and 550 (b). Left: lower and side views of iso-surfaces $\omega^+ = \pm 0.05$. Right: rear view of isolines $|\omega^+| \in [0.05; 0.15]$ obtained at $x/D = 14$ (dark: positive, light: negative).

The streamwise vorticity fields provide additional information on the topology of the flow where the asymmetry is reflected as a 'double-threaded' wake composed of two primary vorticity lobes distributed on both sides of the reflectional symmetry plane (figure 3). Secondary and ternary vorticity lobes of alternate vorticity signs are also observed in the near wake and on the body aft surface respectively. As the Reynolds number is further increased, the tails of the primary vorticity lobes elongate and shift away from the axis of revolution of the bluff body (see also [7]), in accordance with the pelvis-like structure displacement and distortion under free stream-induced shear stresses. At this stage the pelvis-like structure is subjected to increasing shear stresses in conjunction with its displacement towards the external flow.

3.2 RSP Oscillatory States

Eventually as the Reynolds number reaches values close to 590, the structure can no more sustain such stresses and is partially torn. This leads to the formation of

unsteady hairpin structures periodically shed in the wake of the blunt-based axisymmetric bluff body (figure 4(a: right)). The reflectional symmetry is still preserved, denoting the transition from the SS state to the RSP oscillatory state. Figure 4(a: left) depicts iso-surfaces of streamwise vorticity ω^+ at $Re = 600$. It displays regularly spaced vorticity lobes shed at a non-dimensional frequency $St_a = f_a D/U_\infty \approx 0.12$. At this stage the flow exhibits a unique dominant frequency, revealed in figure 5(a) by a single fundamental peak (and its first harmonic) on the FFT of the drag coefficient history. The fundamental peak amplitude increases as Re is varied from 590 to 680. Hereafter this single frequency RSP state will be denoted RSP_a.

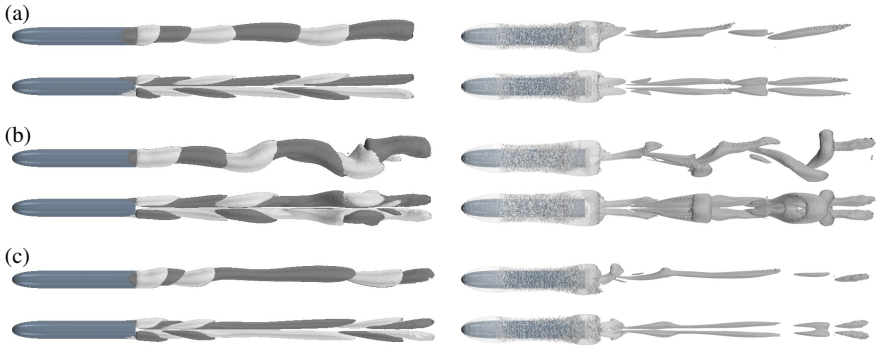

Fig. 4 Lower and side views of the flow structure obtained for Re numbers 600 (a), 700 (b) and 800 (c). Left: iso-surfaces $\omega^+ = \pm 0.05$ (dark: positive, light: negative). Right: iso-surfaces $\lambda_2^+ < 0$.

Beyond $Re = 690$ a second fundamental peak (and its first harmonic) arises at $St_b \approx 0.02$ (figure 5(b)), denoting the occurence of low frequency vorticiy bursts that promote the transient waving of the primary lobes and of the associated hairpin structures in the reflectional symmetry plane (figure 4(b)). The occurence of this second fundamental peak is accompanied with beating frequencies $St_a - St_b$ and $St_a + St_b$ that result from its coupling with the first fundamental peak. This double frequency RSP state will be denoted RSP_b. Note that the second to first fundamental peaks ratio increases with Re, which indicates that drag fluctuations, initially driven by the shedding of hairpin vortices at St_a are progressively dominated by the vorticity bursts and the associated transient waving of the wake at St_b.

Beyond $Re = 750$ a broadband noise appears on the FFT spectrum of the drag coefficient history (figure 5(c, d)), revealing the transition to chaos potentially induced by the occurence of a third fundamental frequency [10]. At this stage the analysis of this chaotic state deserves a deeper attention. To this avail a 12000 time units computation has been conducted at $Re = 800$, which roughly corresponds to the upper bound of the RSP_c state. Here the time unit is defined as $t^+ = tU_\infty/D$. This long term computation allows both a better resolution of the broadband noise and the capture of very low frequency instabilities. The prominent feature of the RSP_c state

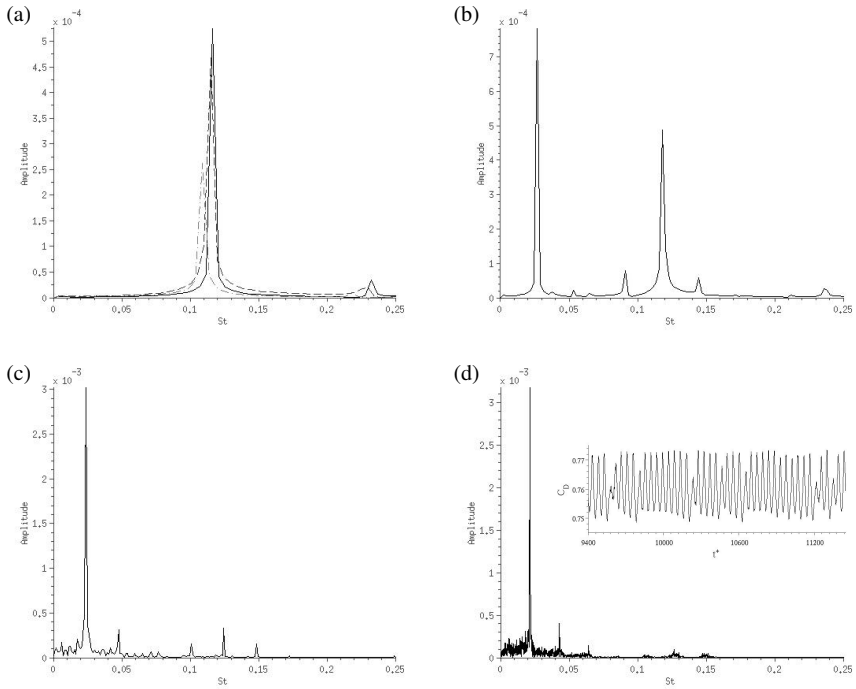

Fig. 5 FFT of the drag coefficient history obtained for *Re* numbers 600 (dotted line), 660 (dashed line), 680 (plain line) (a), 700 (b), 750 (c) and 800 (d)

is the transient stretching of the hairpin vortices in the streamwise direction (figure 4(c)), whose associated vorticity lobes remind the 'double-threaded' wake observed for the SS state. This could suggest a transient restabilization of the wake. It results in the damping of the drag oscillations, clearly observed on the drag coefficient history illustrated on the inset picture of figure 5(d). It is remarkable that this damping occurs intermittently. In that sense, this phenomenon is a marker of the chaotic state of the flow associated with the potential emergence of a third instability.

4 Conclusion

In this paper we have numerically investigated the flow past a blunt-based axisymmetric bluff body for *Re* numbers ranging from 100 to 800. On the basis of iso vorticity and λ_2 flow fields, drag coefficient time history and FFT, we have described the successive transitions that lead to a chaotic flow. In particular the dynamics of the recirculation region from an axisymmetric torus (base flow) to a pelvis-like structure (SS state) and the subsequent hairpin vortex shedding (RSP state) have been detailed. In addition we have shown that the RSP state can be subdivided into three substates, whether the flow unsteadiness is characterized by a single fundamental

frequency (RSP_a), two distinct fundamental frequencies (RSP_b) or a chaotic dynamics (RSP_c). The latter exhibits flow intermittencies associated with the transient stretching of the hairpin structures and the damping of the drag oscillations.

References

1. Kim, J., Choi, H.: Distributed forcing of the flow over a circular cylinder. Phys. Fluids 17, 033103 (2005)
2. Choi, H., Jeon, W.P., Kim, J.: Control of flow over a bluff body. Annu. Rev. Fluid Mech. 40, 113–139 (2008)
3. Jardin, T., Bury, Y.: Spectral and Lagrangian analysis of the forced flow past a circular cylinder using pulsed tangential jets. J. Fluid Mech. 696, 285–300 (2012)
4. Tomboulides, A.G., Orszag, S.A.: Numerical investigation of transitional and weak turbulent flow past a sphere. J. Fluid Mech. 416, 51–73 (2000)
5. Fabre, D., Auguste, F., Magnaudet, J.: Bifurcations and symmetry breaking in the wake of axisymmetric bodies. Phys. Fluids 20, 051702 (2008)
6. Schwarz, V., Bestek, H., Fasel, H.: Numerical simulation of nonlinear waves in the wake of an axisymmetric bluff body. In: 25th AIAA Fluid Dynamics Conference, AIAA-94:2285 (1994)
7. Bohorquez, P., Sanmiguel-Rojas, E., Sevilla, A., Jimenez-Gonzalez, J.I., Martinez-Bazan, C.: Stability and dynamics of the laminar wake past a slender blunt-based axisymmetric body. J. Fluid Mech. 676, 110–144 (2011)
8. Shams, A., Roelofs, F., Komen, E.M.J., Baglietto, E.: Quasi-direct numerical simulation of a pebble bed configuration. Part I: Flow (velocity) field analysis. Nucl. Eng. Des. (2012)
9. Jeong, J., Hussain, F.: On the identification of a vortex. J. Fluid Mech. 285, 69–94 (1995)
10. Eckmann, J.P.: Roads to turbulence in dissipative dynamical systems. Rev. Mod. Phys. 53, 643–654 (1981)

Direct Numerical Simulations of Turbulent Convection and Thermal Radiation in a Rayleigh-Bénard Cell with Solid Plates

Tomasz Czarnota and Claus Wagner

Abstract. In the present study the effect of the surface to surface radiation on the turbulent convection of air (Prandtl number $Pr = 0.7$) in a rectangular Rayleigh-Bénard cell is analysed by means of direct numerical simulations. In order to investigate the influence of the radiative boundary conditions on the temperature distribution, heat transfer and the flow intensity, a horizontal, poorly conducting walls with finite thickness are employed. Additionally, the influence of the radiative parameters is shown for Rayleigh number $Ra = 6.3 \times 10^7$. We notice that the temperature at the warm interface decreases and it increases at the cold interface. Thus, the lower temperature difference appears what reduces the flow intensity. We observe that radiation causes a drop of convective heat flux however, the overall heat transfer increases due to high radiative heat flux. All the effects of radiation are stronger for higher conduction-radiation numbers and for higher temperature ratios.

1 Introduction

Turbulent Rayleigh-Bénard convection (RBC) is one of the classical problems of fluid dynamics. Despite the great effort made in the past to understand the complex physical mechanisms in this type of flow, there are still many open questions which must be answered. Additionally, the role of thermal radiation was not addressed in most studies although it is of interest in many engineering applications such as combustion, fire and plumes or solar collectors. One reason might be that thermal radiation modelling is computationally expensive. One possibility to decrease this effort in numerical simulations of heat radiation and turbulent convection is to assume that the radiation does not depend on the wavelength and additionally approximate its directional nature by diffuse emission. Nevertheless, the intensity of irradiation still

Tomasz Czarnota · Claus Wagner
Institute for Aerodynamics and Flow Technology
German Aerospace Center (DLR), Göttingen, Germany
e-mail: Tomasz.Czarnota@dlr.de

M.O. Deville et al. (eds.), *Turbulence and Interactions*,
Notes on Numerical Fluid Mechanics and Multidisciplinary Design 125,
DOI: 10.1007/978-3-662-43489-5_5,

depends on the geometrical features and thermal properties of radiatively interacting surfaces. The effect of conductive horizontal plates was investigated in many experimental and numerical studies (see [3], [5], [10]). Fixed temperature boundary conditions correspond to an infinite thermal conductivity of the plates while an imposed heat flux can be considered as a model for poorly conducting plates. The above mentioned studies indicate that the heat transfer is suppressed for $Ra > 10^9$ in simulations with plates of finite conductivity whereas for lower Ra the two boundaries lead to a similar flow. Apart from that, the numerical simulations of the flow in a square cavity filled with air, with gray surfaces heated and cooled from the sides were performed by [1] and [2]. They noticed that the convective heat transfer is suppressed due to surface radiation, and that the radiative heat transfer at the heated and cooled walls increases with the emissivity of the walls. [1] also noted that surface radiation altered the temperature distribution inside the cavity and the flow patterns. However, [1] and [2] performed the simulations for steady, laminar and two-dimensional (2D) flow while we conduct DNS of the 3D, turbulent convection. Additionally, the results of [5] or [10] as well as those of [1] and [2] refer to a cell with infinitely thin plates while the finite thickness of the plates is modelled in our computations. Such boundary conditions allow changes of the temperature at the hot and cold interfaces due to turbulent convection and surface radiation.

2 Numerical Procedure

The considered governing equations are the incompressible Navier–Stokes equations derived under the assumption of the Boussinesq approximation. Their non-dimensionalisation is carried out using $x_i = \hat{x}_i/\hat{H}$, $u_i = \hat{u}_i/(\hat{\alpha}\hat{g}\hat{\Delta T}\hat{H})^{1/2}$, $T = (\hat{T}-\hat{T}_0)/\hat{\Delta T}$, $p = \hat{p}/(\hat{\rho}\hat{\alpha}\hat{g}\hat{H}\hat{\Delta T})$ and $t = \hat{t}(\hat{\alpha}\hat{g}\hat{H}\hat{\Delta T})^{1/2}/\hat{H}$, where $\hat{\alpha}$ is the thermal expansion coefficient and $\hat{\rho}$ is the density. $\hat{g}$ represents the gravitational acceleration which acts in vertical z-direction. $\hat{T}$ and $\hat{T}_0$ state for the temperature and the mean bulk temperature, respectively. $\hat{\Delta T}$ denotes the temperature difference between the outer sides of the heating and cooling plates and $\hat{H}$ is the height of the fluid layer. We mark dimensional quantities with $\hat{}$ and dimensionless without. Finally, the dimensionless form of the governing equations is given by equation (1) – (2).

$$\frac{\partial u_j}{\partial x_j} = 0 \qquad \frac{\partial u_i}{\partial t} + u_j\frac{\partial u_i}{\partial x_j} + \frac{\partial p}{\partial x_i} = \left(\frac{Pr}{Ra}\right)^{1/2}\frac{\partial^2 u_i}{\partial x_j^2} + T\,\delta_{3i} \tag{1}$$

$$\frac{\partial T}{\partial t} + u_j\frac{\partial T}{\partial x_j} = (RaPr)^{-1/2}\frac{\partial^2 T}{\partial x_j^2} \tag{2}$$

Here, $u_i (i = x, y, z)$ are the velocity components in i-direction, T and p represent the temperature and pressure, respectively, and δ_{ij} is the Kronecker symbol. The dimensionless control parameters, Prandtl and Rayleigh numbers, are defined by equation (3) where $\hat{\nu}$ is a kinematic viscosity and $\hat{\kappa}_f$ thermal diffusivity of the fluid.

$$Pr = \hat{\nu}/\hat{\kappa}_f \qquad Ra = \hat{\alpha}\hat{g}\hat{H}^3\hat{\Delta T}/(\hat{\nu}\hat{\kappa}_f) \tag{3}$$

In addition, the heat transfer through the solid plates is computed by solving the conduction equation

$$\frac{\partial T}{\partial t} = (RaPr)^{-1/2} \frac{\hat{\kappa}_s}{\hat{\kappa}_f} \frac{\partial^2 T}{\partial x_j^2} \tag{4}$$

where $\hat{\kappa}_s$ is a thermal diffusivity of the solid plates. In considered simulations the solid plates are made out of a poorly conducting material, for which Plexiglas is a common representative, and the working fluid is air (Pr = 0.7). The thermal diffusivity of Plexiglas $\hat{\kappa}_s = 7.49 \times 10^{-8} m^2/s$ and that of air $\hat{\kappa}_f = 2.216 \times 10^{-5} m^2/s$. We conduct direct numerical simulations (DNS) in a rectangular domain of length $\hat{L} = 5\hat{H}$ and aspect ratio $\Gamma = \hat{W}/\hat{H} = 1$, where $\hat{W}$ stands for the width of the enclosed fluid. The dimensionless thickness of the heating and cooling plates equals $h_s = 0.065$. No-slip and impermeability conditions are applied to all solid walls. The outer sides of the top and bottom solid plates are isothermal with non-dimensional temperatures $T_{top} = -0.5$ and $T_{bot} = +0.5$, respectively. The lateral walls are adiabatic with respect to conduction, and the irradiation which reaches a surface on the side walls is completely transmitted to the ambient environment outside the cell (transmissivity $\tau = 1$). Further, this radiation loss is compensated by the incoming radiation calculated by equation (8) based on the constant temperature outside the cell $\hat{T}_{out}$. Finally, we assume that the ambient temperature outside the cell is equal to the mean temperature in the bulk, i.e. $\hat{T}_{out} = \hat{T}_0 = 0.5(\hat{T}_{bot} + \hat{T}_{top})$. The boundary conditions at the solid-fluid interfaces impose the same heat flux on both sides of the interface. To simplify the problem and to maximise effect of these boundary conditions, both interfaces are treated as a blackbody (emissivity $\varepsilon = 1$) and the cell is filled with a radiatively non-participating fluid. Finally, the boundary conditions at the bottom interface are described by equation (5) and the solution of this equation determines the temperature at the bottom interface.

$$\hat{q}_{c,s} + \hat{q}_{ir} = \hat{q}_{c,f} + \hat{q}_e \tag{5}$$

Here, $q_{c,s}$ and $q_{c,f}$ represent conductive heat fluxes from the solid and fluid side of the interface, respectively, and they are given by equation (6) in which $\hat{k}_s$ and $\hat{k}_f$ denotes the thermal conductivity of the solid and fluid layer, respectively.

$$\hat{q}_{c,s} = -\hat{k}_s \frac{\partial \hat{T}}{\partial \hat{x}}\bigg|_{s.side} \qquad \hat{q}_{c,f} = -\hat{k}_f \frac{\partial \hat{T}}{\partial \hat{x}}\bigg|_{f.side} \tag{6}$$

Further, the two radiative heat fluxes which appear in equation (5), i.e. q_e and q_{ir} describe diffuse emission from the interface and the total irradiation coming to the interface, respectively. These fluxes are defined by equation (7) – (8) and are only solved if thermal radiation is considered in the simulation.

$$\hat{q}_e = \hat{\sigma} \hat{T}_i^4 \tag{7}$$

$$\hat{q}_{ir} = \hat{\sigma} \hat{T}_{out}^4 (1 - \sum_{S_i} F_{ij}) + \sum_{S_j} \hat{\sigma} \hat{T}_j^4 F_{ij} \tag{8}$$

In equation (8) summation over the surface element S_j is done for all boundary elements which radiatively interact with the element i. The view factors F_{ij} are determined by a geometry function, and they are calculated according to [4]. Including equation (7) and (8) in the boundary conditions for radiation implies, that additional control parameters have to be fixed, namely the conduction-radiation number Nr and the temperature ratio θ defined by (9). Their values for different radiation cases are given in table 1.

$$Nr = \hat{\sigma}\hat{\Delta T}^3 \hat{H}/\hat{k}_f \qquad \theta = \hat{T}_0/\hat{\Delta T} \tag{9}$$

The finite volume method used to solve the governing equations is based on the volume balance procedure by [7] and the second order accurate explicit Euler-Leapfrog time discretization scheme. Spatial derivatives and cell face velocities are approximated by piecewise integrated fourth-order accurate polynomials as described in more detail in [8]. In order to sufficiently resolve the boundary layers the minimum number of nodes in the thermal boundary layer is estimated with the criterion by [9] which provides the needed grid points to sufficiently resolve a Prandtl–Blasius type boundary layer. The grid spacing needed to resolve all relevant turbulent scales in the core region is in every direction smaller than the Kolmogorov scale. Finally, to satisfy the above requirements, performing our simulations for the Rayleigh number $Ra = 6.3 \times 10^7$, we use at least 13 grid points to resolve the thermal boundary layer and $256 \times 256 \times 1024$ grid points in vertical, spanwise and longitudinal direction, respectively. The convective heat flux, represented by the Nusselt number Nu_c, is calculated for both radiation and no-radiation cases with equation (10).

$$Nu_c = \frac{\langle \hat{u}_z \hat{T} \rangle_{S_z} - \hat{\kappa}_f \langle \frac{\partial \hat{T}}{\partial \hat{x}_z} \rangle_{S_z}}{\hat{\kappa}_f \hat{\Delta T}/\hat{H}} = (RaPr)^{1/2} \langle u_z T \rangle_{S_z} - \langle \frac{\partial T}{\partial x_z} \rangle_{S_z} \tag{10}$$

where $\langle \cdot \rangle_{S_z}$ denotes averaging in vertical z direction. Additionally, at the interfaces, convection and radiation contribute to Nu. Thus, the total Nu at the interfaces for each i-th surface is calculated as $Nu = Nu_c + Nu_r$, where Nu_r reads

$$Nu_r = \frac{\hat{\sigma}\hat{T}_i^4 - \sum_{S_j} \hat{\sigma}\hat{T}_j^4 F_{ij}}{\hat{\kappa}_f \hat{\Delta T}/\hat{H}} = Nr(T_i + \theta)^4 - \sum_{S_j} Nr(T_j + \theta)^4 F_{ij} \tag{11}$$

3 Results

Time averaged temperature fields at the bottom (warm) interface obtained for the cases with and without radiation are shown in figure 1. These fields reflect the fingerprints of the time averaged flow structures. Radiation broadens the structures and makes the temperature more uniform. Increasing temperature ratio θ or the conduction-radiation number Nr emphasises this effect. In figure 2 time and area averaged temperature profiles are plotted. We observe that the temperature at the bottom interface decreases with increasing conduction-radiation number Nr and the temperature ratio θ. Further, for all cases with radiation the temperature at the

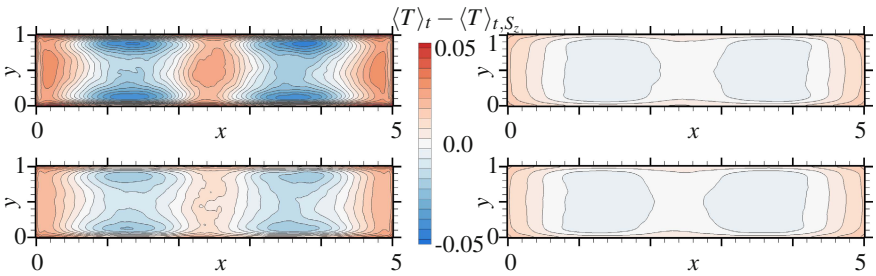

Fig. 1 Time averaged distribution of T at the bottom interface; no-radiation (left, upper fig.), radiation #1 (left, lower fig.), radiation #2 (right, upper fig.), radiation #3 (right, lower fig.)

Table 1 Time and volume averaged convective Nusselt number $\langle Nu_c\rangle_{t,V}$. In addition, time and area averaged temperature with spatial deviations; convective, radiative and total Nusselt number ($\langle Nu_c\rangle_{t,S_z}, \langle Nu_r\rangle_{t,S_z}, \langle Nu\rangle_{t,S_z}$) at the bottom interface.

θ | Nr:	no-radiation	radiation #1 29 | 8×10^{-4}	radiation #2 29 | 3×10^{-3}	radiation #3 45 | 8×10^{-4}
$\langle Nu_c\rangle_{t,V}$	16.78±0.017	9.82 ±0.035	4.36 ±0.005	3.87 ±0.002
$\langle T\rangle_{t,S_z}$	0.34 ±0.022	0.22 ±0.013	0.12 ±0.006	0.11 ±0.006
$\langle Nu_c\rangle_{t,S_z}$	16.76±2.983	9.74 ±2.210	4.37 ±1.148	3.87 ±1.024
$\langle Nu_r\rangle_{t,S_z}$	–	22.6 ±0.791	40.2 ±0.750	42.4 ±0.753
$\langle Nu\rangle_{t,S_z}$	16.76	32.34	44.57	46.27

bottom interface is colder than for no-radiation case and the temperature at the top interface is warmer. This observation is consistent with the analytical solutions presented by [6]. The results by [1] and [2] obtained for a steady and laminar 2D-flow show that the temperature distribution inside the cavity heated from the sides is altered by radiation. We found that for poorly conducting plates radiation influences the temperature distribution near the plates. However, the mean temperature in the bulk is only slightly affected because the absolute values of time and area averaged temperature at the bottom and top interface $|\langle T\rangle_{t,S_z}|$ are very similar (see figure 2). The spatial deviations of the temperature at the bottom interface are shown in table 1. We observe that radiation decreases the temperature variations leading to more homogeneous temperature distribution at the bottom interface.

Analysis of the Nusselt number shown in table 1 reveals a drop of the time- and volume-averaged convective Nusselt number $Nu_c\rangle_{t,V}$ for all radiation cases. The similar effect was noted by [1] and [2]. Additionally, this drop is stronger for higher conduction-radiation numbers and higher temperature ratios, and in each case is largely compensated by the contribution of radiation. The magnitude of radiative Nusselt number increases with increasing conduction-radiation numbers and with increasing temperature ratios. The distribution of the convective part of the Nu calculated at the bottom interface for the cases with and without radiation is presented

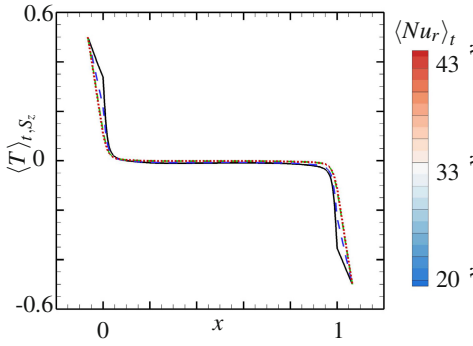

Fig. 2 Time and area averaged temperature profiles; no-radiation (—), radiation #1 (– –), radiation #2 (- -), radiation #3 (. . .)

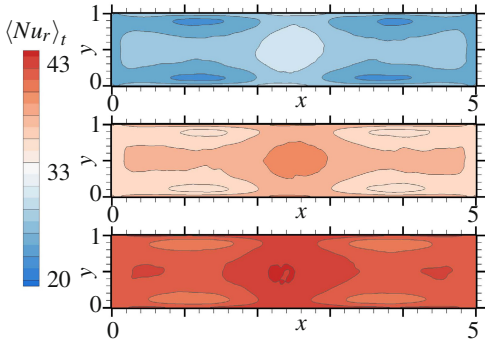

Fig. 3 Time averaged distribution of Nu_r at the bottom interface; radiation #1 (upper fig.), radiation #2 (middle fig.), radiation #3 (lower fig.)

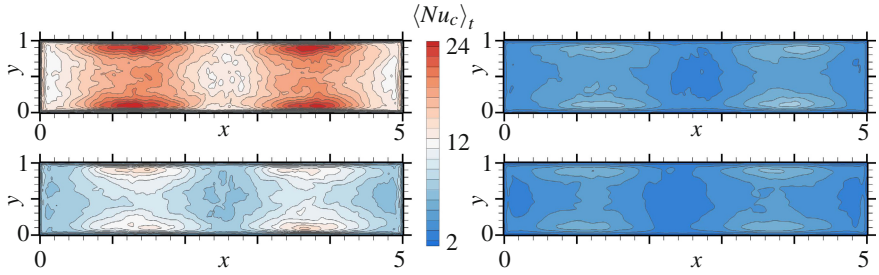

Fig. 4 Time averaged distribution of Nu_c at the bottom interface; no-radiation (left, upper fig.), radiation #1 (left, lower fig.), radiation #2 (right, upper fig.), radiation #3 (right, lower fig.)

in figure 4. We observe that the largest convective Nusselt number appears close to the lateral lengthwise walls and that their lowest values are located close to the widthwise walls and in the centre of the interface. On the other hand, the strongest radiative Nusselt number appears in the centre of the bottom interface for all considered radiation cases (see figure 3). Finally, we conclude that the stronger the convective drop, the higher is radiative heat flux with its maximum in the centre of the interface. Thus, the overall heat transfer is higher for radiation cases than for a pure turbulent convection independently of the radiation parameters (see table 1).

Turbulence intensities are plotted in figure 5. We observe that radiation reduces the temperature and velocity fluctuations in the boundary layers and in the bulk. Additionally, increasing the conduction-radiation number or increasing the temperature ratio causes further a decrease of turbulence intensities.

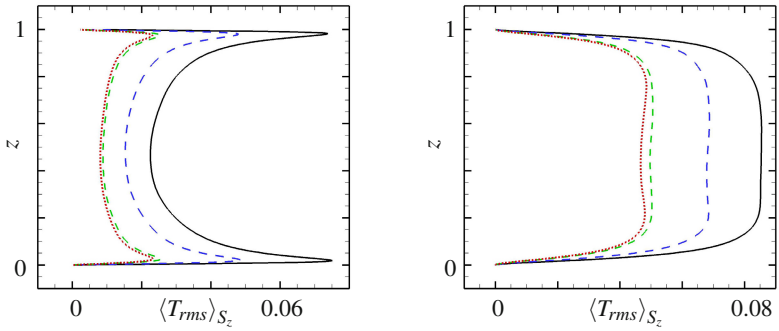

Fig. 5 Profiles of time and area averaged r.m.s. temperature and u-velocity fluctuations; left and right figure respectively; no-radiation (—), radiation #1 (– –), radiation #2 (- -), radiation #3 (. . .)

4 Conclusions

The effect of surface to surface radiation on the turbulent convection of air in a RB cell with horizontal, poorly conducting plates is analysed by means of 3D DNS. We found that the overall temperature value at the warm solid-fluid interface decreases due to radiative heat loss and it increases at the cold solid-fluid interface due to radiative heat gain. Thus, the lower temperature difference slows down the buoyancy driven flow. We observe that radiation causes a drop of convective Nu. Nevertheless, the overall heat transfer increases due to the high radiative Nu with its maximum in the centre of the interface. All the effects of radiation are stronger for higher conduction-radiation numbers and for higher temperature ratios.

References

1. Akiyama, M., Chong, Q.P.: Numerical analysis of natural convection with surface radiation in a square enclosure. Numerical Heat Transfer, Part A: Applications 32(4), 419–433 (1997)
2. Balaji, C., Venkateshan, S.P.: Interaction of surface radiation with free convection in a square cavity. Int. J. Heat Fluid Flow 14(3), 260–267 (1993)
3. Brown, E., Nikolaenko, A., Funfschilling, D., Ahlers, G.: Heat transport in turbulent Rayleigh-Bénard convection: Effect of finite top- and bottom-plate conductivity. Phys. Fluids 17, 075108 (2005)
4. Incropera, F.P., DeWitt, D.P., Bergman, T.L., Lavine, A.S.: Fundamentals of Heat and Mass Transfer, 6th edn. (2006)
5. Johnston, H., Doering, C.R.: Comparison of Thermal Convection between Conditions of Constant Temperature and Constant Flux. PRL 102, 064501 (2009)
6. Lienhard V, J.H.: Thermal radiation in Rayleigh-Bénard instability. Journal of Heat Transfer 112(1), 100–110 (1990)
7. Schumann, U., Grötzbach, G., Kleiser, L.: Direct numerical simulations of turbulence. In: Prediction Methods for Turbulent Flows Number. VKI-lecture series, vol. 2, Von Kármán Institute for Fluid Dynamics (1979)

8. Shishkina, O., Wagner, C.: Boundary and interior layers in turbulent thermal convection in cylindrical containers. Int. J. Sci. Comp. Math. 1(2/3/4), 360–373 (2007)
9. Shishkina, O., Stevens, R.J.A.M., Grossmann, S., Lohse, D.: Boundary layer structure in turbulent thermal convection and its consequences for the required numerical resolution. New J. Phys. 12, 075022 (2010)
10. Verzicco, R., Sreenivasan, K.R.: A comparison of turbulent thermal convection between conditions of constant temperature and constant heat flux. J. Fluid Mech. 595, 203–219 (2008)

Turbulent Simulation of the Flow around Two Cylinders in Tandem Configuration

T. Deloze, F. Deliancourt, Y. Hoarau, and M. Braza

Abstract. The turbulent flow around a generic configuration of a landing gear (the tandem cylinders) is simulated and analysed physically at $Re = 1.66\ 10^5$, by means of hybrid RANS-LES turbulence modelling approaches. In the present study, the Delayed Detached Eddy Simulation (DDES) approach has been employed for two cylinders spaced of $3.7D$ and with a spanwise lentgh of $4D$. The DDES-OES modelling has been considered, especially involving turbulence length scale reconsiderations in the statistical part, by means of the Organised Eddy Simulation, (OES), to take into account non-equilibrium turbulence effects. The results are compared with experiments carried out at the NASA Langley Research Centre in the context of ATAAC EU-program in which the tandem cylinders is one of the stepping stones. In the present study, the benefits of these hybrid approaches have been discussed for capturing the vortex dynamics and frequency modes responsible for aerodynamic noise production in the context of landing gear configurations.

1 Introduction

Within the ATAAC (Advanced Turbulence Simulations for Aerodynamic Application Challenges) EU program, it has been shown through its main test–cases, that DDES (Delayed Detached Eddy Simulation) is a promising approach to capture the unsteady dynamics and the turbulence statistical content in strongly detached unsteady flows, by using reasonably fine grids, comparing to the grid sizes that would be needed by LES, for the present high-Reynolds number range flows around bodies, involving strong detachment. The present configuration highly interests

T. Deloze · F. Deliancourt · M. Braza
IMFT UMR-5502 CNRS-INPT-UPS, Allée du Prof. Camille Soula,
F-31400 Toulouse, France
e-mail: tdeloze@imft.fr

Y. Hoarau
Icube, Université de Strasbourg - C.N.R.S., 2 rue Boussingault, F-67000 Strasbourg, France
e-mail: hoarau@unistra.fr

M.O. Deville et al. (eds.), *Turbulence and Interactions*,
Notes on Numerical Fluid Mechanics and Multidisciplinary Design 125,
DOI: 10.1007/978-3-662-43489-5_6, © Springer-Verlag Berlin Heidelberg 2014

aeroacoustics and aerodynamic noise control, generated by the two supports (tandem cylinders) of a generic configuration of a landing gear. The present test case has been the object of detailed experimental and numerical studies led by the NASA Langley Research Center, (Jenkins et al [5], Lockard [7, 8], among other). The experiments were carried out by standard 2D PIV, at Reynolds number 166 000. In order to avoid natural transition development, the experiments applied two transition strips at two specific upstream locations. A first synthesis of numerical simulations carried out for this test case was carried out by Lockhard, regrouping an order of 13 contributions involving different modelling approaches, as well as previous simulations by Khorrami et al. [6] using URANS kω-SST of Menter (Menter Shear Stress Transport Turbulence Model, Menter [9]). These simulations indicated that the majority of the approaches captured quite well the Strouhal number of the vortex shedding frequency around the first cylinder, ($St = 0.24$) . Furthermore, as is seen in the ATAAC European program, the DES approaches better capture the complex vortex dynamics of the present flow, especially the formation of Kelvin-Helmholz vortices in the separated shear layers. In the experimental context, it was found that the shear layers formed downstream of the first cylinder wrap around the second cylinder and interact non-linearly with the complex turbulence background, producing predominant frequencies in the energy spectrum, in the range of acoustic noise.

The aim of the present paper is to evaluate the ability of the DDES methodology for an accurate prediction of the pressure fluctuations and frequencies responsible for the acoustic noise. In the present study, the DDES approach is considered, involving OES modelling (Braza et al. [3]), in the URANS part, accounting for improvement of the near region flow physics in respect of non-equilibrium turbulence. In Bourguet et al. [2], the DES-OES modelling was successfully applied for the simulation of the strongly detached flow around an airfoil beyond stall. The present DDES-OES, as the previous one, aims at providing a smooth passage from the URANS towards the LES region of flow detachment and at keeping the statistical region extent quite significant around the body.

2 Description of the Test Case

The test case is composed of two cylinders in in–line tandem configuration (see figure 1). The diameter (D) is identical for the both cylinders and the distance between the cylindres (center to center) is equal to $L = 3.7D$. The Reynolds number ($Re = U\ D/\nu$) associated with the diameter D is $Re = 166000$. The height of the cylinders is $H = 4D$. The Mach number is $Ma = 0.128$, corresponding to an incompressible flow. The Reynolds number is subcritical but it is close to the drag crisis.

The experiments with the same parameters were conducted at the NASA Langley Basic Aerodynamic Research Tunnel (BART), which is a subsonic, atmospheric wind tunnel. The free stream velocity was set to 44m/s. The velocities correspond to a Reynolds number based on the cylinder diameter of $Re = 166000$ and the distance

between the cylinders is $L = 3.7D$. The difference with the present numerical study is the height of cylinder equal in the experiments to $H = 16D$. The free stream turbulence level at these conditions is about 0.09%. Figure 1 shows schematically the configuration with the tandem cylinders placed in the wind tunnel, as well as a sketch of the computational domain used.

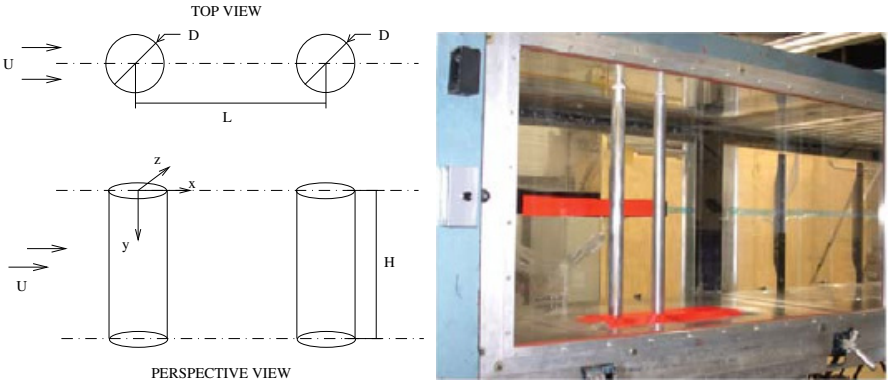

Fig. 1 Schematic representation of the two cylinders in in-line tandem arrangement (left) and picture of NASA experiment (right) for the dimensionless parameters $L = 3.7D$, $Re = 166000$

3 Numerical Method and Turbulence Modeling

The simulations have been performed with the NSMB solver, (Navier-Stokes Multi Block), based on structured grids architecture. IMFT is part of the NSMB consortium (Vos et al. [10]), contributing with turbulence modelling development for strongly detached unsteady aerodynamic flows. For the present simulations, central difference scheme has been applied, among the variety of spacial discretisation schemes available in the solver, after performing detailed tests (Barbut [1], Gual et al. [4]). Dual time stepping is used for the temporal discretisation. The computational grid is of 16 millions of finite volumes. The closest point to the wall at the second cylinder is at a distance of $y/D = 3.0\,10^{-5}$. The computations, using 512 processors in the present study, have been carried out at the SGI Altix supercomputer JADE of CINES, ("Centre Informatique National de l'Enseignement Supérieur") and at the supercomputer CURIE of the CEA ("Commissariat à l'énergie atomique et aux énergies alternatives") of France.

The time step is equal to $\Delta t = 0.001$ in order to be able to allow resolution of frequencies corresponding to a Strouhal number of order $St = 0.25$ and of higher frequencies predominant peaks due to Kelvin-Helmholtz eddies, responsible for the acoustic noise.

The turbulence modelling is the DDES approach, in which the RANS turbulence length scale is improved by means of the Organised Eddy Simulation (Braza et al. [3]). It is recalled that distinction of coherent and chaotic turbulent structures is

performed in OES by dual spectrum splitting, solving the ensemble-averaged Navier-Stokes equations, where the turbulence stresses are modelled by modified turbulence scales modelling (as presented schematically in the figure 2).

The fact that part of the spectrum to be modeled in OES extend from the low to the high frequencies allows the use of statistical turbulence modeling with appropriate modification due the non-equilibrium. In the time-domain, the equations are the phase-averaged Navier-Stokes equations. Due to the nonlinear interaction between the coherent part and the incoherent one, there is a slope modification of the inertial part in the spectrum, in the vicinity of the peak. This yields to a reconsideration of the Eddy-diffusion coefficient for the class of the two-equation modeling, as well as improved damping functions to attenuate turbulence towards the wall.

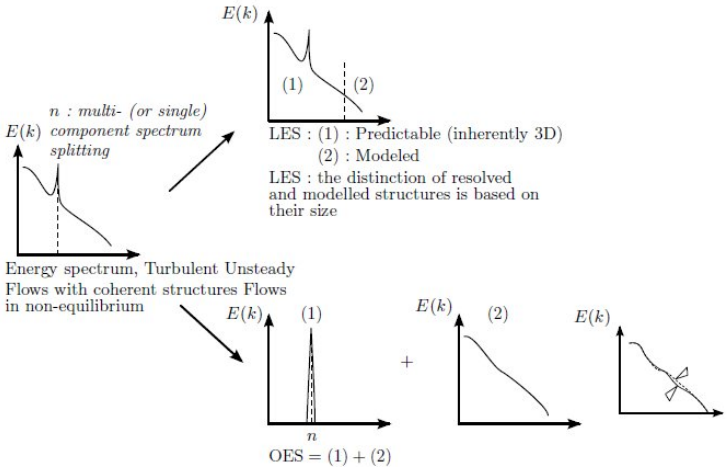

Fig. 2 Dual spectrum splitting : the distinction between the structures to be resolved and those to be modeled is based upon their organised or random character. Part (2) of the non-equilibrium energy spectrum has to be modeled by reconsidering advanced statistical turbulence modeling efficient in high-Re wall flows, due to the inertial-range modulation from equilibrium turbulence, schematically shown on the right.

4 Results

Figure 3 represents the instantaneous spanwise vorticity in the *y*-plane at the mid-height of the cylinder. The results obtained show a rich turbulence statistical content, as well as formation of alternating shear layers and the wrap around mechanism towards the second cylinder. The simulation shows a behavior qualitatively similar to that expected. The averaged streamlines field is shown in figure 3 (right) in comparison with the experiment. A good agreement with the experiments is achieved. It can be seen that the DDES–OES modelling provides fine shear layers, governed by the shedding of Kelvin–Helmholtz vortices, responsible for the acoustic noise.

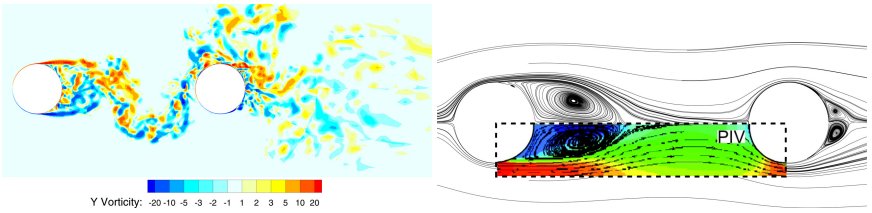

Fig. 3 Instantaneous spanwise vorticity contours (left) and averaged streamlines field for present study and NASA experiments (right)

Figure 4 shows the averaged pressure coefficient corresponding, where the pressure peaks values are quite closer to the experimental ones. Concerning the first cylinder, the averaged maximum pressure values are lower than in the experiment, while a better agreement is obtained for the second cylinder. In the numerical results, the detachment occurs earlier than experiments and can explain the lower pressure value.

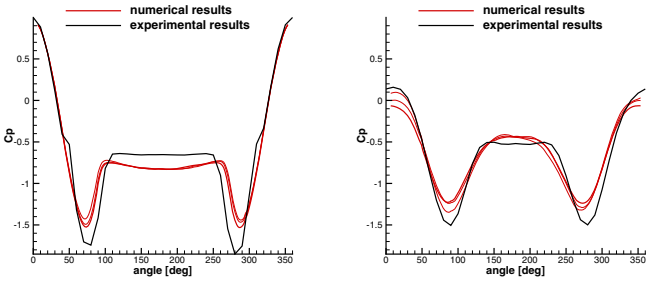

Fig. 4 Wall pressure coefficient (C_p) on the first cylinder (left) and the second one (right) compared with the experiment

The 2D turbulence kinetic energy ($2DTKE = \frac{1}{2}(< u' >< u' > + < v'v' >)/U_\infty^2$) is performed and plotted along the x–line (in the gap region and rear the cylinders) and along the z–line (cross-flow) (figure 5). On the same x–line, the time averaged x-velocity is plotted (figure 5). The results are in good agreement and especially on the time averaged x-velocity. The 2D turbulence kinetic energy shows the same behaviour but it quite over–estimated in the gap region and it is quite underestimated in the rear of cylinder.

The power spectral density are performed with the time-evolution of the pressure at four points (two points in the upstream cylinder at 135°and two points in the downstream cylinder at 45°) and represented at the figure 6. The turbulence spectra show the principal instability modes, among which the von Kármán mode, as well as formation of a spectral bump corresponding to the Kelvin-Helmholtz eddies. Of course, the chaotic turbulence effect provides the fact that these eddies are governed

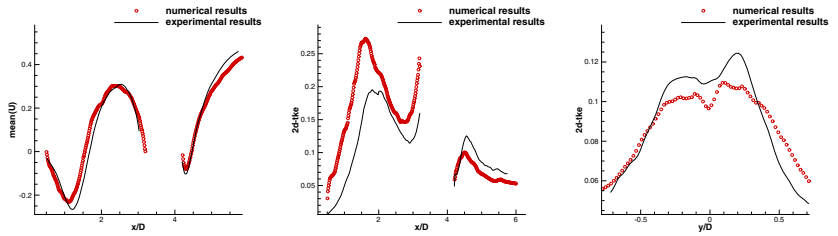

Fig. 5 Time-averaged velocity profile in the gap region and at the rear flow (left), the 2D turbulence kinetic energy following the same line (middle) and following the cross-line $x = 4.45$ (right)

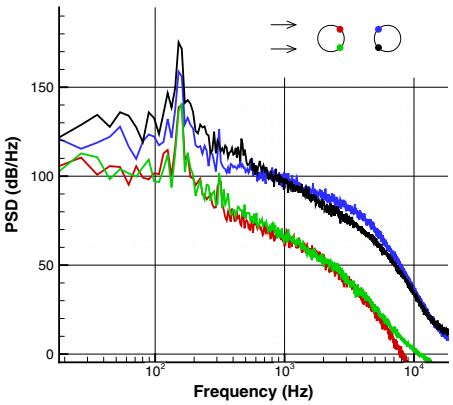

Fig. 6 Wall pressure spectra at four wall points on the first and second cylinder

by a random vortex smearing around a predominant Kelvin-Helmholtz (K-H) mode. The main frequency is identical for the four points and the value is $159Hz$ ($178Hz$ for experiment). This frequency corresponds to the von Kármán vortex shedding. The second peak corresponds to the second instability of Kelvin-Helmhotz with a frequency of $316Hz$ always seen by the four points (362 for experiment). A third peak is visible on the downstream cylinder ($476Hz$). We find similar frequencies to those obtained by experiment with a slight underestimation.

5 Conclusion

A numerical study has been carried out to analyze the complex vortex pattern around two cylinders in tandem at Reynolds number 166,000, by means of Hybrid Turbulence modelling approaches. The Delayed Detached Eddy Simulation DDES-SST has been applied and comparison of results with the experiment is carried out. The results have shown that the flow structure between the two cylinders and past the second cylinder are well produced by the present methods. The statistical content of

the DDES-OES is detailed and the shear layer interfaces are fine and contain a number of Kelvin-Helmholtz vortices. Moreover, the spectral analysis shows that the flow is mainly governed by the von Kármán mode. A reasonably good agreement with the experiments carried out in the NASA-Langley Research Center is shown, especially concerning the mean streamlines structure, velocities and predominant frequencies. The interaction between the von Kármán mode and the shear layer frequencies bump is quantified by means of advanced signal processing. The present study shows the ability of the DDES to simulate the present complex flow dynamics and predominant modes, associated with landing gear aerodynamic noise.

Acknowledgements. This work is part of the ATAAC research program, Advanced Turbulence Simulations for Aerodynamic Application Challenges, coordinated by DLR–Germany (D. Schwamborn). The authors are grateful for the use of the French supercomputing facilities of CINES, IDRIS, CEA, this last in the context of the PRACE EU initiative.

References

1. Barbut, G.: Analyse physique par simulation numérique d'écoulements turbulents instationnaires autour de surfaces portantes fixes ou en mouvement, à nombres de Reynolds et de Mach élevés. INPT, Institut National Polytechnique de Toulouse (September 27, 2010)
2. Bourguet, R., Braza, M., Harran, G., El Akoury, R.: Anisotropic Organised Eddy Simulation for the prediction of non-equilibrium turbulent flows around bodies. J. Fluids and Structures 24(8), 1240–1251 (2008)
3. Braza, M., Perrin, R., Hoarau, Y.: Turbulence Properties in the cylinder wake at high Reynolds number. J. Fluids and Structures 22, 757–771 (2006)
4. Gual-Skopek, M.: Hybrid RANS-LES Modelling on a strongly detached turbulent flow. Aerodays, 30 March-1st April 2011, Madrid, Spain. 3rd Undergraduate/Graduate Award by the Council of European Aerospace Societies (CEAS)
5. Jenkins, L.N., Khorrami, M.R., Choudhari, M.M., McGinley, C.B.: Characterization of unsteady flow structures around tandem cylinders for component interaction studies in airframe noise. AIAA Paper 2005-2812 (2005)
6. Khorrami, M.R., Lockard, D.P., Choudhari, M.M., Jenkins, L.N., Neuhart, D.H., McGinley, C.B.: Simulations of bluff body flow interaction for noise source modelling. AIAA Paper 2006-3203 (2006)
7. Lockard, D.P., Khorrami, M.R., Choudhari, M.M., Hutcheson, F.V., Brooks, T.F., Steed, D.J.: Tandem Cylinder Noise Predictions. AIAA Paper 2007-3450 (2007)
8. Lockard, D.P.: Summary of the Tandem Cylinders solution from the benchmark problems for Airframe noise computations-I workshop. AIAA Paper 2011-353 (2011)
9. Menter, F.R.: Two-equation Eddy-Viscosity Turbulence Models for Engineering Applications. AIAA Journal 32(8), 1598–1605 (1994)
10. Vos, J., Chaput, E., Arlinger, B., Rizzi, A., Corjon, A.: Recent advances in aerodynamics inside the NSMB (Navier-Stokes Multi-Block) consortium. AIAA Paper 1998-0802 (1998)

Potential of Two-Phase Flows DNS to Characterize Interactions between Turbulence and Widely Deformed Interface

B. Duret, T. Menard, J. Reveillon, and F.X. Demoulin

Abstract. DNS of turbulent two phase flows is challenging topics of research. In the case of pressure atomizers, a high speed turbulent liquid jet is produced and forms a spray of droplets, not spherical in a first step. Numerical simulation of such phenomena was investigated (for example [21], [7], [26]). The results show the difficulties to capture accurately all the scales of interface, and consequently the interaction with turbulent structures of the flow and atomization process. Therefore, it is necessary to increase the resolution, with the consequence to increase consequently time computation. To remedy of this, LES computations can be performed. But the behavior of small scales of two- phase flows remains unknown, and must be investigated to improve LES modeling of two-phase flows. Few studies exist of this subject; we can cite [15], [31, 29, 30] and [5] who investigated additional source terms in filter Navier-stokes equations induced by the presence of interface. We purpose in this study to investigate such interaction between liquid/gas interface and turbulent flow in a forced HIT with a DNS. This configuration was used in [8] to the transport of a passive scalar. It is important to point out that our study considers high Reynolds and high Weber numbers, corresponding to the atomization regime. Consequently, the interface will be widely deformed. It is a first attempt to understand turbulence mechanism close to a widely deformed interface. That's why this work may not be generalizable to all kind of interfacial flows.

1 Introduction

Combustion of liquid fuel remains one of the major source of energy in engines. The injection phase is a critical step for mixture preparation and the induced combustion. Hence, many works have been devoted to the description of the injection

B. Duret · T. Menard · J. Reveillon · F.X. Demoulin
CNRS UMR 6614 CORIA, Technopôle du Madrillet, BP 12, Avenue de l'Université,
76801 Saint-Etienne-du-Rouvray Cedex, France
e-mail: {duret,tmenard,reveillon,
francois-xavier.demoulin}@coria.fr

M.O. Deville et al. (eds.), *Turbulence and Interactions*,
Notes on Numerical Fluid Mechanics and Multidisciplinary Design 125,
DOI: 10.1007/978-3-662-43489-5_7,

process and its influence on the vaporisation and mixing. However, experiments allowing these processes to be studied are difficult in particular close to the dense zone of the spray. The last decade has seen the apparition of numerical method devoted to two-phase flows with an accurate description of the interface. These interface tracking methods like the Volume of Fluid method ([13]), Level Set method ([28]) and Front-tracking method ([33]) are the most common stategy used for Direct Numerical Simulation (DNS). Discontinuities at the interface have to be treated carefully. To do this, numerical methods like the delta function method ([3]) and the ghost fluid method ([9]) were developed. The last one made possible to apply sharp jump conditions at the interface. As far as atomization is concerned, successful studies have emerged to describe the primary atomization of liquid jets ([21], [7], [26]).

Unfortunately, these simulations have shown that, even with a resolution of 0.35 micrometers ([26]), the finest scales of the flow are not resolved. To optimize the computational cost, some studies use an adaptive mesh refinement ([1], [10]), but there is still a numerical cutoff scale. It is possible that in few years, improvement of numerical methods and computational efficency will permit to solve the finest scale of two-phase flows. Furthermore, the finest scale in multiphase flows remains unknown, contrary to the Kolmogorov and the Bachelor scale ([2]) in single phase flows.

This issue shows that subgrid models are necessary to model the physics under this particular scale, like the Large Eddy Simulation (LES) of single phase flows. LES of two phase flows have been investigated in few studies. A first approach consist in keeping interface tracking methods to solve the interface, but without solving the finest scales of wrinkling ([15], [31, 29, 30]). Another approach, more phenomenological, is to describe continuously the transition between a well resolved interface and structures smaller than the cell size. This approach introduces the interface density area, which indicates the quantity of interfacial area in each cell, but without indications on the shape of the structures ([5]). These approaches give interesting statistical results, independent of the mesh size and in accordance with two-phase flow DNS.

For a better understanding of interactions between interface and turbulence, and in order to improve LES modeling, it is useful to study simpler configurations which allows us to solve all relevant scales of the flow. In single-phase flows, DNS of Homogeneous Isotropic Turbulence (HIT) is still used to study scalar mixing and the Kolmogorov theory. Extension of this configuration to two-phase flows to characterize interface/turbulence interactions is emerging in recent DNS studies: with a freely decaying turbulent two-phase flow ([32]), with a forced HIT ([18], [19], [8]), with solid particles in an HIT ([6]), and with a downward turbulent flows for bubbly flows ([17]).

The aim of this work is to pursue these studies by analyzing the turbulence behaviour of two-phase flows in a forced HIT. However, it is important to point out that this study considers high Reynolds and high Weber numbers, corresponding to the atomization regime. Consequently, the interface will be widely deformed. It is a first attempt to understand turbulence mechanism close to a widely deformed

interface. That's why this work may not be generalizable to all kind of interfacial flows.

Both phase will be resolved in DNS, the interface tracking method used is a coupled Level Set/VOF method. High density ratio between the two phases is chosen to simulate realistic engine conditions, kinematic viscosities are the same in each phase for easier analysis of the turbulence. Quantitative and qualitative aspects are analyzed.

In the first part, numericals method and forcing scheme are depicted. This is followed by the description of the numerical configuration and by the validation of our DNS. Finally, quantitative and qualitative results are shown and discussed.

2 Navier-Stokes Equations

The joint Level Set/VOF method is coupled with a projection method to carry out the direct numerical simulation of incompressible Navier–Stokes equations:

$$\frac{\partial \boldsymbol{V}}{\partial t} + (\boldsymbol{V}.\nabla)\boldsymbol{V} = -\frac{\nabla p}{\rho(G)} + \frac{1}{\rho(G)}\nabla.(2\mu(G)\boldsymbol{D}) + \boldsymbol{g} + \boldsymbol{f} + \frac{1}{\rho(G)}\sigma\kappa\delta(G)\boldsymbol{n} \qquad (1)$$

where p is the fluid pressure, $\boldsymbol{V}$ the velocity vector, $\boldsymbol{g}$ the gravity vector, μ the dynamic viscosity, and $\boldsymbol{D}$ the viscous deformation tensor. At the interface, the surface tension force can be considered based on the Dirac function $\delta(G)$: σ is the surface tension, $\boldsymbol{n}$ the normal unit vector, κ is the curvature computed from the Level Set function G (not recalled here). The gravity term is neglected in this study. Appropriate jump conditions are imposed on the interface ([14], [16]). To solve the derivatives, a fifth-order scheme, WENO 5 ([27] [20]), is used for convective terms, and a second-order central finite difference scheme is chosen for diffusive terms. (See [21] for further details concerning the numerical procedure.) A forcing method is necessary to maintain the turbulent kinetic energy at a prescribed level. This is achieved through the source term $\boldsymbol{f}$, which induces linear forcing ([25]). It results in $\boldsymbol{f} = A\boldsymbol{v'}$ where A is the forcing coefficient, $\boldsymbol{v'}$ represents velocity fluctuations, and $\overline{\boldsymbol{v}}$ is the mean flow velocity. In this paper, $\overline{(\cdot)}$ refers to volume averaging. A Reynolds decomposition has been applied to the velocity field $\boldsymbol{V}$. The evolution equation of the turbulent kinetic energy $k = \frac{1}{2}\overline{\boldsymbol{v'}^2}$ may be written:

$$\frac{\partial k}{\partial t} + \nabla.(\overline{\boldsymbol{v}}k) = C_k + 2Ak \qquad (2)$$

where C_k regroups the typical energetic contributions (i.e. without forcing) for the sake of clarity. The estimation of C_k involves a liquid-gas interface. It is therefore complex to estimate A directly from equation 2, thus, the following two-stage procedure has been set up:

Stage 1 - Estimation of C_k^{n-1} based on the A^{n-1} constant value :

$$C_k^{n-1} = \frac{k^n - k^{n-1}}{\Delta t} - 2A^{n-1}k^{n-1} \tag{3}$$

Stage 2 - Computation of the forcing constant A^n based on C_k^{n-1} :

$$2A^n k^n = \frac{k_c - k^n}{\tau_f} - C_k^{n-1} \tag{4}$$

where k_c is the chosen level of kinetic energy, τ_f is a characteristic relaxation time ($\tau_f = 3\Delta t$ has been retained in this study) to avoid a sharp forcing term. Thus, the force coefficient A is computed at each time step to introduce the forcing term $\boldsymbol{f}$ in the Navier-Stokes equations.

This method maintains a statistically stationary Homogeneous Isotropic Turbulence (HIT) in the whole domain.

However this kind of forcing have some drawbacks : energy is added at all scales, contrary to usual spectral forcing where the forcing is applied at a chosen wavenumber. But applying a spectral forcing in interface tracking DNS is rather complex due to discontinuities accross the interface, and also leads to much higher computational cost (by using FFT transform). The choice of a linear forcing have been made for its simplicity and because there is a lack of studies concerning forcing method in interface tracking DNS. A better forcing method, preferably in physical space, will be a major improvement for future works.

3 Results and Discussion

The solution is carried out in a 3D cubical domain with periodics boundaries similar to the study of [19] and [8].

3.1 Parameters Choice

Solving realistic turbulent liquid-gas flows is difficult. Several limitations exist despite the significant increase of processor capacities. To define a configuration with effective interactions between the liquid-gas interface and the turbulence, the following dimensionless parameters have been retained: gaseous Weber number $We_g = \rho_g \overline{k} L/(\sigma) = 1$, liquid Weber number $We_l = \rho_l \overline{k} L/(\sigma) = 30$, liquid based Reynolds number $Re_l = \sqrt{\overline{k}} L/\nu_l = 310$, liquid Ohnesorge number $Oh_l = \sqrt{We_l}/Re_l = 1.77\ 10^{-2}$. Where $\overline{k}$ is the mean kinetic energy (usually equal to k_c), σ the surface tension, ν the kinematic viscosity in the appropriate phase, ρ the density and L the box length. The grid resolution is 256^3.

The corresponding set of fluid parameters is summarized in Table 1.

Table 1 Parameters of the simulation (S.I. units)

ρ_l/ρ_g	σ	μ_l	μ_g	k_c	L
30	0.0135	1.879×10^{-5}	5.65×10^{-4}	3.6	1.5×10^{-4}

3.2 Results

3.2.1 Introduction

To evaluate the potential of two-phase flow DNS to extract detailed informations about turbulence close to the interface, the first step is to validate the ARCHER code in classic Single Phase flow HIT (SPHIT). In this context, a comparison between a single phase flow DNS solver ASPHODELE ([12], [24], [23] and [4]) and the ARCHER code is made.

An analysis of two turbulence key quantities (turbulent kinetic energy and dissipation) in decaying turbulence have been performed, and shown in Figure 1. Only a maximum of 1 % difference between the two codes is observed, meaning that the average values of dissipation and turbulent kinetic energy are well captured with our code. At this time a 128^3 mesh is used, leading to a ratio $\frac{\eta}{dx}$ equal to 1.14.

For the following Two-phase flow HIT analysis, a finest mesh is used. For sake of clarity, the Single Phase case is called SPHIT, and the Two Phase case TPHIT.

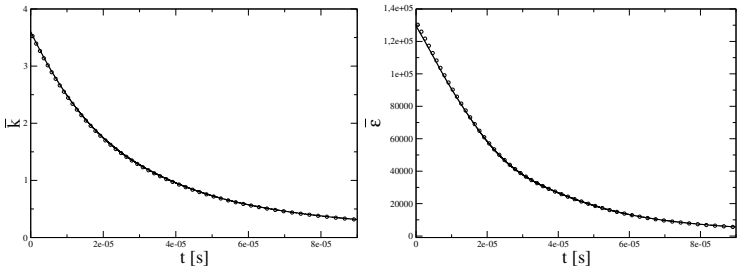

Fig. 1 Comparison of k and ε between Asphodel (circle) and ARCHER (solid line) wih a 128^3 mesh size

3.2.2 Two Phase Flows Results

Initializing Two Phase Flows

The periodic box initialization is based on the work of [19, 8]. Eight droplets are introduced in each corner of the domain, the sum of their volume is equal to the fixed liquid volume fraction equal to 5% in our case. All droplets have an initial rotational velocity in accordance with the prescribed kinetic energy. This initial condition have to be divergence free. Linear forcing is inactive at the beginning of the simulation.

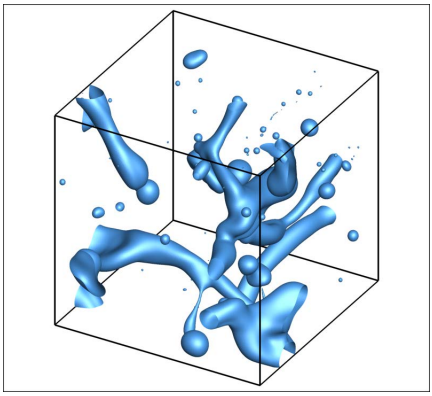

Fig. 2 Liquid structures at a given time

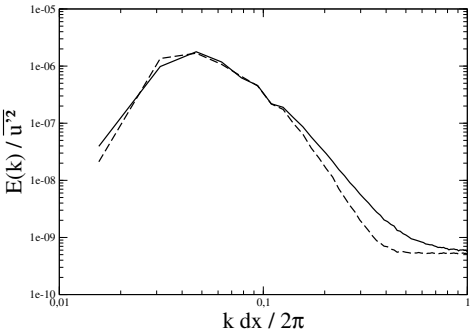

Fig. 3 Comparison of energy spectra of SPHIT (Dashed line) and TPHIT (solid lines) simulations with a 256^3 mesh size

The flow is quickly destabilized. Next, the linear forcing is activated and the turbulent kinetic energy reaches its desired level k_c with a statistically stationary state. Finally we obtain a periodic box with deformed liquid structures (Figure 2).

Interface Effect on Turbulent Properties

The influence of the two phase flow can be shown by comparing energy spectra between SPHIT and TPHIT reported on Figure 3. The two phase flow seems to induce an increasing of small scales as discussed by [32]. The Figure 4 presents a snapshot of turbulent dissipation and interface. We observe a high level of dissipation near the interface and wake induced turbulent near liquid structures. This is confirmed by the curve on Figure 4 where dissipation is drawn versus Level Set (Level 0 is interface).

But it's difficult to conclude about this result. First the dissipation increases with the presence of interface by a factor two in comparison of SPHIT. The higher energy for small structures on Figure 3 confirmed this result. That induces theoretically a decreasing of Kolmogorov scale and certainly an unresolved simulation. Then even

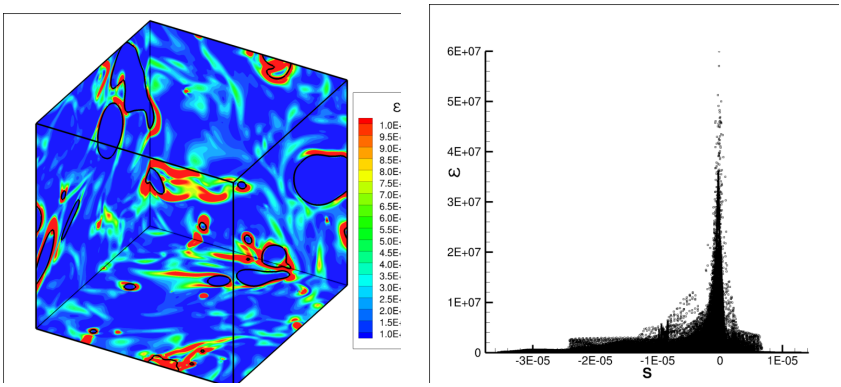

Fig. 4 Snapshot of turbulent dissipation (solid line : interface) and turbulent dissipation versus Level Set

if the mean turbulent kinetic energy is constant in whole the domain, we have two different values in the liquid and the gas (not present in the paper). The gas lost more energy than the liquid, and that can explain this effect. But for the moment we cannot control this effect.

4 Conclusion

A Simulation of two phase turbulent flows is performed with a prescibed turbulent energy. The objectives of this kind of simulation is to extract statistical informations of droplet behaviours in a turbulent flow to improve atomization model. The computationnal code developed in this way presents good results and behaviour in turbulent single phase flow. A greater dissipation near the interface are found in two phase flow as [32].

However, such computations need more validations. Next objective is to decrease the mesh size to confirm or not our results.

Acknowledgements. This work was sponsored in part by Agence National de la Recherche (ANR) in the MODEMI program. The computations had been carrying out in the IDRIS and CRIHAN computational centers.

References

1. Agbaglah, G., Delaux, S., Fuster, D., Hoepffner, J., Josserand, C., Popinet, S., Ray, P., Scardovelli, R., Zaleski, S.: Parallel simulation of multiphase flows using octree adaptivity and the volume-of-fluid method. Comptes Rendus Mécanique 339(2-3), 194–207 (2011), High Performance Computing

2. Batchelor, G.K.: Small-scale variation of convected quantities like temperature in turbulent fluid Part 1. General discussion and the case of small conductivity. Journal of Fluid Mechanics 5(1), 113–133 (1959)
3. Brackbill, J.U., Kothe, D.B., Zemach, C.: A continuum method for modeling surface tension. Journal of Computational Physics 100(2), 335–354 (1992)
4. De Chaisemartin, S., Fréret, L., Kah, D., Laurent, F., Fox, R.O., Reveillon, J., Massot, M.: Eulerian models for turbulent spray combustion with polydispersity and droplet crossing. Comptes Rendus Mécanique 337(6-7), 438–448 (2009), Combustion for aerospace propulsion
5. Chesnel, J., Reveillon, J., Menard, T., Demoulin, F.-X.: Large eddy simulation of liquid jet atomization. Atomization and Sprays 21(9), 711–736 (2011)
6. Corre, C., Estivalezes, J., Vincent, S., Simonin, O.: Direct numerical simulation of the motion of particles larger than the kolomogorov scale in a homogeneous isotropic turbulence. In: 2008 ASME Fluids Engineering Conference, 10-14 August 2008, Jacksonville, Florida USA (2008)
7. Desjardins, O., Moureau, V., Pitsch, H.: An accurate conservative level set/ghost fluid method for simulating turbulent atomization. Journal of Computational Physics 227(18), 8395–8416 (2008)
8. Duret, B., Luret, G., Reveillon, J., Menard, T., Berlemont, A., Demoulin, F.-X.: DNS analysis of turbulent mixing in two-phase flows. International Journal of Multiphase Flow 40, 93–105 (2012)
9. Fedkiw, R.P., Aslam, T., Merriman, B., Osher, S.: A non-oscillatory Eulerian approach to interfaces in multimaterial flows (the ghost fluid method). Journal of Computational Physics 152(2), 457–492 (1999)
10. Fuster, D., Bagué, A., Boeck, T., Moyne, L.L., Leboissetier, A., Popinet, S., Ray, P., Scardovelli, R., Zaleski, S.: Simulation of primary atomization with an octree adaptive mesh refinement and vof method. International Journal of Multiphase Flow 35(6), 550–565 (2009)
11. Gotoh, T., Fukayama, D., Nakano, T.: Velocity field statistics in homogeneous steady turbulence obtained using a high-resolution direct numerical simulation. Physics of Fluids 14(3), 1065–1081 (2002)
12. Guichard, C., Reveillon, J., Haugel, R.: DNS of statistically stationary one-and two-phase turbulent combustion: a turbulent injection procedure. Turb. Flow & Comb. 73, 133–167 (2004)
13. Hirt, C.W., Nichols, B.D.: Volume of fluid (vof) method for the dynamics of free boundaries. Journal of Computational Physics 39(1), 201–225 (1981)
14. Kang, M., Fedkiw, R.P., Liu, X.D.: Boundary conditions capturing method for multiphase incompressible flow. Journal of Scientific Computing 3, 323–360 (2000)
15. Labourasse, E., Lacanette, D., Toutant, A., Lubin, P., Vincent, S., Lebaigue, O., Caltagirone, J.-P., Sagaut, P.: Towards large eddy simulation of isothermal two-phase flows: Governing equations and a priori tests. International Journal of Multiphase Flow 33(1), 1–39 (2007)
16. Liu, X.-D., Fedkiw, R.P., Kang, M.: A boundary condition capturing method for poisson's equation on irregular domains. Journal of Computational Physics 160(1), 151–178 (2000)
17. Lu, J., Tryggvason, G.: Effect of bubble size in turbulent bubbly downflow in a vertical channel. Chemical Engineering Science 62(11), 3008–3018 (2007)
18. Luret, G., Blokkeel, G., Lebas, R., Ménard, T., Berlemont, A., Demoulin, F.X.: Spray interactions: modeling of collision/coalescence phenomena. In: 22nd European Conference on Liquid Atomization and Spray Systems, Como Lake, Italy (2008)

19. Luret, G., Menard, T., Blokkeel, G., Berlemont, A., Réveillon, J., Demoulin, F.X.: Modeling collision outcome in moderately dense spray. Journal of Atomization and Spray 20(3), 93 (2010)
20. Martín, M.P., Taylor, E.M., Wu, M., Weirs, V.G.: A bandwidth-optimized WENO scheme for the effective direct numerical simulation of compressible turbulence. Journal of Computational Physics 220(1), 270–289 (2006)
21. Menard, T., Tanguy, S., Berlemont, A.: Coupling level set/vof/ghost fluid methods: Validation and application to 3d simulation of the primary break-up of a liquid jet. International Journal of Multiphase Flow 33(5), 510–524 (2007)
22. Pope, S.B.: Turbulent flows, 1st edn. Cambridge Univ. Press (January 2000)
23. Reveillon, J., Demoulin, F.-X.: Effects of the preferential segregation of droplets on evaporation and turbulent mixing. Journal of Fluid Mechanics 583(-1), 273–302 (2007)
24. Reveillon, J., Vervisch, L.: Analysis of weakly turbulent dilute-spray flames and spray combustion regimes. Journal of Fluid Mechanics 537, 317–347 (2005)
25. Rosales, C., Meneveau, C.: Linear forcing in numerical simulations of isotropic turbulence: Physical space implementations and convergence properties. Physics of Fluids 17(9), 095106 (2005)
26. Shinjo, J., Umemura, A.: Simulation of liquid jet primary breakup: Dynamics of ligament and droplet formation. International Journal of Multiphase Flow 36(7), 513–532 (2010)
27. Shu, C.-W.: Essentially non-oscillatory and weighted essentially non-oscillatory schemes for hyperbolic conservation laws. Technical Report NASA CR-97-206253 ICASE Report No. 97-65, Institute for Computer Applications in Science and Engineering (November 1997)
28. Sussman, M., Smereka, P., Osher, S.: A level set approach for computing solutions to incompressible two-phase flow. Journal of Computational Physics 114(1), 146–159 (1994)
29. Toutant, A., Chandesris, M., Jamet, D., Lebaigue, O.: Jump conditions for filtered quantities at an under-resolved discontinuous interface. part 1: Theoretical development. International Journal of Multiphase Flow 35(12), 1100–1118 (2009)
30. Toutant, A., Chandesris, M., Jamet, D., Lebaigue, O.: Jump conditions for filtered quantities at an under-resolved discontinuous interface. part 2: A priori tests. International Journal of Multiphase Flow 35(12), 1119–1129 (2009)
31. Toutant, A., Labourasse, E., Lebaigue, O., Simonin, O.: Dns of the interaction between a deformable buoyant bubble and a spatially decaying turbulence: A priori tests for les two-phase flow modelling. Computers & Fluids 37(7), 877–886 (2008)
32. Trontin, P., Vincent, S., Estivalezes, J.L., Caltagirone, J.P.: Direct numerical simulation of a freely decaying turbulent interfacial flow. International Journal of Multiphase Flow 36(11-12), 891–907 (2010)
33. Ozen Unverdi, S., Tryggvason, G.: Computations of multi-fluid flows. Physica D: Nonlinear Phenomena 60(1-4), 70–83 (1992)

Analysis and Optimisation of Cyclone Separators Geometry Using RANS and LES Methodologies

Khairy Elsayed and Chris Lacor

Abstract. The flow field pattern and gas cyclone performance have been investigated using both RANS and LES methodologies. The solid phase has been simulated using the one-way coupling approach. Both the RSM model and LES can be used efficiently to simulate the main features flow field pattern and estimate the performance. However, when looking at the flow details, LES can more accurately capture the unsteady flow phenomena of the highly swirling flow. Two different optimisation techniques have been applied (namely, the Nelder-Mead and the genetic algorithms) to obtain the cyclone geometry for minimum pressure drop. Two sources of data for the objective function have been used, mathematical models and experimental data. Starting from a Stairmand design an improved cyclone geometry is found using seven geometrical design variables. A CFD comparison between the original design and the new design has been performed. The simulations confirm the superior performance of the new design.

Keywords: Cyclone Separator, Optimisation, Reynolds Stress Model, Large Eddy Simulation, Discrete Phase Modeling.

1 Introduction

In cyclone separators, a strongly swirling turbulent flow is used to separate phases with different densities. A typical geometrical layout of a gas cyclone shown in Fig. 1, corresponds to the Stairmand high-efficiency cyclone. The tangential inlet generates the swirling motion of the gas stream, which forces particles toward the outer wall where they spiral in the downward direction. Eventually the particles are collected in the dustbin (or flow out through a dipleg). The cleaned gas leaves

Khairy Elsayed · Chris Lacor
Vrije Universiteit Brussel, Department of Mechanical Engineering, Pleinlaan 2,
1050 Brussels, Belgium
e-mail: {kelsayed,chris.lacor}@vub.ac.be

M.O. Deville et al. (eds.), *Turbulence and Interactions*,
Notes on Numerical Fluid Mechanics and Multidisciplinary Design 125,
DOI: 10.1007/978-3-662-43489-5_8,

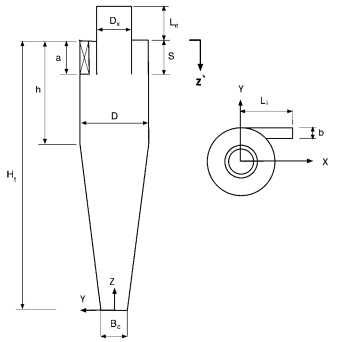

Fig. 1. Cyclone separator geometry

through the exit pipe at the top. Swirl and turbulence are the two competing phenomena in the separation process: the swirl induces a centrifugal force on the solids phase which is the driving force behind the separation; turbulence disperses the solid particles and enhances the probability that particles get caught in the exit stream. Both phenomena are related to the particle size, and the flow conditions in the cyclone [9]. The cyclone geometry is described by seven geometrical parameters, viz. the inlet height a, and width b, the vortex finder diameter D_x and length S, cylinder height h, cyclone total height H_t and cone-tip diameter B_c (Fig. 1).

1.1 Selection of the Turbulence Model

For the turbulent flow in cyclones, the key to the success of CFD lies with the accurate description of the turbulent behavior of the flow. Selection of a suitable turbulence model for the highly swirling flows has been investigated by many researchers [e.g. 10]. Both the standard $k-\varepsilon$ and RNG $k-\varepsilon$ turbulence models give unrealistic distribution for the axial velocity profiles in cyclone separators (upward flow close to the wall) [4, 8, 10]. Due to the turbulence anisotropy of the highly swirling flows, only the Reynolds stress turbulence model (RSM) [11] is capable to predict the combined vortex in accordance with the experimental data [8, 10]. This study presents the results of flow simulations of the Stairmand cyclone using both the Reynolds stress turbulence model (RSM) and large eddy simulation (LES). The present study focuses on the effect of the used turbulence methodology on the estimated cyclone performance and the flow pattern, which is not well reported in previous literatures.

2 Numerical Settings

RSM: The Reynolds-Averaged Navier-Stokes equations are modeled employing the Reynolds stress turbulence model (RSM). QUICK scheme for momentum equation and second-order upwind scheme for both the turbulent kinetic energy k and the

turbulent dissipation rate ε and the Reynolds stress equations were employed for spatial discretisation. The SIMPLEC algorithm was used for pressure-velocity coupling and the PRESTO scheme for pressure discretisation. The simulation is unsteady with a time step of 5E-4s.

LES: In LES, the big three-dimensional eddies which are dictated by the geometry and boundary conditions of the flow involved are directly resolved, whereas the small eddies which tend to be more isotropic and less dependent on the geometry are modeled. The dynamic Smagorinsky model is used in this study to calculate the turbulent viscosity. The bounded central difference scheme for momentum equation was employed for spatial discretisation. The SIMPLEC algorithm was used for pressure-velocity coupling and the PRESTO scheme for pressure discretisation (cf. [5]). The simulations are performed with a time step of 1E-5s. The interested reader can refer to Elsayed and Lacor [7] for more details about the selection of the time step.

DPM: For the discrete phase modeling (DPM) a one-way coupling for both RANS and LES simulation is used with Rosin-Rammler size distribution. The particle density is 860 kg/m^3, the minimum particle diameter equals 5.0E-7 m, the maximum diameter equals 1E-5 m, the mean diameter equals 2.5E-6 m, the spread rate equals 2.0 and the number of particle diameters equals 10. The *frozen field method* of particle tracking [1] was used in the current study with assumed particle velocity equals the gas velocity at inlet.

Boundary Conditions and Grid Refinement Tests: At the inlet, a "velocity inlet" boundary condition has been applied and at the gas outlet the"outflow" boundary condition used. The bottom of the cyclone was closed and a "wall" boundary condition is applied. Grid refinement tests were conducted in order to make sure that the solution was not grid dependent. Three meshes are used for RSM around 65,000 cells, 250,000 cells and 497,000 hexahedral cells. There was no considerable difference in the cyclone performance (both the pressure drop and the cut-off diameter) obtained on the last two meshes. The solution on the 250,000 cells mesh is therefore regarded as a grid independent solution. For the LES simulation a mesh of 1453786 hexahedral cells was used after a grid independent study (cf. [5]). The number of cells used for LES is quite small with respect to the Reynolds number (2.8E5), but it is still sufficient to get the global quantities (pressure drop and cut-off diameter). A similar number of cells has been used for LES simulations in the literature, e.g., [13–15].

Cyclone Geometry and Other Settings: The cyclone geometry and dimensions are given by Table 1 and Fig. 1. The inlet velocity equals 20 m/s, air density 1.225 kg/m^3 and dynamic viscosity 1.7894E-4 Pa.s, which gives a Reynolds number of 2.8E5 based on the cyclone diameter and the area averaged air inlet velocity. The turbulence quantities were uniformly imposed at the inlet by using a turbulence intensity of 5%, and the characteristic turbulence length scale $l_m = 0.07b$ [8].

Table 1. The values of geometrical parameters (D=0.205 m)

a/D	b/D	B_c/D	D_x/D	h/D	H_t/D	S/D	L_i/D	L_e/D
0.5	0.2	0.375	0.5	1.5	4.0	0.5	1.0	0.5

3 RSM versus LES Simulations

Figure 2 compares the time-averaged tangential and axial velocity profiles predicted by both RSM and LES at three stations located at 0.625 D, 0.75 D and 2D from the inlet section top. The velocity profiles at the first two sections are compared with the experimental velocity profiles [8]. Figure 2 indicates a good matching between the experimental and numerical results for both the axial and tangential velocity. In case of RSM, the comparison indicates the overestimation of the maximum tangential velocity and the axial velocity at the central region. The agreement between the RSM simulation and measurements are considered to be quite acceptable taken into account the complexity of the turbulent swirling flow in the cyclones [4]. The LES simulation results exhibit a superior matching with experimental measurements especially at the cyclone center (in case of cyclone separator, this can be achieved only with a good LES mesh and accurate solver settings). Figure 3 shows a comparison between the flow patterns obtained from RSM and LES simulations at sections Y=0 for three flow variables, namely, the time averaged static pressure, tangential and axial velocity. The shape of the pressure contours for RSM and LES are very similar but RSM systematically predicts lower values. From the comparison between the RSM and the LES velocity profiles the following comments are obtained. The tangential velocity distributions for the two cases (RSM and LES) are nearly identical in pattern, with lower velocity values depicted in case of RSM as is clear from the three tangential velocity profiles shown in Fig. 2. The values of tangential velocity in LES match better the experimental values than the RSM results especially for the maximum tangential velocity. The position of maximum velocity is nearly the same for RSM and LES at each section. Away from the vortex finder, the tangential velocity profiles obtained from both RSM and LES simulations become closer (but not identical) whereas, the axial velocity profile obtained from the RSM simulation still distinct from the corresponding LES profile. From the previous analysis, the main flow features in the cyclone separator can be captured by the two models. Unsteady flow phenomena on the other hand, like vortex core procession, can only be modeled accurately with LES [2].

Table 2 shows a comparison between the Euler number Eu (dimensionless pressure drop $\Delta p/(0.5 * \rho * V_{in}^2)$) and the Stokes number Stk_{50} obtained from RSM and LES and the experimental values. The LES results match better the experimental value for the Euler number than the RSM simulation results. The reason behind the distinct difference between the LES Stokes number and the experimental one is that in this LES simulation the interaction with the continuous phase has been neglected. Moreover, the DPM was not the concurrent flow and particle motion method [1] and the effect of subgrid scale (SGS) on the particle has been neglected. These settings may be the reason behind the distinct difference between the LES results and the

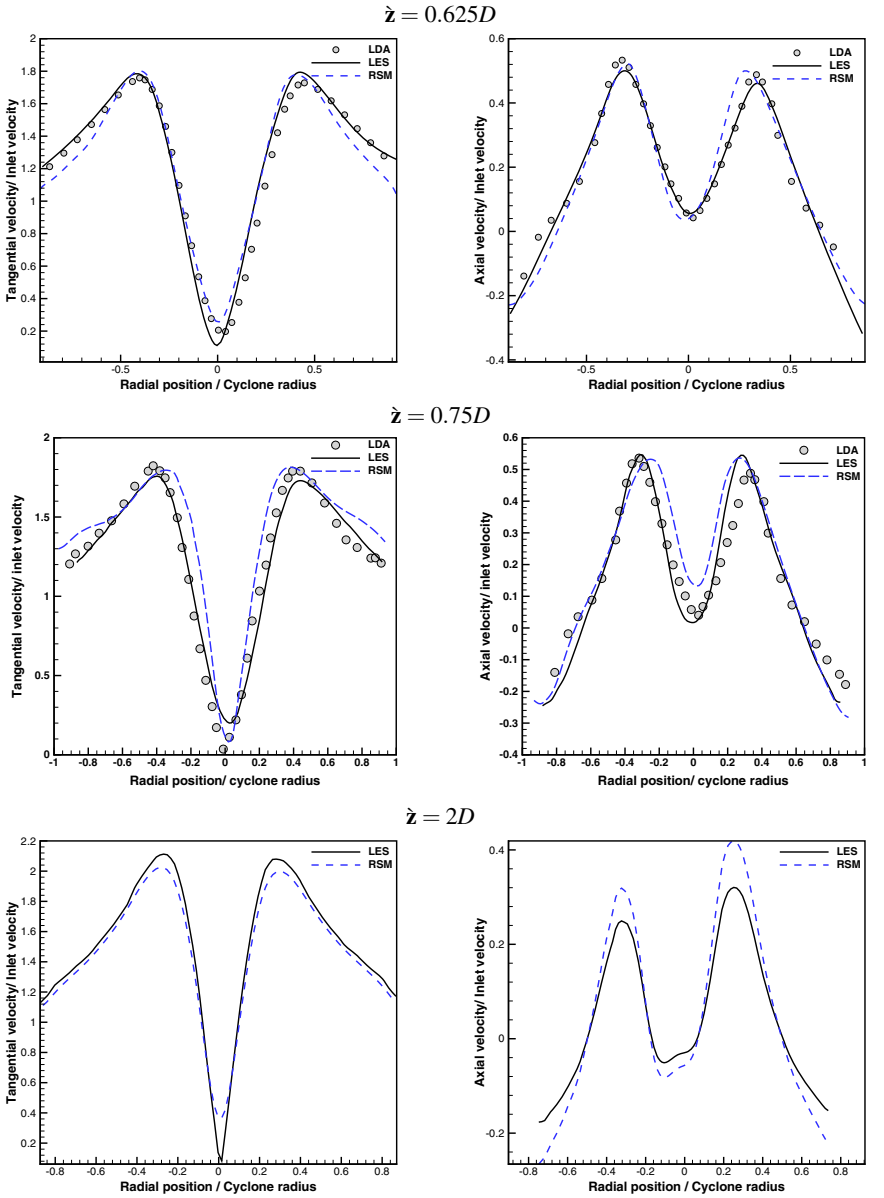

Fig. 2. Comparison of the time averaged tangential and axial velocity between the experimental measurements [8] and the current simulations

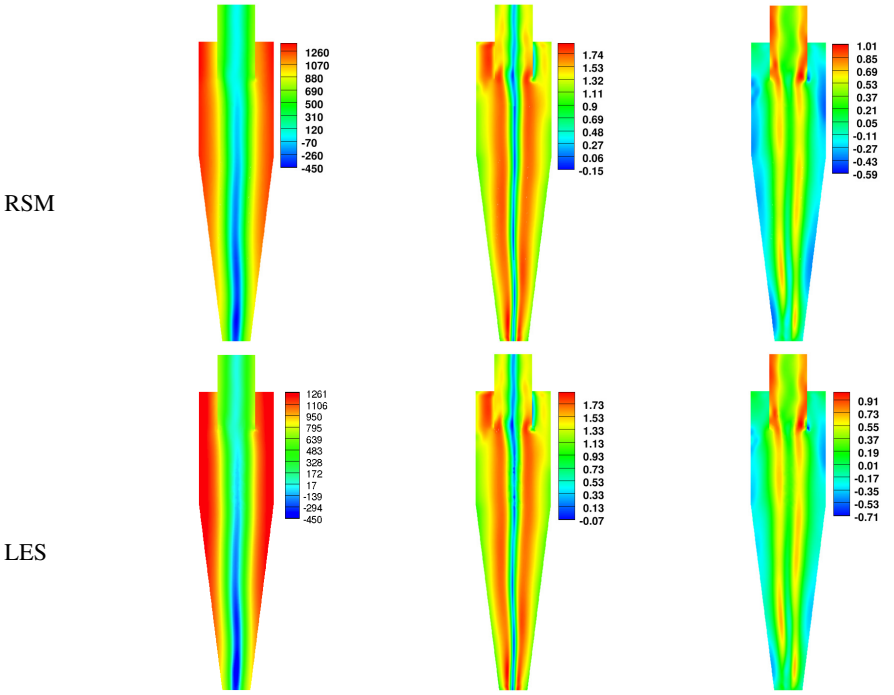

Fig. 3. Contour plots for the time averaged static pressure, tangential and axial velocity.The static pressure unit is [N/m^2], the velocities are normalized by the inlet velocity.

Table 2. Performance parameters

	RSM	LES	Experimental [8]
Eu	6.18	6.09	6.0
$Stk_{50} \times 10^3$*	0.325	0.361	0.349**

* The Stokes number Stk_{50} is the dimensionless cut-off diameter x_{50}. x_{50} is the particle diameter that produces 50% collection efficiency. $Stk_{50} = \rho_p x_{50}^2 V_{in}/(18\mu D) = \frac{\tau_p}{\tau_f}$. It is the ratio between the particle relaxation time (the time constant in the exponential decay of the particle velocity due to drag) $\tau_p = \rho_p x_{50}^2/(18\mu)$ and the gas flow integral time scale $\tau_f = D/V_{in}$ where ρ_p is the particle density, μ is the gas viscosity, V_{in} is the average inlet velocity and D is the cyclone barrel diameter.

** The particle density equals 2470 kg/m^3.

experimental values. But this point still needs more investigations in future studies. The interested reader can refer to Elsayed and Lacor [7] for more details about the effect of the SGS on the predicted grade efficiency curve.

Table 3. The geometrical parameters for different designs (D=0.205 m)*

Cyclone	a/D	b/D	D_x/D	H_t/D	h/D	S/D	B_c/D
Stairmand design	0.5	0.2	0.5	4	1.5	0.5	0.375
New design (RBF & GA)	0.595	0.201	0.549	4.549	1.411	0.595	0.275
New design (MM & Nelder-Mead)	0.618	0.236	0.618	4.236	1.618	0.618	0.382

* The outlet section is above the cyclone surface by $L_e = 0.618D$. The inlet section located at a distance $L_i = D$ from the cyclone center.

4 Optimisation

The second objective is an optimisation study to obtain the most efficient cyclone design for minimum pressure drop using different optimisation techniques (both the Nelder-Mead and the genetic algorithms). Two sources of data for the objective function have been used, mathematical models and experimental data.

First, the Muschelknautz method of modeling (MM) [3] has been applied as a source of data. The Box-Behnken design of experiment has been applied to construct a table of 64 runs, then a second-order response surface model has been fitted and used as an objective function for the Nelder-Mead technique [12]. The geometrical ratios and performance for the new obtained design is depicted in Table 3 and its performance parameters in Table 4 which indicate a better performance in comparison with the standard Stairmand cyclone design.

A dataset of 98 samples obtained from the measurements of pressure drop for different cyclone designs [6] is used in the present investigation to train the radial basis function artificial neural networks (RBF). Then the RBF has been used as a fitness function for the genetic algorithms Matlab code. The new design (RBF & GA presented in Table 3) is different than the other two designs (Stairmand and MM & Nelder-Mead).

A deep inspection of Tables 3 and 4 results in the following comments: The inlet height a of the two new designs is larger than that of the Stairmand design. The vortex finder diameter of the two new designs are larger than the corresponding value for Stairmand. But this small change will reduce the pressure loss [3]. The Euler number (dimensionless pressure drop) for the two new designs is lower than that for the stairmand but the cut-off diameter obtained by the (MM & Nelder-Mead) design is larger than the Stairmand one. This is probably due to the wider vortex finder diameter.

The difference in the Euler number may look quite small, but this is because the optimisation is done at constant mass flow rate. As the inlet section increases this leads to a reduced inlet velocity and hence, for equal dimensional pressure drops, the Euler number would increase.

However, the objective function here is to minimize the Euler number, but the decision maker will prefer to use one design with less power consumption and better collection efficiency, i.e., the (RBF& GA) design. This motivates us to use CFD simulation to compare the new RBF& GA design with the Stairmand design, as given in the next section.

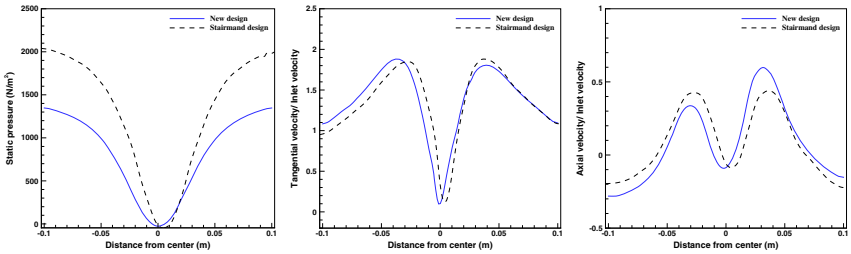

Fig. 4. Comparison between the time averaged static pressure, tangential and axial velocity depicted by the two designs at 0.75 *D* below the inlet section top

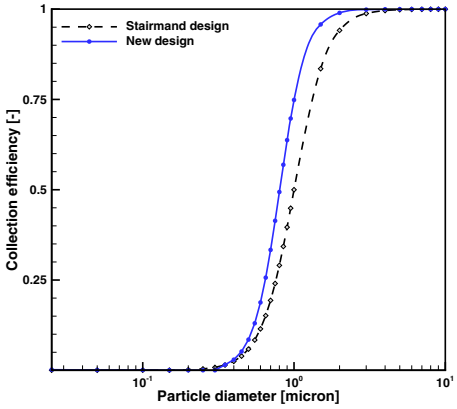

Fig. 5. Comparison between the grade efficiency curves for the two designs (the new RBF& GA and the Stairmand designs)

Table 4. Performance parameters of the different designs

	New design (RBFNN & GA)	New design (MM & Nelder-Mead)	Stairmand design
Eu	6.338	5.672	6.567
x_{50}	0.804	1.6	1.0

4.1 Comparison between the Two Designs

A CFD comparison between the Stairmand design and the new RBF& GA design has been performed using the Reynolds stress turbulence model. The grid refinement study using different levels of grid shows that a total number of 134759 hexahedral cells for the Stairmand cyclone and 378963 hexahedral cells for the new design are sufficient to obtain a grid-independent solution, and further mesh refinement yields only small, insignificant changes in the numerical solution. Figure 4 compares the time averaged static pressure, tangential and axial velocity. The two cyclones have almost the same flow pattern, but the highest pressure value predicted in the

Stairmand cyclone is greater than that for the new design, implying that the new design has a lower pressure drop. Whereas, the range of the tangential and axial velocities for the two designs are very close. In Fig. 5 the grade efficiency curves for the two designs are plotted. It is seen that the new design can capture more particles over the complete range of sizes. Consequently, at all particles sizes, the collection efficiency of the new design will be higher than the high-efficiency Stairmand design.

5 Conclusion

Both RSM and LES have been applied to compare the flow field pattern and the performance parameters in gas cyclones. Both models can be used efficiently to simulate the main features of the flow and estimate the performance. The tangential velocity distributions for both RSM and LES are similar in pattern, with lower velocity values depicted in case of RSM. The values of tangential velocity in LES match better the experimental values than the RSM results. The position of maximum velocity is nearly the same for both models at each section. The shape of the pressure contours for RSM and LES are very similar but RSM systematically predicts lower values. The LES results match better the experimental value for the Euler number than the RSM simulation. The second objective is an optimisation study to obtain the most efficient cyclone design for minimum pressure drop using different optimisation techniques (both the Nelder-Mead and the genetic algorithms). Starting from a Stairmand design an improved cyclone geometry is found using seven geometrical design variables. The computational comparison between the Stairmand design and the new optimum design obtained via the genetic algorithm shows that the new design will consume less power at a better collection efficiency.

References

[1] Derksen, J.J.: Separation performance predictions of a stairmand high-efficiency cyclone. AIChE Journal 49(6), 1359–1371 (2003)
[2] Derksen, J.J., Van den Akker, H.E.A.: Simulation of vortex core precession in a reverse-flow cyclone. AIChE Journal 46(7), 1317–1331 (2000)
[3] Elsayed, K., Lacor, C.: Optimization of the cyclone separator geometry for minimum pressure drop using mathematical models and CFD simulations. Chemical Engineering Science 65(22), 6048–6058 (2010)
[4] Elsayed, K., Lacor, C.: The effect of cyclone inlet dimensions on the flow pattern and performance. Applied Mathematical Modelling 35(4), 1952–1968 (2011)
[5] Elsayed, K., Lacor, C.: Numerical modeling of the flow field and performance in cyclones of different cone-tip diameters. Computers & Fluids 51(1), 48–59 (2011)
[6] Elsayed, K., Lacor, C.: Modeling and pareto optimization of gas cyclone separator performance using RBF type artificial neural networks and genetic algorithms. Powder Technology 217, 84–99 (2012)
[7] Elsayed, K., Lacor, C.: The effect of cyclone vortex finder dimensions on the flow pattern and performance using LES. Computers & Fluids 71, 224–239 (2013)

[8] Hoekstra, A.J.: Gas flow field and collection efficiency of cyclone separators. PhD thesis, Technical University Delft (2000)
[9] Hoekstra, A.J., Derksen, J.J., Van Den Akker, H.E.A.: An experimental and numerical study of turbulent swirling flow in gas cyclones. Chemical Engineering Science 54, 2055–2065 (1999)
[10] Kaya, F., Karagoz, I.: Performance analysis of numerical schemes in highly swirling turbulent flows in cyclones. Current Science 94(10), 1273–1278 (2008)
[11] Launder, B.E., Reece, G.J., Rodi, W.: Progress in the development of a Reynolds-stress turbulence closure. Journal of Fluid Mechanics 68(3), 537–566 (1975)
[12] Nelder, J.A., Mead, R.: A simplex method for function minimization. The Computer Journal 7(4), 308–313 (1965)
[13] Shalaby, H.: On the potential of large eddy simulation to simulate cyclone separators. PhD thesis, Chemnitz University of Technology, Chemnitz, Germany (2007)
[14] Shalaby, H., Pachler, K., Wozniak, K., Wozniak, G.: Comparative study of the continuous phase flow in a cyclone separator using different turbulence models. International Journal for Numerical Methods in Fluids 48(11), 1175–1197 (2005)
[15] Slack, M.D., Prasad, R.O., Bakker, A., Boysan, F.: Advances in cyclone modeling using unstructured grids. Trans. IChemE 78 Part A (2000)

Numerical Study on the Decay and Amplification of Turbulence in Oscillatory Pipe Flow

Daniel Feldmann and Claus Wagner

Abstract. Results of three-dimensional direct numerical simulations of oscillatory pipe flows at two high dimensionless frequencies $Wo \in \{13, 26\}$ are discussed. Starting from a fully-developed turbulent velocity field, the flows either relaminarise or reach a conditionally or fully turbulent state, depending on Re and Wo. Analysing the temporal evolution of several phase-averaged quantities, reveals different behaviour of the wall shear stress and the RMS velocity profiles, while the integral bulk flow only reflects minor differences. Utilising two different initial conditions do not significantly influence the developing oscillatory bulk flow.

1 Introduction

For many industrial applications and especially for biofluidic problems, e.g. respiratory airflow (oscillatory) or vascular blood flow (pulsatile), decay and amplification of turbulence play an important role. The onset of turbulence in such wall-bounded time-periodic fluid motions has major impact on mixing and transport efficiency and can rapidly change shear forces acting on the system's wall. Contrarily to the onset of turbulence in statistically steady pipe flows, see e.g. [1], turbulence in statistically unsteady pipe flows is far from understood. Some of the few existing theoretical, numerical and experimental studies on transition to turbulence in such flows are summarised in e.g. [2, 3]. The most important ones are also assorted in fig. 1. To our knowledge, the existing numerical studies, only consider oscillatory flows over a flat plate or in two-dimensional channels and cover rather few and low Womersley numbers Wo, or focus on pulsatile rather than oscillatory flows. To complement the findings summarised in fig. 1, we perform three-dimensional direct numerical simulations (DNS) of oscillatory pipe (OP) flows and analyse the temporal and phase-averaged evolution of several parameters, as well as the influence of two different initial conditions.

Daniel Feldmann · Claus Wagner
Institute of Aerodynamics and Flow Technology, DLR, Göttingen, Germany
e-mail: daniel.feldmann@dlr.de

M.O. Deville et al. (eds.), *Turbulence and Interactions*,
Notes on Numerical Fluid Mechanics and Multidisciplinary Design 125,
DOI: 10.1007/978-3-662-43489-5_9,

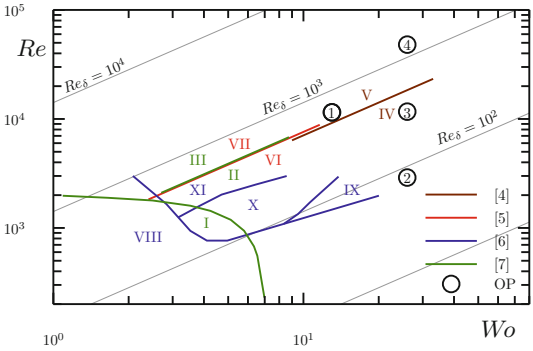

Fig. 1 Parameter map for the onset of turbulence in oscillatory pipe flow. I: laminar; II: weakly turbulent; III: conditionally turbulent; IV: laminar; V: turbulent wall region and stable core flow; VI: laminar; VII: turbulent; VIII: stable; IX: weakly unstable near the wall; X: unstable without significant amplification; XI: unstable with noticeable amplification.

2 Numerical Methodology

We consider a Newtonian fluid driven by an oscillating axial mean pressure gradient

$$\partial_z \langle p \rangle = \cos(\tfrac{4Wo}{Re_\tau} t) \quad \text{with} \quad p = p' + \langle p \rangle \tag{1}$$

confined by a cylindrical wall of diameter D and length $L^+ \in \{1800, 3600, 7200\}$ in wall units, denoted by plus. The governing equations read

$$\partial_j u_j = 0 \quad \text{and} \quad \partial_t u_i + u_j \partial_j u_i = -\partial_i p + \tfrac{1}{Re_\tau} \partial_{jj} u_i \,, \tag{2}$$

where $\mathbf{u}$ is the velocity vector with its components i, j pointing along the cylindrical coordinates in axial (z), azimuthal (φ) and radial (r) direction. By ∂_t we denote the partial derivative with respect to time t. By adopting Reynolds' decomposition the pressure p is separated in its fluctuating and its mean part. Angle brackets with subscripts denote a suitable averaging operation, where $\theta = t + mT/2, m \in \mathbb{N}$ denotes a phase average. According to e.g. [7, 6], the problem is fully characterised by the Womersley number $Wo = D/2 \cdot \sqrt{\omega \nu^{-1}}$ and the Reynolds number $Re = \hat{u} D \nu^{-1}$. Here, $\omega = 2\pi/T$ is the oscillation frequency, $\hat{u} = \max\, \bar{u}(t)$ is the peak velocity in $0 \leqslant t < T$, where $\bar{u}$ is the instantaneous bulk velocity, and ν is the viscosity.

For a laminar, axially symmetric and fully developed flow, the closed-form solution to eqs. (1) and (2) for the velocity u_z is given by the so-called Sexl–Womersley (SW) solution [8, 9]. To directly solve an integral form of eqs. (1) and (2), we make use of a fourth order accurate finite volume method on staggered grids, based on Schumann's [10] volume balance procedure. Further details are given in [11, 12, 2]. In this study, we consider five combinations of initial conditions (IC) and the two control parameters Wo and Re_τ, summarised in tab. 1 and fig. 1. Here, Re_τ is based on the friction velocity u_τ of the statistically steady and fully-developed (SSFD) turbulent flow field for $Wo = 0$. As initial condition, we use a SSFD turbulent flow field predicted in a DNS for $Re_\tau = 1440$. As described in [2], the length of

Table 1 Parameters for the performed oscillatory pipe (OP) flow simulations

Simulation	initial condition	Wo	Re_τ	T	Re	Re_δ
OP1	OP2 at $t = 4$	13	1440	13.384	11 490	625
OP2	SSFD	26	1440	3.3461	2900	79
OP3	OP2 at $t = 84.7$	26	2880	6.6922	11 670	317
OP4	OP2 at $t = 88.7$	26	5760	13.384	48 110	1308
OP5	SWSF	13	1440	13.384	11 520	626

computational domain of $L^+ = 1800$ is long enough and the computational grid is sufficiently fine to resolve all relevant scales in the SSFD. Furthermore, we also use a laminar SW solution with superimposed fluctuations (SWSF) taken from SSFD, or flow fields from the OP2 solution.

3 Numerical Results

For OP2 the pressure gradient starts to vary at $t = 0$ with an oscillation period of $T = \pi Re_\tau/(2Wo^2) = 3.3$. As a consequence, the bulk flow begins to decelerate, as shown in fig. 2. The resulting pulsatile flow needs to relax from the SSFD initial condition. It is still not fully relaxed to pure oscillation until $t \approx 200$ time units, but converges asymptotically, as we conclude from fig. 2. Further, this longsome relaxation effect becomes even more pronounced with increasing Wo, as investigated earlier [13]. We average $|\hat{u}|$ within the last six periods, shown in fig. 2, to calculate a mean $Re = 2901$. This state corresponds to a Reynolds number of $Re_\delta = 79$, based on the Stokes layer thickness δ. Therefore, OP2 roughly falls into regime IV, where oscillatory flow is supposed to be laminar [4], and regime IX, where the near wall flow is expected to be weakly unstable [6], see fig. 1. Although, the pulsating

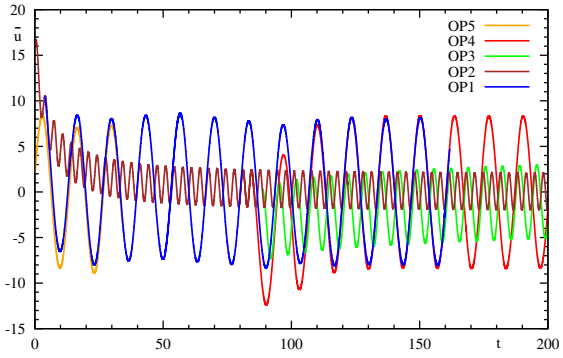

Fig. 2 Temporal evolution of the integral bulk velocity $\bar{u}$ for the oscillatory pipe flow simulations

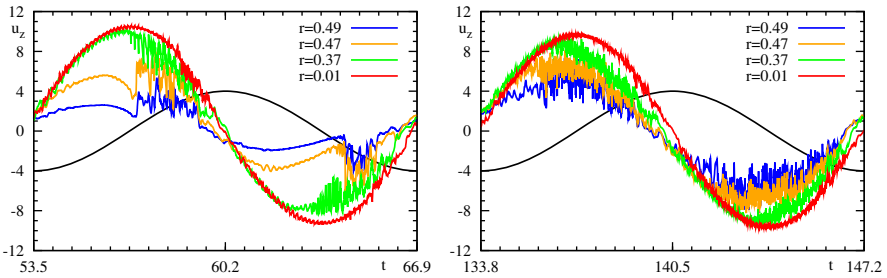

Fig. 3 Temporal evolution of u_z at four probe positions for OP1 (left) and OP4 (right)

flow has not completely converged to a pure oscillation, a laminar state has been reached, when started from a fully developed turbulent flow. We conclude this from evaluating the time series of instantaneous velocity and RMS velocity profiles, not shown here. They do not reflect any fluctuations or instabilities over the last twenty oscillation cycles.

For OP1 the duration of one oscillation cycle increases to $T = 13.4$. Thus, the computational effort to simulate one period is four times higher for the halved Wo. As presented in fig. 2, OP1 relaxes much faster from SSFD and the final $\hat{u}$ is four times higher compared to OP2, due to the halved Wo and the same Re_τ. The bulk flow converges much faster due to turbulent mixing and a smaller Wo, i.e. longer deceleration phases. Whereas in OP2, the flow relatively fast relaminarises and thus a small viscous Stokes layer develops. As shown in fig. 2, from $t \approx 25$ on, the calculated $\bar{u}$ already performs a pure oscillation with a slightly varying $\hat{u}$. To determine Re, we average the last twelve $\hat{u}$ plotted in fig. 2 and obtain $Re = 11\,490 \pm 600$. At this point it is not clear, whether this variation in $\hat{u}$ is a residual effect of the initial condition or a long wave oscillation due to this Wo–Re combination corresponding to $Re_\delta = 625$, i.e. close to the transitional regime depicted in fig. 1. The oscillating bulk in the OP5 flow seems to relax somewhat faster, but a similar variation in $\hat{u}$ still remains. Similar to OP2, the bulk flow in OP3 performs a laminar pulsation and converges rather slowly to a pure oscillation. Additionally, we do not observe any fluctuations or turbulence in this case. Despite the relatively high Re, with $Re_\delta = 317$ this flow lies below the transition line in agreement with [4]. Contrarily, in OP4 turbulence re-establishes within the second oscillation cycle, when started from the same laminar flow field. The onset of turbulence noticeable accelerates the relaxation process to pure oscillation. From the last eight $\hat{u}$ we estimate $Re = 48\,107 \pm 134$, corresponding to $Re_\delta = 1308$, i.e. clearly above the regime V, where a turbulent wall region and a stable core flow was found by [4].

Time series of u_z are presented fig. 3 for OP1 and OP4 at four radial probe locations, i.e. one near the centre line, one close to the wall and two others in between. At all probes, small fluctuations are abruptly amplified near the wall and gradually amplified in the bulk during the early deceleration (ED) phases of OP1. Whereas the fluctuations decay during flow reversal (RV) and, moreover, are damped during the acceleration (AC) phase, at least close to the wall. This confirms experimental

observations by e.g. [4] of growing fluctuations and an asymmetry in the half-cycle for the considered $Re_\delta = 623$ as well as bursts in the vicinity of the wall during DC. Fig. 3 also reveals that fluctuations vary in strength and duration for OP1. This indicates, that turbulence is generated locally and at slightly different phases rather than in the whole pipe domain and at exactly the same oscillation phase. The opposite can be observed in the time lines of u_z for OP4, also shown in fig. 3. Here, the fluctuations gradually increase and decrease with the oscillating bulk flow and, thus show a more or less symmetric trend within one half-cycle. Moreover, the intensity of the fluctuations increases with decreasing wall distance, which is also true throughout the whole oscillation cycle.

The effect of amplification and decay of turbulence during one oscillation half-cycle can be further demonstrated by evaluating integral parameters such as the bulk velocity and the wall shear stress phase averaged over several half-cycles ($m \in \{14, 20\}$), as presented in fig. 4. From $\langle \bar{u} \rangle_\theta$ of OP2 and OP4, which never completely reaches zero, we see again, that the flow still has pulsatile character. Nevertheless, both time lines show a smooth and symmetric trend with a phase shift of $\approx \pi/2$, whereas τ_w has a phase shift of $\approx \pi/4$, as expected from SW theory for high Wo. For OP1 and OP5 $\langle \bar{u} \rangle_\theta$ shows almost the same behaviour with a slightly steeper DC phase, compared to its AC phase. The same behaviour can be found more pronounced in the temporal evolution of the wall shear stress $\langle \tau_w \rangle_\theta$, also shown in fig. 4. The bulk velocity of OP4 does not show this marginal asymmetry, but reaches a little higher peak value at a slightly earlier phase. On the other hand, the wall shear stress exhibits a completely different temporal behaviour. It reflects considerably lower values in the AC phase, a rapid increase during the peak flow and fairly higher values during DC, when compared to OP1 and OP5.

Fig. 5 shows phase averaged velocity profiles for OP1 and OP4. The near-wall maxima and inflexion points in the SW profile, being typical for intermediate Wo, are less pronounced for the higher $Wo = 26$. This characteristics of a viscous Stokes layer are not found in OP1 and OP4 which is again attributed to the turbulent mixing and radial transport of kinetic energy. As an example, in fig. 6 colour encoded contour plots of u_z are presented for OP1 and OP4 at the same phases of the bulk flow.

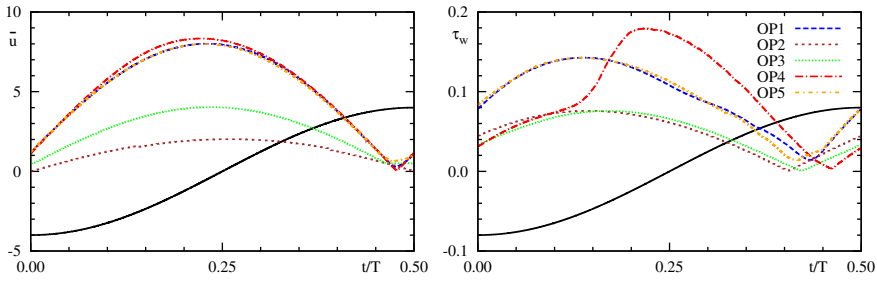

Fig. 4 Phase-averaged bulk velocity $\langle \bar{u} \rangle_\theta$ and wall shear stress $\langle \tau_w \rangle_\theta$ over one oscillation half-cycle. Arbitrary scaled driving pressure gradient as reference (black solid line).

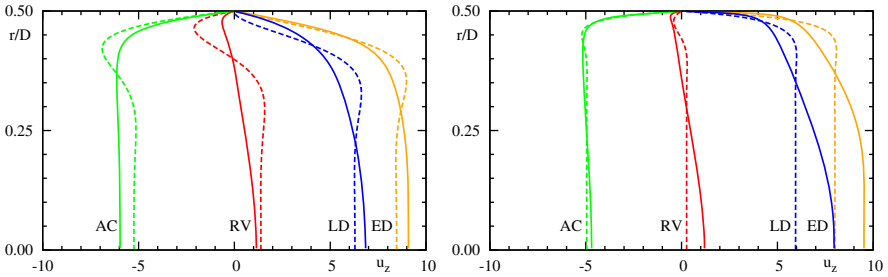

Fig. 5 Radial profiles of the phase-averaged axial velocity component $\langle u_z \rangle_{z,\varphi,\theta}$ for OP1 (left) and OP4 (right) compared to the laminar SW solution (dashed lines).

During ED of the conditionally turbulent case OP1, turbulent structures are generated locally in small parts near the wall, while the core flow and other parts near the wall remain stable. The intensity and extent of these structures increase during late deceleration (LD), despite of the decreasing bulk flow. After RV, the flow relaminarises during AC. Contrarily, the contour plots for the fully turbulent OP4 case, reflect a persistent turbulent state throughout the complete oscillation half-cycle. The intensity of the turbulent structures, visible in the u_z contour plots, increase and decrease with the bulk flow. Vice versa, the associated length scales and the extent of those structures, decrease and increase with the bulk flow. Fig. 7 reflects the differences in the decay and amplification of turbulence obtained in OP1 and OP4 by showing phase averaged RMS velocity fluctuations, i.e. $R(u_z)$ and $R(u_\varphi)$. From ED to LD, the maxima of $R(u_z)$ decrease, while $R(u_\varphi)$ increase for the conditionally turbulent OP1 case. Thus we conclude, that turbulent kinetic energy is shifted from the axial to the azimuthal velocity component, while the flow is decelerated. Contrarily, the maxima of $R(u_z)$ and $R(u_\varphi)$ inccrease and decrease according to the bulk flow for the fully turbulent OP4 case.

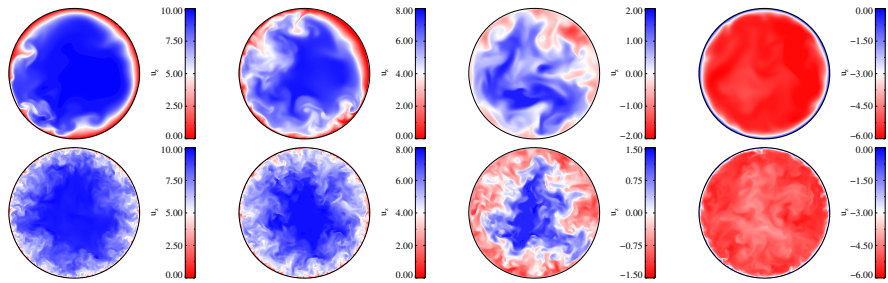

Fig. 6 Colour encoded contour plots of u_z in a cross section of OP1 (top) and OP4 (bottom) at ED, LD, RV and AC (left to right)

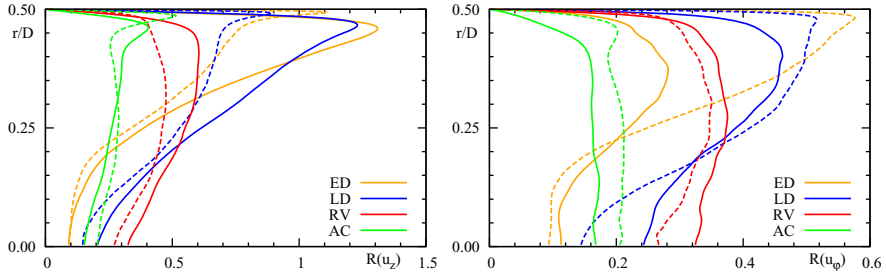

Fig. 7 Radial profiles of the phase-averaged RMS velocity for OP1 (solid lines) and OP4 (dashed lines). For the axial velocity component u_z (left) and the azimuthal velocity component u_φ (right).

4 Concluding Remarks

We report on three-dimensional DNS of oscillatory pipe flows and focus on the decay and amplification of turbulence by analysing instantaneous velocity fluctuations, the integral bulk flow and wall shear stress evolutions as well as phase averaged mean and RMS velocity profiles. When started from a fully developed turbulent velocity field, the oscillatory flows laminarise or reach a conditionally or fully turbulent state, depending on the Wo–Re combination. These two turbulent oscillation states considerably differ in the wall shear stress evolution and the phase-averaged RMS velocity profiles, while the integral bulk flow reflects minor differences. Two different initial conditions seem to have minor influence on the developed conditionally turbulent oscillation for the same parameter set-up.

Acknowledgements. We would like to thank the *Deutsche Forschungsgemeinschaft (DFG)* for providing generous financial support under grant WA 1510/8.

References

1. Avila, K., Moxey, D., de Lozar, A., Avila, M., Barkley, D., Hof, B.: Science 333, 192 (2011)
2. Feldmann, D., Wagner, C.: J. Turb. 13, N32 (2012)
3. Manna, M., Vacca, A., Verzicco, R.: J. Fluid Mech. 700, 246 (2012)
4. Eckmann, D.M., Grotberg, J.B.: J. Fluid Mech. 222, 329 (1991)
5. Zhao, T.S., Cheng, P.: Int. J. Heat Fluid Fl. 17(4), 356 (1996)
6. Trukenmüller, K.E.: Phd thesis, Helmut–Schmidt–Universität, Hamburg (2006)
7. Hino, M., Sawamoto, M., Takasu, S.: J. Fluid Mech. 75(2), 193 (1976)
8. Sexl, T.: Z. Phys. A 61, 349 (1930)
9. Womersley, J.R.: J. Physiol. 127, 553 (1955)
10. Schumann, U.: Phd thesis, Universität Karlsruhe (TH), Karlsruhe (1973)
11. Schmitt, L., Richter, K., Friedrich, R.: Direct and Large Eddy Sim. of Turb. (1986)
12. Shishkina, O., Wagner, C.: Comput. Fluids 36(2), 484 (2007)
13. Feldmann, D., Wagner, C.: 7th Int. Symp. on Turb. and Shear Flow Phen, Ottawa (2011)

Thermal Boundary Layer Instabilities in Near Critical Fluids

G. Gandikota, S. Amiroudine, D. Chatain, and D. Beysens

1 Introduction

Hydrodynamics of near-critical fluids have gained considerable interest since the identification of the thermo-acoustic effect, an effect responsible for a fast thermal equilibration in a cell heated at one boundary [1, 2, 3]. Transport coefficients exhibit strong deviations near the critical point (CP). They are characterized by large density (alike a liquid) and low viscosity, large compressibility (alike a gas). When nearing the CP, some properties (compressibility, thermal expansion, thermal conductivity, specific heat capacity) diverge while others (thermal diffusivity, surface tension) go to zero. The vanishing thermal diffusivity slows down the heat transfer processes (the so-called "critical slowing down"), thus giving a good opportunity to study experimentally the fluid physics. These singular properties imply that the classical dimensionless parameters like the Rayleigh or vibrational Rayleigh numbers diverge at the CP, making the system more and more unstable and ultimately turbulent. Fluids in weightlessness subjected to high frequency vibrations (frequencies greater than the inverse of thermal and hydrodynamic timescales) can be as unstable as on earth. Supercritical fluids, which are highly compressible and expandable amplify these instabilities. Very small temperature inhomogeneities in these fluids can indeed lead to huge density gradients, which make them unstable under the influence of a body-force like gravity (Rayleigh-Benard instability [4]). In this particular

G. Gandikota · D. Chatain
SBT, UMR-E CEA / UJF-Grenoble 1, INAC, Grenoble, F-38054, France
e-mail: gurunath.sharma@gmail.com, denis.chatain@cea.fr

S. Amiroudine
I2M-TREFLE UMR CNRS,16 av. Pey-Berland, 33607 Pessac Cedex
e-mail: sakir.amiroudine@u-bordeaux1.fr

D. Beysens
CEA-ESEME, ESPCI-PMMH 10, rue Vauquelin 75231 PARIS Cedex 05
e-mail: daniel.beysens@espci.fr

M.O. Deville et al. (eds.), *Turbulence and Interactions*,
Notes on Numerical Fluid Mechanics and Multidisciplinary Design 125,
DOI: 10.1007/978-3-662-43489-5_10,

case of highly compressible fluids, the onset of instability saturates when one approaches the CP because the fluid compresses under its own weight (this is related to the Schwarzschild criterion, corresponding to a fluid element climbing adiabatically under a hydrostatic pressure gradient). Under zero gravity conditions, none of these two criteria (Rayleigh and Schwarzschild) applies, however the fluid is still sensitive to vibrations. These vibrations can induce a flow by inertia due to temperature or density inhomogeneities. For the case of a fluid confined between two infinite parallel plates, no convection is observed when the acceleration is parallel to the temperature gradient; convection starts when $Rav > Rav_c \simeq 2100$, where Rav is the Rayleigh vibrational number given by $Rav = \frac{(A'\omega'\beta'_p\delta T'\delta'_{BL})^2}{2\nu' D'_T}$, A' and ω' are the amplitude and the angular frequency of vibration, $\delta T'$ is the thermal quench applied to the boundary, δ'_{BL} is the thickness of the boundary layer and β'_p, ν' and D'_T are the thermal expansion coefficient, kinematic viscosity and thermal diffusivity respectively. This condition holds when the axis of vibration makes an angle of 90° with the temperature gradient [5]. The interest of studying fluids in such conditions is manifold. Firstly, supercritical oxygen, hydrogen, and helium are already used by the space industry. Secondly, their high compressibility and slow dynamics (critical slowing down) emphasize the behavior encountered in regular fluids. Thirdly, fluids in such conditions obey universal, scaled power laws, valid for all fluids [6, 7].

2 Experimental Observations of the Rayleigh Vibrational Instabilities

A typical cylindrical experimental cell is shown in Fig. 1 [8, 9]. It is subjected to horizontal linear harmonic vibrations and a simultaneous fast temperature change (thermal quench). The pictures in Fig. 1 are shown here in the supercritical state. The vibration amplitudes A' are between 0.1 and $0.5mm$ and angular frequencies $\omega' = 2\pi f'$ correspond to frequencies f' between 10 and $60Hz$. Microgravity conditions are different in the two cases. The first picture (Fig. 1a) is concerned with Hydrogen under magnetic compensation of gravity. In the second picture (Fig. 1b) the experiments were performed in the MAXUS-7 sounding-rocket. In both cases, finger - type instabilities appear near the walls where well defined thermal boundary layer slowly develops owing to the vanishing thermal diffusivity. These instabilities are the hall-mark of vibrational Rayleigh - type instabilities. Systematic studies need to be performed to determine the wavelength behavior with the distance to the CP. Two-dimensional numerical simulations have been performed, they are detailed in the next sections.

3 Mathematical and Numerical Models

We consider a square cavity (Fig. 2) of side length H' that contains supercritical fluid and is subjected to horizontal vibration in the x' direction with given amplitude A' and frequency f'. We assume zero-gravity conditions. The fluid is initially

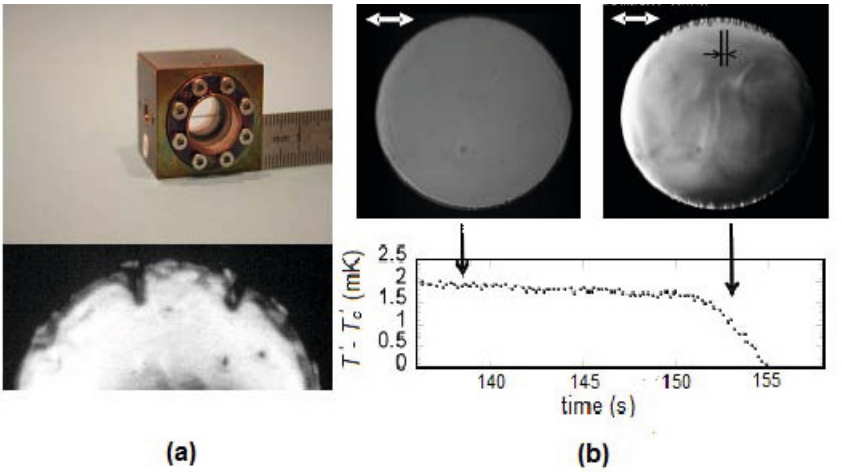

Fig. 1 Experimental photographs for (a) Hydrogen (A'=0.4mm, f'=50Hz; cell of 2mm diameter and 3mm thickness quenched from T_c'+3mK to T_c' +2mK) under magnetic compensation. (b) CO_2 (A'=0.3mm, f'=20 Hz; cell of 10 mm diameter and 2.189 mm thickness quenched from T_c'+2mK to T_c' +1mK) onboard sounding rocket MAXUS-7.

maintained at a temperature T_0', then the temperature of the walls is lowered by an amount $\delta T' \ll T_0' - T_c'$. Our model is based on a Newtonian, compressible, viscous, supercritical fluid that conducts heat and is expandable in a non-stationary state. The dimensionless quantities are defined as follows: density $\rho = \frac{\rho'}{\rho_c'}$, pressure $p = \frac{p'}{\rho_c' c'^2}$, temperature $T = \frac{T'}{T_c'}$, space variables $\mathbf{x} = \frac{\mathbf{x}'}{H'}$, $\mathbf{y} = \frac{\mathbf{y}'}{H'}$, velocity $\mathbf{V} = \frac{\mathbf{V}'}{c'}$ and time $t = \frac{t'}{t_a'}$. Here t' is the real time and $t_a' = \frac{H'}{c'}$ is the acoustic timescale and c' is the sound velocity. The dimensionless equations in weightless conditions can then be written as follows :

$$\begin{cases} \frac{\partial \rho}{\partial t} + \nabla.(\rho \mathbf{V}) = 0 \\ \rho\left(\frac{\partial \mathbf{V}}{\partial t} + (\mathbf{V}.\nabla)\mathbf{V}\right) = -\nabla p + \frac{1}{Re}\left(\Delta \mathbf{V} + \frac{1}{3}\nabla(\nabla.\mathbf{V})\right) + \frac{1}{{Fr_v}^2}\rho \sin(\omega t)\mathbf{i} \\ \rho\left(\frac{\partial T}{\partial t} + \mathbf{V}.\nabla T\right) = \beta_p Ec T \frac{dp}{dt} + \frac{1}{RePr}\nabla.(\nabla T) + \frac{Ec}{Re}\Phi \\ \rho = \rho_0 + \chi_T(p - p_0) - \beta_P(T - T_0) \end{cases}$$

Here ϕ is the non-dimensional dissipation rate defined as: $\phi = V_{i,j}V_{j,i} + V_{i,j}V_{i,j} - \frac{2}{3}V_{i,i}V_{j,j}$. The Einstein summation convention on repeated indices is applied. The dimensionless coefficients appearing in the above equations are: $Fr_v = \frac{c'}{\sqrt{H'\left(A'\omega'^2\right)}}$ (Vibration Froude number), $Pr = \frac{\nu'}{D_T'}$ (Prandtl number), $Re = \frac{H'c'}{\nu'}$ (Reynolds number), $Ec = \frac{c'^2}{C_p' T_c'}$ (Eckert number), $\beta_P = \beta_P' T_c'$ (thermal expansion coefficient), $\chi_T = \chi_T' \rho_c' c'^2$ (isothermal compressibility), $\omega = \omega' t_a'$ (pulsation). All the above dimensionless parameters are thus defined with respect to the physical properties and

depend on only one control parameter $\varepsilon = \frac{T'-T'_c}{T'_c}$, which corresponds to the proximity to the CP. The last equation in the above system corresponds to the equation of state. It is assumed to be linear [10] as the relative temperature difference satisfies: $\delta T' \ll T'_0 - T'_c$ (in the following $\delta T' = 0.1\,(T'_0 - T'_c)$). The thermophysical properties χ_T and β_P can thus be assumed constant and evaluated at the initial state.
The above equations together with the boundary conditions shown in Fig. 2 are solved with a finite volume method by using the Simpler algorithm [11, 12] in a staggered mesh. The space discretization uses the power-law scheme and time discretization is of first-order Euler. The time step is 10^{-3} s, which is much smaller than the involved characteristic timescales. The grid size effect has been carefully tested. The viscous boundary layer thickness is of the order of $\delta'_{vib} = \sqrt{\frac{2\nu'}{\omega'}} \simeq 46\mu m$ for $f' = 20Hz$. The kinematic viscosity is almost constant because the shear viscosity μ' exhibits a very low divergence, $\mu' \sim \varepsilon^{-0.04}$. In all the studied cases, the non-uniform mesh has 80x80 points and the first point of the mesh is at about $14.3\mu m$.

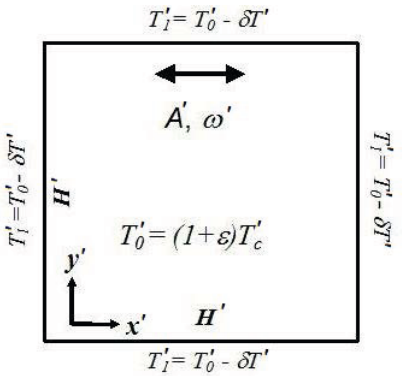

Fig. 2 Geometry of the numerical model

4 Rayleigh Vibrational Intabilities

Numerical simulations have been performed with CO_2 in a square cavity of side length 10 *mm* [13]. Even though the geometry is different with respect to the experimental set-up (cylindrical cell), the purpose here is to establish qualitatively the finger-type instability. In Fig.3, horizontal vibration of frequency $f' = 20Hz$ and amplitude $A' = 0.5mm$ and a temperature quench of $1K$ are simultaneously applied to the cavity with an initial temperature of $T'_c + 3K$. As shown in this figure, the temperature field (for initial temperatures $T'_i = T'_c + 30K$, $T'_c + 2K$ and $T'_c + 0.3K$ and corresponding quenches of $0.1(T'_i - T'_c)$) leads to the appearance of fingers on top and bottom boundaries whose wavelength decreases as the CP is approached. It is the signature of a Rayleigh vibrational instability [5], in agreement with the

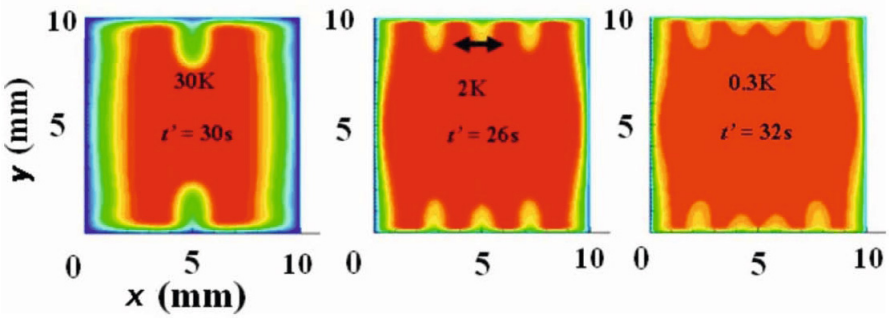

Fig. 3 Temperature fields for $T' - T'_c$= 30, 2, 0.3 K with quenches of 3, 0.2 et 0.03 K and at different times 30, 26 and 32s (vibration of amplitude 0.5mm and frequency 20 Hz for a square cell of 10mm side)

above experimental observations.The variation of the critical vibrational Rayleigh number (Rav_c) as a function of temperature is depicted in Fig. 4 (left) for the vibration ($f' = 20Hz$, $A' = 0.5mm$). This curve shows that Rav_c diverges when the CP is approached. This divergence is more pronounced for $T' - T'_c < 1K$. The critical time, t'_c, which corresponds to the initial appearance of the waviness of the boundary layer interface, is increased when the CP is neared. Fig. 4 (right) shows the corresponding wavelength as a function of temperature. It decreases when approaching the CP. These results have to be completed by a linear stability analysis of the averaged equations, as it has already been tested for an incompressible fluid [14]. This study has confirmed the existence of a Rayleigh vibrational instability and is in fair agreement with our numerical results far from the CP. The next step would be to consider an ideal gas equation of state and then generalize to hyper compressible fluids (supercritical fluids), using a van der Waals equation of state.

5 Faraday Type Instabilities

In order to further investigate these instabilities, a rectangular cell has been built and experiments have been performed under magnetic compensation of gravity. A $3mm$ square cell which contains Hydrogen in near-critical conditions has been constructed. The fluid is initially below the CP (two-phase system). It is heated towards the CP. At the same time, the cell is subjected to a horizontal harmonic linear vibration. Figure 5 shows pictures of the density field as a function of temperature. Initially, two distinct zones of gas and liquid phases are present, the liquid phase wetting completely the walls and surrounding the vapor bubble. As soon as the vibration is applied, the interface perpendicular to the vibration direction undergoes an instability. This latter is Faraday - like as the frequency of the fingers oscillation is half the imposed frequency. When very close to the CP, vertical alternate bands of liquid and gas phases appear, the origin of which is unclear. All pictures are

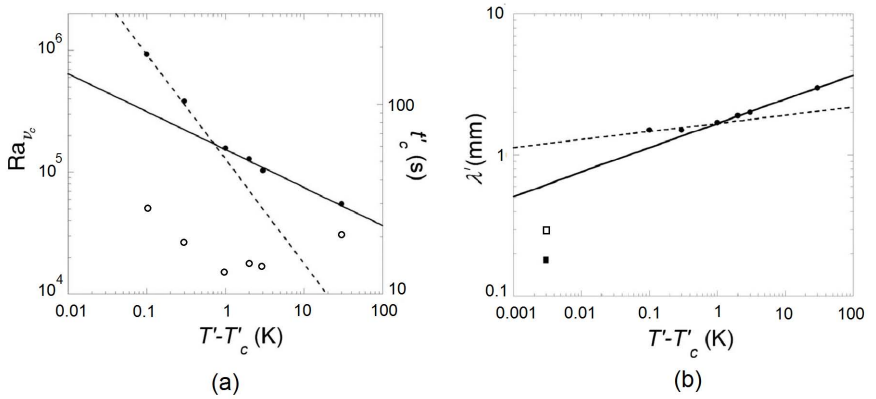

Fig. 4 (a): Critical vibrational Rayleigh number as a function of temperature (vibration: amplitude 0.5 mm, frequency 20 Hz). The critical time corresponds to the apparition of instabilities in forms of fingers. (b): Corresponding wavelength as a function of temperature.

Fig. 5 Experimental density field in a 3 mm cuboidal cell of H_2 below T'_c (=33 K). The cell is heated towards $T'c$ and subjected to vibration (A'=0.28 mm, f'=40 Hz). Temperature is raised from (left) 130 mK below T'_c to T'_c (right).

concerned with temperatures below T'_c. No instability has been observed above the CP (supercritical region). The reason is presumably due to the cell size that may be too small with respect to the instability wavelength. A new rectangular cell of $7mm$ side length has then be fabricated and experiments are underway.

Numerical simulations have been performed for a $10mm$ square cell filled with supercritical CO_2. The frequency has been reduced in order to fulfill the technical standards of the future space experiments. Figure 6 shows the temperature field for a vibration of frequency $f' = 2.8Hz$ and amplitudes $A' = 1mm$, $15mm$ and $31mm$. As seen in these figures, the temperature field undergoes a vibrational Rayleigh instability (fingering perpendicular to the vibration direction) at low amplitudes and a Faraday-type instability at higher amplitudes (fingering parallel to the vibration direction with half of exciting frequency). At intermediate values of the amplitudes, both instabilities are observed. The instability wavelength decreases as the acceleration (or amplitude) increases, in agreement with the studies dealing with Faraday instabilities in immiscible [15] and miscible [16] fluids.

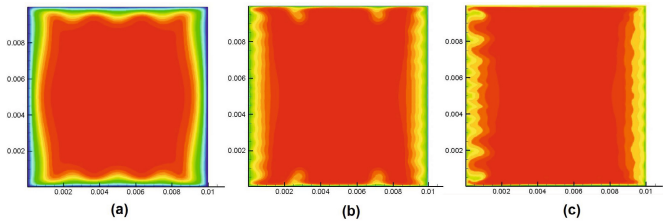

Fig. 6 Numerical temperature field for a square cell (side $10mm$) filled with CO_2 at $T_i' = T_c' + 1K$ subjected to temperature quench of $0.1K$ and horizontal vibration of f'=$2.8Hz$ and (a) A'=$1mm$, (b) $15mm$ and (c) $31mm$ (right).

6 Conclusion

A fluid contained in a cell under weighlessness whose temperature is changed shows an instability of the thermal boundary layers when subjected to a linear harmonic vibration perpendicular to the temperature gradients. These instabilities under weightless conditions known as vibrational Rayleigh instabilities are amplified near the CP since the vibrational Rayleigh number diverges. Two dimensional numerical simulations based on Finite Volume method have confirmed these instabilities. When approaching the CP, the critical vibrational Rayleigh number shows a divergence whereas the instability wavelength decreases. Experiments under the same conditions as the numerical simulations have been performed and show Faraday-like instabilities below Tc that transforms very close to Tc into steady alternate layers of the liquid and vapor phases. Numerical simulations have been performed for low frequency in order to fulfill the technical requirements of a future space experiment. Faraday-type instabilities have been observed on the vertical walls where the temperature gradients are parallel to the axis of vibration. These unusual results have to be verified by experiments under magnetic compensation of gravity and a linear stability analysis of the averaged equations.

References

1. Onuki, A., Hao, H., Ferrel, R.A.: Fast adiabatic equilibration in a single-component fluid near the liquid-vapor critical point. Phys. Rev. A41, 2256–2259 (1990)
2. Boukari, H., Saurneyer, J.N., Briggs, M.E., Gammon, R.W.: Critical speeding up in pure fluids. Phys. Rev. A41, 2260–2263 (1990)
3. Zappoli, B., Bailly, D., Garrabos, Y., Le Neindre, B., Guenoun, P., Beysens, D.: Anomalous heat transport by the piston effect in supercritical fluids under zero gravity. Phys. Rev. A41, 2264–2267 (1990)
4. Amiroudine, S., Bontoux, P., Larroud, P., Gilly, B., Zappoli, B.: Direct numerical simulation of unsteady instabilities inside a near-critical fluid layer under Rayleigh-Bénard configuration. J. Fluid Mech. 442, 119–140 (2001)
5. Gershuni, G.Z., Lyubimov, D.V.: Thermal vibrational convection. Wiley, New York (1998)

6. Stanley, H.E.: Introduction to Phase Transitions and Critical Point Phenomena. Oxford University Press (1971)
7. Onuki, A.: Phase Transition Dynamics. Cambridge University Press (2002)
8. Beysens, D., Garrabos, Y., Chatain, D., Evesque, P.: Phase transition under forced vibrations in critical CO2. EuroPhys. Lett. 86, 16003 (2009)
9. Wunenburger, R., Chatain, D., Garrabos, Y., Beysens, D.: Magnetic compensation of gravity forces in (p-) hydrogen near its critical point: Application to weightless conditions. Phys. Rev. E62, 469–476 (2000)
10. Amiroudine, S., Boutrouft, K., Zappoli, B.: The stability analysis of two layers in a supercritical pure fluid: Rayleigh Taylor-like instabilities. Phys. Fluids 17, 054102 (2005)
11. Patankar, S.: Numerical Heat Transfer and Fluid Flows. McGraw Hill, New York (1980)
12. Amiroudine, S., Ouazzani, J., Zappoli, B., Carls, P.: Numerical solutions of 1D unsteady hypercompressible flows using finite volume methods. Eur. J. Mech. B/Fluids 16, 665 (1997)
13. Amiroudine, S., Beysens, D.: Thermovibrational instability in supercritical fluids under weightlessness. Phys. Rev. E 78, 036323 (2008)
14. Lyubimov, D., Lyubimova, T., Amiroudine, S., Beysens, D.: Stability of a thermal boundary layer in the presence of vibration in weightlessness environment. Eur. Phys. J. ST 192, 129–134 (2011)
15. Kumar, K., Tuckerman, L.S.: Parametric instability of the interface between two fluids. J. Fluid Mech. 279, 49–68 (1994)
16. Zoueshtiagh, F., Amiroudine, S., Narayanan, R.: Experimental and numerical study of miscible Faraday instability. J. Fluid Mech. 628, 43–55 (2009)

Numerical Simulation of Turbulent Flow Physics in a Tube Array

Y. Hoarau, M. Braza, G. Harran, E. Longatte, F. Baj, and T. Marcel

Abstract. The prediction of fluid-elastic instabilities developing in a tube bundle is of major importance in the design of modern heat exchangers for nuclear reactor cooling to prevent accidents associated with fluid-elastic instabilities leading to flutter, material fatigue, shocks between beams and damage of the solid walls. The fluid-elastic instabilities in tube arrays appear in the laminar regime and persist in the high Reynolds number turbulent flow. They are governed by non-linear interaction between fluid-elastic instability and turbulence. It is of major importance for the design to accurately predict the unsteady loads under turbulent flow and the amplification of the fluid-elastic instabilities. This work focuses on the numerical simulation of turbulent flow in tube bundle and prediction of fluid-elastic instabilities.

1 Introduction

There is a considerable effort in the state-of-the-art to improve methodologies able to capture the fluid-structure interaction under turbulent flow, and to assess critical thresholds. These aspects are challenging for the research applications involving the nuclear power industry. The present work is part of the BARESAFE project

Y. Hoarau
ICUBE, UDS - CNRS - ENGEES - INSA, France
e-mail: hoarau@unistra.fr

M. Braza · G. Harran · T. Marcel
Institut de Mécanique des Fluides de Toulouse, UMR CNRS 5502, France

E. Longatte
Laboratoire de Mécanique des Structures Industrielles Durables,
UMR EDF CNRS 2832, France

F. Baj
Commissariat à l'Energie Atomique CEA / Saclay, France

M.O. Deville et al. (eds.), *Turbulence and Interactions*,
Notes on Numerical Fluid Mechanics and Multidisciplinary Design 125,
DOI: 10.1007/978-3-662-43489-5_11,

funded by the French National Research Agency (ANR) with LAMSID, EDF, CEA, IMFT, ICUBE, IRIT and AREVA. The BARESAFE project (Numerical modeling of multi-scale fluid solid coupled systems : advanced hybrid methods for reduction of uncertainty on stability limits and optimization of nuclear safety barrier reliability) is a research project involved in the development of modeling and advanced numerical methods for simulation of large size systems involving multi-physics in the field of mechanics. It addresses the hard issue of stability analysis of dynamical systems submitted to external turbulent flows and aims to establish accurate stability maps applicable for heat exchanger design. The purpose is to provide stability limit dimensionless modeling suitable in a variety of configurations with a maximal accuracy in spite of the large scale of the systems to be considered. The challenge lies in predicting local effects possibly impacting global systems. Therefore the combination of several strategies convenient simultaneously for multi-physics, multi-scale and large size system computation is required. Based on empirical concepts, the heuristic models currently used in the framework of standard stability analysis suffer from a lack of predictive capabilities Blevins (1974, 1979); Tanaka and Takahara (1981, 1982); Chen (1983); Paidoussis and Price (1988), Lever and Weaver (1982). On the other side, numerical approaches based on fully-coupled fluid solid dynamics system computation remain expensive due to the multi-physics patterns of physics and the large number of degrees of freedom to be involved. In this context, since experimentation is not reachable and numerical simulation is unavoidable but prohibitive, the project proposes an hybrid strategy in order to take advantages from both numerical local and empiric global solutions.

The present study focuses on the improvement of the numerical simulation of the fluid-structure interaction in the cylinders arrays, especially in the parametric range favoring the amplification and negative damping of flutter instability. The main objective is to analyze the physics of the appearance of Movement Induced Vibrations in connection with the instabilities coming from the fluid part in an array bundle. Concerning turbulence modeling methods, among URANS approaches, the Organised Eddy Simulation Braza et al. (2006); Bourguet et al. (2008), OES has been used to capture the coherent flow patterns and non-equilibrium effects associated with the fluid-elastic instabilities. Furthermore, the OES version of the Delayed Detached Eddy Simulation and the Scale Adaptive Simulation has been used for the 3-D simulations.

First we focused on a two-dimensional study in static configuration, in order to assess the predictive ability of 2-D mechanisms. Secondly, the spontaneous motion of a central cylinder, in SDOF (single degree of freedom) vertical displacement is studied, below and beyond critical values for the appearance of flutter instability in the array of cylinders. Then the three-dimensional flow structure is studied by OES-DDES Skopek et al. (2012) and SAS Menter and Egorov (2005); Menter and Bender (2003).

Only the static approach is presented in this paper.

2 Problem Set-Up

The configuration fit an experimental set-up (DIVA) designed by the CEA where 20 cylinders are arranged in 5 columns with a pitch of 1.5*D*, *D* being the diameter of the cylinders. The Reynolds number is 20.000 which corresponds to an inter-tube Reynolds number of 60.000. The grid (Fig. 1) is composed with 392 600 cells distributed on 80 structured blocs. On the entry and on the outlet boundary, the conditions are :

- inlet : far field boundary condition using characteristic variables,
- outlet : subsonic outflow with imposed static pressure based on Riemann invariants.
- top-bottom : no-slip walls.

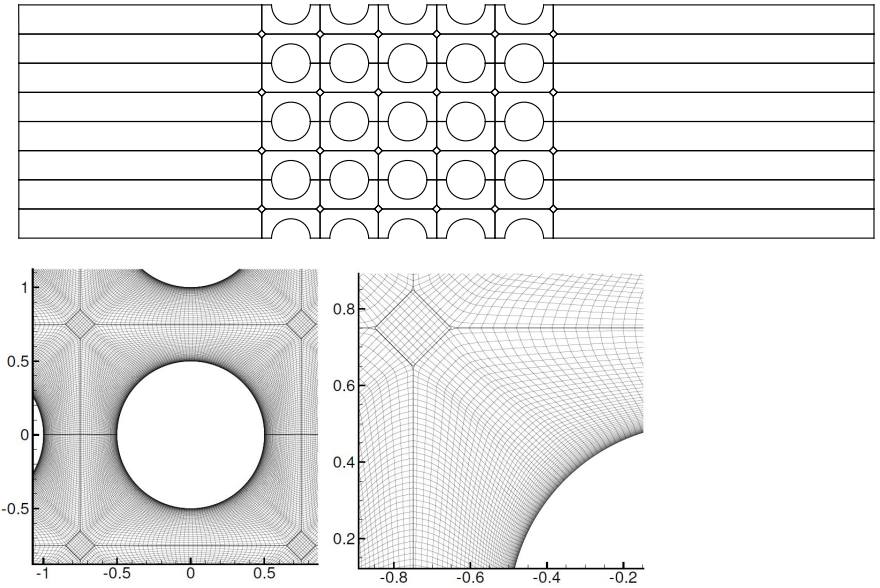

Fig. 1 Grid overview

3 Numerical Modeling

The simulations are performed with our parallelized Navier-Stokes Multi-Block (*NSMB*) solver Vos et al. (1998). NSMB solves the compressible Navier-Stokes equations using a finite volume formulation on Multi-Block structured grids. Various spatial discretization schemes are available like Jameson's central difference, Roe or AUSM+. The time integration is based on the full matrix implicit LU-SGS (Lower-Upper Symmetric Gauss-Seidel) method Yoon and Jameson (1986) and on the dual-time stepping. In the present work, the artificial compressibility method Chorin (1968) is employed. NSMB is parallelized using the Message Passing Interface.

4 Turbulence Modeling

The URANS turbulence models used in this study are the Spalart and Allmaras (1992), the $k-\omega$ models (baseline and SST) of Menter (1994), the OES $k-\varepsilon$ and the OES $k-\omega$ baseline models, described in Braza et al. (2006); Bourguet et al. (2008). The Delayed Detached Eddy Simulation, DDES is employed by using for the RANS part the turbulence length scale from the OES method.

The association of the OES modeling in the RANS part of the DES/DDES is reported in a number of studies of the present research group, that have been the object of applications in a variety of test cases in the European research programs DESIDER (Detached Eddy Simulation for Industrial Aerodynamics) and ATAAC (Advanced Turbulence Modeling for Aeronautics Applications Challenges) in aeronautics. The introduction of a turbulence length scale from OES in the Delayed DES, DDES Spalart et al. (2006) is reported in Haase and Revell (2009), Bourguet et al. (2008) and in Skopek et al. (2012). The use of this variety of turbulence models allows assessment of their predictive capabilities in respect of the strongly detached unsteady flow character in the array of cylinders.

The OES modeling approach is used to capture the two aspects of fluid structure instability : organized and chaotic.

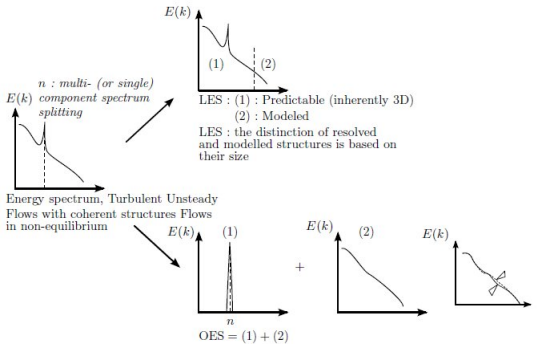

Fig. 2 Dual spectrum splitting : the distinction between the structures to be resolved and those to be modeled is based upon their organized or random character. Part (2) of the non-equilibrium energy spectrum has to be modeled by reconsidering advanced statistical turbulence modeling efficient in high-Re wall flows, due to the inertial-range modulation from equilibrium turbulence, schematically shown on the right.

In this approach, the turbulent spectrum is decomposed in a first part regrouping all the coherent structures (resolved part) and in a second part regrouping all the chaotic processes independently on their size (spectrum to be modeled), as presented schematically in Fig. 2. It is recalled that in LES the distinction is done according to the size of the structures which limits its application to moderate Reynolds numbers. The fact that part of the spectrum to be modeled in OES extend from the low to the high frequencies allows the use of statistical turbulence modeling with appropriate modification due the non-equilibrium. In the time-domain, the equations are the

phase-averaged NavierStokes equations. Due to the nonlinear interaction between the coherent part and the non-coherent one, there is a slope modification of the inertial part in the spectrum, in the vicinity of the peak. This yields to a reconsideration of the eddy-diffusion coefficient for the class of the two-equation modeling, as well as improved damping functions to attenuate turbulence towards the wall.

5 Results

The unsteady loads obtained with this four turbulence models are examined and their average values, their minimum and maximum values (Table 1) their frequency distribution (Table 2) are compared.

Table 1 Lift coefficient of unsteady loads

Models	$C_{L,RMS}$	$C_{L,min.}$	$C_{L,max.}$
Spalart-Allmaras	0.44	−0.89	1.04
$k-\omega-$SST	0.19	−0.68	0.58
$k-\omega-$BL$-$OES	0.65	−1.84	1.69
$k-\varepsilon-$OES	0.46	−1.08	1.11
DIVA Experiment	0.45	−1.86	2.33

We have a good match between the turbulent simulations and the experimental data. The $k-\varepsilon-$OES and Spalart-Allmaras approaches give the best prediction of the RMS values of the lift coefficient. However, for the extrema values, the $k-\omega-$BL$-$OES prediction brings the best results.

Extrema values of the lift coefficient are also important in a study on the fluid-structure interaction. Indeed, it is possible that not only the signal strength (RMS values) but also the extent of the values will trigger the instability. This is why the prediction of unsteady loads have to be accurate for these two aspects. In this context, OES approaches seem to bring better results than conventional URANS approaches.

This can be explained by the fact that this complex flow configuration of the tube bundle at this Reynolds number caused a mixed boundary layer. OES approach allow to have a better capture of the mixed boundary layer than the classical URANS approaches.

Concerning the frequencies, results are presented on Power Spectral Density (PSD) on Fig. 3.

We can find also a good match between models and experimental data. This is the first time to our knowledge that unsteady numerical simulations have so good agreement with this test bench of the configuration of a tube bundle under cross flow at a Reynolds number of 20.000.

OES approaches seem to predict a more accurate power level than the URANS classical ones which slightly underestimate this level.

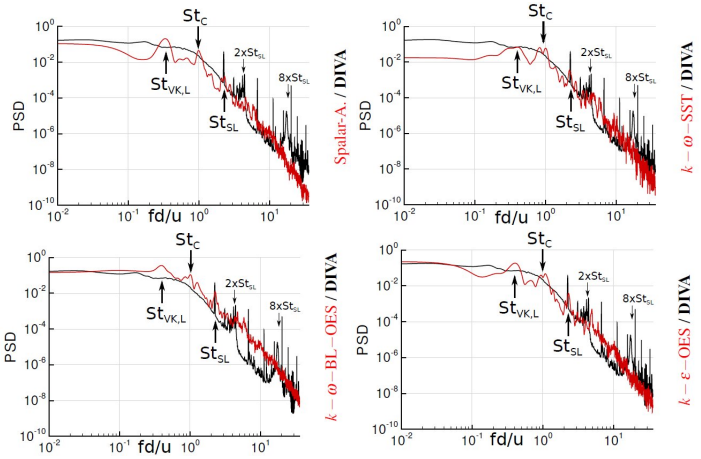

Fig. 3 Power spectrum density of the lift coefficient for the models SA, $k-\omega-$SST, $k-\omega-$Baseline$-$OES and $k-\varepsilon-$OES closures with hanning windows

Three predominant frequencies appear on the spectra. After a study of the cartography of the separation point, we have linked the values of these frequencies to known physical phenomena : the von Kármán vortex shedding St_{VK}, the confinement phenomenon St_C and the shear layer phenomenon St_{SL}.

We can define a Strouhal number with the free stream velocity, but also a Strouhal number with inter-tube velocity, which we denote $St_{.,it}$

$$St_{.,it} = f\ du_{it} = (P^* - 1P^*)\ St \quad with \quad P^* = Pd \tag{1}$$

with P^* the reduced step. Values of predominant frequencies are summarized in Tab. 2.

Table 2 Values of predominant frequencies

Models	St_{VK}	$St_{VK,it}$	St_C	St_{SL}
Spalart-Allmaras	0.34	0.11	0.99	2.25
$k-\omega-$SST	0.36	0.12	0.99	2.25
$k-\omega-$OES	0.39	0.13	1.01	2.25
$k-\varepsilon-$OES	0.39	0.13	1.01	2.25

The inter-tube value observed for the von Kármán Strouhal number is nearly that the conventional value known for a Reynolds number of 60.000 for one cylinder ($St_{cyl.} \approx 0.2$). Furthermore the four models predict almost the same values for the three predominant frequencies.

As for the study of the cartography of the separation point, we focused only on the central cylinder and we looked at the position of the point of detachment on the

wall of the cylinder for a series of snapshots. We found a periodical appearance of grounds which correspond to the predominant frequencies of the spectral study. The frequency which is linked to the von Kármán vortex shedding phenomenon, whose value is rather low (relative to the other two), is located to the rear of the cylinder. One that matches the shear layer phenomenon is located just above this area with a higher value. Finally, the third frequency is linked to a phenomenon related to the impact of coherent structures on the zone $|\alpha| \approx 60°$. This zone corresponds to the area where the structures issued from the previous rows of cylinders are crashing. That's why this predominant frequency is linked to a confinement phenomenon, caused by the geometry of the tube bundle.

6 Conclusions

The present study shows the prediction of unsteady loads in a tube bundle at high Reynolds number in the context of fluid-structure interaction.

URANS and OES turbulence modeling comparison on the static configuration is performed. The oscillatory characteristics is well predicted, particularly concerning the power spectrum density. OES modeling improves the coherent structure prediction in the cylinder wake, which is under-predicted with the classical URANS approach.

There is a good match with the experimental data, even if the simulations have been computed in two dimensions. The 3-D simulations are in progress in order to find the purely 3-D phenomenon.

There are three phenomena which involve three predominant frequencies in the tube bundle under cross flow at Reynolds number of 20.000: the von Kármán vortex shedding, the confinement and the shear layer. The demonstration of the existence of this three predominant frequencies is a first step to the numerical study of fluid-elastic instability.

The classical URANS and OES approaches are good tools to compute simulations at this Reynolds number. DNS is too expensive in term of computational cost. So there is an obvious interest to use hybrid approaches for 3-D simulation.

Acknowledgements. This study was made using high performance computing facilities of nationals centers as CINES, TGCC/CCRT and the computing center of the Strasbourg University. This work was conducted in the context of the BARESAFE project (http://www-imfs.u-strasbg.fr/baresafe/index.html), ANR 11-MONU-004.

References

Blevins, R.: Fluid-elastic whirling of a tube row. J. of Pressure Vessel Tech. 96, 263–267 (1974)

Blevins, R.D.: Formulas for natural frequency and mode shapes. Krieger Publishing Company (1979)

Bourguet, R., Braza, M., Harran, G., El Akoury, R.: Anisotropic organised eddy simulation for the prediction of non-equilibrium turbulent flows around bodies. J. of Fluid and Struct. 24(8), 1240–1251 (2008)

Braza, M., Perrin, R., Hoarau, Y.: Turbulence properties in the cylinder wake at high Reynolds number. J. of Fluid and Struct. 22, 7551–7771 (2006)

Chen, S.S.: Instability mechanisms and stability criteria of a group of circular cylinders subjected to cross flow. part i: Theory. J. of Vibration, Acoustics, Stress and Reliability in Design 105(1), 51–58 (1983)

Chorin, A.: Numerical solution of the Navier-Stokes equations. J. Math. Computation 22, 745 (1968)

Haase, W., Braza, M., Revell, A.: DESider A European Effort on Hybrid RANS-LES Modelling. Notes on Numerical Fluid Mechanics and Multidisciplinary Design, vol. 103. Springer (2009)

Lever, J., Weaver, D.: A theoretical model for fluid-elastic instability in heat exchanger tube bundles. J. of Pressure Vessel Tech. 104, 147–158 (1982)

Menter, F.: Two-equation eddy-viscosity turbulence models for engineering applications. AIAA J. 32(8), 1598–1605 (1994)

Menter, F.R., Kuntz, M., Bender, R.: A scale-adaptive simulation model for turbulent flow prediction, Reno, NV. AIAA paper 2003-0767 (2003)

Menter, F., Egorov, Y.: A scale-adaptive simulation model using two-equation models, Reno, NV. AIAA paper 2005-1095 (2005)

Paidoussis, M.P., Price, S.J.: The mechanisms underlying flow-induced instabilities of cylinder arrays in crossflow. J. of Fluid Mech. 187, 45–59 (1988)

Schwamborn, D., Strelets, M.: ATAAC an EU-project dedicated to hybrid RANS/LES methods. Notes on Num. Fluid Mech. and Multidisciplinary Design 117, 59–75 (2012)

Skopek, M.G., Braza, M., Hoarau, Y., Thiele, F.: Hybrid rans-les modeling of a strongly detached turbulent flow around a tandem cylinders configuration. In: Fu, S., Haase, W., Peng, S. (eds.) Progress in Hybrid RANS-LES Modelling, Papers Contributed to the 4th Symposium on Hybrid RANS-LES Methods, Beijing, China. Notes on Num. Fluid Mech. and Multidisciplinary Design, vol. 117, pp. 219–229. Springer, Berlin (2012)

Spalart, P., Allmaras, S.: A one-equation turbulence model for aerodynamic flows. AIAA Paper 439 (1992)

Spalart, P., Deck, S., Shur, M., Squires, K., Strelets, M., Travin, A.: A new version of detached-eddy simulation, resistant to ambiguous grid densities. Theor. Comput. Fluid Dyn. 20, 181–195 (2006)

Tanaka, H., Takahara, S.: Fluid elastic vibration of tube array in cross flow. Journal of Sound and Vibration 77, 19–37 (1981)

Tanaka, H., Takahara, S.: Flow induced vibration of tube arrays with various pitch-to-diameter ratios. J. Pressure Vessel Technol. 104(3), 168–174 (1982)

Yoon, S., Jameson, A.: A Multigrid LU-SSOR Scheme for Approximate Newton Iteration Applied to the Euler Equations. NASA-CR-179524 (1986)

Vos, J., Chaput, E., Arlinger, B., Rizzi, A., Corjon, A.: Recent advances in aerodynamics inside the NSMB (Navier-Stokes Multi-Block) consortium. AIAA Paper 0802 (1998)

Non-Oberbeck-Boussinesq Effects in Rayleigh-Bénard Convection of Liquids

Susanne Horn, Olga Shishkina, and Claus Wagner

Abstract. The influence of temperature-dependent material properties on Rayleigh–Bénard convection is investigated in three different liquids, ranging from a very small Prandtl number for mercury with $Pr = 0.0232$, over a moderate one for water with $Pr = 4.38$, to a very large one for glycerol with $Pr = 2548$. For this purpose, three-dimensional direct numerical simulations were performed in a cylindrical cell with a unity aspect ratio. Local quantities such as the viscous and thermal boundary layer thicknesses, the centre temperature and the wind velocity show a breakdown of the top-bottom symmetry. The intensity of this asymmetry strongly depends on the respective fluid.

1 Introduction

Thermal convection is one of the most fundamental problems in geo- and astrophysics. Examples to mention here are the convection in the outer layer of stars, in the Earth's atmosphere and oceans or the mantle convection on Earth and other rocky planets. Furthermore, it is also important for engineering applications. Examples here are crystal growth or the air flow in aircraft cabins. However, the physical process itself is still not completely understood. Thus, the idealised scenario, i.e. a fluid heated from below and cooled from above, the so-called Rayleigh-Bénard convection, has received ongoing attention for over a century now.

For theoretical and numerical investigations commonly the classical Oberbeck-Boussinesq (OB) approximation is employed. That means, the fluid is considered to be incompressible and all material properties are constant with respect to the pressure and the temperature. The only exception is the density, which varies linearly with the temperature. However, the validity range of this approach is often very

Susanne Horn · Olga Shishkina · Claus Wagner
German Aerospace Center, Institute for Aerodynamics and Flow Technology,
Göttingen, Germany
e-mail: susanne.horn@dlr.de

M.O. Deville et al. (eds.), *Turbulence and Interactions*,
Notes on Numerical Fluid Mechanics and Multidisciplinary Design 125,
DOI: 10.1007/978-3-662-43489-5_12,

restrictive and deviations due to the violation of the OB assumption are referred to as non-Oberbeck-Boussinesq (NOB) effects. NOB effects in gases are mostly induced by compressibility and the pressure dependence of the material properties. On the contrary, in liquids the temperature dependence is crucial for NOB effects. This is what we will focus on in the following. As a step in the direction to predict the flow behaviour of realistic fluids, we study the influence of temperature-dependent material properties in liquids by means of Direct Numerical Simulations (DNS).

2 Validity Range of the OB Approximation

A rigorous mathematical deduction for the validity range of the OB approximation was given by Gray & Giorgini [1]. In short, it states that if certain ε_i are smaller than a requested accuracy, e.g. 0.1, a residual error of at most 10 % is guaranteed.

$$\varepsilon_1 = \frac{\alpha_m g H}{c_{p,m}} \frac{T_m}{\Delta},\ \varepsilon_2 = \frac{\alpha_m g H}{c_{p,m}} \frac{\nu_m}{\kappa_m},\ \varepsilon_3 = -\frac{\Delta}{\rho_m} \frac{\partial \rho}{\partial T}\bigg|_{T_m},\ \varepsilon_4 = \frac{\Delta}{c_{p,m}} \frac{\partial c_p}{\partial T}\bigg|_{T_m}, \tag{1}$$
$$\varepsilon_5 = \frac{\Delta}{\rho_m \nu_m} \frac{\partial(\rho\nu)}{\partial T}\bigg|_{T_m},\ \varepsilon_6 = \frac{\Delta}{\Lambda_m} \frac{\partial \Lambda}{\partial T}\bigg|_{T_m},\ \varepsilon_7 = \frac{\Delta}{\alpha_m} \frac{\partial \alpha}{\partial T}\bigg|_{T_m}.$$

Here T is the temperature, H the height of the Rayleigh–Bénard cell, g the gravitational acceleration, α the isobaric expansion coefficient, ρ the density, ν the kinematic viscosity, Λ the heat conductivity, c_p the specific heat at constant pressure and $\Delta = T_b - T_t$ the imposed adverse temperature difference. The indices t, b and m refer to the quantity at the top, the bottom and the arithmetic mean temperature $T_m = (T_t + T_b)/2$, respectively.

We exemplarily applied their method to three different liquids, which significantly distinguish themselves through their different Prandtl numbers, $Pr = \nu_m/\kappa_m$. Namely, glycerol with $Pr = 2548$ (figure 1(a)), water with $Pr = 4.38$ (figure 1(b))

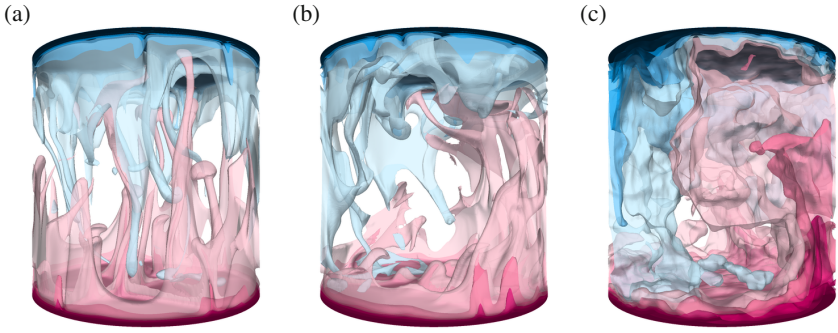

Fig. 1 Instantaneous flow fields for (a) glycerol ($Pr = 2548$), (b) water ($Pr = 4.38$) and (c) mercury ($Pr = 0.0232$) for $Ra = 10^8$ under OB conditions, obtained by DNS on a $N_r \times N_\phi \times N_z = 192 \times 512 \times 384$ mesh. Shown are ten temperature isosurfaces equidistantly distributed between the top and bottom temperature.

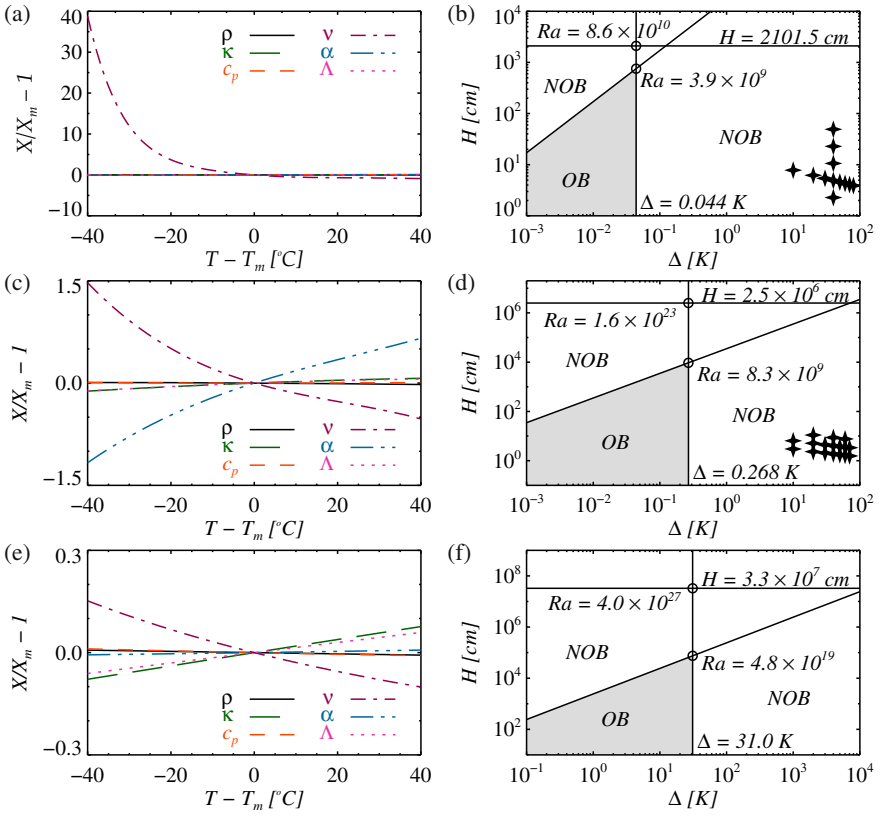

Fig. 2 Material properties $X \in \{\rho, \kappa, c_p, \nu, \alpha, \Lambda\}$ for (a) glycerol, (c) water and (e) mercury. The corresponding regions of validity of the Oberbeck–Boussinesq approximation for (b) glycerol, (d) water and (f) mercury at $T_m = 40\,°\mathrm{C}$, according to Gray & Giorgini [1]. The grey shaded areas show the parameter range where the OB assumption is valid. The stars denote our NOB DNS parameters.

and mercury with $Pr = 0.232$ (figure 1(c)). The material properties of each fluid [2, 3, 4] are shown in figure 2(a), (c) and (e), respectively. Glycerol only exhibits a strongly temperature-dependent viscosity, while all the other thermophysical properties are virtually constant. This suggests that NOB effects occur already at small Δ. Indeed, the validity range diagram according to Gray & Giorgini [1], presented in figure 2(b), confirms it, showing that the maximal admissible temperature difference is $\Delta = 0.044\,\mathrm{K}$. It also shows that the maximal attainable Rayleigh number $Ra = \alpha_m g \Delta H^3/(\kappa_m \nu_m)$ under OB conditions is 3.9×10^9. For water, the variation of the material properties is much weaker, however, the variation in ν and α is of the same strength, and also the variation in Λ and κ, respectively, is not negligible. The validity range presented in figure 2(d) shows that OB conditions are limited to $\Delta < 0.268\,\mathrm{K}$. Finally, mercury has almost constant material properties, and thus

NOB factors are only to be expected for larger Δ (figure 2(f)). Since our objective is the investigation of NOB effects, we will concentrate on water and glycerol.

3 Numerical Method

For our studies of Rayleigh–Bénard convection we perform DNS with a well-tested fourth order accurate finite volume code for cylindrical domains. The code is based on `flowsi`, originally developed by Schmitt & Friedrich [5]. It solves the Navier–Stokes equations on staggered grids and uses the volume balance procedure motivated by Schumann [6]. Later on, it was advanced with a fourth order accurate spatial integration scheme and for the simulation of Rayleigh–Bénard convection by Shishkina & Wagner [7]. For the purpose of investigating NOB effects, we implemented temperature-dependent material properties, adopted from Ahlers et al. [2] and Segur & Oberstar [3]. The viscosity ν, the heat conductivity Λ, the diffusivity κ and the density ρ in the buoyancy term are described by polynomials up to third order in the case of water and up to seventh order in the case of glycerol. Hence, we solve

$$\frac{1}{r}\partial_r(ru_r) + \frac{1}{r}\partial_\phi u_\phi + \partial_z u_z = 0, \tag{2}$$

$$\begin{aligned} D_t u_r - \frac{u_\phi^2}{r} + \frac{1}{\rho_m}\partial_r p &= \frac{1}{r}\partial_r\left(r\nu\tilde{\tau}_{rr}\right) + \frac{1}{r}\partial_\phi\left(\nu\tilde{\tau}_{r\phi}\right) + \partial_z\left(\nu\tilde{\tau}_{rz}\right) - \frac{1}{r}\nu\tilde{\tau}_{\phi\phi}, \\ D_t u_\phi + \frac{u_r u_\phi}{r} + \frac{1}{\rho_m}\frac{1}{r}\partial_\phi p &= \frac{1}{r^2}\partial_r\left(r^2\nu\tilde{\tau}_{\phi r}\right) + \frac{1}{r}\partial_\phi\left(\nu\tilde{\tau}_{\phi\phi}\right) + \partial_z\left(\nu\tilde{\tau}_{\phi z}\right), \\ D_t u_z + \frac{1}{\rho_m}\partial_z p &= \frac{1}{r}\partial_r\left(r\nu\tilde{\tau}_{zr}\right) + \frac{1}{r}\partial_\phi\left(\nu\tilde{\tau}_{z\phi}\right) + \partial_z\left(\nu\tilde{\tau}_{zz}\right) + \frac{\rho_m-\rho}{\rho_m}g, \end{aligned} \tag{3}$$

$$\rho_m c_{p,m} D_t T = \frac{1}{r}\partial_r(\Lambda r\partial_r T) + \frac{1}{r^2}\partial_\phi(\Lambda\partial_\phi T) + \partial_z(\Lambda\partial_z T). \tag{4}$$

Here D_t denotes the material derivative, p the pressure and u_r, u_ϕ, u_z the radial, azimuthal and vertical velocity component, respectively. The tensor $\tilde{\tau}$ is defined as $\tilde{\tau} = \tau/(\rho_m\nu)$, with τ being the deviatoric stress tensor. All other variables have their usual meaning and were already introduced in the previous section.

4 Results and Discussion

The main feature of Rayleigh-Bénard convection under NOB conditions is the breakdown of the top-bottom symmetry, found under OB conditions. This can be realised at first glance by comparing figure 1 and 3. Thus, one of the objectives of NOB studies is to understand and quantify these asymmetries.

The probably best analysed NOB characteristic is the deviation of the centre temperature T_c from the arithmetic mean temperature T_m, as depicted in figure 4. For $\Delta = 70\,\mathrm{K}$, we obtain a T_c that is 11.9 K higher than T_m in the case of glycerol, whereas in contrast, in the case of water the observed increase of T_c is only about 5.6 K. The reason lies in the different viscosities in the cold top and hot bottom layer. That is, the lower viscosity at the warm bottom makes the plumes more mobile, i.e. faster. The cold plumes from the top show the exact opposite behaviour,

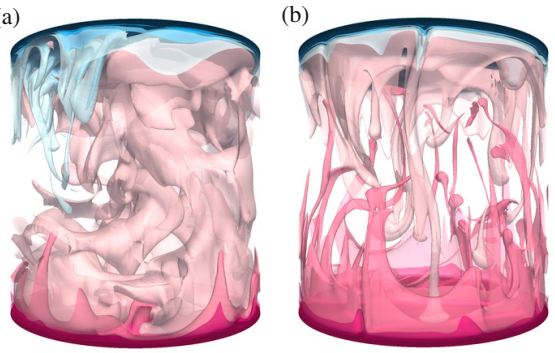

Fig. 3 Instantaneous flow fields (a) water and (b) glycerol for $Ra = 10^8$ under NOB conditions ($\Delta = 40\,\mathrm{K}$). Shown are ten temperature isosurfaces equidistantly distributed between the top and bottom temperature.

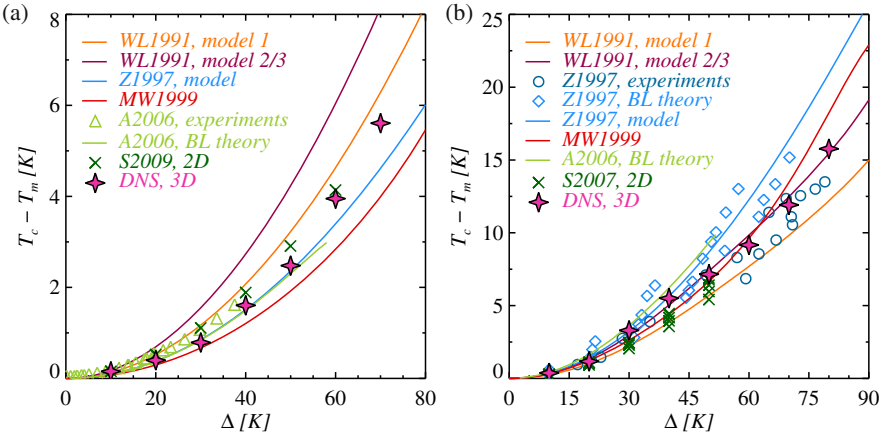

Fig. 4 Comparison of the centre temperature T_c as function of Δ for (a) water and (b) glycerol obtained by our three-dimensional DNS with models by Wu & Libchaber [8] (WL1991), Zhang et al. [9] (Z1997), Manga & Weeraratne [10] (MW1999) and Ahlers et al. [2] (A2006). Additionally, experimental data by Ahlers et al. [2] and Zhang et al. [9], and results from two-dimensional simulations by Sugiyama et al. [11, 12] (S2007, S2009) are shown.

i.e. they are very viscous and move much slower. Hence, they are much longer in contact with the ambient medium in the bulk and heat up on their way down. Thus, the much stronger viscosity dependence in glycerol leads to a significantly higher T_c than observed in water. Several models exist to predict T_c, either based on the Prandtl-Blasius boundary layer theory or on classical scaling theories, see Horn et al. [13] for details. These theories work differently well for a particular fluid.

The asymmetric plume dynamics are also reflected in the velocity profiles. In figure 5 the specific kinetic energy

$$U^E = \sqrt{\tfrac{1}{2}\left(u_r^2 + u_\phi^2 + u_z^2\right)} \tag{5}$$

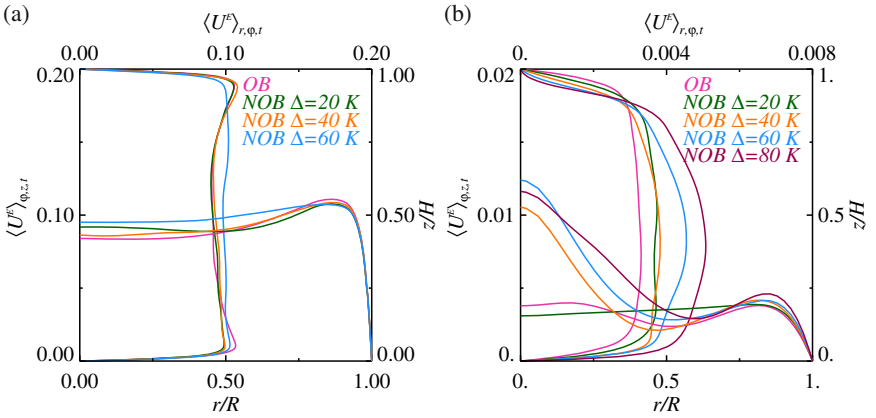

Fig. 5 Specific kinetic energy normalised by the buoyancy velocity $\sqrt{g\alpha_m R\Delta}$ for (a) water and (b) glycerol. The profiles are averaged in time and radial and azimuthal direction and shown as function of the vertical coordinate z/H, as well as averaged in time and the azimuthal and vertical direction as function of the radial coordinate r/R.

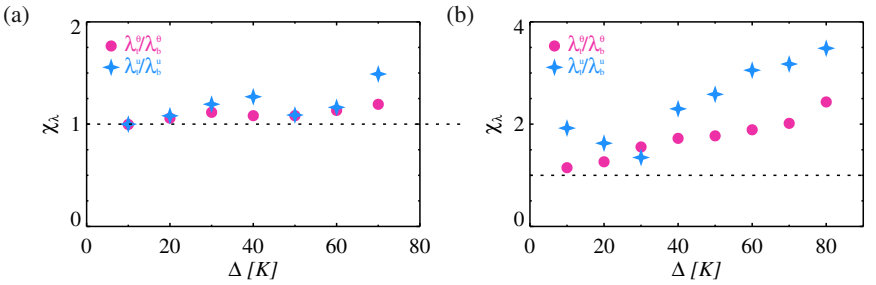

Fig. 6 Ratio of the thermal top and bottom boundary layers, $\chi_{\lambda^\theta} = \lambda_t^\theta/\lambda_b^\theta$, and the viscous ones, $\chi_{\lambda^u} = \lambda_t^u/\lambda_b^u$ as function of Δ for (a) water and (b) glycerol

is presented. While for water (figure 5(a)) a difference is only hardly visible between the OB and NOB profiles, the NOB profiles for glycerol (figure 5(b)) are clearly bended away from the plate at the top and towards the plate at the bottom. This bending increases with Δ.

In line with this, the top viscous boundary layer λ_t^u is always thicker than the bottom one λ_b^u, defined as

$$\lambda_t^\theta = \left(\frac{\partial\langle T\rangle_{r,\phi,t}}{\partial z}\bigg|_t\right)^{-1}(T_t - T_c), \qquad \lambda_b^\theta = \left(\frac{\partial\langle T\rangle_{r,\phi,t}}{\partial z}\bigg|_b\right)^{-1}(T_c - T_b). \tag{6}$$

The same is true for the thermal boundary layers,

$$\lambda_t^u = \max\left(z|_{\frac{\partial\langle u_{r,rms}\rangle}{\partial z}=0}\right), \qquad \lambda_b^u = \min\left(z|_{\frac{\partial\langle u_{r,rms}\rangle}{\partial z}=0}\right), \tag{7}$$

as seen in figure 6. However, this behaviour is non-linear with Δ and in the case of glycerol, this leads to different coherent flow structures [13].

5 Concluding Remarks

A series of three-dimensional DNS has been conducted to study the effects of temperature-dependent material properties in real liquids by considering the examples of water and glycerol. Our simulations revealed that NOB effects lead to a breakdown of the top-bottom symmetry typical for OB simulations. The observed NOB effects include, but are not limited to, different thermal and viscous boundary layer thicknesses, asymmetric plume dynamics and an increase of T_c. Their intensity strongly depends on the particular fluid.

Acknowledgements. The authors acknowledge support by the *Deutsche Forschungsgemeinschaft (DFG)* under grant SH405/2-1.

References

[1] Gray, D.D., Giorgini, A.: Int. J. Heat Mass Transfer 19 (1976)
[2] Ahlers, G., Brown, E., Fontenele Araujo, F., Funfschilling, D., Grossmann, S., Lohse, D.: JFM 569 (2006)
[3] Segur, J.B., Oberstar, H.E.: Ind. Eng. Chem. 43 (1951)
[4] International Atomic Energy Agency, Vienna, Thermophysical properties of materials for nuclear engineering: A tutorial and collection of data (2008)
[5] Schmitt, L., Friedrich, R.: 7th GAMM-Conference on Numerical Methods in Fluid Mechanics. Vieweg und Sohn (1988)
[6] Schumann, U.: J. Comput. Phys. 18(4) (1975)
[7] Shishkina, O., Wagner, C.: C. R. Mécanique 333 (2005)
[8] Wu, X.Z., Libchaber, A.: Phys. Rev. A 43(6) (1991)
[9] Zhang, J., Childress, S., Libchaber, A.: Phys. Fluids 9(4) (1997)
[10] Manga, M., Weeraratne, D.: Phys. Fluids 11(10) (1999)
[11] Sugiyama, K., Calzavarini, E., Grossmann, S., Lohse, D.: EPL 80 (2007)
[12] Sugiyama, K., Calzavarini, E., Grossmann, S., Lohse, D.: JFM 637 (2009)
[13] Horn, S., Shishkina, O., Wagner, C.: J. Fluid Mech. 724, 175 (2013)

A Study of Sheared Turbulence/Shock Interaction: Velocity Fluctuations and Enstrophy Behaviour

S. Jamme, M. Crespo, and P. Chassaing

Abstract. Direct Numerical Simulations of the idealized interaction of a normal shock wave with several turbulent shear flows are conducted. We analyse the behaviours of velocity and vorticity fluctuations and compare them to what happens in the isotropic situation. Investigation of the budgets of these quantities allows to isolate the mechanisms underlying the physics of the interaction, and reveals the importance of enthalpic production and baroclinic torque in such flows.

1 Introduction

The interaction of free isotropic turbulence with a normal shock wave has been the focus of several numerical studies in the past (see e.g. Lee *et al.* [3], Mahesh *et al.* [5]); and this subject is still a matter of concern in the scientific community (see e.g. Larsson and Lele [2]). In the above-mentioned works, Linear Interaction Analysis (LIA) and Direct Numerical Simulations (DNS) have been used to understand the main features of shock-turbulence interaction when the upstream turbulent flow is isotropic. Experimental investigations have also been conducted. However, the influence of anisotropy on the interaction has seldom been investigated. The purpose of the present work is to investigate how the presence of an idealized mean shear upstream of the shock may modify the interaction phenomenon compared to cases where no shear is present. In a previous paper (Jamme *et al.* [1]), we presented some DNS results explaining how thermodynamic fluctuations behave when a sheared turbulent flow interacts with a normal shock wave. We propose here to complete the picture of the flow by focusing on the behaviour of velocity and vorticity variances in such an interaction, and on the physical mechanisms responsible for this behaviour.

S. Jamme · M. Crespo · P. Chassaing
Université de Toulouse, ISAE, 10 avenue Edouard Belin, 31055 Toulouse, France
e-mail: {stephane.jamme,matthieu.crespo,
patrick.chassaing}@isae.fr

M.O. Deville et al. (eds.), *Turbulence and Interactions*,
Notes on Numerical Fluid Mechanics and Multidisciplinary Design 125,
DOI: 10.1007/978-3-662-43489-5_13,

2 Flow Configuration and Numerical Method

We consider the interaction of a normal shock wave with a sheared turbulent flow involving a uniform (constant) mean velocity gradient and a non-uniform mean density (and temperature) gradient. The turbulent flow is no more homogeneous in the tranverse direction (x_2) of the shock wave (which was the case in the isotropic configuration). We solve the full three-dimensional Navier-Stokes equations in non-dimensional conservative form using a finite difference approach. The inviscid part is resolved using a fifth-order Weighted Essentially Non-Oscillatory scheme [7]. Viscous terms are computed using a sixth-order accurate compact scheme, and a third-order Runge Kutta algorithm is used to advance in time.

Equations are solved on a cubic domain of size 2π in the three directions (cf. Figure 1) and a grid of 256x128x128 points is used. The mean flow is aligned with x_1. Periodic conditions are specified in the x_3 direction, and non-reflecting boundary conditions of Poinsot & Lele [6] along with a sponge layer are used for the top and bottom boundaries as well as for the outflow where the flow is subsonic. At the beginning of the calculation, a plane shock wave at Mach number M_1 is specified in the middle of the computational domain; the flow is steady on each side of the shock, satisfying the Rankine-Hugoniot relations.

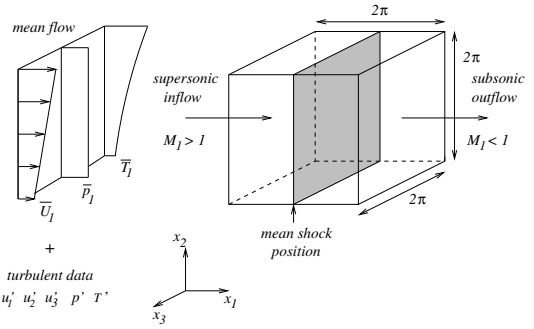

Fig. 1 Flow configuration

At each time step, velocity, pressure, temperature, and density fields are specified at the inflow. These fields are superpositions of a supersonic mean flow and turbulent fluctuations (denoted further by a prime) in velocity, pressure, temperature, and density. The mean velocity at the inflow varies linearly across streamlines while the mean pressure is uniform. The mean temperature and density vary such as the mean Mach number is uniform :

$$\overline{U}_1(x_2) = U_0 + S(x_2 - x_{2\min}), \quad \overline{U}_2 = \overline{U}_3 = 0, \quad \overline{P}(x_2) = 1/(\gamma M_r^2), \quad \overline{T}(x_2) = M_r^2 \overline{U}_1^2 / M_1^2, \tag{1}$$

where the overbar denotes the conventional Reynolds average. The shear stress magnitude is controlled by the parameter S where $S = \partial \overline{U}_1 / \partial x_2$. Turbulent fluctuations are then superposed onto the mean upstream flow and advected through the

Table 1 Turbulence characteristics just before the shock wave (case STSI1)

$Re_\lambda = 27$	$\widetilde{u_1''^2}/q^2 = 0.352$	$\rho_{rms}/\overline{\rho} = 0.121$	$C_{\rho' u_1'} = -0.319$
$M_t = 0.159$	$\widetilde{u_2''^2}/q^2 = 0.299$	$p_{rms}/\overline{P} = 0.028$	$C_{\rho' u_2'} = 0.647$
$\chi = 0.031$	$\widetilde{u_3''^2}/q^2 = 0.349$	$T_{rms}/\overline{T} = 0.119$	$C_{T' u_1'} = 0.298$
$q^2/2 = 1.249$	$\widetilde{u_1'' u_2''}/q^2 = -0.127$	$C_{\rho' T'} = -0.873$	$C_{T' u_2'} = -0.649$

inflow boundary using Taylor's hypothesis. These turbulent data come from preliminary calculations of temporally evolving sheared turbulence so that the anisotropy of the velocity field used in the inflow plane is typical of a turbulent shear flow ($\widetilde{u_1''^2} > \widetilde{u_3''^2} > \widetilde{u_2''^2}$ and $\widetilde{u_1'' u_2''} \neq 0$). This inflow state slightly evolves in the first half of the computational domain, and the turbulence characteristics just before the shock are provided in Table 1.

3 Results and Discussion

A first DNS (STSI1) is conducted with the following values of the numerical parameters: $Re_r = \frac{\rho_r^* u_r^* L_r^*}{\mu_r^*} = 94$, $M_r = \frac{u_r^*}{c_r^*} = 0.1$, $Pr = 0.7$, where $(\cdot)_r^*$ refers to a dimensional reference variable. The mean Mach number is fixed to $M_1 = 1.5$, and the turbulence parameters in the inflow plane are the following : $Re_\lambda = Re_r \frac{\lambda u_{rms}}{\overline{\nu}} = 47$, $\frac{q^2}{2} = 1.5$, $M_t = \frac{q}{\overline{c}} = \frac{\sqrt{\overline{u_i' u_i'}}}{\overline{c}} = 0.173$. The mean velocity gradient equals $S = 1.5$, with $U_0 = 15$. The presence of a density and temperature gradient in the mean flow leads to non-isentropic thermodynamic fluctuations on both sides of the shock. Temperature and density fluctuations (entropy mode) dominate, and the entropy fluctuations are correlated with the velocity field such that the correlation between u_1' and T' is positive (see Table 1). Three complementary DNS are also considered: they have the same parameters as STSI1, except that either u_1' and T' correlate negatively as in a compressible turbulent boundary layer ($C_{T' u_1'} = -0.462$) for case STSI2, or the mean Mach number is higher ($M = 3$) for case STSI3, or the mean shear is more important ($S = 6$) for case STSI4.

3.1 Velocity Fluctuations

The turbulent kinetic energy is non-uniformly distributed on the normal Reynolds stresses. As in the isotropic situation, these quantities are first amplified across the shock wave, and then behave differently in the near field behind the shock : we observe a non-monotonic evolution of $\widetilde{u_1''^2}$, whereas the transverse normal Reynolds stresses decrease continuously (see Figure 2a). This corresponds to the classical transfer of energy between acoustical and vortical modes behind the shock and

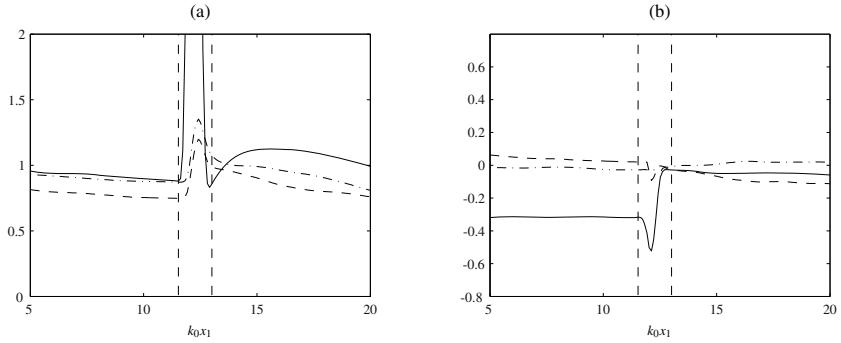

Fig. 2 STSI1: Streamwise evolution of the Reynolds stresses - $x_2 = L_2/2$. Normal components (a); (——) $\widetilde{u_1''^2}$; (— — —) $\widetilde{u_2''^2}$; (— · —) $\widetilde{u_3''^2}$. Off-diagonal components (b); (——) $\widetilde{u_1''u_2''}$; (— — —) $\widetilde{u_1''u_3''}$; (— · —) $\widetilde{u_2''u_3''}$.

redistribution of energy from $\widetilde{u_2''^2}$ and $\widetilde{u_3''^2}$ towards $\widetilde{u_1''^2}$. It can also be noticed that the turbulent kinetic energy is more amplified across the shock wave for case STSI2 than for case STSI1 (amplification factors of 1.58 and 1.21 respectively). The same influence of upstream entropy fluctuations with a negative correlation between u_1' and T' has been reported in the isotropic situation with a uniform mean upstream flow both by DNS and LIA: see Mahesh *et al.* [5].

A negative cross-correlation $\widetilde{u_1''u_2''}$ is also created in this flow as a consequence of the mean velocity shear. The budget of this quantity is given by equation (2).

$$\underbrace{\frac{3}{2}\frac{\overline{\rho}}{|\overline{\varepsilon}^\star|}\widetilde{U}_1\frac{\partial}{\partial x_1}\left(\widetilde{u_1''u_2''}\right)}_{(I)} = \underbrace{-\frac{3}{2}\frac{\overline{\rho}}{|\overline{\varepsilon}^\star|}\left(\widetilde{u_1''u_2''}\frac{\partial\widetilde{U}_1}{\partial x_1}\right)}_{(IIa)} \underbrace{-\frac{3}{2}\frac{\overline{\rho}}{|\overline{\varepsilon}^\star|}\left(\widetilde{u_2''^2}\frac{\partial\widetilde{U}_1}{\partial x_2}\right)}_{(IIb)} \underbrace{-\frac{3}{2|\overline{\varepsilon}^\star|}\left[\frac{\partial}{\partial x_1}\left(\overline{\rho}\widetilde{u_1''^2u_2''}\right)+\frac{\partial}{\partial x_2}\left(\overline{\rho}\widetilde{u_1''u_2''^2}\right)\right]}_{(III)}$$
$$\underbrace{-\frac{3}{2}\frac{\overline{u_2''}}{|\overline{\varepsilon}^\star|}\frac{\partial\overline{P}}{\partial x_1}}_{(IVa)} \underbrace{-\frac{3}{2|\overline{\varepsilon}^\star|}\left[\frac{\partial\left(\overline{p'u_2''}\right)}{\partial x_1}+\frac{\partial\left(\overline{p'u_1''}\right)}{\partial x_2}\right]}_{(IVb)} \underbrace{+\frac{3}{2}\frac{\Pi_{12}^d}{|\overline{\varepsilon}^\star|}}_{(IVd)} \underbrace{+\frac{3}{2}\frac{\overline{\varepsilon}_{12}^d}{|\overline{\varepsilon}^\star|}}_{(Vb)} \quad (2)$$

where: $\Pi_{ij} = \overline{p'\left(\frac{\partial u_i''}{\partial x_j}+\frac{\partial u_j''}{\partial x_i}\right)}$, $\Pi_d^\star = \overline{p'\left(\frac{\partial u_i''}{\partial x_i}\right)}$ (spherical part of Π_{ij}) and $\Pi_{ij}^d = \Pi_{ij} - \frac{2}{3}\Pi_d^\star\delta_{ij}$ (deviatoric part of Π_{ij}). Similarly, we have: $\overline{\varepsilon}_{ij} = \overline{u_j''\frac{\partial\tau_{ik}}{\partial x_k}} + \overline{u_i''\frac{\partial\tau_{jk}}{\partial x_k}}$, $\overline{\varepsilon}^\star = \overline{u_i''\frac{\partial\tau_{ik}}{\partial x_k}}$ (spherical part of $\overline{\varepsilon}_{ij}$) and $\overline{\varepsilon}_{ij}^d = \overline{\varepsilon}_{ij} - \frac{2}{3}\overline{\varepsilon}^\star\delta_{ij}$ (deviatoric part of $\overline{\varepsilon}_{ij}$).

Upstream of the shock wave, production by the mean shear (IIb) is balanced by the pressure-strain correlation (IVd), leading to a quasi-constant behaviour of $\widetilde{u_1''u_2''}$. We then notice a decrease of the magnitude of $\widetilde{u_1''u_2''}$ during the interaction with the shock (see Figure 2b). We present in Figure 3 the different terms of the budget equation (2) inside the shock zone (region where $\partial\overline{U}_1/\partial x_1 < 0$). All the terms of this

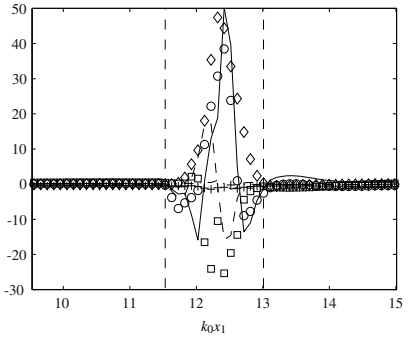

Fig. 3 STSI1 : budget of $\widetilde{u_1''u_2''}$ - $x_2 = L_2/2$. ($\circ\circ\circ\circ\circ$) (I); $(+++++)$ $(IIa+IIb)$; $(---)$ (III); ($\diamond\diamond\diamond\diamond\diamond$) (IVa); (——) (IVb); ($\square\square\square\square\square$) (IVd); $(-\cdot-\cdot-)$ (Vb).

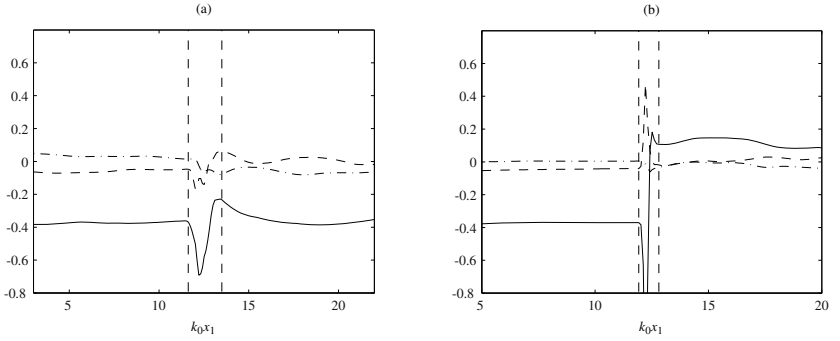

Fig. 4 Streamwise evolution of the off-diagonal components of the Reynolds stresses - $x_2 = L_2/2$. STSI2 (a); STSI3 (b). (——) $\widetilde{u_1''u_2''}$; $(---)$ $\widetilde{u_1''u_3''}$; $(-\cdot-)$ $\widetilde{u_2''u_3''}$.

budget are normalized by the absolute value of the dissipation, which allows to easily evaluate the importance of each term in comparison with viscous effects. Even if the statistics are clearly overestimated inside the shock zone because of the shock corrugations, it can however be concluded that the main "integral" contribution to the evolution of $\widetilde{u_1''u_2''}$ inside the shock thickness can be attributed to the action of enthalpic production (IVa). This is supported by the evolutions of $\widetilde{u_1''u_2''}$ for cases STSI2 and STSI3 (cf. Figure 4) where enthalpic production is either lower (case STSI2) or greater (case STSI3) than in the reference case STSI1, which respectively leads to a smaller or higher effect on the cross-correlation $\widetilde{u_1''u_2''}$ during the interaction with the shock wave. This result is in contradiction with the RDT conclusions of Mahesh *et al.* [4] who assigned the tendency of $\widetilde{u_1''u_2''}$ to decrease upon normal compression to an amplification of the pressure-strain correlation (IVd) and the consequent upsetting of the initial balance between production and the pressure strain correlation in the shear flow. It should also be noticed that, since the intensity of the enthalpic production depends on the mean pressure gradient across the shock and also on the turbulent mass fluxes that are generated in this flow (due to the simultaneous presence of a mean shear for the velocity and the density), the production mechanisms

of the thermodynamic fluctuations described in Jamme *et al.* [1] are closely linked to the behaviour of $\widetilde{u_1'' u_2''}$ during the interaction. Finally, downstream of the shock, the flow reorganises itself since the new level of $\widetilde{u_1'' u_2''}$ is not consistent with the value of the mean shear after the interaction ($S_{downstream} < S_{upstream}$).

3.2 Vorticity Fluctuations

Figure 5 shows that the global behaviour of vorticity variances is similar to the one observed in isotropic turbulence/shock interaction cases : outside the shock zone, viscous dissipation (*VIII*) is in competition with turbulent vortex stretching (*III*) [see bugdet equation (3) for the analytical expression of the different terms]. These terms are nearly balanced upstream of the shock, leading to a quasi-constant evolution of the vorticity variances, whereas downstream of the shock, dissipation overwhelms stretching for the transverse vorticity variances only, leading to a clear decrease of these quantities. Then, across the shock wave, the transverse components are clearly amplified while the streamwise component remains nearly unaffected. Inside the shock zone, mean vortex stretching (*II*) balances mean compression (*IV*) for $\overline{\omega_1'^2}$ only, as in the isotropic situation. However, as reported in Table 2, $\overline{\omega_3'^2}$ appears more amplified than $\overline{\omega_2'^2}$ in the sheared configurations. Figure 6 shows that this behaviour can be attributed to the action of the baroclinic term inside the shock zone that is more intense for $\overline{\omega_3'^2}$ than for $\overline{\omega_2'^2}$. For $\overline{\omega_3'^2}$, the baroclinic torque can be written: $2\overline{\frac{1}{\rho^2}\omega_3' \frac{\partial \rho}{\partial x_1}\frac{\partial P}{\partial x_2}} - 2\overline{\frac{1}{\rho^2}\omega_3' \frac{\partial \rho}{\partial x_2}\frac{\partial P}{\partial x_1}}$, which involves the product of $\frac{\partial P}{\partial x_1}$ and $\frac{\partial \rho}{\partial x_2}$ that are clearly non-negligible inside the shock zone. Moreover, for a given shock intensity, this term is all the more important that the mean density gradient along x_2 is pronounced. This explains why the difference in the amplifications of $\overline{\omega_2'^2}$ and $\overline{\omega_3'^2}$ is greater for case STSI4 than for case STSI1 (see Figure 5b).

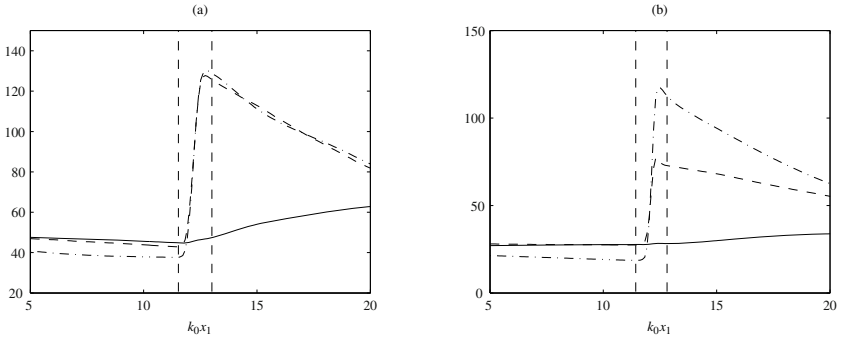

Fig. 5 Streamwise evolution of the vorticity variances - $x_2 = L_2/2$. STSI1 (a); STSI4 (b). (——) $\overline{\omega_1'^2}$; (– – –) $\overline{\omega_2'^2}$; (– · –) $\overline{\omega_3'^2}$.

Table 2 Amplification factors of the vorticity variances for different cases ($x_2 = L_2/2$)

Amplification of	LIA ($M_1 = 1.5$)	isotropic DNS ($M_1 = 1.5$)	STSI1	STSI4
$\overline{\omega_1'^2}$	1	1.1	1.05	1.02
$\overline{\omega_2'^2}$	3.21	2.83	2.95	2.63
$\overline{\omega_3'^2}$	3.21	2.83	3.44	5.61

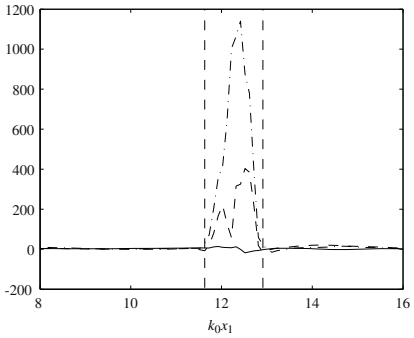

Fig. 6 STSI1 - $x_2 = L_2/2$. Comparison of the baroclinic torque (VI) in the budget equations of $\overline{\omega_1'^2}$ (——); $\overline{\omega_2'^2}$ (− − −) and $\overline{\omega_3'^2}$ (− · −)

$$\underbrace{\overline{U}_j \frac{\partial \overline{\omega'_\alpha \omega'_\alpha}}{\partial x_j}}_{(I)} = \underbrace{2\overline{\omega'_\alpha \omega'_j}\overline{s}_{\alpha j}}_{(II)} + \underbrace{2\overline{\omega'_\alpha \omega'_j s'_{\alpha j}}}_{(III)} \underbrace{-2\overline{\omega'_\alpha \omega'_\alpha}\overline{s}_{jj}}_{(IV)} \underbrace{-\overline{\omega'_\alpha \omega'_\alpha s'_{jj}}}_{(V)} + \underbrace{2\varepsilon_{\alpha jk}\overline{\frac{1}{\rho^2}\omega'_\alpha \frac{\partial \rho}{\partial x_j}\frac{\partial P}{\partial x_k}}}_{(VI)}$$

$$\underbrace{-\frac{\partial\left(\overline{\omega'_\alpha \omega'_\alpha u'_k}\right)}{\partial x_k}}_{(VII)} \underbrace{+2\varepsilon_{\alpha jk}\overline{\omega'_\alpha \frac{\partial}{\partial x_j}\left(\frac{1}{\rho}\frac{\partial \tau_{kq}}{\partial x_q}\right)}}_{(VIII)} \quad (3)$$

with: $s_{ij} = \frac{1}{2}\left(\frac{\partial u_i}{\partial x_j} + \frac{\partial u_j}{\partial x_i}\right)$, and ε_{ijk} stands for the permutation tensor (no summation on α).

References

1. Jamme, S., Crespo, M., Chassaing, P.: Thermodynamic fluctuations behaviour during a sheared turbulence/shock interaction. In Turbulence and Interactions, proceedings of the TI 2009 conference. Notes on Numerical Fluid Mechanics and Multidisciplinary Design **110** (2010).
2. Larsson, J., Lele, S.K.: Direct numerical simulation of canonical shock/turbulence interaction. Phys. Fluids **21**, 126101 (2009).
3. Lee, S., Lele, S.K., Moin, P.: Interaction of isotropic turbulence with shock waves: effect of shock strength. J. Fluid Mech. **340**, 225-247 (1997).

4. Mahesh, K., Lele, S.K., Moin, P.: The response of anisotropic turbulence to rapid homogeneous one-dimensional compression. Phys. Fluids **6**, 1052-1062 (1993).
5. Mahesh, K., Lele, S.K., Moin, P.: The influence of entropy fluctuations on the interaction of turbulence with a shock wave. J. Fluid Mech. **334**, 353-379 (1997).
6. Poinsot, T.J., Lele, S.K.: Boundary conditions for direct simulations of compressible viscous reacting flows. J. Comput. Phys. **101**, 104-129 (1992).
7. Ponziani, D., Pirozzoli, S., Grasso, F.: Development of optimized Weighted-ENO schemes for multiscale compressible flows Int. J. Numer. Meth. in Fluids **42**, 953-977 (2003).

WRF Modelling of Turbulence Triggering Convective Thunderstorms over Singapore

S. Jolivet and F. Chane-Ming

Abstract. Convective storms represent the main weather threats on Singapore where the amount of water discharged frequently turns into flash floods. Moreover forecasting is a challenging task in this tropical region due to the high instability state of the atmosphere. Therefore Numerical Weather Prediction (NWP) represents an essential tool in flood mitigation. Yet identifying the ideal configuration and parameterization of a NWP model is a milestone to reach accurate forecast. This paper presents the results of a sensitivity analysis of the turbulence and convective schemes of the Weather Research and Forecasting (WRF) model in the framework of Singapore weather forecasting.

1 Introduction

Weather forecasting is a challenging task in the wet Tropics due to the high instability state of the atmosphere. Therefore Numerical Weather Prediction (NWP) is an essential tool to address the weather prediction. Indeed NWP is based on the use of advanced atmospheric models that predict the future state of the atmosphere on the basis of past and data assimilation of ground-based monitoring stations, satellites and radar. The choice of convective scheme (cumulus parameterization) is known to affect the accuracy of rainfall predictions of various convective environments and their associated surface features and evolution (see [1, 2, 3] for a review). Thus defining the good set of parameterization for a NWP model is a key point to address weather forecasting in tropics where convective energy is the major component of

S. Jolivet
Singapore Delft Water Alliance, National University of Singapore, Singapore
e-mail: samuel@nusdeltares.org

F. Chane-Ming
Laboratoire de l'Atmosphre et des Cyclones,
UMR 8105 Universit de La Runion/Mto-France/CNRS, Saint Denis de La Runion, France
e-mail: fabrice.chane-ming@univ-reunion.fr

M.O. Deville et al. (eds.), *Turbulence and Interactions*,
Notes on Numerical Fluid Mechanics and Multidisciplinary Design 125,
DOI: 10.1007/978-3-662-43489-5_14,

energy balance. Using the good turbulent scheme as well as the good convection parameterization is essential to be able to predict convective thunderstorms. Running a sensitivity analysis on the NWP model for a specified geographical area is needed in order to define the suitable parameterizations to achieve the most accurate weather forecast.

Several studies have focused on the influence of cumulus parameterization in the framework of large scale monsoon event in Asia. Das et al. (1988) [4] showed that there was a systematic rainfall underestimation with the Anthes-Kuo scheme (see [5] for a full description of the scheme) in monsoon period. Recently Juneng et al. (2007) [6] modeled a 100-year return period extreme rainfall event which occurred during the 2004-2005 North East (NE) monsoon over the east coast Peninsular Malaysia. Following this work, Salinum et al. (2010) [7] performed a sensitivity study on cumulus parameterization based on the same event. They showed that the Betts-Miller scheme (see [8] for a full description of the scheme) performed better than the others in term of rainfall intensity and distribution. But they pointed out that this result might not be generalized for other events or convective environments referring to the results of their previous study where the Kain-Fritsch scheme (see [9] for a full description of the scheme) performed better in the case of tropical cyclone Vamei (2001) modeling. On the other hand no studies have focused in the Southeast Asia region on locally induced convective event e.g. events driven by the local scale land/sea interaction including heat fluxes, moist fluxes, humidity, temperature and wind conditions. Indeed all the aforementioned studies focused on rainfall events driven by large scale atmospheric conditions such as monsoon environment. Thus our study aims at investigating the skills of different cumulus schemes in the framework of nearequatorial locally induced convective system. Preliminary results of the sensitivity analysis give insights of the appropriateness of turbulence and cumulus parameterizations in Singapore.

2 Singapore Case Study and Methodology

Singapore (1.28N, 103.83E) is a small island (710 km2) surrounded by open seas and located on the south of Peninsular Malaysia. Thus large area of ocean water around the land contributes to the instability by changing the dynamics of the whole system (land+ocean) and modifying the global moisture and heat fluxes. Indeed heavy convective storms are observed all the year. Associated huge amounts of water can turn into flooding leading then from time to time to tremendous damages up to several millions of Singapore Dollars by event. In fact Singapore experiences more intense relatively short rainfall events compared to mid latitudes locations. The weather is mainly driven by the monsoon seasons. The NE monsoon occurring from November to February/March is the wettest season and brings strong rainfalls coming from the South China Sea (see [10] for climatology of the region). The South West monsoon from June to September is really less intense compared to the NE one. During the inter-monsoon seasons Sumatra squall lines, coming from the westward Indonesian Sumatra Island, usually shower Singapore on early

mornings. Moreover, added to this large scale pattern, convection enhanced by the warm water pool surrounding the island, the high relative humidity of the atmosphere and the hot spots of heat spread all over the island especially in urban areas, brings heavy rainfall associated with strong relative fast thunderstorms (2-3 hours). These thunderstorms are difficult to predict at long lead time using NWP model because of the strong influence of small scale parameters (humidity, temperature, winds) and the high instability of the atmosphere.

Therefore National Weather Service of Singapore (MSS) uses the Weather Research and Forecasting (WRF) model for delivering guidelines on the future weather. Thus our study uses WRF (ARW core version 3.3) model as a single high-resolution limited-area model (Meso Scale Model) limited to the territory of Singapore (see [11] for a full description of the model) with boundary forcing conditions derived from the final analysis (FNL) of the Global Forecast System (GFS). Indeed their combination has been evaluated by MSS to be the most efficient so far in Singapore context. For our purpose we use WRF with a single domain centered on Singapore region at 1 km horizontal resolution with a grid of 1800 points (60 points in E-W by 30 points in N-S) and 27 vertical levels are used with: WRF Single-Moment 3-class simple ice scheme for the microphysics; Rapid Radiative Transfer Model and Dudiah schemes respectively for the radiative transfer at long and short wave; Monin-Obukhov and Yonsei University schemes respectively for the surface and the boundary layer; unified Noah land-surface model for the interaction at the land-surface; heat and moisture fluxes from the surface to the atmosphere being allowed, and a 15 second computational time step (named Config1). 14 intense thunderstorm events over 10 locations chosen from the 2011 rain gauge dataset are considered (listed in Table 1). As we want to assess the skills for local induced thunderstorm the dataset contains 11 events that occurred on early afternoon as a result of thermally induced convection. Thus the simulations consist of only 18 hours of simulation starting at 00h00. These events are simulated using different sets of the 4 turbulence parameterizations (listed in Table 2) and the 8 convection parameterizations (listed in Table 3) available in WRF. Comparison between rain gauges observations and the simulated precipitation at the same location (we took the maximum within a 3*3 square centered on the specified location) help assessing the skills of the parameterizations and thus defining the best combination of turbulence and convection schemes for predicting thunderstorms accurately in time, space and intensity on Singapore.

3 Sensitivity Results and Discussion

In the present study as the model setup and other physical parameterizations are identical in all experiments, hence any difference in the simulation performance could be associated with the cumulus and turbulence parameterization schemes used. 32 (4*8) combinations are tested on 14 rainfall events. From the 448 (32*14) runs, results were not as good as expected with comparison to similar studies such as Salinum et al. (2010) [7]. Indeed the rain intensity is not adequately retrieved. For instance from all the 448 simulations, the maximum 10 minutes accumulated

rain that is produced is 3.53 mm (from the 11/11/2011 event with the T1C8 configuration) which is 17% of the observed value. Another interesting characteristic is that in each case the non convective rain is negligible compared to convective rain production. Despite the disability for the model to retrieve realistic rain intensity, the 5 more intense event simulations out of the 14 have been used to investigate the best combination of turbulence and cumulus scheme: 21/10, 27/10, 31/10, 08/11 and 11/11. Therefore no statistical study was performed on the results as this new dataset was too small for deriving results from any statistical method. From the analysis of the 5 simulated events T2C3 configuration e.g. 3D TKE turbulence scheme (which is a LES approach resolving the large scales of turbulence and modeling the effect of the smaller scales by adding a subgrid viscosity) together with Grell-Devenyi ensemble cumulus scheme seems to be the combination producing the more coherent pattern of rainfall in term of time, space and relatively in intensity. So in agreement with Salinum et al. (2010) [7] conclusions, another cumulus scheme different from the Betts-Miller or the Kain Fritsch of Salinum et al. (2010) [7] or even the Simple Arakawa Schubert [14] used in the NOAA operational Hurricane Weather Research and Forecasting (HWRF) model is identified. In addition we observed on strong events such as 31/10 that the turbulence influence seemed to be negligible which indicates the prevalence of cumulus scheme for strong convective events.

Based on the T2C3 combination identification, we wanted to extend the sensitivity experiment on model time and space resolution. Thus we selected 4 intense events from the observations dataset: 01/06, 21/10, 31/10, 23/12. We used 2 new methodologies for WRF use in addition to the initial configuration Config1. First we implemented 3 nested domains of 25, 5, and 1 km horizontal resolution with

Table 1 List of simulated rainfall events

Number	Date	Max 10 min accumulated rain: obs/sim (mm)	Hour of max obs	Location
1	01/06/2011	25.2/0.6	14h40	S120 Botanic Garden
2	26/09/2011	21.6/0.3	03h30	S110 Peicai Secondary School
3	04/10/2011	18.4/0.2	04h50	S78 Poole Road
4	19/10/2011	15.8/0.8	14h30	S43 Upper Air Observatory
5	21/10/2011	18.2/3.0	12h10	S36 Woodleigh Filters
6	26/10/2011	26.2/0.9	14h20	S46 Singapore Golf Club
7	27/10/2011	22.2/2.8	14h30	S69 Upper Peirce Reservoir
8	31/10/2011	28.6/3.4	13h50	S46 Singapore Golf Club
9	08/11/2011	13.6/2.5	8h50	S108 Marina Barrage
10	11/11/2011	20.4/3.5	13h30	S36 Woodleigh Filters
11	13/11/2011	18/0.6	16h40	S78 Poole Road
12	28/11/2011	25.8/0.9	14h50	S08 Lower Peirce Reservoir
13	07/12/2011	21/0.0	14h40	S69 Upper Peirce Reservoir
14	23/12/2011	15.8/0.7	17h00	S79 TripeOne Somerset

Table 2 List of turbulence schemes tested in WRF3.3 [ARW]

Turbulence Schemes	Code	Description
Constant	T1	K is constant and specified for vertical and horizontal
3D TKE	T2	A prognostic equation for turbulent kinetic energy is used and K is based on TKE (1.5 order closure)
3D deformation	T3	K is diagnosed from 3D deformation and stability following a Smagorinsky (1 order closure) approach
2D deformation	T4	K for horizontal diffusion is diagnosed from just horizontal deformation and stability following a Smagorinsky (1 order closure) approach. The vertical diffusion is done by boundary layer scheme

Table 3 List of convection schemes tested in WRF3.3 [ARW]

Convection Schemes	Code	Description
Kain-Fritsch [9]	C1	Deep and shallow convection sub-grid scheme using a mass flux approach with downdrafts and CAPE removal time scale
Betts-Miller-Janjic [12]	C2	Operational Eta scheme. Column moist adjustment scheme relaxing towards a well-mixed profile
Grell-Devenyi ensemble [13]	C3	Multi-closure, multi-parameter, ensemble method with typically 144 sub-grid members
Simplified Arakawa-Schubert [14]	C4	Simple mass-flux scheme with quasi-equilibrium closure with shallow mixing scheme
Grell 3D [13]	C5	improved version of the GD scheme that may also be used on high resolution (in addition to coarser resolutions)
Tiedtke [15]	C6	Mass-flux type scheme with CAPE removal time scale, shallow component and momentum transport
New Simplified Arakawa-Schubert [16]	C7	New mass-flux scheme with deep and shallow components and momentum transport
Old Kain-Fritsch [17]	C8	Deep convection scheme using a mass flux approach with downdrafts and CAPE removal time scale

a 15, 3 and 0.6 s time step respectively (named Config2). The last domain is the same as the only one in Config1. Then we used the same 3 nested domains but with a 15 s time step for all the 3 domains (named Config3). The simulations of the 21/10 and 31/10 events allowed investigating any enhancement due to the increase in time and space resolution. Indeed by comparison with the Config1 simulations we observed an increase of convective rain production using Config3 and a further increase while using Config2. These results showed that the model space and time resolution can influence the accuracy of the cumulus scheme used. Then the simula-

tions of the 01/06 and 23/12 events allow investigating the cumulus scheme capacity to trigger convection. Indeed with the Config1, even if they were based on strong observed events, the simulations were not able to retrieve good rainfall patterns especially in term of intensity. By comparison between all the model configurations we observed that using both Config2 and Config3 the events were still not properly simulated. These results indicated that the higher time or space resolution was not able to overcome the cumulus scheme failure by triggering convective rainfall production. Moreover it has to be noted that higher time and/or space resolution is possible through the use of hypercomputing.

In their study Salinum et al. (2010) [7] concluded that the failures of the schemes in simulating the event may be attributed to the trigger function, closure assumption and precipitation scheme and that their finding was not applicable to other cases or convective environment. But with regards to these results one can argue that the horizontal resolution as well can influence the skills of any cumulus scheme. Even though WRF geographical data is based on the GTOPO30 dataset with a resolution of 30 arc second (approximately 1 km), the simulation results were not relevant. Actually by examining the GTOPO30 dataset, we found that it is accurate on most part of the world but not in Singapore region. Indeed the delimitations between land and sea water as well as inland water are not realistic. This delimitation is essential for a proper assessment of the heat fluxes, humidity fluxes and temperature which

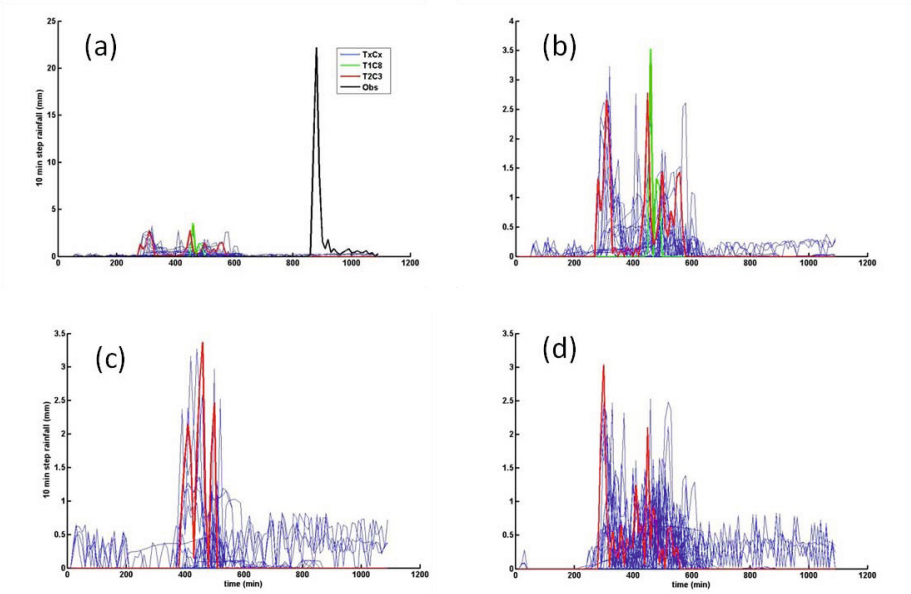

Fig. 1 (a) 11/11 simulations and observations on S36. We can see the skills of the parameterizations compared to the observations. (b), (c) and (d) are respectively simulations for 11/11 on S36, for 31/10 on S46 and for 21/10 on S36. We can observe the skills of T2C3 compared to the other parameterizations TxCx.

are the sources of convection. Thus these results suggest the need of an accurate geographical dataset on which can be built realistic atmospheric and land/sea parameters interactions.

4 Summary and Further Research

The aim of this paper is to assess the skills of the different turbulence and cumulus parameterizations in WRF model and to identify the best combination in Singapore context in the framework of locally induced convective system. Although the simulations of 14 events are not able to realistically retrieve rainfall patterns and especially in term of intensity, the results of the sensitivity analysis indicates that the 3D TKE turbulence scheme together with Grell-Devenyi ensemble cumulus scheme performed better compared to the others in term of time, space and relatively in intensity. The turbulence is also observed to be less critical for the accuracy for strong convective events. Moreover higher model time and space resolution (through hypercomputing) are observed to enhance the accuracy of the results when convective rainfall is already produced but are not able to overcome the cumulus scheme failure by triggering convection. Finally the need of using an accurate geographical dataset for developing a land/sea coupled model is also identified. Currently an accurate DEM is being processed on Singapore together with an accurate land cover map (up to 10 m horizontal resolution). Our future research will focus on using these data in a coupled land surface model with advanced surface physics for improved heat and moisture fluxes in order to better trigger convective rainfall.

Acknowledgements. The research presented in this work was carried out as part of the SDWA Multi-Objective Multiple-Reservoir Management research programme (R-303-001-005-272).

References

1. Kerkhoven, E., Gan, T.Y., Shiiba, M., Reuter, G., Takana, K.: A comparison of cumulus parameterization schemes in a numerical weather prediction model for a monsoon rainfall event. Hydrol. Process 20, 1961–1978 (2006)
2. Vaidya, S.S.: The performance of two convective parameterization schemes in a mesoscale model over the Indian region. Meteor. Atmos. Phys. 92, 175–190 (2006)
3. Ratnam, V.J., Cox, E.A.: Simulation of monsoon depressions using MM5: sensitivity to cumulus parameterization schemes. Meteor. Atmos. Phys. 93, 53–78 (2006)
4. Das, S., Mohanty, U.C., Sharma, O.P.: Study of Kuo-type cumulus parameterization during different epochs of the Asian summer monsoon. Mon. Wea. Rev. 116, 715–729 (1988)
5. Anthes, R.A.: A cumulus parameterization scheme utilizing a one-dimensional cloud model. Mon. Wea. Rev. 105, 270–286 (1977)
6. Juneng, L., Tangang, F.T., Reason, C.J.: Numerical case study of an extreme rainfall event during over the east coast Peninsular Malaysia. Meteorol. Atmos. Phys. 98, 81–98 (2007)

7. Salimun, E., Tangang, F.T., Juneng, L.: Simulation of heavy precipitation episode over eastern Peninsular Malaysia using MM5: sensitivity to cumulus parameterization schemes. Meteor. Atmos. Phys. 107, 33–49 (2010)
8. Betts, A.K., Miller, M.J.: A new convective adjustment scheme. Part II: single column test using GATE wave, BOMEX, ATEX, and Arctic air mass data sets. Q. J. R. Meteorol. Soc. 112, 693–709 (1986)
9. Kain, J.S.: The Kain–Fritsch Convective Parameterization: An Update. Journal of Applied Meteorology 43(1), 170–181 (2004)
10. Johnson, R.H., Houze, R.A.: Precipitating systems of the Asian monsoon. In: Chang, C.P., Krishnamurti, T.N. (eds.) Monsoon Meteorology. Oxford University Press, New York (1987)
11. Weather Research and Forecasting ARW Version 3 Modeling System User Guide. In: Mesoscale and Microscale Meteorology Division. National Center for Atmospheric Research (2011)
12. Janjic, Z.I.: The step-mountain eta coordinate model: further developments of the convection, viscous sublayer and turbulence closure schemes. Mon. Wea. Rev. 122, 927–945 (1994)
13. Grell, G.A., Devenyi, D.: A generalized approach to parameterizing convection combining ensemble and data assimilation techniques. Geophys. Res. Lett. 29(14), 1693 (2002)
14. Arakawa, A., Schubert, W.H.: Interaction of a cumulus cloud ensemble with the large scale environment. Part I. J. Atmos. Sci. 31, 674–701 (1974)
15. Tiedtke, M.: A comprehensive massflux scheme for cumulus parameterization in large scale models. Mon. Wea. Rev. 117, 1779–1800 (1989)
16. Hong, S.-Y., Pan, H.-L.: Convective Trigger Function for a Mass-Flux Cumulus Parameterization Scheme. Mon. Wea. Rev. 126, 2599–2620 (1998)
17. Kain, J.S., Fritsch, J.M.: A One-Dimensional Entraining/Detraining Plume Model and Its Application in Convective Parameterization. J. Atmos. Sci. 47(23), 2784–2802 (1990)

Prediction of Broadband Noise from Two Square Cylinders in Tandem Arrangement Using a Combined DDES/FWH Approach

Thilo Knacke and Frank Thiele

Abstract. A combined CFD/CAA method is used to study the turbulent flow and the flow-induced noise generated by two square cylinders in tandem arrangement. The selected test case activates noise generation mechanisms which are typical of realistic landing gear struts under approach conditions and the employed prediction methods prove capable of capturing all relevant physical effects. The nearfield and farfield results are discussed in close comparison to experimental data.

1 Introduction

The interaction of turbulent wakes with downstream solid surfaces and edges is known to be an efficient noise generation mechanism [6]. Ocurring e.g. between individual landing gear or high-lift system components, such mechanisms can contribute significantly to the noise perceived from airplanes during their landing approach, while the engines operate at reduced power. This paper describes an attempt to predict the wake/surface interaction noise emitted from two square cylinders in tandem arrangement using a two-step CFD/CAA method. The Mach-number of this testcase is $Ma = 0.2$ and the Reynolds-number based on the strut width is $Re_D = 182\,000$, which is a setting representative of realistic landing gear struts under approach conditions. A compressible Delayed Detached-Eddy Simulation (DDES) [19] of the turbulent flow around the configuration is performed as a first step, whereby most of the energetic vortical motion following separation at the upstream edges of the 1st strut is resolved. Subsequent farfield noise predictions are made based on the acoustic analogy of Ffowcs-Williams and Hawkings (FWH) using unsteady flow field data acquired throughout the DDES.

Thilo Knacke · Frank Thiele
Technische Universität Berlin,
Institut für Strömungsmechanik und Technische Akustik,
Müller-Breslau-Straße 8, D–10623 Berlin, Germany
e-mail: thilo.knacke@cfd.tu-berlin.de

M.O. Deville et al. (eds.), *Turbulence and Interactions*,
Notes on Numerical Fluid Mechanics and Multidisciplinary Design 125,
DOI: 10.1007/978-3-662-43489-5_15,

2 Numerical Method and Setup

For the nearfield simulations, the compressible finite-volume code *ELAN* is used, which is based on the SIMPLE pressure-correction algorithm and of 2nd order accuracy in both time and space [20]. A time-implicit solver with colocated storage arrangement is employed to solve the Reynolds-averaged/filtered Navier-Stokes equations on structured multi-block grids, whereby the decoupling of pressure and velocity fields is prevented through a generalised Rhie & Chow interpolation suitable for the simulation of unsteady flows [10]. Non-reflecting boundary conditions allow sound-waves and convective disturbances to leave the computational domain without major reflections [2]. The Strain-Adaptive Linear Spalart-Allmaras one-equation turbulence model [14] is used as background RANS/LES model in the DDES, with $C_{\mathrm{DES}} = 0.5$ (calibrated against the decay of isotropic turbulence).

To obtain the farfield pressure time-series, an integral solution of the FWH equation is applied, using unsteady flow data acquired on several surfaces throughout the nearfield simulation. The solution is based on formulation 1A as proposed by Farassat and is valid for both nearfield and farfield [3]. A sourcetime-dominant algorithm [4] is used in the *C3NOISE* FWH code and the required time-interpolation and differentiation is done applying 2nd order schemes.

Two square cylinders, each with a width of $D = 0.04\,\mathrm{m}$, are immersed in-line with a center-to-center distance of $4D$ in a uniform flow at $u_\infty = 70\,\mathrm{m/s}$ (see fig. 1). This configuration is studied at two different inclinations of $0°$ (case 1) and $-15°$ (case 2). In the turbulence-resolving nearfield simulations, periodicity is assumed in the homogeneous direction, whereby the spanwise extent of the computational domain, $L_{\mathrm{sim}} = 3D$, is resolved with 96 approximately cubic cells in the LES focus regions. The conventional "low-Reynolds" requirement $y^+ \leq 1$ on the wall normal distance y_n of wall-adjacent cell centers is relaxed through application of a universal wall-boundary condition [15]. The employed formulation gives valid solutions for any positioning of the first mesh point up to (and including) the log-layer and therefore allows to reduce the number of points spent in the near-wall region [16]. On each strut surface the innermost cell centers are positioned at $y_n = 7.92 \times 10^{-4} D$, which keeps the normalised wall distances below $y^+ \approx 15$. To save resources further away from walls, hanging nodes are used at some of the block-interfaces, successively reducing the resolution towards the outer domain regions. The meshes for the simulations of case 1 and 2 consist of 8.7 and 8.8 mio cells, respectively.

Due to the implicit time-integration, there is no stability constraint on the timestep Δt. It can therefore be chosen to support the convective transport of spatially resolvable vortical structures via $u_{\max}\,\Delta t/\Delta_{\mathrm{DES}} \approx 1$ [18]. Taking $u_{\max} \approx 1.75\,u_\infty$ and $\Delta_{\mathrm{DES}} = L_{\mathrm{sim}}/96$ the global timestep is set to $\Delta t = 1 \times 10^{-5}\,\mathrm{s} = 1.75 \times 10^{-2} D/u_\infty$. The resulting Courant numbers based on the local fluid velocity rarely exceed a value of 1 within the LES focus regions and a 4 kHz signal is represented by 25 discrete samples in the nearfield simulations. Unsteady surface data for the FWH predictions is stored on every 2nd timestep only. Both nearfield simulations were run for 60 000 timesteps, corresponding to 210 characteristic flow-through times

over each configuration. The first 5 000 timesteps were discarded in order to exclude initial transients from the analysis. The flow-field statistics presented below are thus based on 0.55 s physical time.

3 Results

In Figure 1, streamlines of the time-averaged velocity fields from the DDES of case 1 and case 2 are compared to experimental data, which was obtained with PIV in an anechoic open jet tunnel [12]. The flow field topology of case 1 is nearly symmetric, indicating a sufficiently large statistical sample for the DDES (PIV data is mirrored at the symmetry plane). Comparing the streamlines for case 1, the agreement between simulation and experiment is very good. The recirculation regions following flow separation at the upstream strut edges are very similar in shape, size and position. Some deviations in flow direction are visible in the outer flow regions, which could be due to the limited extent of the potential core of the wind tunnel jet ($H_{\text{nozzle}} = 9.5D$, nozzle exit plane is located $6.625D$ upstream of the 1st strut center) or due to other installation effects which are not included in the simulation.

For the inclined case 2, the symmetry is broken and the differences between simulation and experiment are larger, since the recirculation bubbles in the upstream strut wake clearly disagree. Comparing the outer regions, the deviations above the configuration are also more pronounced, however the streamlines below the configuration match quite closely, which might indicate a slight deflection of the wind tunnel jet due to an overall positive mean lift ($c_L^{\text{DDES}} \approx 0.59 - 0.11 = 0.48$) generated by the two struts in this configuration.

As can be deduced from figures 2 and 3, the quantitative agreement between DDES and PIV results is again quite good for case 1 in terms of time-averaged and fluctuating velocity components. It should be noted that the displayed velocity fluctuations are based on resolved scales only. Considering the differing LES and PIV resolutions a perfect match cannot be anticipated, however a large part of the fluctuating energy is contained in a narrow low-frequency band (see figure 7) which

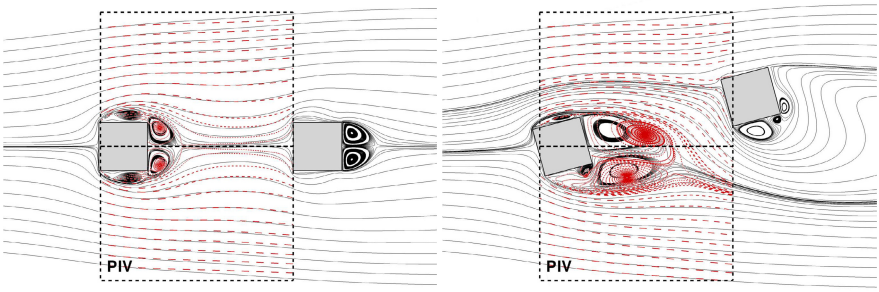

Fig. 1 Streamlines of time-averaged velocity fields obtained from DDES (solid) and PIV (dashed) for case 1 (left) and case 2 (right)

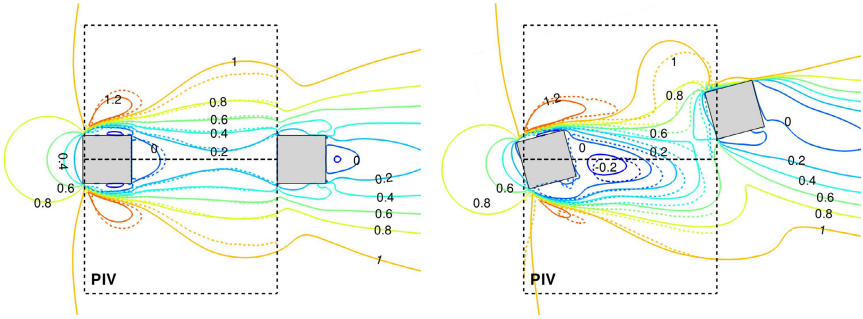

Fig. 2 Comparison of time-averaged x-velocity contours between DDES (solid) and PIV (dashed) for case 1 (left) and case 2 (right)

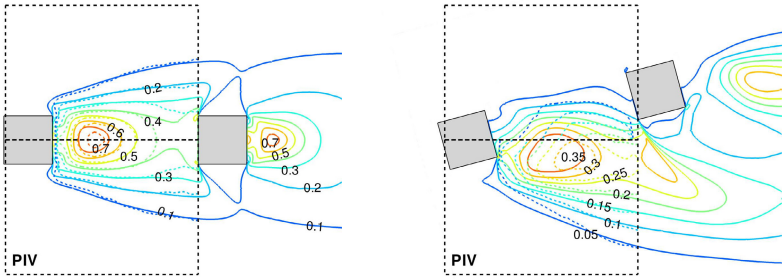

Fig. 3 Comparison of vertical velocity fluctuations $< v'v' > /u_\infty^2$ (DDES: solid, PIV: dashed) for case 1 (left) and case 2 (right). Note that the contour levels for case 1 are larger by a factor of 2.

is assumed to be resolved by both approaches. Although the contour line deviations are larger for the case 2 simulation, both experiment and simulation exhibit strongly-reduced turbulent intensities for the inclined setup.

An impression of the vortical motion captured in the nearfield simulations can be obtained from figure 4, which displays isosurfaces of the λ_2-criterion [8]. The DDES snapshots reveal large scale quasi-2D rollers superimposed by small scale 3D turbulent structures, which slowly decay downstream. Although the 2$^{\text{nd}}$ strut is placed in the wake of the 1$^{\text{st}}$ in both cases, for case 2 it sometimes experiences an undisturbed incoming flow as displayed in figure 4 (right). As a consequence, the time-averaged stagnation pressure on the 2$^{\text{nd}}$ strut is significantly higher for case 2 than for case 1. The time-averaged mid-span surface pressure distributions from experiment and simulation are compared in figures 5 and 6. In these plots, the center of the front surface is the origin of the normalised distance coordinate d/D, which runs on both sides of each strut from 0 to 2 up to the center of its back surface. For case 1 the pressure and suction side c_p-distributions coincide on both struts due to the symmetric flow conditions. While the agreement between experiment and simulation is quite good for the upstream strut, the predicted surface pressures on the

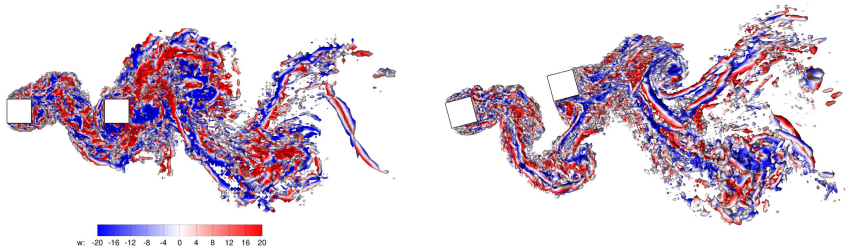

Fig. 4 Snapshots from DDES of case 1 (left) and case 2 (right) showing resolved vortical structures coloured with spanwise velocity

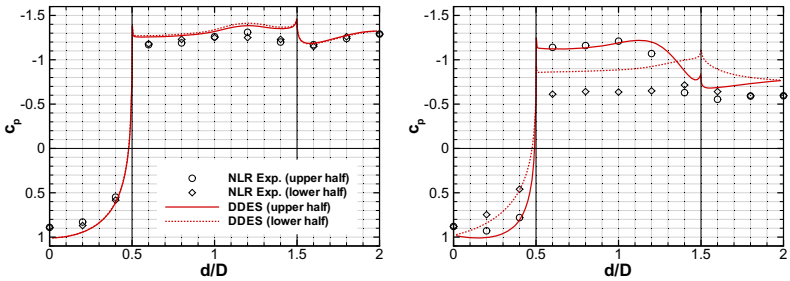

Fig. 5 Time-averaged surface pressures on 1st (upstream) strut from DDES of case 1 (left) and case 2 (right) compared to experimental data

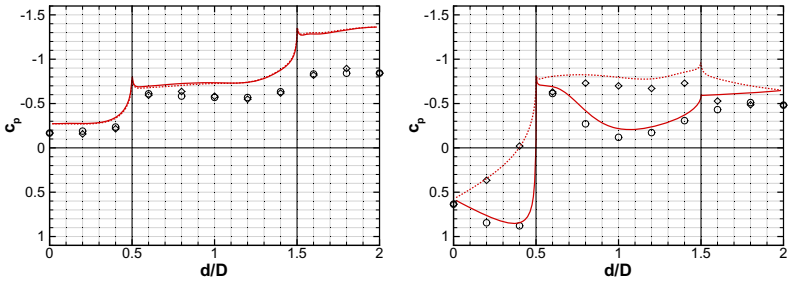

Fig. 6 Time-averaged surface pressures on 2nd (downstream) strut from DDES of case 1 (left) and case 2 (right) compared to experimental data

back surface of the downstream strut are significantly lower than in the experiment. Since similar deviations were observed with different numerical approaches [7], our hypothesis is that the free-stream simulations fail to predict interferences of the broad wake (see figure 4) with free shear-layers from the open jet tunnel, which could lead to mixing with ambient fluid outside of the jet and lower the effective speed behind the configuration in the experiment. Interestingly, the c_p-differences

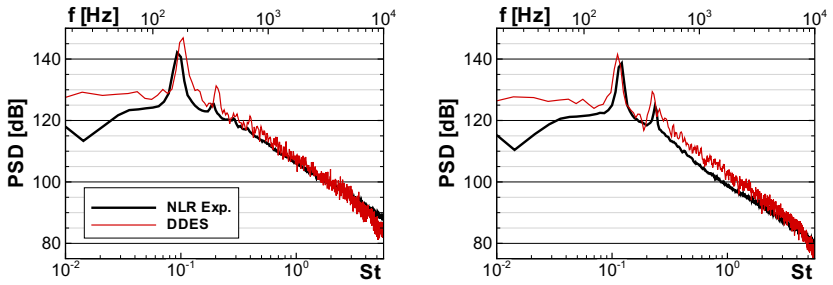

Fig. 7 Predicted surface pressure spectra on bottom surface of the 2nd (downstream) strut for DDES of case 1 (left) and case 2 (right) compared to experimental data

between experiment and simulation are relatively small for the 2nd strut surfaces of the inclined configuration, which on the other hand shows larger deviations for the upstream strut bottom side.

The predicted surface pressure fluctuations reach the highest sound pressure levels on the top and bottom surfaces of the 2nd strut for case 1 (SPL = 163 dB) and on the top surface of the 2nd strut for case 2 (SPL = 159 dB), which is 0 dB or 4 dB below the free-stream dynamic pressure level, respectively. In figure 7, surface pressure spectra from the center point of the 2nd strut bottom surface are compared between experiment and simulation. 8192 samples and Hanning windows with 50 % overlap were used in the FFT processing, resulting in a frequency resolution of $\Delta f = 12.2$ Hz for the averaged power-spectral-density (PSD) levels. The main features of the measured spectra are very well captured by the DDES in both cases. Increased intensities in narrow bands at the main shedding frequencies and at higher harmonics can be seen to emerge from broadband background noise levels, whereby the peak frequencies are shifted from $\mathrm{St}_D = fD/u_\infty = 0.10$ to a 10% higher value of $\mathrm{St}_D = 0.11$ for the inclined case.

Based on unsteady flowfield data acquired on the FWH-integration surfaces shown in figure 8, several farfield noise predictions have been made. In order to avoid artificial coherence caused by periodic boundary conditions imposed in the spanwise direction, only half of the simulated span was used in these FWH predictions. To check for a possibly disturbing effect of wake vortices convecting over the permeable surface, the closing surface (green dashed line in figure 8) is left out from the permeable surface integration for the FWH (open) results. In figure 9, results from solid-wall integration surfaces (blue, solid) and from the permeable integration surfaces (green, open and closed) are presented juxtaposed with experimental data for an observer located approx. 2 m above the configuration. To compare the farfield pressure spectra between experiment and simulation, corrections for sound refraction through shear layers [1, 12] and differing spanwise extent ($L_{\mathrm{exp}}/L_{\mathrm{sim}} = 4.25$) are taken into account, whereby completely independent phase angles are assumed in the limited-span correction [9]. This assumption is probably valid for the broadband content but will lead to an underprediction of the farfield peak PSD levels,

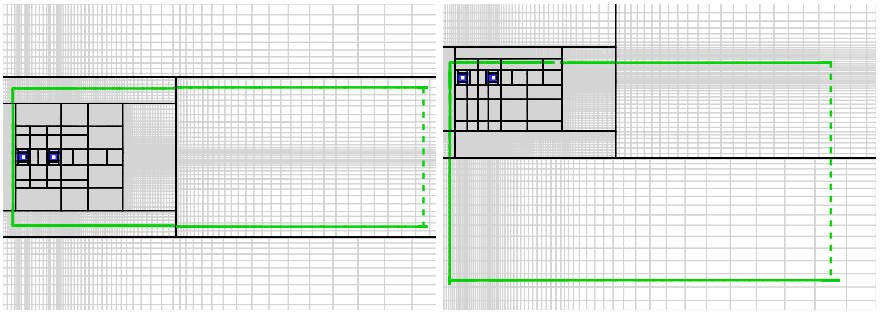

Fig. 8 Block-structured grids for DDES of case 1 (left) and case 2 (right) and FWH integration surfaces (solid: blue, permeable: green). Light grey lines connect every 2nd cell center, black lines are block interfaces.

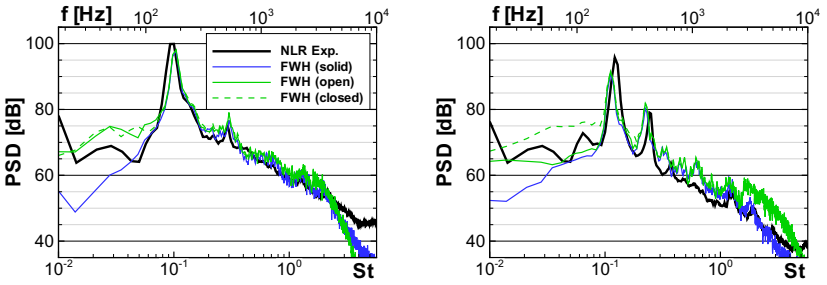

Fig. 9 Predicted farfield pressure spectra for case 1 (left) and case 2 (right) obtained from solid and open/closed permeable FWH integration for an observer fixed on a 2 m radius measured from the center of the upstream strut at 79° w.r.t. the downstream direction compared to experimental data.

since the large-scale vortex shedding was seen to be highly coherent over the span in fig. 4 and in experimental results [13] as well.

For case 1, the predicted PSD levels agree quite well with the experimental data over a wide range of frequencies. Except for very low and very high frequencies (considering the doubled timestep, reliable FWH predictions are not expected above 2 kHz), the results basically resemble the shape of the surface pressure spectra and appear to be insensitive to the integration method. This is a reasonable result, since the contribution of quadrupoles to the noise emitted into the farfield is expected to be small for the low Mach number considered. As anticipated from the differing flow field results, the deviations between experiment and simulation are larger for case 2. However, differences between the integration methods are again restrained to the low and high frequency ranges, whereby the latter can be explained by insufficient grid resolution for the 2nd order nearfield simulation code. Since extensions of the Rhie & Chow interpolation for time-accurate simulations can introduce unsteady mass-sources into the discretised continuity equation (see e.g. [11], [5] and [17]), insufficient spatial resolution cannot only lead to excessive damping but also

to the generation of pseudo-sound in the high-frequency range [10]. The up to 10 dB differences in PSD between different FWH-integration results seen for case 2 in the high-frequency range are therefore assumed not to be caused by quadrupoles but instead by artificial monopole sources, which are primarily captured by the permeable surface integration in the coarse mesh wake region. However, the contribution of this high-frequency content to the fluctuating energy is rather small and an analysis of farfield SPL directivities exhibited typical dipole shapes with maximum intensities perpendicular to the meanflow directions, whereby only for case 1 a symmetric pattern was obtained.

4 Conclusion

A combination of CFD and CAA methods was used to predict the turbulent flow and broadband noise generated by a tandem square cylinder configuration. Both noise generation and radiation were successfully captured in the simulation and an assessment of the prediction quality was made, based on comparisons of time-averaged flow quantities and surface/farfield pressure spectra with experimental data. Considering the good agreement obtained for the symmetric flow setup, the combined DDES/FWH approach is judged to be a very suitable candidate for application to broadband noise predictions in the high-Reynolds, low-Mach number regime.

Acknowledgements. The work presented in this paper was kindly supported by the European Commission through the VALIANT research project under Grant Agreement number ACP8-GA-2009-233680, which is gratefully acknowledged by the authors. The authors also want to acknowledge Stefan Oerlemans, Peter Toth and Christophe Schram for production and provision of the experimental database. Finally the authors want to express their appreciation to Matthias Lemke for careful generation of the block-structured meshes and setup of the FWH integration surfaces.

References

1. Amiet, R.: Refraction of sound by a shear layer. Journal of Sound and Vibration 58(4), 467–482 (1978)
2. Bogey, C., Bailly, C.: Three-dimensional non-reflective boundary conditions for acoustic simulations: far-field formulation and validation test cases. Acta Acustica United with Acustica 88, 463–471 (2002)
3. Brentner, K.S.: Prediction of Helicopter Rotor Discrete Frequency Noise - A Computer Program Incorporating Realistic Blade Motions and Advanced Acoustic Formulation. NASA Technical Memorandum 87721 (1986)
4. Brentner, K.S.: Numerical algorithms for acoustic integrals - the devil is in the details. AIAA Paper 96-1706 (1996)
5. Choi, S.K.: Note on the use of momentum interpolation method for unsteady flows. Numerical Heat Transfer, Part A 36, 545–550 (1999)
6. Curle, N.: The influence of solid boundaries upon aerodynamic sound. Proc. R. Soc. Lond. A 231(1187), 505–514 (1955)

7. Deconinck, T., Temmerman, L., Hirsch, C., Oerlemans, S., Knacke, T., Thiele, F., Duben, A., Gorobets, A., Kozubskaya, T., Baiges, J., Codina, R., Espinoza, H.: Two-struts test case. VALIANT project report D27, NUMECA (2011)
8. Jeong, J., Hussain, F.: On the identification of a vortex. J. Fluid Mech. 285, 69–94 (1995)
9. Kato, M., Launder, B.: The modelling of turbulent flow around stationary and vibrating square cylinders. In: Proc. of 9th Symp. on Turb. Shear Flows, Kyoto (1993)
10. Knacke, T.: Potential effects of Rhie & Chow type interpolations in airframe noise simulations. In: Schram, C. (ed.) Accurate and Efficient Aeroacoustic Prediction Approaches for Airframe Noise. Von Kármán Institute for Fluid Dynamics, Rhode-Saint-Genèse, Belgium (to be published)
11. Lien, F.S., Leschziner, M.A.: A general non-orthogonal collocated finite volume algorithm for turbulent flow at all speeds incorporating second-moment turbulence-transport closure, Part 1: Computational implementation. Comput. Methods Appl. Mech. Engrg. 114, 123–148 (1994)
12. Oerlemans, S.: Acoustic wind tunnel tests on two-struts configuration. VALIANT project report D20, NLR (2011)
13. Oerlemans, S.: Coherence analysis for VALIANT 2-struts experimental benchmark data. VALIANT memo, NLR (2011)
14. Rung, T., Bunge, U., Schatz, M., Thiele, F.: Restatement of the Spalart-Allmaras Eddy Viscosity Model in Strain-Adaptive Formulation. AIAA Journal 41(7), 1396–1399 (2003)
15. Rung, T., Lübcke, H., Thiele, F.: Universal wall–boundary conditions for turbulence–transport models. Zeitschrift für Angewandte Mathematik und Mechanik 81(S3), 481–482 (2000)
16. Schmidt, T., Mockett, C., Thiele, F.: Adaptive wall function for the prediction of turbulent flows. In: Kroll, N., Schwamborn, D., Becker, K., Rieger, H., Thiele, F. (eds.) MEGADESIGN and MegaOpt - German Initiatives for Aerodynamic Simulation and Optimization in Aircraft Design. Notes on Numerical Fluid Mechanics and Multidisciplinary Design, vol. 107, pp. 21–33. Springer, Heidelberg (2009)
17. Sotiropoulos, F., Abdallah, S.: The discrete continuity equation in primitive variable solutions of incompressible flow. Journal of Computational Physics 95, 212–227 (1991)
18. Spalart, P.R.: Young-person's guide to detached-eddy simulation grids. CR-2001-211032, NASA (2001)
19. Spalart, P.R., Deck, S., Shur, M.L., Squires, K.D., Strelets, M.K., Travin, A.: A new version of detached-eddy simulation, resistant to ambiguous grid densities. Theor. Comput. Fluid Dyn. 20, 181–195 (2006)
20. Xue, L.: Entwicklung eines effizienten parallelen Lösungsalgorithmus zur dreidimensionalen Simulation komplexer turbulenter Strömungen. Ph.D. thesis, Technische Universität Berlin (1998)

Correlation Functions and Spectra of Reactive Scalars in Turbulent Premixed Flames

H. Kolla, E.R. Hawkes, A.R. Kerstein, and J.H. Chen

Abstract. One dimensional auto and cross correlation functions, and corresponding spectra, of reactive scalars in turbulent premixed flames are studied using fully compressible three dimensional direct numerical simulations (DNS) with detailed chemical kinetics and transport properties. The configuration considered is a temporally evolving rectangular slot-jet premixed flame interacting with intense shear driven turbulence. Three simulations were performed by keeping the jet Reynolds number fixed at 10000 and varying the Damköhler number by a factor of four. The fuel is lean premixed hydrogen at an equivalence ratio of 0.7 pre-heated to 700 K and the pressure is 1 atm. Spectra of velocities and scalars, both major species and intermediate radicals, resemble the classical shape with at least one decade of $k^{-5/3}$ scaling denoting the inertial range. Qualitative differences arise only in the high wave number reactive-diffusive range with a spike observed in the hydrogen spectrum. However the spectral coherence between various species, which is highest at low wave numbers, begins to drop before suddenly rising significantly at the high wave numbers corresponding to laminar flame scales. This is very likely due to the non-negligible influence of finite rate chemistry effects at high wave numbers.

H. Kolla · J.H. Chen
Combustion Research Facility,
Sandia National Laboratories,
Livermore, California, USA
e-mail: {hnkolla,jhchen}@sandia.gov

E.R. Hawkes
The University of New South Wales,
Sydney, Australia
e-mail: evatt.hawkes@unsw.edu.au

A.R. Kerstein
72 Lomitas Road, Danville,
CA 94526, USA
e-mail: alan.kerstein@gmail.com

M.O. Deville et al. (eds.), *Turbulence and Interactions*,
Notes on Numerical Fluid Mechanics and Multidisciplinary Design 125,
DOI: 10.1007/978-3-662-43489-5_16,

1 Introduction

The study of spectra of scalars, both passive and reactive, is of great importance for modelling of turbulent reactive flows. With few notable exceptions, such as the spectral closure of EDQNM [13, 16], virtually every modelling methodology relies on some implicit or explicit assumptions about the dynamics of turbulence-scalar mixing and associated scalar spectra. For instance, the widely used laminar flamelet model for non-premixed turbulent combustion relies on representing the thermo-chemical manifold with a single scalar whose evolution equations employ models based on passive scalar mixing assumptions. While such assumptions are strictly valid for purely passive scalars in incompressible homogeneous isotropic turbulence, it is unclear what the consequences of variable density, finite rate chemical kinetics and differential diffusion are on the evolution of scalar spectra. Indeed, even the assumption of universality of velocity spectra might appear questionable for flows with strong local density change and dilatation, such as turbulent premixed flames, although it is routinely used for closing sub-grid Reynold's stresses in large eddy simulations (LES).

While spectra of passive scalars have been widely studied, spectra of reactive scalars have received limited attention. It is well known from Batchelor's early theory [1] that passive scalars with large Schmidt number exhibit a k^{-1} scaling of the power spectrum in the so-called viscous-convective wave number k-range in which the spectral transfer of velocity is diffusive but that of the scalar is convective. On the other hand, scalars with small Schmidt number [2] have an inertial-diffusive range with a $k^{-17/3}$ scaling for the scalar spectrum. Corrsin [6] extended these scaling laws for the case of a scalar undergoing a first order reaction and elucidated the influence of the reactivity on the scalar spectrum in the relevant wave number ranges for both large and small Schmidt numbers. However, Corrsin's analysis is restricted to a very dilute reactant whose dynamics do not affect the flow field. Similarly, Kosály [8] examined a bi-variate reacting system in an incompressible turbulent mixing layer and derived the reacting scalar spectra in the slow and fast chemistry limits to compare against the measurements of Bilger *et al.* [4]. More recently Wang *et al.* [15] and Vaishnavi *et al.* [14] report dissipation spectra of mixture fraction, a conserved scalar, in turbulent non premixed flames using experiments and DNS respectively. Knaus and Pantano [11] examined spectra of kinetic energy, mixture fraction and temperature using DNS of non-premixed reacting shear layers. They note that the influence of heat release on the spectra can be accounted simply by considering density weighted large scale quantities in the classical scaling laws (except for the dissipation range of the temperature spectrum). Even though their results are based on DNS with single step chemical kinetics, they are very encouraging. They essentially confirm the arguments of Bilger [3] who showed that for most practical flows the turbulence will overwhelm the dilatation due to heat release in non-premixed flames and hence passive scalar behaviour is to be expected. This is however not true of premixed flames in which the local dilatation due to the heat release is relatively very strong [3]. Hence the spectral dynamics, of both velocity and scalars, in premixed flames are likely to be very different from those of non-premixed flames.

To the best of our knowledge the only work that has reported reacting scalar spectra in turbulent premixed flames is the experimental work of Guttenfelder *et al.* [9] who report spectra of hydroxyl radical from single-point time series measurements in jet premixed flames. Little is known of spectra and co-spectra of reacting scalars at realistic levels of heat release in premixed flames, as noted by Dimotakis [7] and Knaus and Pantano [11], and this is the focus of the present study.

The study of spectra is made difficult by the fact that measuring spectra is very challenging in both experiments and direct numerical simulations (DNS). In experiments of reacting flows selectively imposing conditions such as incompressibility, homogeneity or isotropy is not straightforward. Furthermore, for statistically stationary flames estimation of spectra require two-point correlation measurements in the three dimensional field, which are very difficult to obtain experimentally. These restrictions are alleviated somewhat in DNS, but performing well resolved DNS with a large range of dynamic scales for long durations to achieve statistical convergence becomes expensive, sometimes prohibitively so for reacting flows. However, with rapid increase in computing power DNS of turbulent reacting flows at realistic turbulence levels have become feasible in recent years. In the present work we employ one such DNS [10] to study spectra of reacting scalars in a premixed flame interacting with intense shear driven turbulence.

2 DNS Configuration

The DNS configuration corresponds to a temporally evolving premixed rectangular slot-jet flame interacting with a turbulent shear layer in a rectangular box, as shown in Figure 1. Two inwardly propagating planar premixed flames of lean hydrogen-air mixture of equivalence ratio 0.7 and unburnt temperature of 700 K were initialised outside a rectangular shear layer of width, H, formed between a stream of fresh reactants alongside two co-flowing streams of burnt products. A purely stream wise mean velocity, varying in the transverse direction via a smooth *tanh* profile, was initialised in the domain. Turbulence velocity fluctuations corresponding to a

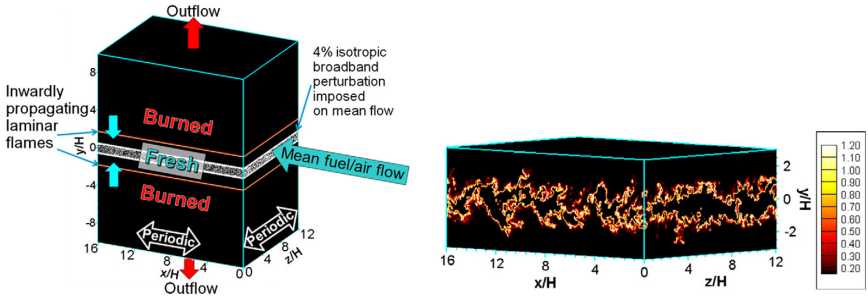

Fig. 1 Schematic showing the configuration of the DNS (left). The stream wise direction is x, transverse is y and span wise is z. Instantaneous local heat release rate, normalised by the maximum laminar flame value, is shown on the right for the Da+ case at $t = 15t_j$.

prescribed Passot-Pouquet energy spectrum were superimposed on top of the mean velocity to trigger the development of the shear turbulence. The root-mean-square of the initial velocity fluctuation values was 4% of the main jet velocity. The initial location of the flames was far enough from the shear layer in the transverse direction to ensure that by the time the flames interact with the shear layer, the turbulence has fully evolved from the intial artificial field. Periodic boundary conditions were imposed on the streamwise (x) and spanwise (y) boundaries while the transverse (z) boundaries were specified as non-reflecting outflow. More details about the initial and boundary conditions can be found in [10].

The simulations were performed with the DNS code S3D [5] which solves the fully compressible form of continuity, Navier-Stokes, internal energy and species conservation equations. S3D incorporates finite rate chemical kinetics and detailed transport properties via the CHEMKIN and TRANSPORT packages and the hydrogen oxidation mechanism of Li *et al.* [12], with 9 species and 21 elementary reactions, were employed in the present DNS. Three cases were simulated by varying the jet and co-flow mean velocities and jet width, H, such that the jet Reynolds number

$$\mathrm{Re}_j \equiv \frac{\Delta U H}{\nu_o} \tag{1}$$

was held constant at 10000 while the jet Damköhler number

$$\mathrm{Da}_j \equiv \frac{t_j}{t_L} \equiv \frac{(H/\Delta U)}{(\delta_L/s_L)} \tag{2}$$

was varied by a factor of four where $t_j = (H/\Delta U)$ is the jet time and t_L is the laminar flame time. The difference between the mean jet and co-flow velocities is ΔU, the unburnt mixture kinematic viscosity is ν_o and the laminar flame speed and thickness are s_L and δ_L respectively. For each case the simulation domain was $16H \times 20H \times 12H$ in the x, y and z directions respectively which was discretised using a uniform grid in the x, and z directions while a stretched grid was used in the y direction with the coarse mesh close to the transverse boundaries and the uniform fine mesh in the regions of the flame. The finite difference form of the conservation equations were solved in the physical space using an explicit eighth order

Table 1 Numerical parameters of the three DNS cases

Parameter	Case Da-	Baseline	Case Da+
Da_j	0.13	0.27	0.54
H (mm)	2.7	3.84	5.4
ΔU (m/s)	312.6	219.8	156.3
δx^a (μm)	18	25.6	36
δt^a (ns)	2.5	4	5

[a] δx and δt are the grid resolution and time step respectively.

central difference scheme for spatial derivatives and an explicit fourth order six-stage Runge-Kutta scheme with a constant time step. The main numerical parameters of the DNS are listed in Table 1.

3 Results and Discussion

Since the present simulations were for temporally evolving fields, wave number and not frequency spectra could be extracted from instantaneous snapshots of the solution. Furthermore, since x and z were homogeneous directions, spectra on $x-z$ (constant y) planes were considered. Since averaging in time was not meaningful, one-dimensional wave number spectra were computed instead of two-dimensional spectra in the interest of statistical convergence. Here, we define the auto, E_{AA}, and co-spectra, E_{AB}, as Fourier transforms of the corresponding stream wise auto and cross-correlation functions R_{AA} and R_{AB} respectively, which are written as,

$$R_{AA}(l) = \langle \phi'_A(x_0)\phi'_A(x_0+l)\rangle, \;\; R_{AB}(l) = \langle \phi'_A(x_0)\phi'_B(x_0+l)\rangle \tag{3}$$

where ϕ' is the fluctuation of the scalar about the average, x_0 is the origin and l is the stream wise distance coordinate. The angle brackets $\langle\cdot\rangle$ denote an averaging in the x direction. On a chosen $x-z$ plane, the auto correlation function was computed at each z location, and the spectra was computed as the average of the Fourier transforms of the N_z samples of the correlation function i.e.

$$E_{AA}(k) = (1/N_z)\Sigma_{j=1}^{N_z}\mathscr{F}\{R_{AA}^j(l)\}, \tag{4}$$

where the operator $\mathscr{F}$ is

$$\mathscr{F}\{\cdot\}(k) \equiv \int_{-\infty}^{+\infty}(\cdot)e^{-2\pi ikl}dl. \tag{5}$$

Figure 2 shows the auto-spectra of normalised oxygen and hydrogen species mass fractions from the Da- and the Da+ cases at an instant corresponding to $t = 15t_j$. These are extracted from an $x-z$ plane[1] corresponding to a mean progress variable value of 0.5 which is in the middle of the flame brush where most of the turbulence-chemistry interaction occurs. The progress variable is defined as a normalised oxygen mass fraction such that its value is 0 in fresh reactants and 1 in burnt products. Also indicated in the plots are the wave numbers corresponding to the laminar flame thickness, δ_L and $\delta_L/10$. The spectra in both cases have a classical shape with a considerable wave number range in which a $k^{-5/3}$ scaling is evident. The hydrogen spectrum seems to have a slightly higher slope compared to that of oxygen but in most of the low and moderate wave number ranges the spectra are almost coincident. They seem to diverge noticeably in the high wave number range, particularly for $k > 2\pi/\delta_L$, which might be construed as a diffusive-reactive range. Interestingly, the hydrogen spectrum has a slight blip in this range, particularly noticeable in the

[1] Note that in this configuration mean quantities vary only in the transverse (y) direction.

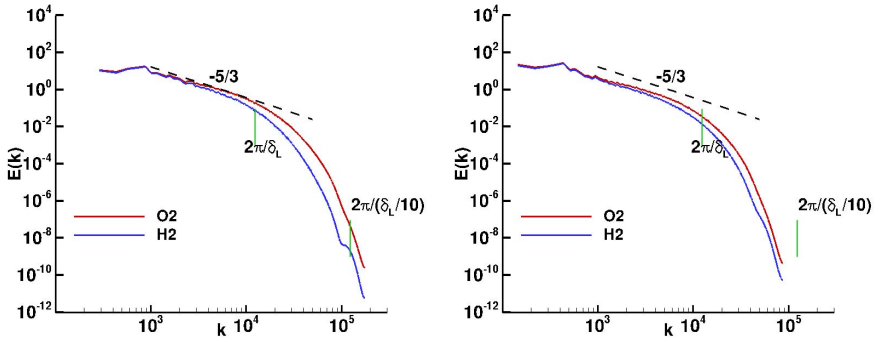

Fig. 2 The one-dimensional auto-spectra of normalised O_2 and H_2 mass fractions from the Da- (left) and the Da+ (right) cases at $t = 15t_j$

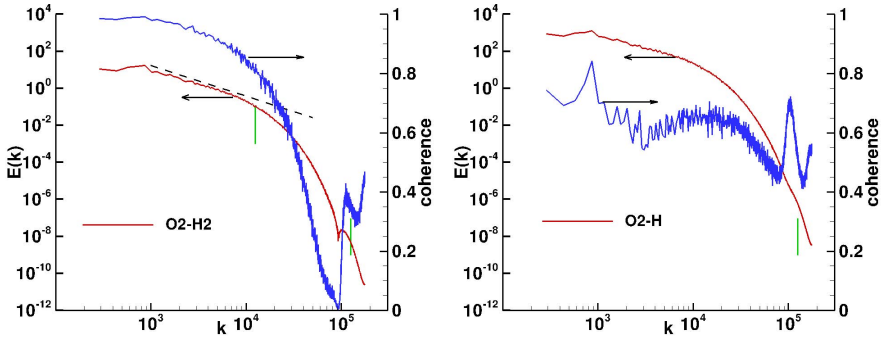

Fig. 3 The one-dimensional co-spectra (red) and spectral coherence (blue) of normalised species mass fractions from the Da- case at $t = 15t_j$. The left plot corresponds to $O_2 - H_2$ and the right corresponds to $O_2 - H$ co-spectra.

Da- case, which is not apparent for oxygen. This is likely due to a non-negligible influence of chemical reactions on the spectral dynamics of these scalars.

This aspect is more apparent from the spectral coherence values for these two scalars plotted in Figure 3, along with the co-spectra. Also shown are the coherence and co-spectra for oxygen-hydrogen radical. The spectral coherence is very high at low wave numbers as expected, since the spectral dynamics in this range are dominated by convection by large scale eddies. As wave number increases the coherence drops indicating the emergence of isotropy. However, for very high wave numbers in the diffusive-reactive range, the coherence suddenly increases significantly. The coherence of reactive scalars reported by Kosály [8] do not show such a behaviour and they asymptotically approach zero at high wave numbers. Also note that the low wave number coherence values for $O_2 - H$ are smaller than that for $O_2 - H_2$ as

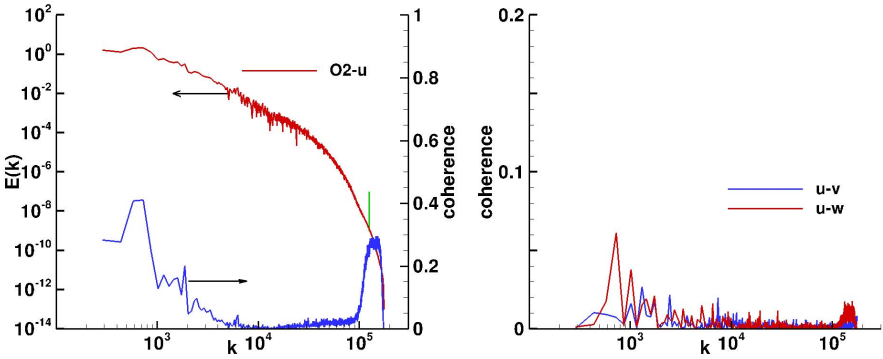

Fig. 4 The one-dimensional co-spectra (red) and spectral coherence (blue) from the Da- case at $t = 15t_j$. The left plot corresponds to $O_2 - u$ and the right corresponds to spectral coherence of velocity components.

expected. This behaviour clearly indicates that the influence of chemical reactions on high wave number reactive scalar spectral dynamics are not negligible.

To examine whether such an influence exists on the velocity-scalar correlations, co-spectra and coherence of strea mwise velocity, u, and oxygen mass fraction are plotted in Figure 4. Also shown are the coherence values between $u - v$ and $u - w$ velocities. The high coherence at large wave numbers is evident between O_2 and u as well indicating that the chemical reactions influence the velocity-scalar spectral dynamics too. However the coherence values for velocity components are markedly lower and almost zero at high wave numbers.

Acknowledgements. Computational support for this project was supported by and this research used resources of the National Center for Computational Sciences at Oak Ridge National Laboratory, which is supported by the office of Science of the US Department of Energy under contract DE-AC05-00OR22725. The work at Sandia National Laboratories was supported by the Division of Chemical Sciences, Geosciences, and Biosciences, Office of Basic Energy Sciences of the US Department of Energy and by the US Department of Energy SciDAC Program. SNL is a multiprogramme laboratory operated by Sandia Corporation, a Lockheed Martin Company for the US DOE under Contract DE-AC04-94AL85000.

References

1. Batchelor, G.K.: Small-scale variation of convected quantities like temperature in turbulent fluid. Part 1. General discussion and the case of small conductivity. J. Flu. Mech. 5, 113–133 (1959)
2. Batchelor, G.K., Howells, I.D., Townsend, A.A.: Small-scale variation of convected quantities like temperature in turbulent fluid. Part 2. The case of small conductivity. J. Flu. Mech. 5, 134–139 (1959)

3. Bilger, R.W.: Some aspects of scalar dissipation. Flow Turb. Comb. 72, 93–114 (2004)
4. Bilger, R.W., Saetran, L.R., Krishnamoorthy, L.V.: Reaction in a scalar mixing layer. J. Flu. Mech. 233, 211 (1991)
5. Chen, J.H., Choudhary, A., de Supinski, B., DeVries, M., Hawkes, E.R., Klasky, S., Liao, W.K., Ma, K.L., Mellor-Crummey, J., Podhorski, N., Sankaran, R., Shende, S., Yoo, C.S.: Terascale direct numerical simulations of turbulent combustion using S3D. Comp. Sci. Disc. 2, 1–31 (2009)
6. Corrsin, S.: The reactant concentration spectrum in turbulent mixing with a first order reaction. J. Flu. Mech. 11, 407–416 (1961)
7. Dimotakis, P.E.: Turbulent mixing. Annu. Rev. Fluid Mech. 37, 329–356 (2005)
8. Kosály, G.: Frequency spectra of reactant fluctuations in turbulent flows. J. Flu. Mech. 246, 489–502 (1993)
9. Guttenfelder, W.A., King, G.B., Gore, J.P., Laurendeau, N.M., Renfro, M.W.: Hydroxyl time-series measurements and simulations for turbulent premixed jet flames in the thickened preheat regime. Comb. Flame 135, 381–403 (2003)
10. Hawkes, E.R., Chatakonda, O., Kolla, H., Kerstein, A.R., Chen, J.H.: A petascale direct numerical simulation study of the modelling of flame wrinkling for large-eddy simulations in intense turbulence. Comb. Flame (available online) (2012)
11. Knaus, R., Pantano, C.: On the effect of heat release in turbulence spectra of non-premixed reacting shear layers. J. Flu. Mech. 626, 67–109 (2009)
12. Li, J., Zhao, Z., Kazarov, A., Dryer, F.L.: An updated comprehensive kinetic model of hydrogen combustion. Int. J. Chem. Kinet. 36, 566–575 (2004)
13. Ulitsky, M., Collins, L.: Application of the eddy damped quasi-normal Markovian spectral transport theory to premixed turbulent flames. Phys. Fluids 9(3410) (1997)
14. Vaishnavi, P., Kronenburg, A., Pantano, C.: On the spatial length scales of scalar dissipation in turbulent jet flames. J. Flu. Mech. 596, 103–132 (2008)
15. Wang, G., Karpetis, A.N., Barlow, R.S.: Dissipation length scales in turbulent non-premixed jet flames. Comb. Flame 148, 62–75 (2007)
16. Xia, Y., Liu, Y., Vaithianathan, T., Collins, L.R.: Eddy damped quasinormal Markovian theory for chemically reactive scalars in isotropic turbulence. Phys. Fluids 22(045103) (2010)

Numerical Study of Local Deposition Mechanisms of Nanoparticles in a Human Upper Airway Model

F. Krause, G. Ghorbaniasl, S. Verbanck, and Chris Lacor

Abstract. We carried out large-eddy simulation to study turbulent air flow and local deposition of inhaled nanoparticles with a $10nm$ diameter in an idealized human upper airway model for a steady inspiratory flow rate of $30\frac{l}{min}$. We described the particles in an Eulerian framework and accounted for their Brownian motion by a diffusion coefficient calculated from the Stokes-Einstein relation. We calculated the turbulence subgrid-scale stresses and the subgrid-scale particle mass flux by a localized dynamic Smagorinsky subgrid-scale model. Predicted mean velocity and turbulent kinetic energy profiles were in good agreement with particle image velocimetry measurements and slightly superior to Reynolds-averaged Navier-Stokes simulations in the same model. We further showed that the most pronounced particle deposition hot-spots are located in the vicinity of intense turbulent structures and that their shapes are strongly correlated.

1 Introduction

There is good evidence from epidemiological and toxicological studies, that the inhalation of ambient and engineered nanosized particles with a diameter smaller than $100nm$ (NP_{100}) is associated with significant adverse health effects. These are determined by several interacting factors: particle size and surface area, particle surface chemistry, their potential to translocate into the blood circulation and reach

F. Krause · G. Ghorbaniasl · C. Lacor
Vrije Universiteit Brussel, Department of Mechanical Engineering,
Pleinlaan 2, 1050 Brussel, Belgium
e-mail: {florian.krause,ghader.ghorbaniasl,
chris.lacor}@vub.ac.be

S. Verbanck
University Hospital UZ Brussels, Respiratory Division,
Laarbeeklaan 101, 1090 Brussels, Belgium
e-mail: sylvia.verbanck@uzbrussel.be

M.O. Deville et al. (eds.), *Turbulence and Interactions*,
Notes on Numerical Fluid Mechanics and Multidisciplinary Design 125,
DOI: 10.1007/978-3-662-43489-5_17,

secondary organs and the overall inhaled particle dose as well as the local dose of deposited particles [1].

Several numerical studies addressed the latter issue and predicted the deposition of NP_{100} in models of the human upper airway (or parts of it). However, accurate deposition predicitions were limited by either (i) the use of idealized respiratory tract geometries or (ii) an inaccurate prediction of the complicated laminar-turbulent air flow and its effect on local particle deposition [2]. The present study focused on the latter issue and intends to gain a better understanding of the interplay between turbulent flow structures and the formation of local deposition hot-spots in a human upper airway model (UAM), which shows all relevant morphological features [3].

The deposition of NP_{100} is predominantly determined by Brownian diffusion, while other mechanisms such as inertial impaction or gravitational settling are negligible [2]. Thus, we modeled the two-phase air-nanoparticle system in an Eulerian framework and modeled the particle concentration as a passive scalar. We calculated the Brownian diffusion by the Stokes-Einstein equation, which relates the Brownian particle motion to the Stokes particle drag [4]. By using large-eddy simulation (LES) and a localized dynamic subgrid-scale (SGS) model, we predicted the laminar-turbulent flow field and the particle transport and deposition due to resolved and unresolved turbulent fluctuations.

2 Simulation Approach

2.1 Governing Equations

The governing equations are the low-pass filtered incompressible continuity and Navier-Stokes equations

$$\frac{\partial \overline{u}_i}{\partial x_i} = 0\,, \tag{1}$$

$$\frac{\partial \overline{u}_i}{\partial t} + \frac{\partial}{\partial x_j}\left(\overline{u}_i \overline{u}_j\right) = -\frac{1}{\rho}\frac{\partial \overline{p}^*}{\partial x_i} + \frac{\partial}{\partial x_j}\left(\sigma_{ij} - \tau_{ij}\right)\,, \tag{2}$$

where σ_{ij} denotes the viscous stress tensor, τ_{ij} the anisotropic SGS stress tensor and $\overline{p}^*$ the modified pressure including the isotropic SGS stress. The filtered scalar advection-diffusion equation for the particle concentration reads

$$\frac{\partial \overline{C}}{\partial t} + \frac{\partial}{\partial x_j}\left(\overline{C}\,\overline{u}_j\right) = \frac{\partial}{\partial x_j}\left(D\frac{\partial \overline{C}}{\partial x_j} - q_i\right)\,, \tag{3}$$

where q_i denotes the scalar-flux term accounting for turbulent particle diffusion. The Brownian diffusion coefficient D is calculated by the Stokes-Einstein equation for spherical particles with diameter d_p as $D = (k_B T C_s)\,/\,(3\pi\mu d_p)$[4]. The slip correction factor $C_s = 1 + Kn\,(1.142 + 0.558\exp(-0.999/Kn))$ accounts for non-continuum effects in the transition- and free-molecular regime [5]. Furthermore, we

assumed the particles to be absorped upon contact with the (airway) wall and thus employed zero particle concentration wall boundary conditions.

The anisotropic part of the SGS stress and the scalar-flux term were dynamically calculated from the resolved velocity and particle concentration scales using the dynamic Smagorinsky model [6]. The model coefficients were averaged locally over a control volume and negative SGS viscosity and diffusivity were clipped to zero to ensure numerical stability and an accurate prediction of the SGS quantities in the near-wall region. It is noted that some averaging procedures, e.g., global averaging over the entire computational domain, might be suitable to control stability, but can lead to an over- or underestimation of the SGS quantities in the near-wall region.

2.2 Numerical Method

The simulations were carried out using the open-source software OpenFOAM® [7]. The governing equations were discretized using the finite volume method with colocated variable arrangement. The inter-equation coupling of the pressure-velocity system was treated with the PISO procedure. Decoupling in the pressure field was avoided by applying a variant of the Rhie and Chow interpolation technique. The advection terms of the Navier-Stokes equation and the particle concentration equation are discretized with a second-order linear upwind scheme. The implicit second-order Crank-Nicholson scheme is used for temporal discretization.

The multi-block structured computational grid consisted of 2.65 million hexahedral cells. To resolve the viscous and thinner diffusive sublayer, we followed a two-step procedure. First we estimated the diffusive sublayer thickness as proposed in [8] by $\delta_C^+ = (\nu/D)^{-1/3}\delta_u^+$ (with the viscous sublayer thickness δ_{u^+} calculated from previous Reynolds-averaged Navier-Stokes (RANS) simulation for the same flow conditions [9]). Then we clustered cells towards the wall to ensure that the viscous- and diffusive sublayer were resolved with at least 3 cells.

3 Results and Discussion

3.1 Air Flow

We evaluated the accuracy of the LES simulations by comparing the time-averaged (denoted by angle brackets) velocity magnitude $\langle u \rangle^*$ (normalized by the inlet velocity u_{in}) and turbulent kinetic energy profiles $\langle k \rangle^*$ (normalized by u_{in}^2) with particle image velocimetry (PIV) measurements [3] and RANS simulations [9] for the same flow configuration.

Figures 1b-1d show the developement of the so-called laryngeal jet, a turbulent wall jet, which formed downstream of the larynx separation point. The profile in the upmost section one tracheal diameter downstream of the larynx shows the typical recirculation bubble at the posterior side ($0 \leq x/D < 0.27$) and the high-velocity laryngeal jet ($0.27 < x/D \leq 1$). It further shows the peak turbulent kinetic energy close to free shear layer of the jet (strong mean strain rate) and an almost uniform

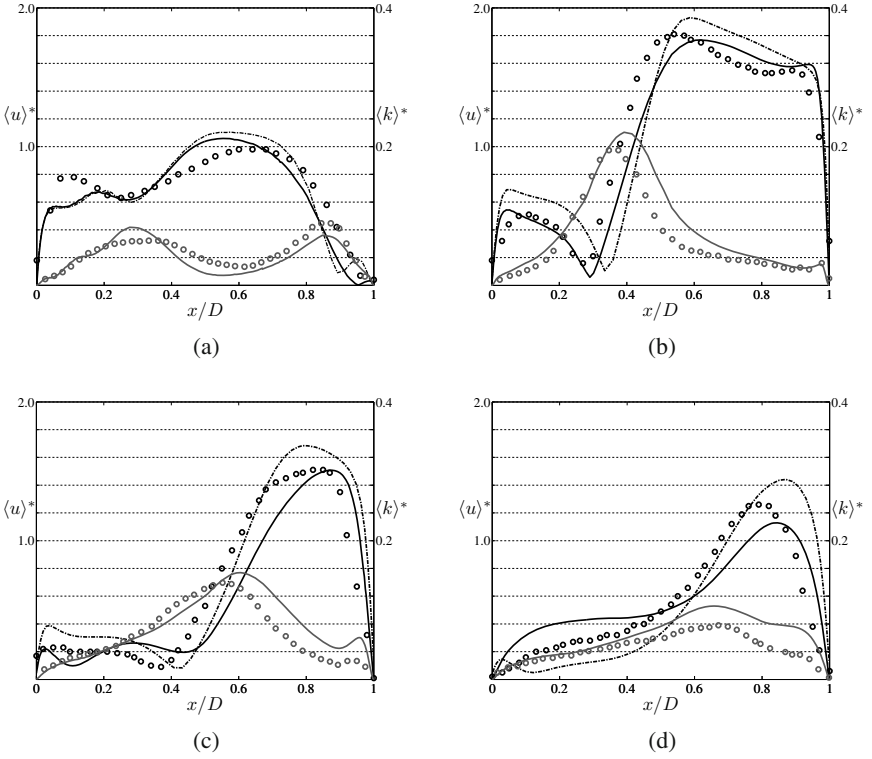

Fig. 1 Profiles of normalized two-component velocity magnitude $\langle u \rangle^* = \left(\langle \overline{u}_x \rangle^2 + \langle \overline{u}_z \rangle^2\right)^{1/2} / u_{in}$ (black) and turbulent kinetic energy $\langle k \rangle^* = \frac{1}{2}\left(\langle u_x' \rangle^2 + \langle u_z' \rangle^2\right) / u_{in}^2$ (gray) in four different sections in the saggital plane: 5*mm* above the epiglottis (a) and one (b), two (c) and three (d) tracheal diameters downstream of the larynx [3]. Closed circles show PIV measurements, solid and dash-dotted lines LES and RANS predictions.

turbulent kinetic energy profile across the laryngeal jet (weak mean strain rate). As the laryngeal jet developed further downstream, its width was decreasing and the location of the free shear layer and the peak turbulent kinetic energy were moving towards the anterior side of the trachea.

Despite the consistent underprediction of the laryngeal jet width, the LES predictions are in good overall agreement with the PIV measurements and superior to the RANS simulations (e.g. in the prediction of the recirculation zone in the larynx).

3.2 Local Nanoparticle Deposition

We identified vortical flow structures by calculating the second invariant of the time-averaged velocity gradient tensor (Q-criterion). Local particle deposition hot-spots

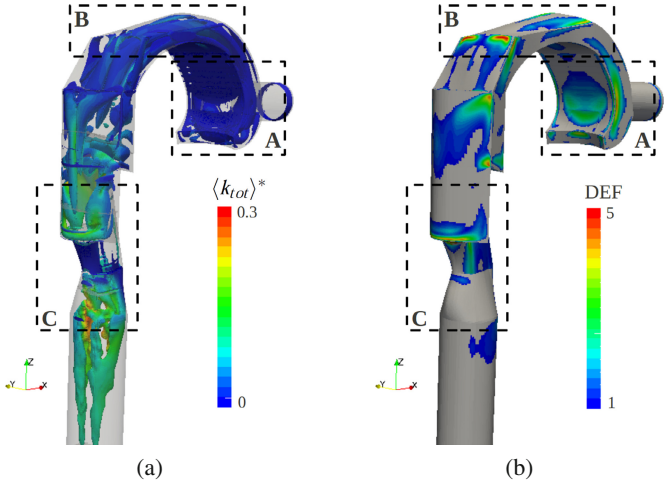

Fig. 2 Time-averaged iso-surfaces of $2 \leq \langle Q \rangle^* \leq 20$ colored by time-averaged total turbulent kinetic energy $\langle k_{tot} \rangle^* = \left(\frac{1}{2} \left(\langle u_x' \rangle^2 + \langle u_y' \rangle^2 + \langle u_z' \rangle^2 \right) + \langle k^{sgs} \rangle \right) / u_{in}^2$ (a) and contours of DEF ≥ 1 indicating local particle deposition hot-spots (b)

were quantified by the deposition enhancement factor (DEF), which is calculated as the ratio of specific local and total mass flow rate to the wall [10].

Figure 2a shows iso-surfaces of $\langle Q \rangle^*$ (normalized by u_{in}^2 / d_{in}^2) colored by total turbulent kinetic energy $\langle k_{tot} \rangle^*$. While the vortical structures were weak in the oral cavity, they showed a gradually increasing turbulence intensity downstream of the entrance to the oropharynx and below the epiglottis (first and second distinct flow separation point). Downstream of the larynx (third separation point), we observed regions of strong vortical motion and turbulence intensity respectively, emphasizing the presence of the highly turbulent laryngeal jet. As depicted in Figure 2b, local particle deposition hot-spots (DEF ≥ 1) showing a clear contour were located at the tongue (region A), the bended channel formed by the hard- and soft palate (region B), at the posterior side of the oro- and laryngopharynx and the anterior- and posterior side of the larynx (region C).

The dominating deposition hot-spot in region A (Figure 3a) was located at the tongue (indicated by HS). It is apparent that its circle-like shape matched very well with the contours of the neighbouring near-wall vortex sheets located at the upper (clockwise rotating: cw) and lower half (counterclockwise rotating: ccw) of the deposition hot-spot. Further downstream in region B (Figure 3b), we observed a pair of large (long and narrow) counter-rotating vortex tubes as well as similar shaped deposition hot-spots above each vortex tube at the hard palate. It is remarkable that both hot-spots are not located directly above the vortex core, but shifted to the left of the ccw rotating vortex and right of the cw rotating vortex (corresponding to the side of upward fluid motion). Region C (Figure 3c) showed a range of different vortical structures (e.g. counter-rotating vortical structures of complex shape, hairpin-like vortices and vortex sheets), which complicates a detailed analysis. However,

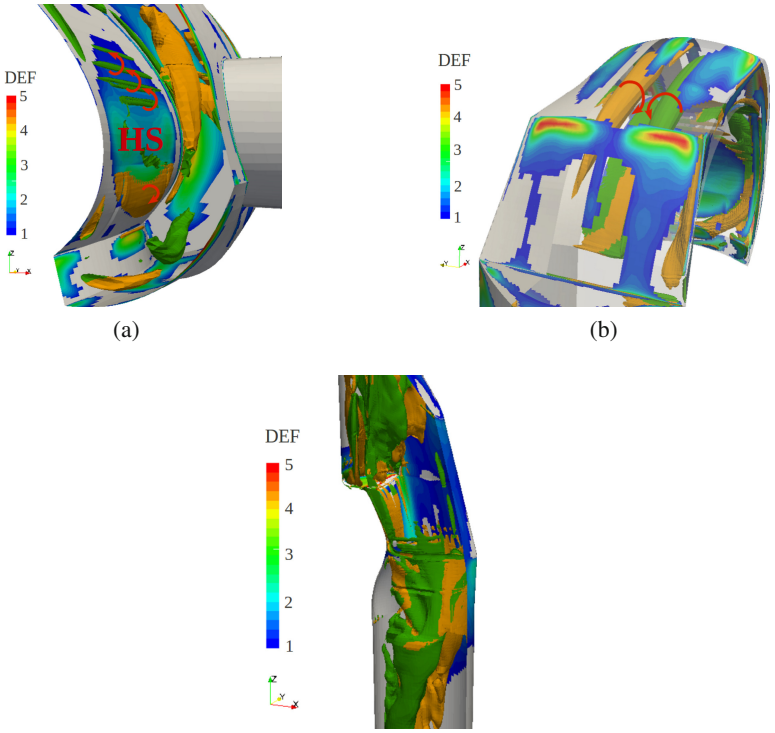

Fig. 3 Local particle deposition hot-spots (contours of DEF ≥ 1) and vortical flow structures in region A: $\langle Q \rangle^* = 18$ (a), region B: $\langle Q \rangle^* = 18$ (b) and region C: $\langle Q \rangle^* = 2$ (c). Colors indicate the direction of rotation around the global Y-axis (a), X-axis (b) and Z-axis (c): counterclockwise rotation (yellow), clockwise rotation (green)

we observed that large patches of increased deposition are located close to vortical structures, mainly at the posterior side of the laryngopharynx and the anterior side of the larynx (in the vicinity of the turbulent laryngeal jet).

The apparent influence of turbulent flow structures on local particle deposition hot-spots is due to two mechanisms: the rotational motion of near-wall vortices (i) increases the convective particle transport to the wall (contribution from resolved scales) and (ii) induces an added turbulent diffusion (contribution from unresolved scales)

4 Conclusions

The present LES predictions were in good agreement with PIV measurements and superior to RANS simulations in the same UAM. We further revealed that

vortical flow structures determine the location and shape of deposition hot-spots in the different compartments of the UAM.

Since the UAM showed all physiologically relevant features, we claim that the aforementioned regions (tongue, hard- and soft palate, posterior side of the pharynx, larynx) are prone to an increased particle deposition and independent of minor patient-specific topological variations.

Acknowledgements. This work was funded by the Concerted Research Action (GOA) ASiLung.

References

1. Oberdörster, G., Oberdörster, E., Oberdörster, J.: Nanotoxicology: An Emerging Discipline Evolving from Studies of Ultrafine Particles. Environmental Health Perspectives 113, 823–839 (2005)
2. Kleinstreuer, C., Zhang, Z.: Airflow and Particle Transport in the Human Respiratory System. Annu. Rev. Fluid Mech. 42, 301–334 (2010)
3. Jayaraju, S., Brouns, M., Lacor, C., Belkassem, B., Verbanck, S.: Large eddy and detached eddy simulations of fluid flow and particle deposition in a human mouth-throat. J. Aerosol Sci. 39, 862–875 (2008)
4. Einstein, A.: Über die von der molekularkinetischen Theorie der Wärme geförderte Bewegung von in ruhenden Flüssigkeiten suspendierten Teilchen. Annalen der Physik 1, 549–560 (1905)
5. Allen, M.D., Raabe, O.G.: Slip Correction Measurements of Spherical Solid Aerosol Particles in an Improved Millikan Apparatus. Aerosol Sci. Technol. 4, 269–286 (1985)
6. Cabot, W., Moin, P.: Large Eddy Simulation of Scalar Transport with the Dynamic Subgrid-Scale Model. In: Galperin, B., Orszag, S.A. (eds.) Large Eddy Simulation of Complex Engineering and Geophysical Flows, pp. 141–158. Cambride University Press, Cambridge (1993)
7. Weller, H.G., Tabor, G., Jasak, H., Fureby, C.: A tensorial approach to computational continuum mechanics using object oriented techniques. Computers in Physics 12, 620–631 (1998)
8. Shaw, D.A., Hanratty, T.J.: Turbulent mass transfer rates to a wall for large Schmidt numbers. AIChE J. 23, 28–37 (1977)
9. Krause, F., Wenk, A., Lacor, C., Kreyling, W.G., Möller, W., Verbanck, S.: Numerical and experimental study on the deposition of nanoparticles in an extrathoracic oral airway model. J. Aerosol Sci. 57, 131–143 (2013)
10. Balashazy, I., Hofmann, W., Heistracher, T.: Computation of local enhancement factors for the quantification of particle deposition patterns in airway bifurcations. J. Aerosol Sci. 30, 185–203 (1999)

Probability Distribution of Intrinsic Filtering Errors in Lagrangian Particle Tracking in LES Flow Fields

M.V. Salvetti, S. Chibbaro, M. Tesone, C. Marchioli, and Alfredo Soldati

1 Introduction

The dispersion of small inertial particles in inhomogeneous turbulent flows is important in a number of industrial applications and environmental phenomena, such as, for instance, mixing, combustion, depulveration, spray dynamics, pollutant dispersion or cloud dynamics. Direct Numerical Simulations (DNS) of turbulence coupled with Lagrangian Particle Tracking (LPT) have demonstrated their capability to capture the mechanisms characterizing particle dynamics in turbulent flows (see e.g. [1]). Due to the computational requirements of DNS, however, analysis of problems characterized by complex geometries and high Reynolds numbers demands alternative approaches; Large-Eddy Simulation (LES) is increasingly gaining in popularity, especially for cases where the large flow scales control particle motion. LES is based on a filtering approach of the fluid phase governing equations, in which the unresolved Sub-Grid Scales (SGS) of turbulence are modeled.

A major issue associated with LES of particle-laden flows is modeling the effect of these scales on particle dynamics. Recent studies on particle dispersion in wall-bounded turbulence (see, e.g., [2, 3]) have shown that use of the filtered fluid velocity in the equation of particle motion with no model for the effect of the SGS fluid velocity fluctuations leads to significant underestimation of preferential

M.V. Salvetti · M. Tesone
DICI, Università di Pisa, Italy
e-mail: mv.salvetti@ing.unipi.it

S. Chibbaro
Institut Jean Le Rond D'Alembert,
University Pierre et Marie Curie, France and CNRS, UMR 7190, France
e-mail: chibbaro@lmm.jussieu.fr

C. Marchioli · A. Soldati
Dip. Matematica e Informatica and Centro Interdipartimentale di
Fluidodinamica e Idraulica, Università di Udine, Italy
e-mail: marchioli,soldati@uniud.it

M.O. Deville et al. (eds.), *Turbulence and Interactions*,
Notes on Numerical Fluid Mechanics and Multidisciplinary Design 125,
DOI: 10.1007/978-3-662-43489-5_18,

concentration and, consequently, to weaker deposition fluxes and lower near-wall accumulation. Different techniques have been used to reintroduce in the particle motion equations the fluid velocity fluctuations eliminated by filtering (see, e.g., [4]-[8]), but, although some improvements have been obtained especially with filtering inversion or approximate deconvolution, this did not guarantee an accurate quantitative prediction of particle preferential concentration and near wall accumulation.

In order to devise efficient SGS models for LPT, the quantification and the analysis of the errors present in LPT in LES flow fields is clearly a necessary step. In a previous work [9], we focused on the error purely due to filtering of the fluid velocity field seen by the particles, for which we quantified a lower bound. To this aim, we used a DNS database of inertial particle dispersion in turbulent channel flow and we performed *a priori* tests in which the error purely due to filtering was singled out by removing error accumulation effects, which would otherwise lead to progressive divergence between DNS and LES particle trajectories. In those tests, particles in DNS were initially randomly distributed and a joint analysis of the Eulerian higher-order statistical moments and of the probability distribution functions of the filtering error was carried out. This analysis emphasized the stochastic nature of the filtering error. Moreover, the error behavior was found to be intermittent and strongly affected by flow anisotropy. The results in [9], therefore, suggested the possibility to correct this error by a generalized stochastic Lagrangian model [10, 11] in which the statistical *signature* of coherent turbulent structures (e.g. low-speed streaks, sweeps and ejections) on particle dynamics is accounted for explicitly. In our opinion, the most promising way to model these effects would be through a statistical Lagrangian description of the relevant geometrical features of turbulence in the near-wall region, where preferential concentration and accumulation are controlled by structures like sweeps and ejections[11, 12, 13]. We refer to [9] for a more detailed description of the general form of the proposed model. The first necessary step is the characterization of the statistical properties (PDFs in particular) of the pure filtering error computed along the Lagrangian particle trajectories and conditioned to specific subsets of particles sampling prescribed topological regions of the flow. To this aim, in the present work, we repeat the same tests as in [9], but in DNS particles are initially released in regions sampling sweep or ejections events. Moreover, the statistical properties of the particle dynamics in DNS and of the pure filtering error are characterized from a Lagrangian viewpoint along the particle trajectories.

2 Methodology

The reference flow configuration consists of two infinite flat parallel walls: the origin of the coordinate system is located at the center of the channel and the $x-$, $y-$ and $z-$ axes point in the streamwise, spanwise and wall-normal directions respectively. Periodic boundary conditions are imposed on the fluid velocity field in x and y, no-slip boundary conditions are imposed at the walls. The flow is driven by a mean

pressure gradient, and the shear Reynolds number is $Re_\tau = u_\tau h/\nu = 150$, based on the shear (or friction) velocity, u_τ, and on the half channel height, h. The shear velocity is defined as $u_\tau = (\tau_w/\rho)^{1/2}$, where τ_w is the mean shear stress at the wall and ρ the fluid density.

The velocity flow field is obtained using a pseudo-spectral Fourier-Chebyshev DNS flow solver for the space discretization of the governing equations (Continuity and Navier-Stokes for incompressible flow). A two level, explicit Adams-Bashforth scheme for the non-linear terms, and an implicit Crank-Nicolson method for the viscous terms are employed for time advancement. Further details of the method can be found in previous articles (e.g. [14]). Calculations were performed on a computational domain of size $L_x \times L_y \times L_z = 4\pi h \times 2\pi h \times 2h$ in x, y and z respectively, discretized in physical space with $N_x \times N_y \times N_z = 128 \times 128 \times 129$ grid points (corresponding to 128×128 Fourier modes and to 129 Chebyshev coefficients in the wavenumber space).

Particles are modeled as pointwise, non-rotating rigid spheres; they are much heavier than the carrier fluid ($\rho_p/\rho \simeq 769$, ρ_p being the particle density) and are injected into the flow at concentration low enough to consider dilute system conditions (no inter-particle collisions) and one-way coupling between the two phases (no turbulence modulation by particles). The motion of particles is described by the following set of ordinary differential equations for particle velocity and position:

$$\frac{d\mathbf{x}_p}{dt} = \mathbf{v}_p \ , \ \frac{d\mathbf{v}_p}{dt} = \frac{\mathbf{u}_s - \mathbf{v}_p}{\tau_p}(1 + 0.15Re_p^{0.687}) \ . \tag{1}$$

In Eqns. (1), $\mathbf{x}_p$ is particle position, $\mathbf{v}_p$ is particle velocity, $\mathbf{u}_s = \mathbf{u}(\mathbf{x}_p(t),t)$ is the fluid velocity at the particle position. $\tau_p = \rho_p d_p^2/18\mu$ is the particle relaxation time, and $Re_p = d_p|\mathbf{v}_p - \mathbf{u}_s|\rho/\mu$ is the particle Reynolds number, d_p and μ being the particle diameter and the fluid dynamic viscosity respectively.

To calculate particle trajectories a Lagrangian tracking routine is coupled to the flow solver. The routine solves for Eqns. (1) using a 4^{th}-order Runge-Kutta scheme for time advancement and 6^{th}-order Lagrangian Polynomials for fluid velocity interpolation at the particle location. Periodic boundary conditions are imposed on particles moving outside the computational domain in the homogeneous directions, perfectly-elastic collisions at the smooth walls are assumed when the particle center is at a distance lower than one particle radius from the wall. For the simulations presented here, particles characterized by different response times, are considered. When the particle response time is made dimensionless using wall variables, the Stokes number for each particle set is obtained as $St = \tau_p/\tau_f$ where $\tau_f = \nu/u_\tau^2$ is the viscous timescale of the flow. Three different sets of particles corresponding to values of the Stokes number $St = 1$, 5 and 25 have been considered. These values were selected based on previous studies of particle preferential concentration in turbulent channel flow at the same Reynolds number considered here, in which it was shown that maximum segregation and preferential concentration occurs for particles having $St = 25$. The two smaller values, $St = 1$ and $St = 5$, were thus chosen

to highlight trends in the behavior of the filtering error as preferential concentration effects become weaker. We refer to [9] for a more complete description of the physical parameters characteristic of the considered particle sets.

In the *a priori* tests, LPT is carried out replacing $\mathbf{u}_s$ in Eq. (1) with the filtered fluid velocity field, $\bar{\mathbf{u}}(\mathbf{x_p},t)$. This field is obtained through explicit filtering of the DNS velocity by either a cut-off filter or a top-hat filter. Both filters are applied in the wave number space in the homogeneous streamwise and spanwise directions. Three different filter widths are considered, which provide CF= 2, 4 and 8 with respect to DNS, corresponding to 64×64, 32×32 and 16×16 Fourier modes respectively. Data are not filtered in the wall-normal direction, since the wall-normal resolution in LES is often DNS-like.

The pure filtering error is computed under the ideal assumption that all further sources of error affecting particle tracking in LES can be disregarded and that the exact dynamics of the resolved velocity field is available. Errors due to the SGS model for the fluid and to numerics are thus neglected and a lower bound for the filtering error is identified by removing error accumulation effects due to progressive divergence between DNS and LES particle trajectories. Time accumulation of the pure filtering error is prevented by computing particle trajectories in DNS fields and then forcing particles to evolve in filtered DNS fields along the DNS trajectories. At each time step n and for each particle k we thus impose:

$$\mathbf{x}_{p,k}^{f-DNS}(t^n) = \mathbf{x}_{p,k}^{DNS}(t^n) \equiv \mathbf{x}_{p,k}(t^n) \;\; ; \;\; \mathbf{v}_{p,k}^{f-DNS}(t^n) = \mathbf{v}_{p,k}^{DNS}(t^n) \equiv \mathbf{v}_{p,k}(t^n) \;\; , \qquad (2)$$

where superscripts $f-DNS$ and DNS identify particle position and velocity in filtered DNS (i.e. *a priori* LES) and in DNS, respectively. The pure filtering error made on the k-th particle at time t^n is computed as:

$$\delta\mathbf{u} \equiv \delta\mathbf{u}(\mathbf{x}_{p,k}(t^n),t^n) = \mathbf{u}(\mathbf{x}_{p,k}(t^n),t^n) - \bar{\mathbf{u}}(\mathbf{x}_{p,k}(t^n),t^n) \equiv \mathbf{u}_s - \bar{\mathbf{u}}_s \;\; . \qquad (3)$$

This error is made non-dimensional using the shear velocity: $\delta\mathbf{u}^+ = \delta\mathbf{u}/u_\tau$. Eq. (3) is thus used to quantify the error affecting the fluid velocity seen by the particles in an idealized situation which serves the purpose of isolating the contribution due to filtering of the velocity field to the total error associated with LPT in LES. We recall that $\delta\mathbf{u}$ is computed along the "exact" trajectory of each particle, that is at $\mathbf{x}_{p,k}^{DNS}(t^n)$.

3 Results and Discussion

Two different types of tests are carried out, starting by tracking in DNS velocity fields particles which are initially released in regions characterized by sweep and ejection events respectively. In order to identify these regions, the same criterion as in [15] was used, i.e. the sign of the fluid Reynolds stress component $|u'|w'$ was analyzed on five horizontal planes in the near wall region (at $z^+ = 4,6,8,10,12$).

An event is recorded at a given point when at least on four of the five considered planes $|u'|w'$ has the same sign. In the instantaneous flow field used as initial condition for LPT, ten regions characterized by sweep events are detected, as well as ten ejection zones. As previously mentioned, two sets of initial conditions were considered for LPT in DNS flow fields; in the first one, 10000 particles are released in each sweep region on the plane at $z^+ = 8$, while in the second one 10000 particles are released in each ejection zone on the same plane. In all cases the initial particle velocity is the same as that of the fluid at the particle location. For each type of boundary conditions, three sets of particles having $St = 1, 5, 25$ respectively, are tracked. Statistics are computed along the trajectories of all the particles belonging to each considered set.

The dynamics of each set of particles in DNS has been characterized in terms of Lagrangian pdf of the particle position and velocity and of the fluid velocity seen by the particles. This analysis is not reported here for the sake of brevity. As an example, in Figure 1 the pdfs of the wall-normal position computed at $t^+ = 182$ for the particles initially seeded in sweep and ejection regions are reported, together with that obtained at the same instant for particles initially uniformly distributed on the horizontal plane at $z^+ = 5$; all the plots refer to particles having $St = 25$. The probabilistic results assess the criterion chosen to disentangle different structures. As expected, particles released in a sweep structure tend to remain trapped near-to-the-wall, whereas particles transported by the ejections are efficiently dispersed in the center of the channel. Neutral regions appear to be naturally in the middle amidst the two. This is in line with the present understanding of particle deposition onto walls, whose mechanism seems dominated by these features [15].

As for the filtering error, computation and statistical characterization of $\delta\mathbf{u}$ were carried out by applying filters of different type and width for all the considered

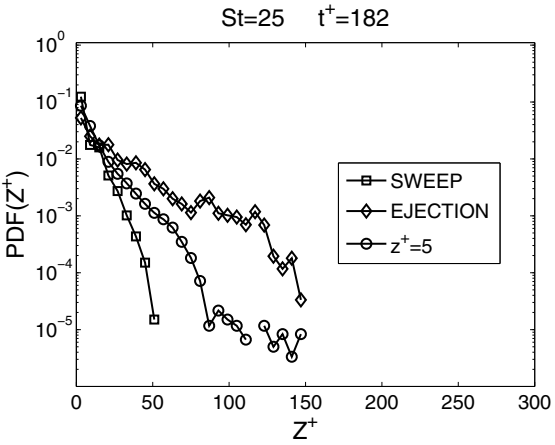

Fig. 1 Comparison of particle position PDF for particles released in sweep environments, ejection regions and at $z^+ = 5$. Profiles refer to St=25 and they are evaluated at $t^+ = 182$.

particle sets. Due to length limitations, we report herein only the results obtained with the cut-off filter and CF=4. In figure 2, we show the conditional pdfs of the pure filtering error computed initially imposing particles in sweeps, whereas in 3 we show the pdf conditioned on ejections. From the comparison some remarks are in order. (i) Lagrangian results confirm Eulerian ones [9], showing that the characteristic filtering error of LES in non-homogeneous flows is clearly stochastic and non-Gaussian. However, Lagrangian statistics appear better approximated by a normal function than Eulerian ones. (ii) In particular in the short time, the structures (mostly ejections) seem to show a strong subgrid anisotropic effect only in the z-direction. This feature underlines the link between coherent structures and strain. (iii)In the long-time limit, as expected, the Lagrangian conditional pdfs recover the Eulerian behavior. (iv)The effect of the Stokes number is very limited.

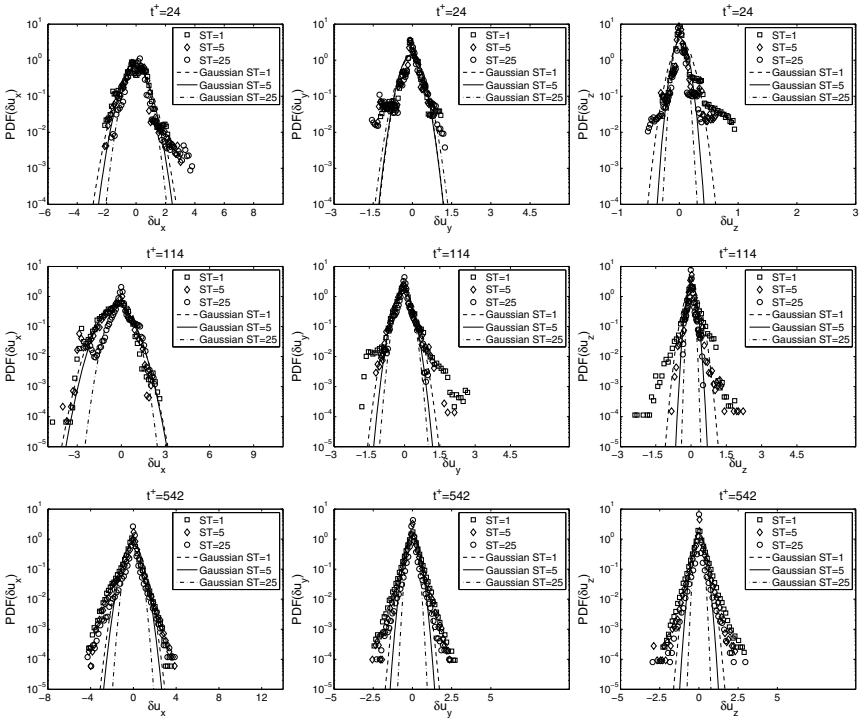

Fig. 2 Probability density function of the filtering error δu for different Stokes number compared with the corresponding Gaussian evaluated for the particles initially released in sweeps at $t^+ = 24, 114, 542$ and at $z^+ = 8$ (cut-off filter and CF=4). Left: streamwise component; middle: spanwise component; right: wall-normal component. The corresponding Gaussian distributions are also reported.

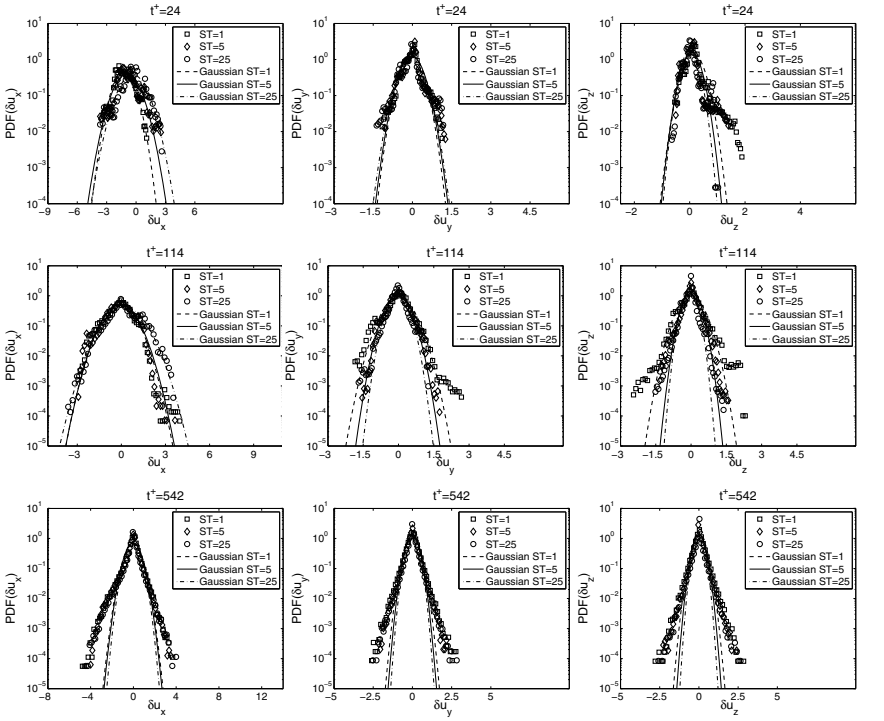

Fig. 3 Probability density function of the filtering error δu for different Stokes number compared with the corresponding Gaussian evaluated for the particles initially released in ejections at $t^+ = 24, 114, 542$ and at $z^+ = 8$ (cut-off filter and CF=4). Left: streamwise component; middle: spanwise component; right: wall-normal component. The corresponding Gaussian distributions are also reported.

4 Concluding Remarks

In this work, we have analyzed some statistics of the pure filtering error in LPT in filtered DNS flow fields. In particular we have studied the Lagrangian pdfs of this error obtained for different initial particle distributions. The initial conditions are chosen such as to trap particles initially in different coherent structures, namely sweeps and ejections, which are thought to play a major role in preferential concentration. Preliminary results are presented which point out two important conclusions: Lagrangian statistics are in principle different from Eulerian ones and may offer new insights for the physical modelling. For this reason, they should be investigated in more details. Present results also suggest the possibility to model coherent structures with a direct link to velocity gradients.

References

1. Soldati, A., Marchioli, C.: Physics and modelling of turbulent particle deposition and entrainment: review of a systematic study. Int. J. Multiphase Flow 20, 827 (2009)
2. Kuerten, J.G.M., Vreman, A.W.: Can turbophoresis be predicted by large-eddy simulation? Phys. Fluids 17, 011701 (2005)
3. Marchioli, C., Salvetti, M.V., Soldati, A.: Some issues concerning large-eddy simulation of inertial particle dispersion in turbulent bounded flows. Phys. Fluids 20, 040603-1 (2008)
4. Kuerten, J.G.M.: Subgrid modeling in particle-laden channel flow. Phys. Fluids 18, 025108 (2006)
5. Marchioli, C., Salvetti, M.V., Soldati, A.: Appraisal of energy recovering sub-grid scale models for large-eddy simulation of turbulent dispersed flows. Acta Mech. 201(1-4), 277 (2008)
6. Gobert, C.: Analytical assessment of models for large eddy simulation of particle laden flow. J. Turbulence 11, 1 (2010)
7. Shotorban, B., Mashayek, F.: A stochastic model for particle motion in large-eddy simulation. J. Turbulence 7, N18 (2006)
8. Khan, M.A.I., Luo, X.Y., Nicolleau, F.C.G.A., Tucker, P.G., Lo Iacono, G.: Effects of LES sub-grid flow structure on particle deposition in a plane channel with a ribbed wall. Int. J. Num. Meth. Biomed. Eng. 26, 999 (2010)
9. Bianco, F., Chibbaro, S., Marchioli, C., Salvetti, M.V., Soldati, A.: Intrinsic filtering errors of Lagrangian particle tracking in LES flow fields. Phys. Fluids 24, 045103-1 (2012)
10. Pope, S.B.: Turbulent Flows. Cambridge University Press, Cambridge (2000)
11. Minier, J.P., Peirano, E.: The PDF approach to polydispersed turbulent two-phase flows. Physics Reports 352, 1 (2001)
12. Minier, J.P., Peirano, E., Chibbaro, S.: PDF model based on Langevin equation for polydispersed two-phase flows applied to a bluff-body gas-solid flow. Phys. Fluids 16, 2419 (2004)
13. Peirano, E., Chibbaro, S., Pozorski, J., Minier, J.P.: Mean-Field/PDF Numerical approach for polydispersed turbulent two-phase flows. Progress in Energy and Combustion Sciences 32, 315 (2006)
14. Pan, Y., Banerjee, S.: Numerical simulation of particle interactions with wall turbulence. Phys. Fluids 17, 2733 (1996)
15. Marchioli, C., Soldati, A.: Mechanism for particle transfer and segregation in a turbulent boundary layer. J. Fluid Mech. 468, 283 (2002)

Temperature Oscillations in Turbulent Mixed Convective Air Flows

D. Schmeling, J. Bosbach and Claus Wagner

Abstract. We report on measurements of temperature oscillations observed in turbulent mixed convection in a rectangular enclosure. They are correlated to fluctuations and spontaneous reorientations of the large-scale circulations in the flow. Stable temperature configurations, periodic reconfigurations as well as spontaneous reversals and reorientations were detected. We ascribe the observed dynamics of the large-scale flow to the interaction between the superimposed shear forces of the forced convective flow and the buoyancy driven flow. Comparison with smoke visualisations allowed to assign the observed temperature distributions to a certain number and configuration of convection rolls. A frequency analysis of the oscillations as a function of the characteristic numbers is conducted revealing a sophisticated dependency of the dynamics of the large-scale flow on Ar, Re or Ra.

1 Introduction

Mixed convection (MC) denotes a flow in which forced convection, caused by inertia forces, and thermal convection, initiated by buoyancy forces, are of the same order of magnitude. In MC, the Archimedes number $Ar = Ra \times Re^{-2} \times Pr^{-1}$ serves as a measure for the ratio between thermal and inertia forces. Here, Ra denotes the Rayleigh number with the height of the cell H and the temperature difference ΔT between bottom and ceiling as characteristic length and temperature difference, respectively. For the Reynolds number Re, the mean inflow velocity u and again the height of the cell serve as characteristic values while the Prandtl number Pr merely depends on the fluid material properties.

Previous investigations of the flow in the rectangular convection cell addressed structure formation, heat transport and low-frequency oscillations [1, 2, 3]. Thereby, temperature oscillations in the out-flowing air, the arrangement of large-scale circulations (LSCs) and oscillations of time development coefficients of Proper Orthog-

D. Schmeling · J. Bosbach · Claus Wagner
German Aerospace Center (DLR),
Institute of Aerodynamics and Flow Technology, Bunsenstraße 10, D-37073 Göttingen
e-mail: {daniel.schmeling,johannes.bosbach,claus.wagner}@dlr.de

M.O. Deville et al. (eds.), *Turbulence and Interactions*,
Notes on Numerical Fluid Mechanics and Multidisciplinary Design 125,
DOI: 10.1007/978-3-662-43489-5_19,

onal Decomposition modes of the velocity fields were analysed. The details of the underlying dynamics of the LSCs, which govern these effects, however, are still open issues. In pure Rayleigh-Bénard convection (RBC) in a similar rectangular cell with aspect ratio five, the arrangement and the dynamics of the LSCs [4] were studied for $10^7 < Ra < 10^{10}$ by means of Large Eddy Simulations (LES). In their study they observed two, three and four roll configurations. Dynamical effects like cessations or spontaneous reorientations of the LSC are well known from turbulent RBC in cylindrical geometries [5]. Thereby, the aspect ratio strongly affects the azimuthal motion, reorientation, cessation and reversals of the LSC [6]. Besides the detailed studies on the dynamics of the LSCs in pure RBC, little is known about the effects in systems for which thermally induced LSCs are interacting with externally driven shear flows.

2 Experimental Set-Up and Measurement Techniques

All investigations presented below were conducted in a rectangular convection cell with a length of $L = 2500\,\text{mm}$ and aspect ratios of $\Gamma_{xz} = L/H = 5$ and $\Gamma_{yz} = W/H = 1$, see Fig. 1. In order to accomplish nearly isothermal boundary conditions the heating device at the bottom consists of five separated sub-plates, each of them being actively heated via a temperature controlled water circuit. The ceiling is passively cooled close to ambient temperature via an air-air heat exchanger. This configuration provides isothermal boundary conditions at the bottom and ceiling with maximal spatial temperature deviations smaller than $\pm 0.3\,\text{K}$. All side walls consist of double glazing polycarbonate plates with a 5 mm air gap and an additional 100 mm polystyrene insulation, in order to minimise heat losses through the side walls. The air inflow is supplied through a slot below the ceiling, while exhausting is provided

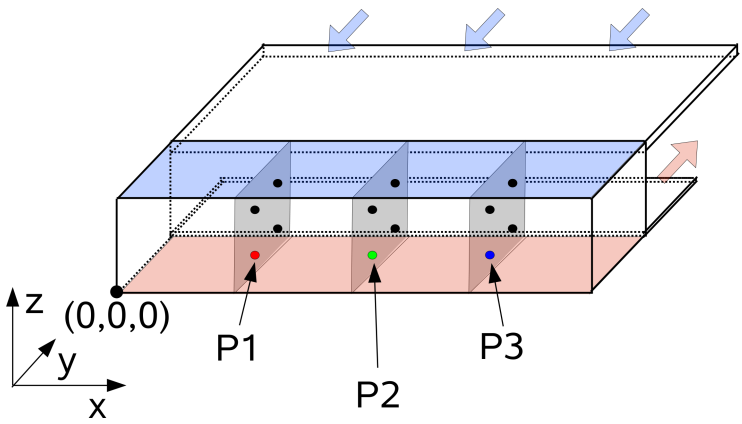

Fig. 1 Sketch of the convection cell. The bottom of the cell is heatable (red) while the ceiling is kept at ambient temperature (blue). Inflow (blue arrows) and outflow (red arrows) channel are located at the same side and span the whole length of the cell. Black dots mark the positions of the PT-100 sensors within the cell.

by another slot above the floor. Both vents extend over the whole length of the cell. The working fluid is air at ambient pressure ($Pr = 0.71$). The measurements were conducted using twelve PT-100 temperature sensors placed within the cell and another 86 PT-100 sensors for control reasons, e.g. in the cooling plate or the heating plate. Furthermore, the inflow velocity was monitored by controlling and measuring the volume flow rate during the experiment.

3 Results

We studied mixed convection in a range of $0.5 < Ar < 6.9$ under variation of ΔT and u. It should be noted, that the heating system of the cell was running the whole time and that prior to each measurement the flow was allowed to stabilise for at least one hour after stable Re and Ra were reached.

Figure 2 presents the result of a "stair-measurement" in which the inflow velocity was abruptly decreased in constant steps of $2.7\,\mathrm{cm}\cdot\mathrm{s}^{-1}$ every hour starting with $34.7\,\mathrm{cm}\cdot\mathrm{s}^{-1}$. This resulted in a stepwise change of Re in the range $1.1\times10^4 > Re > 0.7\times10^4$ while Ra was kept constant at $Ra \cong 1.1\times10^8$. Consequently, Ar was increased in turn stepwise from $Ar \cong 1.3$ to $Ar \cong 3.1$ at the same time.

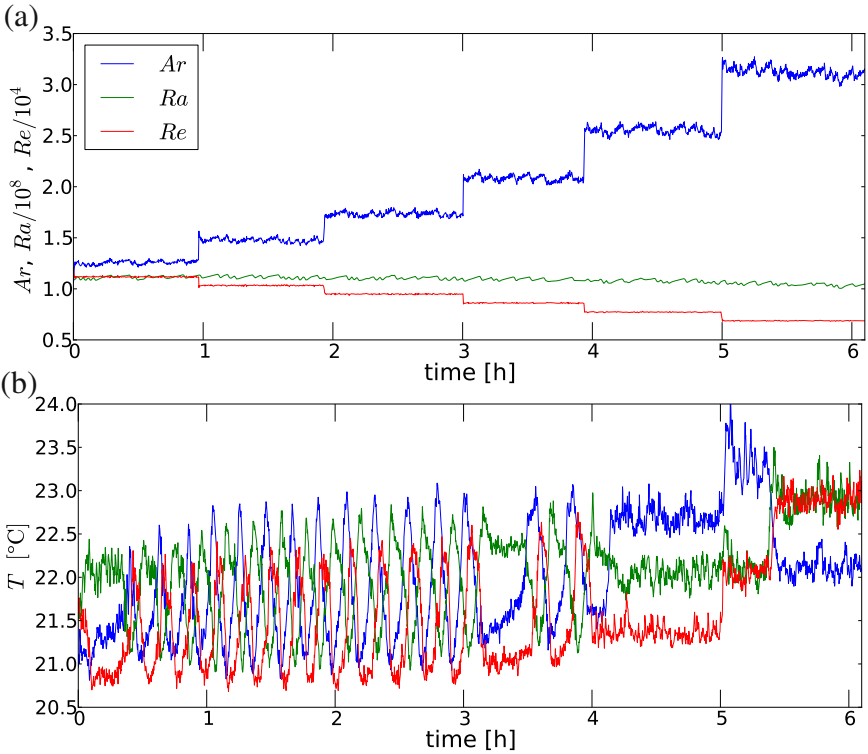

Fig. 2 "Stair-measurement". (a) Time series of Re (red), Ra (green) and Ar (blue). (b) Temperature time series at P1 (red), P2 (green) and P3 (blue), see Fig. 1.

The resulting time series of the characteristic numbers are depicted in Fig. 2 (a), while Fig. 2 (b) shows the temperature time series of three selected sensors at $X/L = 0.25\,(P1)$, $0.50\,(P2)$ and $0.75\,(P3)$ at the same $Y/W = 0.25$ and $Z/H = 0.20$. At the beginning of the measurement, i.e. for the highest *Re*, we found a stable configuration with warm air in the middle (P2) and cold air at one and three quarters of the cell (P1 and P3). This points to an arrangement of four convection rolls in the cell with warm air rising in the centre and at the sides as well as cold air falling in between. These convection rolls are superimposed on the forced mean flow, which leads to a non-uniform temperature distribution in a layer parallel to the bottom plate (not shown here for the sake of brevity). Warm air rises in the rear part of the cell whereas cold air descents close to the front wall. After approximately half an hour the temperatures start to oscillate with a frequency of $f \cong 1.2 \times 10^{-3}$Hz. Barely visible is that the frequency is slightly influenced by the change of Ar from $Ar \cong 1.3$ to $Ar \cong 1.5$ and $Ar \cong 1.7$. An interesting point of this oscillation is that the centre (P2) region is the warmest for a few minutes, then suddenly cools down and meanwhile first at P3 and shortly afterwards at P1 the temperature increases strongly. The configuration with the cold air in the centre and warmest regions at one and three-quarters of the cell point to an inverted configuration to the firstly observed stable one.

Upon the further increase of Ar the oscillations suddenly disappear at $Ar \cong 2.1$ until they start again after half an hour at the same Ar and finally stop completely upon the next increase to $Ar \cong 2.6$. At this Ar, the temperature field reflects warm air at P3, cold air at P1 and an intermediate temperature at P2. This temperature configuration points to the alignment of three large-scale convection rolls with rising warm air at $X \approx 0$ and $0.66 \times L$ and falling cold air at $X \approx 0.33$ and $1 \times L$. Combined smoke visualisations confirmed the existence of such a three-roll-configuration. After increasing Ar to the highest investigated value of $Ar \cong 3.1$ another reorientation occurs, which we interpret as a short-circuit flow condition. The sudden increase of the mean cell temperature as well as a negative temperature gradient in y-direction indicate this. Inertia forces are now so small that the incoming air jet is not able to follow the ceiling, but descends directly towards the air outlet. Additionally, after approximately 30 minutes this state undergoes a spontaneous flow reversal as indicated by the temperature signals at P1, P2 and P3.

In this experiment the stepwise decrease of the inflow velocity, rather than a continuous one has been chosen mainly by experimental circumstances. Nevertheless, the changes in the topology result rather from a natural transition than the abrupt change of *Re*, because the same topologies were detected in long time measurements with constant characteristic numbers as well. Furthermore, the step size was just of the order of 10% and additionally, we performed a measurement with the same mean gradient, but a by a factor of five smaller step size. Again, periodic oscillations were found over a wide characteristic number range framed from some steady states.

Besides the "stair-measurement", other measurements were conducted under steady inflow and thermal boundary conditions. Figure 3 (a) and (b) show detailed views of temperature time series at two different Ar at constant $Ra \cong 1.1 \times 10^8$.

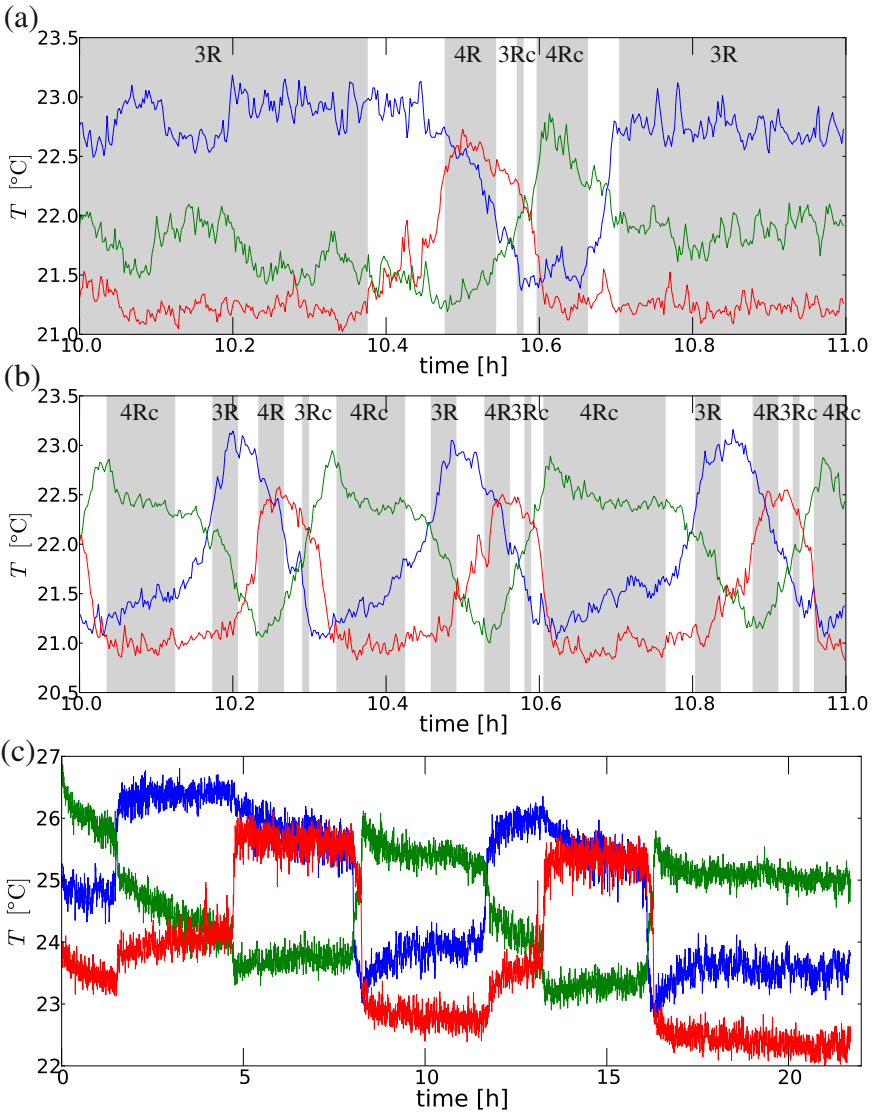

Fig. 3 Temperature time series, P1 (red), P2 (green) and P3 (blue). One hour detail views (beginning at the measurement time of 10 h) at $Ra \cong 1.1 \times 10^8$ (a) $Re \cong 0.8 \times 10^4$ ($Ar \cong 2.3$) and (b) $Re \cong 0.9 \times 10^4$ ($Ar \cong 1.9$). (c) Full 22 hours temperature series at $Re \cong 1.4 \times 10^4$, $Ra \cong 2.0 \times 10^8$ and $Ar \cong 1.6$.

Again, three different dynamics are found. A stable temperature distribution (not shown here for the sake of brevity), a stable three roll configuration (3R) with a suddenly occurring change to four (4R), three counter rotating (3Rc), four counter rotating (4Rc) and back to the original three rolls (Fig. 3, a) as well as periodic oscillations (Fig. 3, b) are observed. An interesting fact is that the transition of the

large-scale flow configuration seems to be the same for the spontaneously occurring (Fig. 3, a) case and the periodic (Fig. 3, b) one. The temperature decreases at P3 and simultaneously increases at P1. After approximately 200 s the temperature decreases at P1 to its initial value, while it rises at P2 and stays constantly low at P3. Approximately $200 - 400$ s later all temperatures return to their initial values. We think, that the underlying motion of the large-scale circulation is a shift of the roll configuration in the longitudinal cell direction (x). Resulting in a change of the number and the rotation direction of the large-scale convection rolls from three rolls (3R) to four rolls (4R) to three counter rotating rolls (3Rc) to four counter rotation rolls (4Rc) and back to the initial three roll configuration (3R) (see Fig. 3, a and b).

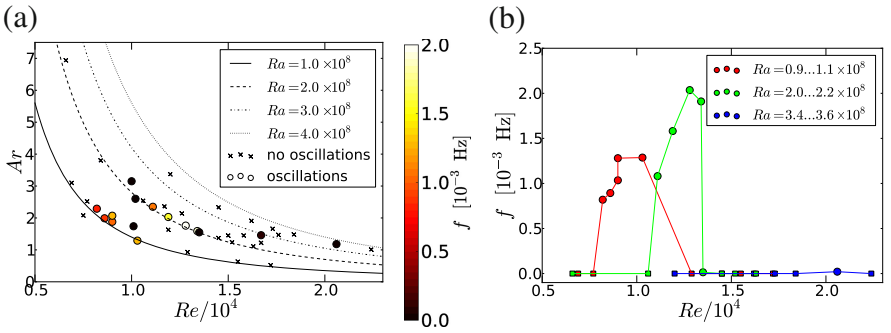

Fig. 4 (a) Observed frequencies in the temperature time series in the (Ar, Re) parameter space, lines indicate constant Ra: Crosses mark cases with no periodic oscillations, while the colour of the circles is scaled with the value of the main frequency. (b) Main frequency as a function of Re with Ra colour coded. Squares: no oscillations, circles: oscillations were detected.

Temperature time series were analysed using fast Fourier transform and a peak detection algorithm in order to determine the characteristic frequency. Figure 4 (a) shows the dependency of the found oscillation frequencies as a function of Re and Ar. The lines indicate constant Ra. All marks depict a measured parameter combination. Crosses mark cases for which stable temperatures were found. Circles indicate cases with oscillations of the temperatures, thereby the colour of the circles is scaled by the value of the main frequency. So far, we did not find a simple dependency of the flow state on the characteristic numbers, which describes whether oscillations will occur, neither on Ar, Re, Ra nor the Grashof number Gr (which is proportional to Ra). Nevertheless, some statements restricting the degree of freedom of the occurrence of oscillations can be made. First, the smaller Re and the smaller Ra the higher is the possibility for the occurrence of oscillations. Second, for a given (and not too high) Ra, oscillations occur only in an intermediate regime of Ar (Re), neither at too high nor at too low values. Third, with increasing Ra oscillations occur at higher Re (Ar) and have higher frequencies (see Fig. 4, b).

Furthermore, we found some very low frequencies, e.g. $f \cong 2.0 \times 10^{-5}$ Hz at $Ra \cong 2.0 \times 10^8$, $Re \cong 1.4 \times 10^4$ and $Ar \cong 1.6$, meaning that there were just two complete oscillations during a measurement time of almost 22 h, see Fig. 3 (c). As

opposed to the dynamics observed in Fig. 3 (a) and (b) complete reversals of the rotation direction as well as a change of the number of convection rolls occurred for this parameter configuration.

Sergent and Le Quéré [4] found in Rayleigh-Bénard convection the existence of two, three or four convection rolls as a function of time as well as reversals of their rotation directions, but no fast oscillations as depicted in Fig. 3 (b). We ascribe the occurrence of the oscillations to the interaction between the superimposed shear forces of the forced convective flow to the buoyancy driven flow.

Ongoing measurements with more sensors revealed for $Ra \cong 2 \times 10^8$ ($1.3 < Ar < 2.3$ and $1.1 \times 10^4 < Re < 1.5 \times 10^4$) that the oscillations are a continuous sequence with four, three, four counter rotating and three counter rotating convection rolls within the cell.

4 Conclusion

Temperature oscillations, which we observed during experiments in turbulent mixed convection in a rectangular enclosure, were analysed. These temperature fluctuations are ascribed to oscillations and spontaneous reorientations of the large-scale circulations in the flow. Stable temperature configurations, periodic oscillations as well as spontaneous reversals and reorientations were detected. So far, we could not find a simple dependency on the characteristic numbers (*Ar*, *Re* and *Ra*) which describes whether oscillations will occur. But we can state the following: The smaller *Re* and the smaller *Ra* the higher is the possibility for the occurrence of oscillations. Furthermore, with increasing *Ra*, oscillations occur at higher *Re* (*Ar*) and have higher frequencies. Due to the fact that the occurrence of the oscillations and the spontaneous reorientations of the large-scale flow depend on both *Re* and *Ra*, we ascribe them to the interaction between the superimposed shear forces of the forced convective flow to the buoyancy driven flow.

Measurements with more sensors as well as combined temperature and velocity measurements are currently performed and are expected to shed more light on the observed processes.

References

1. Kühn, M., Ehrenfried, K., Bosbach, J., Wagner, C.: Exp. Fluids 50, 929 (2011)
2. Schmeling, D., Westhoff, A., Kühn, M., Bosbach, J., Wagner, C.: Int. J. Heat Fluid Flow 32, 889 (2011)
3. Westhoff, A., Bosbach, J., Schmeling, D., Wagner, C.: Int. J. Heat Fluid Flow 31, 794 (2010)
4. Sergent, A., Quéré, P.L.: 13th European Turbulence Conference, Warswa, Poland (2011)
5. Brown, E., Ahlers, G.: J. Fluid Mech. 568, 351 (2006)
6. Xi, H.D., Xia, K.Q.: Phys. Rev. E 78, 036326 (2008)

A Phase-Conditioned Filtering of Incompressible Interfacial Multiphase Flow Equations: *A Priori* Study for the Modeling of LES Subgrid Scale Terms

P. Trontin*, J.-L. Estivalezes, S. Vincent, and J.P. Caltagirone

Abstract. A priori analysis consists in deriving subgrid scale terms from the explicit filtering of a 3D Direct Numerical Simulation (DNS) database. It is a step in the development of subgrid scale models for Large Eddy Simulation (LES). The main issue for LES multiphase flows is the development of subgrid scale models well suited for two-phase interfacial flows. More particularly, coupling between turbulence and the interface separating both liquid and gas phases is not yet taken into account accurately by two-phase flow LES models. To improve the understanding of this coupling, DNS about a freely decaying homogeneous isotropic turbulence case in a periodic cubic box has been performed in a previous work. Two planar interfaces are added in the middle of the computational box separated by 5% of the length box. Two-phase interfacial flow simulations are carried out with an incompressible flow solver coupled to a ghost-fluid level-set front capturing method. A parametric study based on the surface tension coefficient has been performed. The aim of the work presented in this manuscript is to evaluate subgrid scale terms deriving from the explicit filtering of this DNS database. Classical central filter is not used, but rather a phase-conditioned filter to derive phase-filtered LES equations for separated two-phase flows. Three subgrid scale terms are obtained. The first one derives from the convective (classical) term. The two last ones derive from the phase-coupling terms and are related to the stress tensor jump across the interface. The magnitudes of the different subgrid scale terms are compared for different Weber numbers and for different filter sizes.

P. Trontin · J.-L. Estivalezes
Onera, The French Aerospace Lab, F-31055 Toulouse, France
e-mail: {pierre.trontin,jean-luc.estivalezes}@onera.fr

S. Vincent · J.P. Caltagirone
Université de Bordeaux, Institut de Mécanique et Ingénierie (I2M) - UMR 5295,
F-33400 Talence, France
e-mail: {svincent,calta}@enscbp.fr

* Corresponding author.

M.O. Deville et al. (eds.), *Turbulence and Interactions*,
Notes on Numerical Fluid Mechanics and Multidisciplinary Design 125,
DOI: 10.1007/978-3-662-43489-5_20,

1 Introduction

A priori analysis consists in deriving subgrid scale terms from the explicit filtering of a Direct Numerical Simulation (DNS) database. It is a step in the development of subgrid scale models for Large Eddy Simulation (LES). Literature about single phase flow LES models is widely detailed and, in the same way, applications for industrial concerns are increasingly widespread. State-of-the-art is different for two-phase interfacial flows involving non miscible fluids. Indeed, LES for multiphase flow still remains a challenging task and the main issue is the development of subgrid scale models well suited for two-phase interfacial flows. More particularly, coupling between turbulence and the interface separating both liquid and gas phases is not yet taken into account accurately by two-phase flow LES models. To improve the understanding of this coupling, DNS about a freely decaying homogeneous isotropic turbulence case in a periodic cubic box has been performed [1]. Two-phase interfacial flow simulations are carried out with an incompressible flow solver coupled to a ghost-fluid level-set interface capturing method [2]. The aim of the present work is to study subgrid scale (denoted as SGS hereafter) terms deriving from the *a priori* analysis of the resulting DNS database and to point out specific contributions deriving from interface/turbulence interactions. In a first part, the equations used in the present work are presented. Then, phase-conditioned filtering is introduced and equations deriving from the filtering of incompressible interfacial multiphase flow equations are written. In a second part, DNS database is presented and phase-conditioned filtering is applied on it. Results and analysis are discussed and finally conclusions are drawn.

2 Equations, Numerical Methods and Phase-Conditioned Filtering

2.1 Equations

As the simulation of liquid-gas flow at moderate velocities is performed, the incompressible Navier-Stokes equations are used. Interfacial multiphase flows involving immiscible phases are considered. They are modelled as follows:

$$\begin{aligned} \frac{\partial \mathbf{u}}{\partial t} + (\mathbf{u}\cdot\nabla)\mathbf{u} &= -\frac{1}{\rho}\nabla p + \frac{1}{\rho}\nabla\cdot\left(\mu(\nabla\mathbf{u} + {}^{T}\nabla\mathbf{u})\right) \\ \nabla\cdot\mathbf{u} &= 0 \end{aligned} \tag{1}$$

The boundary conditions at the interface between two immiscible fluids are the continuity of the velocity components:

$$[\mathbf{u}]_{\Gamma} = 0 \tag{2}$$

and the dynamic boundary conditions for the normal and tangential stresses:

$$\begin{aligned}[p]_\Gamma - \mathbf{n}\cdot[\mu(\nabla\mathbf{u}+\nabla\mathbf{u}^T)]_\Gamma\cdot\mathbf{n} &= \sigma\kappa \\ \mathbf{t}\cdot[\mu(\nabla\mathbf{u}+\nabla\mathbf{u}^T)]_\Gamma\cdot\mathbf{n} &= 0\end{aligned} \tag{3}$$

where $\mathbf{n}$ is the normal to the interface, $\mathbf{t}$ the tangent. The brackets $[\mathbf{u}]_\Gamma$ for example stand for $[\mathbf{u}]_\Gamma = \mathbf{u}^+ - \mathbf{u}^-$, with $\mathbf{u}^+$ the velocity in the phase 1 and $\mathbf{u}^-$ the velocity in the phase 2. As a level-set method [3, 4] is used to capture the interface, it is implicitly given by the zero of the smooth function $\phi(x,y,z,t)$. ϕ is imposed to be the signed distance function to the interface. This function obeys to the following evolution equation:

$$\frac{\partial\phi}{\partial t} + (\mathbf{u}\cdot\nabla)\phi = 0 \tag{4}$$

2.2 Numerical Methods

Classical projection methods are performed to enforce the incompressibility constraint [5]. The convection terms in the momentum equations are approximated in a conservative way with 5^{th} order accurate WENO schemes [6]. Time integration is performed with 3^{rd} order accurate TVD Runge-Kutta scheme. The Poisson equation for the pressure is solved by a fast multigrid preconditioned conjugate gradient method [7].

The jump conditions for pressure and pressure gradient in the Poisson pressure equation as well as jump condition for the viscous terms are taken into account by the Ghost Fluid Method (GFM) [8]. The full mathematical details of this method can be found in [9]. An artificial fluid (the Ghost Fluid) is created which implicitly gives the proper conditions at the interface. The GFM can be used to model the Navier-Stokes equations directly, without the addition of source terms to model the effects of surface tension. The previous models and methods have been validated in [2].

2.3 Phase-Conditioned Filtering

A priori analysis is classically performed by using a high-pass filter for turbulent scales [10]. The classical filtering of a function $f(\mathbf{x},t)$ is defined by:

$$\bar{f}(\mathbf{x},t) = \int_{-\infty}^{+\infty}\int_{-\infty}^{+\infty} f(\mathbf{x}',t')G(\mathbf{x}-\mathbf{x}',t-t')\,dt'\,d\mathbf{x}' \tag{5}$$

where G is the kernel. Sagaut [11] shows that the classical filtering method (Eq. (5)) is not adapted when fields to be filtered present jumps across an interface Γ. Indeed, a term corresponding to the jump of the mean field across the interface Γ appears in the subgrid fluctuations. And this term can even be larger than the turbulent part of the subgrid fluctuations. This invalidates LES models which suppose that subgrid fluctuations are turbulent. This problem can be encountered when filtering pressure and viscous terms. Indeed, as done in the present work, GFM is used and sharp jumps for pressure and viscous terms appear without volume regularization across

the interface. Therefore, phase-conditioned filtering is performed to cancel jumps of mean contributions across the interface in subgrid fluctuations. Such filtering is defined as:

$$\overline{\psi_k(\mathbf{x},t)}^{\phi} = \frac{1}{\theta_k(\mathbf{x},t)} \int_{\Omega_k} G(\mathbf{x}-\mathbf{x}')\psi_k(\mathbf{x}',t)\,d\mathbf{x}' \tag{6}$$

where k is the phase, Ω_k the space occupied by phase k and $\theta_k(\mathbf{x},t)$ is defined by $\theta_k(\mathbf{x},t) = \int_{\Omega_k} G(\mathbf{x}-\mathbf{x}')\,d\mathbf{x}'$. If Eq. (1) are written in conservative form and $\mathbf{T}_k$ is defined as $\mathbf{T}_k = -p_k\mathbf{I} + \mu_k\left(\nabla\mathbf{u}_k +^T \nabla\mathbf{u}_k\right)$, phase-condionned filtering of Eq. (1) can be written (see [12, 13] for a complete description):

$$\begin{aligned} \nabla\cdot\left(\theta_k\rho_k\overline{\mathbf{u}_k}^{\phi}\right) &= 0 \\ \tfrac{\partial}{\partial t}\left(\theta_k\rho_k\overline{\mathbf{u}_k}^{\phi}\right) + \nabla\cdot\left(\theta_k\rho_k\overline{\mathbf{u}_k}^{\phi}\otimes\overline{\mathbf{u}_k}^{\phi}\right) &- \nabla\cdot\tau_k - \nabla\cdot\left(\theta_k\overline{\mathbf{T}_k}^{\phi}\right) \\ &= -\left[\overline{(\mathbf{T}_k)}_s\cdot\overline{(\mathbf{e}^I_{n,k})}_s - \lambda_k\right]\tfrac{\theta_k A_k}{V_k} \end{aligned} \tag{7}$$

where k is the phase. $\tau_k = \theta_k\rho_k\overline{\mathbf{u}_k}^{\phi}\otimes\overline{\mathbf{u}_k}^{\phi} - \theta_k\rho_k\overline{\mathbf{u}_k\otimes\mathbf{u}_k}^{\phi}$ is the classical term deriving from the filtering of convective terms and $\lambda_k = \overline{(\mathbf{T}_k)}_s\cdot\overline{(\mathbf{e}^I_{n,k})}_s - \overline{(\mathbf{T}_k\cdot\mathbf{e}^I_{n,k})}_s$ the one deriving from phase coupling terms. A_k and V_k are respectively the surface and volume occupied by phase k. Vector $\mathbf{e}^I_{n,k}$ is the unit normal vector to the interface. $\overline{(\cdot)}_s$ defines phase-conditioned surface filtering $\overline{(\psi_k(\mathbf{x},t))}_s = \oint_{\partial\Omega_k}\psi_k(\mathbf{x},t)G(\mathbf{x}'-\mathbf{x})\,d\mathbf{x}'/\oint_{\partial\Omega_k}G(\mathbf{x}'-\mathbf{x})\,d\mathbf{x}'$. The term λ_k is divided into two contributions $\lambda_k = \lambda_k^{press} + \lambda_k^{visc}$ where $\lambda_k^{press} = \overline{(p_k\mathbf{I})}_s\cdot\overline{(\mathbf{e}^I_{n,k})}_s - \overline{(p_k\mathbf{I}\cdot\mathbf{e}^I_{n,k})_s}$ and $\lambda_k^{visc} = \mu_k(\overline{(\nabla\mathbf{u}_k)}_s + \overline{^T(\nabla\mathbf{u}_k)_s})\cdot\overline{(\mathbf{e}^I_{n,k})} - \overline{(\mu_k(\nabla\mathbf{u}_k +^T \nabla\mathbf{u}_k)\cdot\mathbf{e}^I_{n,k})_s}$.

Subgrid terms $\nabla\cdot\tau_k$, $\lambda_k^{press}\theta_k A_k/V_k$ and $\lambda_k^{visc}\theta_k A_k/V_k$ will now be compared from the *a priori* analysis of a DNS database.

3 *A Priori* Analysis of 3D DNS Database

DNS about a freely decaying homogeneous isotropic turbulence case in a 512^3 periodic cubic box has been performed [1]. Two planar interfaces are added in the middle of the computational box separated by 5% of the length box. In the rest of this document, $\phi > 0$ corresponds to phase 1 whereas $\phi < 0$ to phase 2. Viscous and density jumps are not considered in a first approach, so that $\rho(\phi<0)/\rho(\phi>0) = 1$ and $\mu(\phi<0)/\mu(\phi>0) = 1$. A parametric study based on the surface tension coefficient σ has been performed. Results are presented in function of the dimensionless relevant Weber number (W_e). Figure 1 represents the sheet for different W_e numbers at different times (T_e is the eddy turnover time). A complete analysis about DNS database used in the present work can be found in [1].

DNS database is phase-filtered (Eq. (6)) and magnitudes of resulting SGS terms (Eq. (7)) are compared. To do so, the following average is introduced: $<\cdot>_\phi = (1/V(C_\phi))\int_{C_\phi}\cdot\,d\mathscr{V}$ where C_ϕ is a corona centered around the iso level-set ϕ and whose radius is $d\phi$, the elementary variation of ϕ. $V(C_\phi)$ is the volume of this

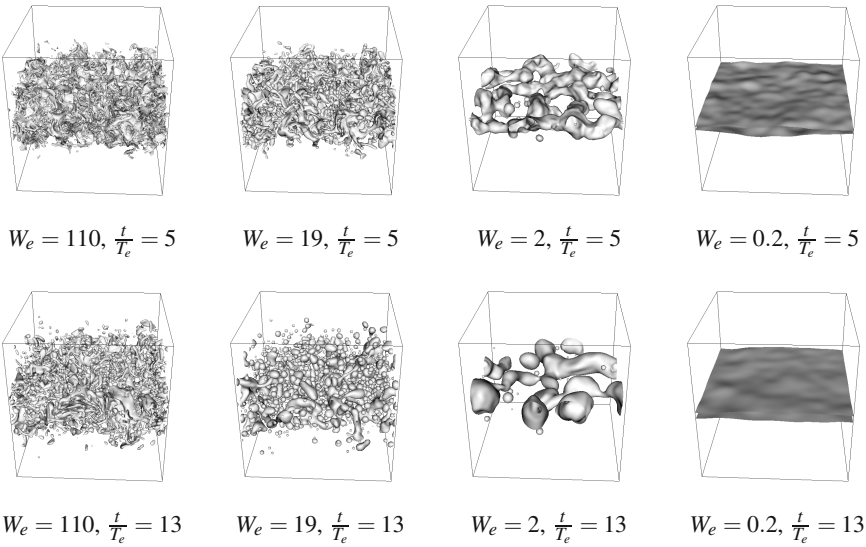

Fig. 1 Sheet for different W_e at $\frac{t}{T_e} = 5$ and 13

corona. In the rest of the document, T_1, T_2 and T_3 are respectively defined to be $< ||\nabla \cdot \tau_k|| >_\phi$, $< ||\lambda_k^{press}|| >_\phi \theta_k A_k / V_k$ and $< ||\lambda_k^{visc}|| >_\phi \theta_k A_k / V_k$ divided by the maximum norm of the resolved part of the convective terms. T_1, T_2 and T_3 represent the magnitudes of the different subgrid scale terms vs. $\phi/\overline{\Delta}$ where ϕ is the level-set function (i.e. the signed distance to the interface) and $\overline{\Delta}$ the numerical space step. Filter size $\overline{\Delta}$ is chosen to be $\overline{\Delta} = 7\Delta$. Results are presented in Fig. 2. Different W_e numbers are represented at different times. $t/T_e = 5$ corresponds to a short time where moderate curvatures on the interface can be seen (see Fig. 1) except for large W_e. $t/T_e = 13$ is a larger time and the interface is much widely disturbed with large curvatures. T_1, T_2 and T_3 are represented vs. $\phi/\overline{\Delta}$.

For every W_e, single phase results can be found far from the interface (i.e. $\phi/\overline{\Delta} >> 1$). Indeed, T_2 and T_3 are related to phase coupling terms and disappear far from the interface. A constant value for T_1 appears for $\phi/\overline{\Delta} >> 1$. This value does not depend on the surface tension coefficient σ and is around 10% and 5% of the resolved part of the convective terms for respectively $t/T_e = 5$ and $t/T_e = 13$.

Now the focus is on $|\phi|/\overline{\Delta} < 1$. For small times $t/T_e = 5$, two kinds of behavior can be seen depending on the W_e number. For large W_e (110, 63 and 19), T_2 is locally larger than T_1 just around the interface ($\approx \overline{\Delta}$). This trend is more significant with increasing W_e. To explain this, back to Fig. 1 at $t/T_e = 5$. Large curvatures are observed for large W_e. Indeed, the interface is widely deformed with local high curvatures, which causes high subgrid fluctuations of the normal vector to the interface $\mathbf{e}_{n,k}^I$. Thus, T_2 is high for large W_e due to the subgrid contributions of $\mathbf{e}_{n,k}^I$,

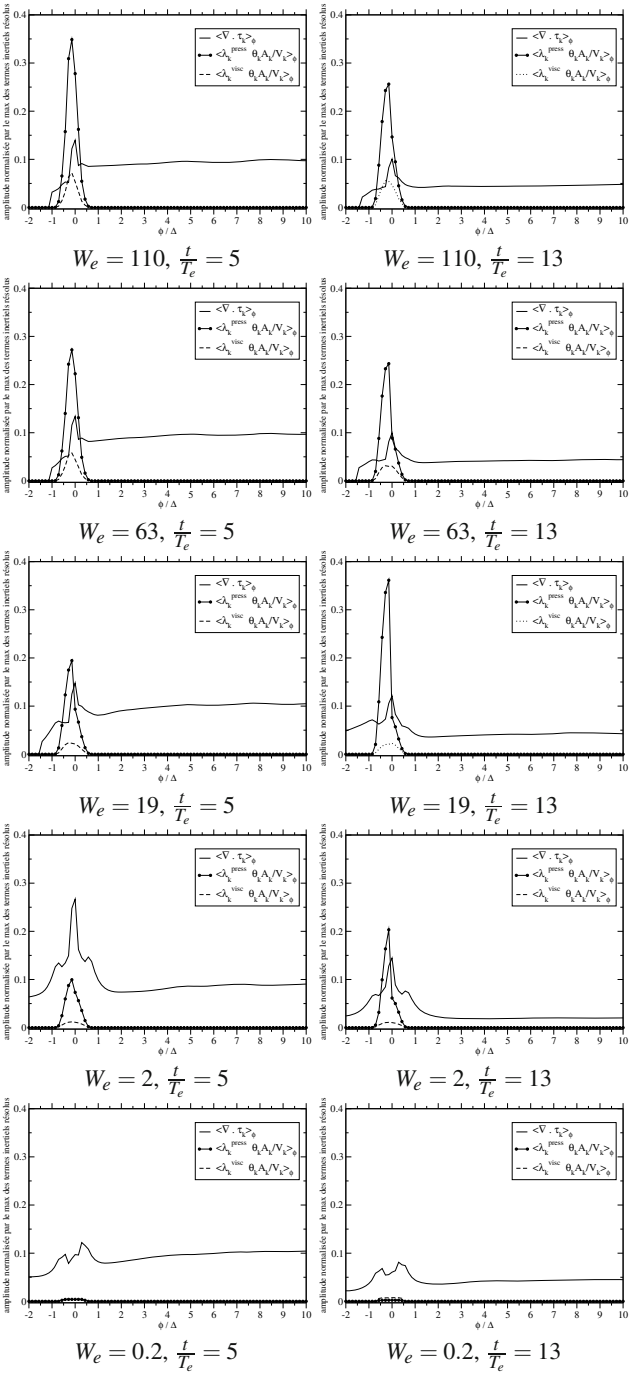

Fig. 2 Comparison between terms T_1, T_2 and T_3. Ordinate axis represents magnitudes of each term normalized by the max. norm of the resolved part of inertial term. $\bar{\Delta} = 7\Delta x$.

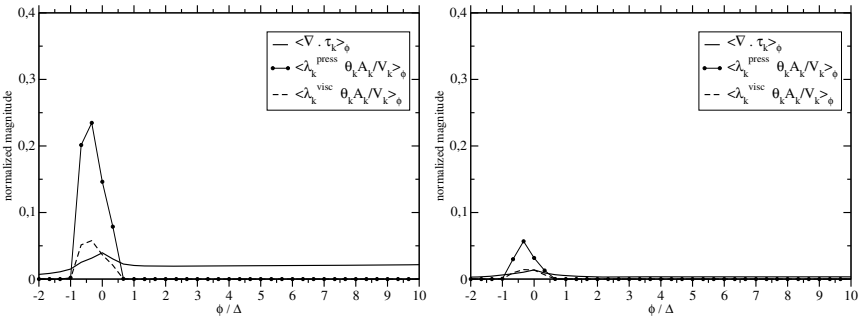

Fig. 3 Comparison between terms T_1, T_2 and T_3. Every term is normalized by the max. norm of the resolved part of inertial term. $\overline{\Delta} = 3\Delta x$.

even if σ remains small. Therefore a LES model for $\mathbf{e}^I_{n,k}$ should adapt with the local topology of the interface (curvature dependent). In Fig. 2, allways for small times ($t/T_e = 5$) but for small W_e (2 and 0.2), predominant term here is T_1. Back to Fig. 1, curvatures are less significant for $W_e = 2$ and $W_e = 0.2$ at small times. Only wave surfaces appear for $W_e = 0.2$ (see [1]). Thus, for small W_e and at small times, subgrid contribution of $\mathbf{e}^I_{n,k}$ is small and $T_2/T_1 < 1$.

For large times $t/T_e = 13$, trends observed at $t/T_e = 5$ are confirmed. For large W_e (110, 63 and 19), T_1 decreases as global turbulent kinetic energy decreases. On the other hand, T_2 remains large and can be even larger than for $t/T_e = 5$ at $W_e = 19$. Indeed, the interface is more and more divided with droplets and the surface of the interface increases. Therefore, A_k increases which explain the increase of T_2. For $W_e = 2$, $T_2/T_1 > 1$ at $t/T_e = 13$. Once again, the subgrid contribution of $\mathbf{e}^I_{n,k}$ becomes large enough to make T_2 predominant. For $W_e = 0.2$, $T_2 << T_1$. This is confirmed by Fig. 1 at $t/T_e = 13$ where the interface is slightly deformed resulting in low subgrid contributions for $\mathbf{e}^I_{n,k}$.

About T_3, its magnitude remains smaller than the magnitudes of T_1 and T_2.

Figure 3 shows the same results as in Fig. 2 at $W_e = 110$ for $\overline{\Delta} = 3\Delta$. The same trends as explained previously can be found. The only impact of filtering size seems to be the classical result of a global decrease for magnitudes of subgrid scale terms when $\overline{\Delta} \to \Delta$.

4 Conclusions

Magnitudes of the subgrid scale terms deriving from the phase coupling terms present in the GFM conservation equations (mainly λ_k^{press}) are driven by the subgrid scale fluctuations of the normal vector to the interface $\mathbf{e}^I_{n,k}$. Therefore, a LES model

for λ_k^{press} has to take into consideration the local subgrid scale contribution of the normal vector to the interface. This study will be completed in the near future on other DNS, yet being realized, for density and viscosity ratios different than 1.

References

1. Trontin, P., Vincent, S., Estivalezes, J.L., Caltagirone, J.P.: Direct numerical simulation of a freely turbulent interfacial flow. Int. J. Mult. Flow 36, 891–907 (2010)
2. Trontin, P., Vincent, S., Estivalezes, J.L., Caltagirone, J.P.: Detailed comparisons of front-capturing methods for turbulent two-phase flow simulations. Int. J. Numer. Meth. Fluid 56, 1543–1549 (2008)
3. Osher, S., Sethian, J.: Fronts Propagating with Curvature Dependent Speed: Algorithms based on Hamilton-Jacobi Formulations. J. Comput. Phys. 79, 12–49 (1988)
4. Sussman, M., Smereka, P., Osher, S.: A Level Set Approach for Computing Solutions to Incompressible Two-Phase Flow. J. Comput. Phys. 114, 146–159 (1994)
5. Chorin, A.J.: Numerical solution of the Navier-Stokes equations. Math. Comp. 22, 745–762 (1968)
6. Shu, C.-W.: Essentially non-oscillatory and weighted essentially non-oscillatory schemes for hyperbolic conservation laws. ICASE - NASA Report (1997)
7. Trottenberg, U., Schuller, A.: Multigrid. Academic Press, Inc. (2001)
8. Fedkiw, R., Aslam, T., Merriman, B., Osher, S.: A non-oscillatory Eulerian approach to interfaces in multimaterial flows (the ghost fluid method). J. Comput. Phys. 152, 457–492 (1999)
9. Couderc, F.: Développement d'un code de calcul pour la simulation d'écoulements de fluides non miscibles. Application à la désintégration assistée d'un jet liquide par un courant gazeux. PhD thesis, University of Toulouse, Toulouse, France (2007)
10. Sagaut, P.: Large eddy simulation for incompressible flows. Springer (2006)
11. Sagaut, P., Germano, M.: On the filtering paradigm for LES of flows with discontinuities. J. of Turbulence 6, Art. No. N23 (2005)
12. Trontin, P.: Développement d'une approche de type LES pour la simulation d'écoulements diphasiques avec interface. Application à l'atomisation primaire. PhD thesis, University of Toulouse, Toulouse, France (2009)
13. Carrara, M.D., Desjardin, P.E.: A filtered mass density function approach for modeling separated two-phase flow for LES I: mathematical formulation. Int. J. Multiphase Flow 32, 365–384 (2006)

Analysis of Unsteady Lagrangian and Eulerian Characteristics of a Liquid Fluidized Bed by Direct Numerical Simulation

S. Vincent, J.-L. Estivalezes, J.C. Brändle de Motta, O. Simonin, and O. Masbernat

Abstract. The characterization of fluidized beds is still a challenging task for macroscopic modeling issues and industrial applications. The macroscopic models require to be fed with parameters or laws that are not well understood or even impossible to estimate as soon as the solid fraction is larger than 0.1. The aim of the present work is to investigate Direct Numerical Simulation [1] of unsteady particle flows in order to solve all the time and space scales of the flow and the particles and to allow for the estimate of unknown macroscopic or stochastic characteristics of the flow. In the DNS, the particles are fully resolved, i.e. the particle diameter is larger than the grid size and to the smallest hydrodynamic scale. A benchmark experimental fluidized bed [2] is simulated and analyzed in terms of macroscopic and Lagrangian characteristics. Comparisons of numerical solutions to measurements are achieved with success.

S. Vincent
Universit de Bordeaux,
Institut de Mécanique et Ingénierie (I2M) - UMR 5295,
F-33400 Talence, France
e-mail: vincent@enscbp.fr

J.-L. Estivalezes · J.C. Brändle de Motta · O. Simonin
Institut de Mécanique des Fluides de Toulouse IMFT, UMR 5502,
Allée Camille Soula, 31400 Toulouse, France
e-mail: Jean-Luc.Estivalezes@onera.fr,
brandlejc@gmail.com,
olivier.simonin@imft.fr

O. Masbernat
Laboratoire de Génie Chimique LGC, UMR 5503,
Campus INP-ENSIACET, 4 alle Emile Monso,
31432 Toulouse Cedex 4, France
e-mail: olivier.masbernat@ensiacet.fr

M.O. Deville et al. (eds.), *Turbulence and Interactions*,
Notes on Numerical Fluid Mechanics and Multidisciplinary Design 125,
DOI: 10.1007/978-3-662-43489-5_21,

1 Introduction

The characterization of dense liquid-solid flows and in particular fluidized beds is still a challenging task for macroscopic modeling issues and industrial applications as the granular dynamics based models or scale separation Eulerian-Eulerian or Eulerian-Lagrangian approaches. These macroscopic models require to be fed with parameters or laws that are not well understood or even impossible to estimate as soon as the solid fraction is larger than 0.1. The aim of the present work is to investigate Direct Numerical Simulation [1] of unsteady particle flows in order to solve all the time and space scale of the flow and the particle and to allow for the estimate of unknown macroscopic or stochastic characteristics of the flow. In the DNS, the particles are fully resolved, i.e. the particle diameter is larger than the grid size and to the smallest hydrodynamic scale.

Simulating a fluidized bed where particle and fluid have the same characteristic scales, *i.e.* resolved scale particle flows, is the scope of the present work. The Direct Point Simulation (DPS) approaches based on a Lagrangian modeling of the particles does not remain valid for that purpose [3] [4] [5]. The field of numerical methods devoted to the simulation of particulate flows involving finite size particles was widely developed the last 20 years concerning the study of the flow over a small number of fixed or moving particle [6] [7] [8] [9] [10] [11] or a fixed arrangement of spheres [12]. All the previously mentioned works were developed on fixed grids. The unstructured Arbitrary Eulerian-Lagrangian (ALE) grid simulations were developed for particle flows in the $90's$ by Hu *et al.* [6] concerning two-dimensional flows involving two particles. The works of Maury [13] with the ALE method are also to be noticed concerning the flow of 1000 non spherical particles in a two-dimensional biperiodic domain. A majority of the particulate flow simulations were carried out on structured grids to avoid the complexity of managing an evolving adapted mesh. Among them, the most relevant existing works concern the distributed Lagrangian multiplier (DLM) method of Glowinski and co-workers [14], the Physalis CFD code of Zhang and Prosperetti [15], the Immersed Boundary (IB) with direct forcing approach proposed by Uhlmann [16] [17], the lattice Boltzmann scheme [18, 19], the modified version of Uhlmann IB method published by Lucci *et al.* [20] [21] and the viscous penalty techniques of Ritz and Caltagirone [22] and Randrianarivelo *et al.* [23] [24] [1]. The present work uses the second order in space penalty method for the DNS of particulate flows based on the Implicit Tensorial Penalty Method [1].

2 Simulation of Real Fluidized Bed

2.1 Presentation of the Fluidized Bed

The fluidized bed chosen for the simulations is taken from the experiments of Aguilar Corona [2]. In a cylinder of 0.64 *m* height and 0.08 *m* diameter, 2133 pyrex particles are fluidized by the circulation of potassium thiocyanate KSCN at various fluidization velocities. The diameter of the particles is 0.006 *m* and the simulated

fluidization velocity is 0.12 $m.s^{-1}$. The density of the pyrex is $\rho_s = 2230\ kg.m^{-3}$ whereas the density ρ_l and the dynamic viscosity μ_l of the KSCN are 1400 $kg.m^{-3}$ and 3.8 10^{-3} $Pa.s$. For the chosen particles in KSCN, the terminal settling velocity is equal to 0.226 $m.s^{-1}$, the particle Reynolds number based on this velocity is equal to 530 and the Stokes number is 0.8. Concerning the DNS of particles, a parallelepiped box of dimensions 8 $cm \times 8\ cm \times 64\ cm$ is used with a grid mesh containing $160 \times 160 \times 1280$ cells. With such a grid resolution, nearly 12 cell length Δx per particle diameter is achieved. The cylinder is accounted for on the Cartesian mesh by a Darcy penalty technique [25].

2.2 Macroscopic Results

The macroscopic characteristics of the fluidized bed are first presented in order to validate the global interaction between the 2133 particles and the carrier fluid. The typical particle structures are illustrated in Figure 1 over time. It is observed that from $t = 0\ s$ to 6 s, a packing occurs as the initial particle concentration α, *i. e.* $\alpha = 0.1$, is small compared to the fluidization velocity of 0.12 $m.s^{-1}$. After 6 s, the fluidization regime is reached and the average bed height and resulting solid concentration in the vertical cylinder remain almost constant over time. The average numerical solid concentration α_n so obtained is 0.24. For the chosen operating conditions, this value of α_n can be compared to the reference experimental correlation of Richardson and Zaki [26] which reads

$$\alpha_{RZ} = 1 - \left(\frac{U_0}{U_t}\right)^{1/2.41} \tag{1}$$

where the parameter 2.41 is correct for Reynolds numbers Re_t based on the settling particle velocity larger than 500. In our configuration, $Re_t = 530$. Concerning the

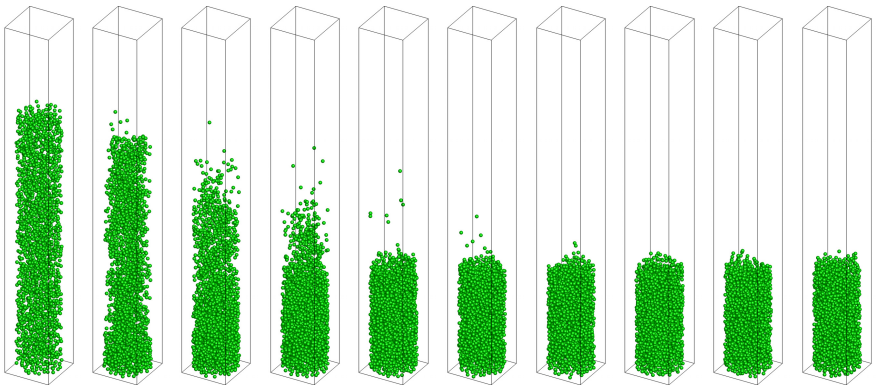

Fig. 1 Three-dimensional view of the particles inside the fluidized bed - from left to right, $t = 1, 2, 3, 4, 5, 6, 7, 8, 9$ and 10 s

fluidization velocity U_0 and the settling particle velocity U_t, the values of $0.12\ m.s^{-1}$ and $0.226\ m.s^{-1}$ are measured in the experiments of [2]. Finally, it is found that $\alpha_{RZ} = 0.231$. A very good agreement is found between experiments and numerical solutions. This comparison validates the use of two numerical radii for the particles, one for the definition of the density and the treatment of the collisions and the other for the penalty viscosity. A correct global equilibrium between the gravity and drag forces is so obtained.

2.3 Lagrangian Characteristics

The first Lagrangian characteristics that can be studied are the particle velocity fluctuations over time in the fluidization regime, for $t > 6\ s$. In this particular flow conditions, the mean particle positions are null as the height of the bed height is constant over time. The numerically obtained time averaged particle velocities are $\bar{U}_x = 7.2150\ 10^{-5}\ m.s^{-1}$, $\bar{U}_y = 7.7822\ 10^{-5}\ m.s^{-1}$ and $\bar{U}_z = 1.4128\ 10^{-5}\ m.s^{-1}$ respectively in the x, y and z directions. These values are four orders of magnitude smaller than the fluidization velocity and can be considered as zero.

A last parameter of interest to feed the macroscopic Eulerian-Eulerian models devoted to fluidized beds is the autodiffusion coefficient $D_{\alpha\alpha}$. It is defined [2] according to the variance of the particle displacement $M_{\alpha\alpha} = < \mathbf{X}_i - \mathbf{X}_{i,0} >$ as

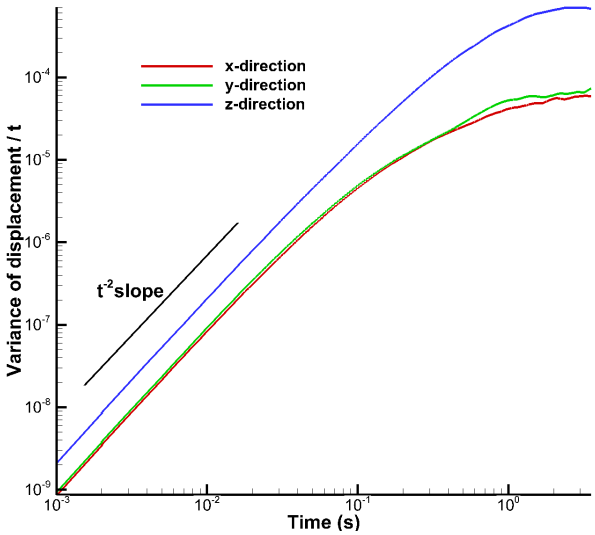

Fig. 2 Variance of the displacement of the particles $\frac{M_{\alpha\alpha}}{t}$ according to time

Table 1 Asymptotic values of $\frac{M_{\alpha\alpha}(t)}{t}$ for each Cartesian direction

	x-direction	y-direction	z-direction
experiments of [2] ($m^2.s^{-1}$)	5.4×10^{-5}	5.1×10^{-5}	6.8×10^{-4}
simulations ($m^2.s^{-1}$)	4.55×10^{-5}	5.5×10^{-5}	7.5×10^{-4}

$$D_{\alpha\alpha} = lim_{t-t_0 \to +\infty} \frac{M_{\alpha\alpha}(t)}{t} \tag{2}$$

where $\mathbf{X}_i$ is the coordinate vector of one particle at a given time step and $\mathbf{X}_{i,0}$ is the coordinate vector of the same particle at an initial time t_0. The notation $< \cdot >$ stands for the average over all the particles $i, i = 1..2133$. In the experiments [2], it has been demonstrated that for small time steps, a t^{-2} slope was observed for $D_{\alpha\alpha}$ whereas an asymptotic value was reached for larger times. This asymptotic value is the autodiffusion coefficient in a given direction. The curve of $\frac{M_{\alpha\alpha}(t)}{t}$ is presented in Figure 2. The same slope as in the experiments in found numerically for small time steps. The asymptotic values obtained numerically and in the experiments for $D_{\alpha\alpha}$ are proposed in Table 1. A good agreement is found between experiments and numerical solutions, the vertical component being one order of magnitude larger than in the horizontal directions. A 16% gap is observed between both approaches.

3 Conclusion and Perspectives

A fictitious domain approach based on augmented Lagrangian techniques and penalty methods has been used for handling particulate flows of resolved scale particle. The work have been concentrated on the simulation of a real fluidized bed, in order to illustrate the ability of the ITPM to deal with dense particulate flows. The simulations have been favorably compared to reference experiments or theoretical results of the literature such as the fluidization velocity, variance of particle position or auto-diffusion coefficient. These simulations are a first step for managing numerical experiments with the DNS of particle flows. This is now possible on massively parallel computers, as 512 processors were used in the proposed simulations of fluidized beds.

References

1. Vincent, S., Brändle de Motta, J.C., Sarthou, A., Estivalezes, J.-L., Simonin, O., Climent, E.: A Lagrangian VOF tensorial penalty method for the DNS of resolved particle-laden flows. Under Correction in Journal of Computational Physics (2012)
2. Aguilar Corona, A.: Agitation of particles in a liquid fluidized bed. Experimental study. PhD thesis, Toulouse University (2008)

3. Ferrante, A., Elghobashi, S.: On the physical mechanisms of two-way coupling in particle-laden isotropic turbulence. Physics of Fluids 15, 315–329 (2003)
4. Ahmed, A.M., Elghobashi, S.: Direct numerical simulation of particle dispersion in homogeneous turbulent shear flows. Physics of Fluids 13, 3346–3364 (2001)
5. Fede, P., Simonin, O.: Numerical study of the subgrid fluid turbulence effects on the statistics of heavy colliding particles. Physics of Fluids 18, 45103–45120 (2006)
6. Hu, H.H., Joseph, D.D., Crochet, M.J.: Direct Simulation of Fluid Particle Motions. Theoretical and Computational Fluid Mechanics 3, 285–306 (1992)
7. Fadlun, E.A., Verzicco, R., Orlandi, P., Mohd-Yusofz, J.: Combined Immersed-Boundary Finite-Difference Methods for Three-Dimensional Complex Flow Simulations. Journal of Computational Physics 161, 35–60 (2000)
8. Kim, J., Kim, D., Choi, H.: An immersed-boundary finite-volume method for simulations of flow in complex geometries. Journal of Computational Physics 171, 132–150 (2001)
9. Takagi, S., Oguz, H.N., Zhang, Z., Prosperetti, A.: PHYSALIS: a new method for particle simulation Part II: two-dimensional Navier-Stokes flow around cylinders. Journal of Computational Physics 187, 371–390 (2003)
10. Coquerelle, M., Cottet, G.H.: A vortex level set method for the two-way coupling of an incompressible fluid with colliding rigid bodies. Journal of Computational Physics 227, 9121–9137 (2008)
11. Simeonov, J.A., Calantoni, J.: A pressure boundary integral method for direct fluid-particle simulations on Cartesian grids. Journal of Computational Physics 230, 1749–1765 (2011)
12. Höfler, K., Schwarzer, S.: Navier-Stokes simulation with constraint forces: Finite-difference method for particle-laden flows and complex geometries. Physical Review E 61, 7146–7160 (2000)
13. Maury, B.: Direct simulations of 2D fluid-particle flows in biperiodic domains. Journal of Computational Physics 156, 325–351 (1999)
14. Glowinski, R., Pan, T.W., Hesla, T.I., Joseph, D.D., Périaux, J.: A fictitious domain approach to the direct numerical simulation of incompressible viscous flow past moving rigid bodies: application to particulate flow. Journal of Computational Physics 169, 363–426 (2001)
15. Zhang, Z., Prosperetti, A.: A second-order method for three-dimensional particle simulation. Journal of Computational Physics 210, 292–324 (2005)
16. Uhlmann, M.: An immersed boundary method with direct forcing for the simulation of particulate flows. Journal of Computational Physics 209(2), 448–476 (2005)
17. Uhlmann, M.: Interface-resolved direct numerical simulation of vertical particulate channel flow in the turbulent regime. Physics of Fluids 20(5), 053305 (2008)
18. Ten Cate, A., Derksen, J.J., Portela, L.M., Van Der Akker, E.A.: Fully resolved simulations of colliding monodisperse spheres in forced isotropic turbulence. Journal of Fluid Mechanics 519, 233–271 (2004)
19. Gao, H., Wang, L.-P.: Lattice Boltzmann simulation of turbulent flow laden with finite-size particles. In: Proceedings of the 7th International Conference on Multiphase Flows, ICMF 2010 (2010)
20. Lucci, F., Ferrante, A., Elghobashi, S.: Modulation of isotropic turbulence by particles of Taylor length-scale size. Journal of Fluid Mechanics 650, 5–55 (2010)
21. Lucci, F., Ferrante, A., Elghobashi, S.: Is Stokes number an appropriate indicator for turbulence modulation by particles of Taylor-length-scale size? Physics of Fluids 23, 025101:1–025101:7 (2011)
22. Ritz, J.-B., Caltagirone, J.P.: A numerical continuous model for the hydrodynamics of fluid particle systems. International Journal for Numerical Methods in Fluids 30, 1067–1090 (1999)

23. Randrianarivelo, T.N., Pianet, G., Vincent, S., Caltagirone, J.-P.: Numerical modelling of the solid particle motion using a new penalty method. International Journal for Numerical Methods in Fluids 47, 1245–1251 (2005)
24. Randrianarivelo, T.N., Vincent, S., Simonin, O., Caltagirone, J.-P.: A DNS approach dedicated to the analysis of fluidized beds. Fluid Mechanics Applications 81, 207–214 (2007)
25. Khadra, K., Angot, P., Parneix, S., Caltagirone, J.P.: Fictitious domain approach for numerical modelling of Navier-Stokes equations. International Journal for Numerical Methods in Fluids 34, 651–684 (2000)
26. Richardson, J.F., Zaki, W.N.: Sedimentation and fluidization. Part 1. Transactions of the Institution of Chemical Engineering 32, 35–53 (1954)

Numerical Investigation of the Spatial Resolution Requirements for Turbulent Rayleigh-Bénard Convection

Sebastian Wagner, Olga Shishkina, and Claus Wagner

Abstract. The key requirement for setting up a direct numerical simulation (DNS) is a sufficiently fine grid allowing to resolve locally all relevant micro-scales. In case of turbulent Rayleigh-Bénard convection (RBC) this is usually done by fulfilling different analytically derived criteria for the boundary layers and the bulk flow. In order to analyse if these requirements are sufficient, DNS of turbulent RBC in a cylindrical container with aspect ratio unity and Prandtl number $Pr = 0.786$ have been performed for Rayleigh numbers Ra up to 10^9. The micro-scales obtained in the DNS as well as their scaling with Ra are compared with the corresponding theoretical predictions. The analysis reveals that the smallest scales, occurring close to the wall, are about half of the estimated ones. Furthermore, their scaling differs slightly from the estimations while the criterion for the bulk flow fits quite well.

1 Introduction

The flow driven by the temperature difference between a heated bottom and a cooled top plate, called Rayleigh–Bénard convection (RBC), is a simplified model of many convective flow problems occurring in nature and technology (for recent reviews we suggest [1], [2]). Due to its simplicity, it can be investigated by means of direct numerical simulations (DNS) which is the most accurate ansatz in computational fluid dynamics due to the fact that no turbulence-model is needed. This accuracy is only provided if the computational grid is fine enough to resolve even the smallest scales occurring in the flow.

Sebastian Wagner
German Aerospace Center (DLR),
Institute of Aerodynamics and Flow Technology,
Bunsenstrasse 10, 37073 Göttingen, Germany
e-mail: Sebastian.Wagner@DLR.de

Olga Shishkina · Claus Wagner
DLR, Göttingen, Germany
e-mail: {Olga.Shishkina,Claus.Wagner}@DLR.de

M.O. Deville et al. (eds.), *Turbulence and Interactions*,
Notes on Numerical Fluid Mechanics and Multidisciplinary Design 125,
DOI: 10.1007/978-3-662-43489-5_22,

In the past different attempts to deduce the necessary resolution have been made. In general, two types of investigations exist. On the one hand, grid studies can be performed in which the grid is refined until certain quantities, like the integral vertical heat-flux (called Nusselt number Nu), are converged with respect to the grid spacing (e.g. [3]). The general result is that a certain number of grid points within the viscous and thermal boundary layers (BLs) are needed (which results in a very fine mesh close to rigid walls). In addition, a weaker restriction apart from the walls needs to be fulfilled to resolve the motion of the bulk flow. The results on the necessary points in the BLs is collected and published in [4]. To obtain proper computational meshes by performing grid resolution studies is ineffective since a lot of simulations have to be performed while most of them are meaningless due to a lack of spatial resolution. Therefore, on the other hand different attempts have been made to estimate the spatial resolution requirements analytically (see [4],[5]). Based on the insight that different criteria for the BLs and the bulk flow are necessary, Shishkina et al. [4] estimated besides a global mesh resolution also the necessary number of nodes to resolve Prandtl-Blasius (laminar) BLs.

In a recent numerical study [6] the BLs close to the horizontal walls showed deviations from Prandtl-Blasius (PB) theory. This leads to the question whether the assumption of laminar BLs can lead to proper estimates on the boundary layer resolution. Therefore, in the present paper a direct comparison of estimated micro-scales with the results from over-resolved DNS is made.

2 Numerical Method

Direct numerical simulations (DNS) have been performed using a fourth-order accurate finite-volume code in cylindrical coordinates (r, ϕ, z). Some more details and literature on the solver are collected in [6].

We solve the dimensionless conservation laws of momentum, energy and mass in Oberbeck-Boussinesq approximation

$$\partial_t \mathbf{u} + \mathbf{u} \cdot \nabla \mathbf{u} = -\nabla p + \sqrt{\frac{Pr}{Ra\Gamma^3}} \nabla^2 \mathbf{u} + T\mathbf{e}_z, \tag{1}$$

$$\partial_t T + \mathbf{u} \cdot \nabla T = \sqrt{\frac{1}{PrRa\Gamma^3}} \nabla^2 T, \quad \nabla \cdot \mathbf{u} = 0, \tag{2}$$

in a cylindrical computational domain with aspect ratio Γ (diameter $D = 2R$ per height H) equal to one.[1] Due to non-dimensionalization the characteristic dimensionless Rayleigh number $Ra = \alpha g H^3 \, \Delta T/(\nu\kappa) \in [10^6, 10^9]$ and Prandtl number $Pr = \nu/\kappa = 0.786$ occur. On the cylinder's surface no slip-conditions are prescribed, the vertical wall is adiabatic and on the top and bottom plate the temperature is fixed with $T_{\text{bottom}} > T_{\text{top}}$.

For simplicity and computational effectiveness the computational mesh is chosen structured and non-uniform (i.e. the nodes are clustered close to the rigid walls). Structured grid means that the distribution of nodes in one spatial direction is

[1] ∂_t denotes the partial derivative with respect to time t, while $\mathbf{e}_z$ is the unit vector in z direction.

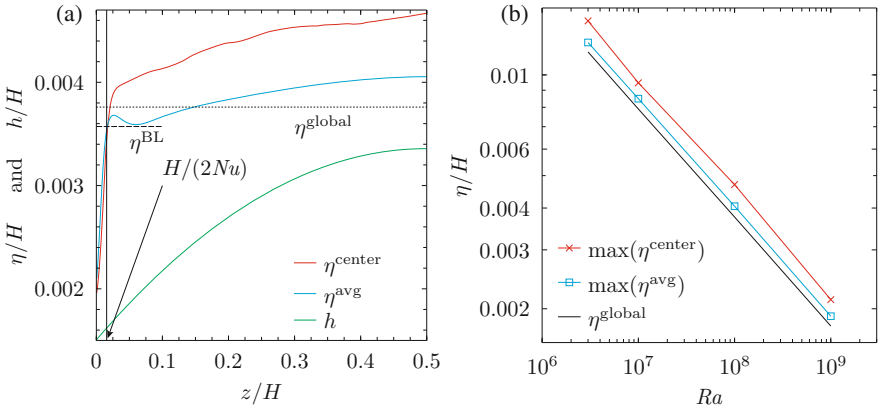

Fig. 1 (a)(—) Mesh spacing h in vertical direction in comparison with the local micro-scales (—) $\eta^{\mathrm{center}} = (\nu^3/\langle\varepsilon\rangle_{t,\phi,r\leq 0.1R})^{1/4}$, (—) $\eta^{\mathrm{avg}} = (\nu^3/\langle\varepsilon\rangle_{t,r,\phi})^{1/4}$ as well as the theoretical estimates $(\cdots)$ $\eta^{\mathrm{global}} = Pr^{1/2}Ra^{-1/4}(Nu-1)^{-1/4}H$ and $(---)$ $\eta^{\mathrm{BL}} = 2^{-3/2}a^{-1}Nu^{-3/2}Pr^{0.5355-0.033\log(Pr)}H$ (see text) for $Ra = 10^8$ and (b) their largest values for different Ra, $Pr = 0.786$, $\Gamma = 1$

Table 1 Simulation parameters in the DNS: N_i number of computational nodes in $i \in \{r, \phi, z\}$ -direction and smallest and largest mesh-spacing h in vertical direction, $Pr = 0.786$, $\Gamma = 1$

Ra	$N_r \times N_\phi \times N_z$	$\min(h/H) \times 10^3$	$\max(h/H) \times 10^3$
3×10^6	$96 \times 256 \times 192$	4.51	5.60
10^7	$96 \times 256 \times 192$	4.51	5.60
10^8	$192 \times 512 \times 384$	1.51	3.36
10^9	$384 \times 1024 \times 768$	0.65	1.78

independent from the other directions. The distribution of the nodes follows a tanh-function [7] and is visualized in figure 1(a). Since the usual criteria for the mesh-resolution should be investigated and discussed in the present paper, the spatial resolution in the DNS is chosen finer than the one estimated by theory. The numbers of computational nodes in the DNS along different directions with further simulation parameters are collected in table 1.

3 Spatial Resolution Requirements in RBC

In a proper DNS, the smallest scales occurring in a turbulent flow need to be resolved. Apart from the walls, i.e. in case of (at least locally) isotropic turbulence and for $Pr \leq 1$ the resolution of Kolmogorov scales η_K is required. This means $h/\eta_K \leq 1$ should be fulfilled, where h is the mean grid spacing of the computational grid [4],[5].

In case of isotropic turbulence, Kolmogorov defined $\eta_K = (\nu^3/\varepsilon)^{1/4}$ where ν is the kinematic viscosity and ε is the kinetic dissipation rate which is given as $\varepsilon = (\nu/2)\sum_i \sum_j (\partial_{x_j} u_i + \partial_{x_i} u_j)^2$ (see e.g. [8]). Close to the walls, the requirement of isotropy is not longer fulfilled, thus the question of the resolution of this area arises. Assuming that we fulfill $h/(\nu^3/\varepsilon)^{1/4} \leq 1$ everywhere in the computational domain and there is a wind in x direction parallel to a rigid wall (with no-slip condition). Further, let z be the direction orthogonal to the wall and (without loss of generality) $\partial u_x/\partial z \geq 0$. Then we obtain at this wall

$$1 \geq h(\nu^3/\varepsilon)^{-1/4} \gtrsim h\sqrt{\nu \partial_z u_x}\nu^{-1} = h u_\tau \nu^{-1} \equiv h^+ \tag{3}$$

Here h^+ denotes the grid spacing in wall-units ν/u_τ. The restriction $h^+ \leq 1$ at the wall (to resolve large velocity gradient in the viscous sub-layer) is well known from the literature [8]. Thus the requirement $h/(\nu^3/\varepsilon)^{1/4} \leq 1$ lets us fulfill the two criteria $h/\eta_K \leq 1$ (apart from the wall in case of isotropic turbulence) and $h^+ \leq 1$ at the wall. We assume that in between these regions the restriction needs to be fulfilled, as well. Therefore, only the requirement $h/(\nu^3/\varepsilon)^{1/4} \leq 1$ needs to be fulfilled everywhere in the domain. For a simpler notation, we call $(\nu^3/\varepsilon)^{1/4}$ as *micro-scales* η in the following.

For the sake of simplicity, we focus on $Pr = 0.786$. Further we restrict ourselves to time- (and spatial-) averaged dissipation rates to make analytical derivations feasible.

From the conservation law of momentum, it can be derived analytically [4] that

$$\langle \varepsilon \rangle_{t,r,\phi,z} = \frac{\nu^3}{H^4}(Nu - 1)RaPr^{-2} \tag{4}$$

while the Nusselt number $Nu \equiv \frac{\langle u_z T - \kappa \partial_z T \rangle_{t,r,\phi}}{\kappa \Delta T/H}$ is the integral heat flux in vertical direction, which is a function of Ra, Pr and the geometry of the convection cell. Since $\langle \varepsilon \rangle_{t,r,\phi,z}$ includes the boundary layers close to the rigid walls in which ε is large [9], the question must be answered whether the global micro-scale η^{global} based on $\langle \varepsilon \rangle_{t,r,\phi,z}$ can be used to estimate the bulk flow micro-scales.

To estimate the required resolution of kinetic and thermal boundary layers in the vicinity of the rigid walls Shishkina et al. [4] derived:

$$\langle \varepsilon \rangle_{t,r,\phi,z=z_0 \in \text{BL}} \gtrsim \frac{64\nu^3 a^4 Nu^6}{H^4}\left(\frac{\delta_\theta}{\delta_u}\right)^6 \tag{5}$$

Here $a \approx 0.482$ is a parameter obtained from experiments and δ_θ, δ_u are the thicknesses of the thermal and viscous BL, respectively. In the derivation, the boundary layers have been assumed to be of PB type. By this estimation

$$\left(\frac{\delta_\theta}{\delta_u}\right) = Pr^{-0.357 + 0.022\log(Pr)} \tag{6}$$

can be obtained for $3 \times 10^{-4} \leq Pr \leq 3$. Further the necessary number of grid-points within the thermal and viscous BL is estimated by distributing points equidistantly based on $\langle \varepsilon \rangle_{t,r,\phi,z=z_0 \in \mathrm{BL}}$. Since in a recent publication [6] the question was addressed, whether the PB theory is the proper description of the boundary layers occurring in turbulent RBC, we further tested whether (5) together with (6) can be used as a proper estimate η^{BL} for the BL resolution.

4 Micro-scales Predicted in DNS

Similar as in the analytical derivations we obtain in our DNS time-averaged dissipation rates $\langle \varepsilon \rangle_t$ as defined above. Due to azimuthal symmetry in the cylindrical convection cell we further analyse $\phi-$averaged dissipation rates and concentrate on the lower half of the convection cell (up-down-symmetry). In figure 2(a) the resulting micro-scales

$$\eta^{\mathrm{local}} = (\nu^3 / \langle \varepsilon \rangle_{t,\phi})^{1/4} \tag{7}$$

(in units of η^{global}) are shown for $Ra = 10^8$. As expected from the literature [9] η is largest at the center of the convection cell and decreases strongly near the walls.

In the following, we will concentrate on vertical profiles $\eta(z)$ since at the horizontal walls thermal BLs exist in addition to the viscous BLs. First it seems worth clarifying, whether a structured grid is suitable for our DNS. Since a viscous BL develops close to the vertical wall, resolving the smallest $\eta(r)$ for each z in a structured grid (i.e. the grid spacing h in $z-$direction is independent of ϕ and r) is too strict since it requires an extremely fine mesh in the whole domain. However, considering $|\partial_z \langle u_r \rangle_t|$ and $|\partial_r \langle u_z \rangle_t|$ (as shown in units of its maximum in figures 2(b) and 2(c)) we obtain that close to the wall only the components of the gradient orthogonal to the wall contribute significantly to the dissipation rates. Therefore, the boundary layer

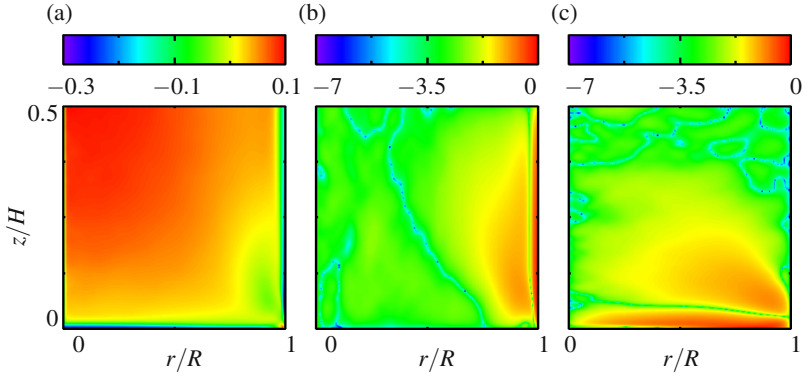

Fig. 2 Spatial distribution of (a) micro-scales in units of their volume average $\log_{10}(\eta^{\mathrm{local}}/\eta^{global})$, (b),(c) single components of gradient tensor in units of their maximum $\log_{10}(|\partial_r \langle u_z \rangle_t| / \max(|\partial_r \langle u_z \rangle_t|))$ and $\log_{10}(|\partial_z \langle u_r \rangle_t| / \max(|\partial_z \langle u_r \rangle_t|))$, respectively, for $Ra = 10^8$, $Pr = 0.786$, $\Gamma = 1$.

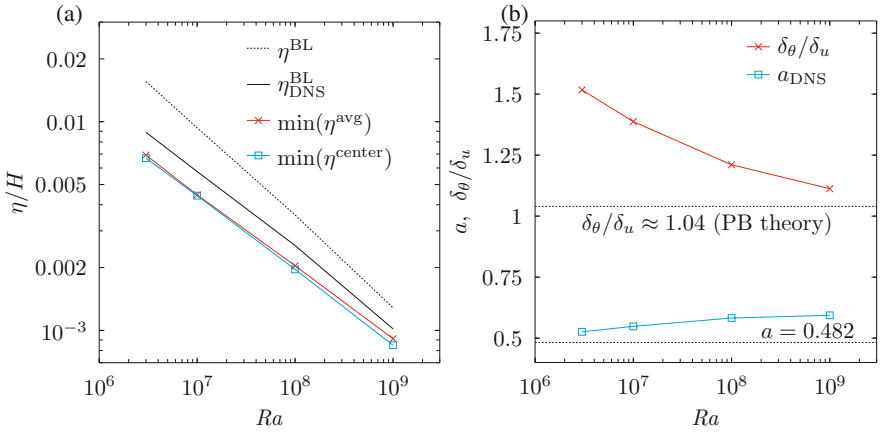

Fig. 3 (a) Comparison of micro-scales (at the wall) (—) η^{avg} (9),(—) η^{center} (8) with theoretical estimates (5) based on $a = 0.482$ from experiment, (b) δ_θ/δ_u from theory (6) $(\cdots)$ η^{BL} and a, δ_θ/δ_u from DNS (—) $\eta^{\mathrm{BL}}_{\mathrm{DNS}}$, for different Ra, $Pr = 0.786$, $\Gamma = 1$.

at the vertical wall mainly requires resolution in $r-$ direction but not in $z-$direction. Nevertheless, in the following not only profiles $\eta(z)$ at the cell center

$$\eta^{\mathrm{center}} = (\nu^3/\langle\varepsilon\rangle_{t,\phi,r\leq 0.1R})^{1/4}, \tag{8}$$

but also profiles based on dissipation rates averaged in radial direction

$$\eta^{\mathrm{avg}} = (\nu^3/\langle\varepsilon\rangle_{t,r,\phi})^{1/4} \tag{9}$$

will be discussed to be on the safe side. The resulting smallest and largest η are collected in figures 1(b), 3(a) for different Ra and the corresponding profiles for $Ra = 10^8$ are depicted in figure 1(a).

Figure 1(a) reveals that the largest micro-scales (occurring at the convection cell center) are larger than the estimate η^{global} (as obtained from equation (4)). The largest difference is obtained for η^{center}. Nevertheless, $\max(\eta^{\mathrm{center}})$ and $\max(\eta^{\mathrm{avg}})$ reflect the same Ra dependence as η^{global} does (see figure 1(b)). Therefore, η^{global} can be used as an estimate for the micro-scales at the cell center η^{bulk} if an additional constant prefactor c is introduced, i.e. $\eta^{\mathrm{bulk}} = c\eta^{\mathrm{global}}$. For the case of η^{center} the prefactor is $c \approx 1.22$ while for η^{avg} we obtain $c \approx 1.07$. Nevertheless, the lower bound requirement η^{global} can be used if we want to be on the safe side.

Considering the micro-scales at the wall, i.e. the overall smallest micro-scales, the situation is more complex. Already figure 1(a) reveals that the micro-scales strongly increase in the boundary layer region ($z \leq H/(2Nu)$) and are much smaller than the estimate η^{BL}. From this we conclude that this requirement is not restrictive enough. Recalling equation (5) reveals that η^{BL} contains two problematic parameters: a and δ_θ/δ_u. While $a \approx 0.482$ is obtained from experiments, δ_θ/δ_u is usually predicted by using PB theory (6). If we evaluate these two parameters using the

DNS results (based on [6]) we obtain their tendency with respect to Ra as depicted in figure 3(b) revealing deviations from the ones given Shishkina et al. In figure 3(a) η^{BL} is compared with the micro-scales at the wall obtained in DNS. Further a and δ_θ/δ_u from DNS have been used to evaluate $\eta^{\mathrm{BL}}_{\mathrm{DNS}}$ from (5). The comparison shows that the deviations of η^{BL} from η^{center} (which is almost equivalent to considering η^{avg}) can be reduced by using $\eta^{\mathrm{BL}}_{\mathrm{DNS}}$. Even the scaling with Ra fits better to the DNS results. Nevertheless, even $\eta^{\mathrm{BL}}_{\mathrm{DNS}}$ is not restrictive enough. As a proper resolution requirement at the wall we suggest to use $\eta^{\mathrm{BL}}/2$ for the considered Ra, Pr. The number of points is thereby not necessarily increased, since the equidistant distribution of nodes does not fit to the strong increase of the micro-scales within the BLs. A clever distribution of computational nodes (fulfilling $h \leq \eta^{\mathrm{BL}}/2$ at the wall and $h \leq c\eta^{\mathrm{global}}$ at the cell center) is thus required to match η^{center} (or η^{avg}) as depicted in 1(a). For example, if the nodes are distributed as described by η^{avg} the number of points in $z-$direction for $Ra = 10^8$ is 263, which is about 70% of the nodes we used in the simulation.

5 Conclusions

We compare theoretical estimates on the BL and bulk resolution with the resolution requirements derived from over-resolved DNS of RBC. It was shown that the analytical derivation based on the volume- (and time-) averaged kinetic dissipation rates leads to a proper estimate for the resolution required at the convection cell center. Considering the boundary layers the theoretically predicted smallest micro-scales in the boundary layers are larger than the ones obtained by analysing the DNS results. For the considered Ra, Pr the estimate for the micro-scales needs to be decreased by a factor of two to guarantee a proper resolution at the wall. Further, the dramatic changes of the micro-scales within the BLs compel us to distribute the computational nodes non-equidistantly close to the walls. Therefore, even though the mesh at the walls needs to be finer, the required overall number of nodes in the BLs might be unchanged.

Acknowledgements. The authors acknowledge support by the Deutsche Forschungsgemeinschaft (DFG) under grant SH405/2-1.

References

1. Ahlers, G., Grossmann, S., Lohse, D.: Rev. Mod. Phys. 82, 503 (2009)
2. Lohse, D., Xia, K.Q.: Annu. Rev. Fluid Mech. 42, 335 (2010)
3. Stevens, R.J.A.M., Verzicco, R., Lohse, D.: J. Fluid Mech. 643, 495 (2010)
4. Shishkina, O., Stevens, R.J.A.M., Grossmann, S., Lohse, D.: New J. Phys. 12, 075022 (2010)
5. Grötzbach, G.: J. Comp. Phys. 49, 241 (1983)
6. Wagner, S., Shishkina, O., Wagner, C.: J. Fluid Mech. 697, 336 (2012)
7. Thompson, J.E., Warsi, Z.U.A., Wayne Mastin, C.: Numerical Grid Generation: Foundations and Applications. Elsevier Science Publishing Co. (1985)
8. Pope, S.B.: Turbulent Flows, 1st edn. Cambridge University Press (2000)
9. Kunnen, R.P.J., Clercx, H.J.H., Geurts, B.J., Bokhoven, L.J.A.V., Akkermans, R.A.D., Verzicco, R.: Phys. Rev. E 77, 016302 (2008)

Stable Stratification in Wall-Bounded Turbulent Flows

Francesco Zonta and Alfredo Soldati

Abstract. Direct Numerical Simulation (DNS) is used to study the behavior of stably-stratified turbulent channel flow with temperature-dependent fluid properties: specifically, viscosity (μ) and thermal expansion coefficient (β). The governing equations are solved using a pseudo-spectral method for the case of turbulent water flow in a channel at $Re_\tau = 150$ and $Gr \simeq 10^7$. After an initial transient evolution of the flow, a statistically-stationary condition occurs, in which active turbulence and Internal Gravity Waves (IGW) coexist. In this condition, the transport efficiency of momentum and heat reduces considerably with respect to the condition of non-stratified turbulence. The crucial role of temperature-dependent viscosity and thermal expansion coefficient is directly demonstrated. The most striking feature produced by the temperature-dependent of viscosity is flow relaminarization in the cold side of the channel (where viscosity is higher). The opposite behavior, with flow relaminarization occurring in the hot side of the channel, is observed when a temperature-dependent thermal expansion coefficient is considered.

1 Introduction

Turbulence subject to thermal stratification (stratified flow) is of great interest due to the importance in geophysical, industrial and environmental applications. In the atmosphere, stable stratification of air is induced by thermal inversion. In urban areas, stratification is detrimental for air quality, since pollutants released by road traffic and factories remain trapped in the stably-stratified layer of air. In terrestrial water bodies (oceans, lakes or rivers) stratified turbulence influences the vertical

Francesco Zonta
Department of Physis, University of Torino, Torino, Italy
e-mail: francesco.zonta@uniud.it

Alfredo Soldati
Center of Fluid Dynamics and Hydraulics, University of Udine, Udine, Italy
e-mail: soldati@uniud.it

M.O. Deville et al. (eds.), *Turbulence and Interactions*,
Notes on Numerical Fluid Mechanics and Multidisciplinary Design 125,
DOI: 10.1007/978-3-662-43489-5_23,

transport of nutrients and chemical/biological species. In industrial applications, stratification may strongly reduce mixing and in turn heat transfer. Stable stratification often occurs in the presence of high temperature gradients. The analysis of stably-stratified turbulent flows is customary performed assuming constant and uniform thermophysical fluid properties. However, most fluids exhibit temperature-dependent thermophysical properties with significant variations for large temperature differences. Viscosity of water decreases from $\mu \simeq 0.8 \times 10^{-3}$ Pa s at 303 K to $\mu \simeq 0.4 \times 10^{-3}$ Pa s at 343 K (a value two times lower), while the thermal expansion coefficient increases from $\beta \simeq 3 \times 10^{-4}$ K^{-1} at 303 K to $\beta \simeq 5.7 \times 10^{-4}$ K^{-1} at 343 K (a value almost two times higher). Ignoring these variations may produce inaccurate prediction of momentum and heat transfer rates. Despite the number of experiments and atmospheric observations of stratified turbulence [4] phenomenology and evolution of the flow are not yet fully understood. In particular, DNS of stably-stratified turbulence in a closed channel was performed by [1] using Boussinesq approximation and constant thermophysical properties, and solving the energy equation for temperature distribution. They showed that, at high Richardson number, velocity fluctuations may lose symmetry about the channel centerline. More recently, [3] used Large Eddy Simulation (LES) to study a stably-stratified channel flow under non-Boussinesq conditions. They used a low-Mach number approximation for fluid density variation and showed that, at $Re_\tau = 180$, $Pr = 0.71$, $Ri_\tau \leq 60$ and for strong temperature gradient, the velocity field may be asymmetric. Unlike in [1] (where thermophysical properties of the fluid were uniform), the flow asymmetry in [3] was purely induced by non-uniform thermophysical properties.

The aim of this work is to contribute to the current physical understanding by performing accurate numerical experiments in a stably-stratified channel flow of water in which fluid viscosity (μ) and fluid thermal expansion coefficient (β) vary with temperature. Simulations are based on a pseudo-spectral method for the numerical solution of momentum and energy equation. We found that one-sided turbulence may be sustained either by an inhomogeneous distribution of viscosity or by an inhomogeneous distribution of thermal expansion coefficient.

2 Methodology

We consider an incompressible and Newtonian turbulent flow of water in a plane channel with differentially-heated walls. The reference geometry consists of two infinite flat parallel walls; the origin of the coordinate system is located at the center of the channel and the $x-$, $y-$ and $z-$ axes point in the streamwise, spanwise and wall-normal directions. The size of the channel is $4\pi H$ x $2\pi H$ x $2H$ in x, y and z, respectively. The bottom wall is kept at uniform low temperature ($T_{bottom} = T_C$), whereas the top wall is kept at a uniform high temperature ($T_{top} = T_H$). As a consequence, there is a constant negative temperature difference $\Delta T = (T_{bottom} - T_{top})$ between the bottom and the top wall which cause a stable buoyancy effect (the gravitational acceleration acting downward along the wall-normal direction). All the thermophysical properties of the fluid, with the exception of the dynamic viscosity μ and the

thermal expansion coefficient β are assumed to be constant. Variations of μ and β are indeed larger than those of the other thermophysical properties [2]. Hence, we assume $\beta = \beta(T)$ and $\mu = \mu(T)$. The dimensionless governing balance equations read as:

$$\frac{\partial u_i}{\partial x_i} = 0 \,, \tag{1}$$

$$\frac{\partial u_i}{\partial t} = S_i + \frac{1}{Re_\tau}\left(\frac{\partial^2 u_i}{\partial {x_j}^2}\right) - \frac{\partial p}{\partial x_i} \,, \tag{2}$$

$$\frac{\partial T}{\partial t} = -u_j \frac{\partial T}{\partial x_j} + \frac{1}{Re_\tau Pr}\left(\frac{\partial^2 T}{\partial {x_j}^2}\right) \tag{3}$$

where u_i is the i^{th} component of the velocity vector, p is pressure, T is temperature, whereas the S-terms include the non-linear terms, the mean pressure gradient and the buoyancy term. In these equations, $Re_\tau = \frac{\rho u_\tau H}{\mu}$ and $Pr = \frac{\mu c_p}{\lambda}$ are the Reynolds number and the Prandtl number, defined in terms of the thermophysical properties (ρ is density, μ is viscosity, c_p is specific heat and λ is thermal conductivity) at the reference temperature ($T_{ref} = \frac{T_C + T_H}{2}$). Note that $u_\tau = \sqrt{\frac{\tau_w}{\rho}}$ is the shear velocity (with τ_w the shear stress at the wall) and the expression of the S-terms depends on the specific problem (i.e. on the temperature behavior of the fluid properties). Equations 1-3 are discretized using a pseudo-spectral method based on transforming the field variables into wavenumber space, through Fourier representations for the periodic (homogeneous) directions x and y, and Chebyshev representation for the wall-normal (non-homogeneous) direction z [6, 7].

3 Results

The fluid is driven by an imposed pressure gradient and flows between the two walls, which are kept at constant temperature T_H^* and T_C^*, whereas buoyancy acts along the wall-normal direction (z). A temperature difference $\Delta T^* = T_H^* - T_C^* = 40$ K is imposed between the hot and the cold wall, which are kept at $T_H = 343$ K and $T_C = 303$ K, respectively. All the simulations are performed at Reynolds number $Re_\tau = 150$, Prandtl number $Pr = 3$ and Grashof number $Gr = 1.12 \times 10^7$. As a consequence, computations are run at the shear Richardson number $Ri_\tau = Gr/Re_\tau^2 = 498$. Together with the reference simulation of stratified turbulence assuming uniform fluid properties (*Boussinesq approximation*), we performed simulations with temperature-dependent fluid properties. In simulations where viscosity is a function of temperature, we assumed $\mu^*(T^*) = A \cdot 10^{B/(T^* - C)}$, where T^* is the local fluid temperature in Kelvin, while A, B and C are constants associated to the specific fluid considered. For water, $A = 2.414 \times 10^{-5}$, $B = 247.8$ and $C = 140$. In simulations where the thermal expansion coefficient is a function of temperature, we assumed $\beta^*(T) = \beta^*_{ref}\left(1 + 0.29 \times T - 0.037 \times T^2\right)$, where β^*_{ref} is the thermal

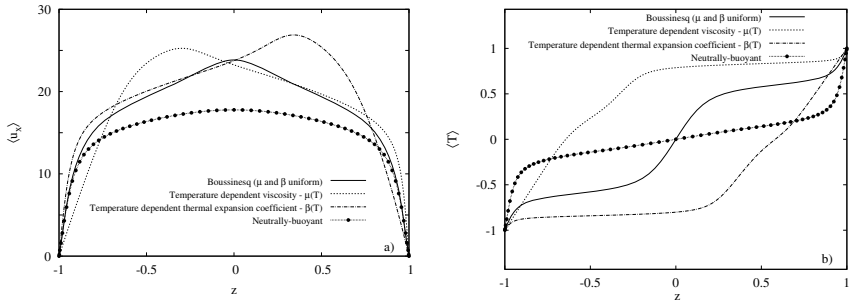

Fig. 1 Mean fluid streamwise velocity $\langle u_x \rangle$ for stably-stratified turbulent channel flow at $Ri_\tau = 498$ ($Re_\tau = 150$): comparison between simulations with uniform thermophysical properties (solid line) and simulations with temperature-dependent viscosity (dashed line) and temperature-dependent thermal expansion coefficient (dash-dotted line). Results from simulation of neutrally-buoyant turbulent channel flow (symbols) are also included.

expansion coefficient at the reference temperature. In Fig. 1a the mean streamwise velocity profiles, $\langle u_x \rangle$, are shown as a function of the dimensionless wall-normal coordinate $z = z^*/h^*$. Brackets indicate the average in time and in space (over the homogeneous directions). Results from simulations with uniform thermophysical properties (solid line), with temperature-dependent viscosity (dotted line) and with temperature-dependent thermal expansion coefficient (dash-dotted line) are compared. Profile of mean streamwise velocity from the simulation of neutrally-buoyant turbulent channel flow (symbols) is also included for comparison purposes. Stable stratification suppresses wall-normal momentum transport with respect to the neutrally buoyant case, where temperature is a passive scalar. Since the driving pressure gradient is held constant among simulations, the viscous wall stress and, therefore, the slope of the mean velocity profile in case of stable stratification should be invariant with respect to those of neutrally-buoyant case. This is true only for stable stratification with uniform fluid properties [3]. For the Richardson number considered here ($Ri_\tau = 498$), both viscosity and thermal expansion coefficient have a dramatic impact on the behavior of the flow field. Temperature-dependent viscosity alters the symmetry of the velocity profile, since the rate of change of $\langle u_x \rangle$ with z (velocity gradient at the wall) is directly linked to the local value of viscosity. In particular, velocity gradients are higher at the hot wall (lower viscosity) and lower at the cold wall (higher viscosity). The symmetry of the velocity profile is lost even in case of temperature-dependent thermal expansion coefficient. In Fig. 1b the mean temperature profiles from simulations of stable stratification ($Ri_\tau = 498$, $Re_\tau = 150$) with uniform and temperature-dependent fluid properties are shown and compared with that from the corresponding neutrally-buoyant simulation. Stable stratification (solid line) has a twofold effect on the temperature field compared to the neutrally-buoyant case (symbols): it reduces the temperature gradient at the wall (i.e the Nusselt number) and at the same time it increases the temperature gradient in the core of the channel. In particular, the increased temperature gradient in the

core of the channel indicates a tendency to form a kind of thick interface in this region (*thermocline*). The influence of temperature-dependent viscosity (dotted line) is rather evident. Near the cold wall ($-1 < z < -0.7$), where the flow is laminar, the mean temperature profile is roughly linear. Near the hot wall, where turbulence is sustained, the mean temperature profile is flat. A reversed situation is observed for temperature-dependent thermal expansion coefficient (dash-dotted line). In this case, the mean temperature profile is roughly linear near the hot wall and flat near the cold wall. This behavior is a direct consequence of the sharp separation of the channel into a laminar zone (near the hot wall) and a turbulent zone (near the cold wall). In Fig. 2 contour maps of the temperature field for simulations of stable stratification at $Ri_\tau = 498$ with uniform (Fig. 2a) and temperature-dependent (Fig. 2b-c) fluid properties are shown. In Fig. 2a we consider the base simulation with uniform thermophysical properties. It is clear that turbulence and internal waves coexist. In particular, internal waves (moving from left to right) are found in a narrow region of the channel around the centerline, whereas intermittent *bursts* associated with turbulence characterize the near-wall region. In Fig. 2b we focus on stable stratification with temperature-dependent viscosity. A strong asymmetry on the structure of the flow field is observed. The flow is laminar at the cold side of the channel (where viscosity is higher), but remains turbulent at the hot side (where viscosity is lower). In this situation, the thermocline (and the associated internal waves) moves towards the cold wall and extends over a wider proportion of the channel (more than $1/3$ of the entire height of the channel). The situation reverses in Fig. 2c, where the effect of the temperature-dependent thermal expansion coefficient is considered. In this case, flow laminarization occurs at the hot side of the channel, where the thermal expansion coefficient is higher. Note that the thermocline and the associated internal waves move accordingly towards the hot side of the channel.

To study the effect of buoyancy and temperature-dependent thermophysical properties on eddy sizes, we measured the streamwise energy spectra of velocity fluctuations [1, 5]. In particular, in Fig. 3 we consider the streamwise energy spectra of the wall-normal velocity fluctuations ($u_z'^2$) at three different positions (expressed in wall units, $z^+ = z^* u_\tau^* / \nu_{ref}^*$) along the wall-normal direction. For each position, results from the simulation with uniform thermophysical properties (*filled circles*) are compared with those with temperature-dependent viscosity (*filled triangles*) and temperature-dependent thermal expansion coefficient (*filled squares*). Results from simulation of neutrally-buoyant flow (*open circles*) are also shown for comparison purposes. To highlight the effects of stratification, we compare the results from simulation of neutrally-buoyant flow (*open circles*) and those from simulation of stable stratification with uniform thermophysical properties (*filled circles*). In the core region of the channel (Fig. 3b), the energy spectrum increases for $1 < kh < 4$, with a peak value for $kh \simeq 2.5$ (where k is wave number). This is the footprint of internal waves which induce fluctuations of wall normal velocity (u_z') occurring at the characteristic frequency of the wave. Unlike the case of uniform thermophysical properties, the effect of $\mu(T)$ (resp. $\beta(T)$) is higher (Fig. 3a) in the cold side of the channel (resp. hot side of the channel, Fig. 2c), where wave actvity was observed.

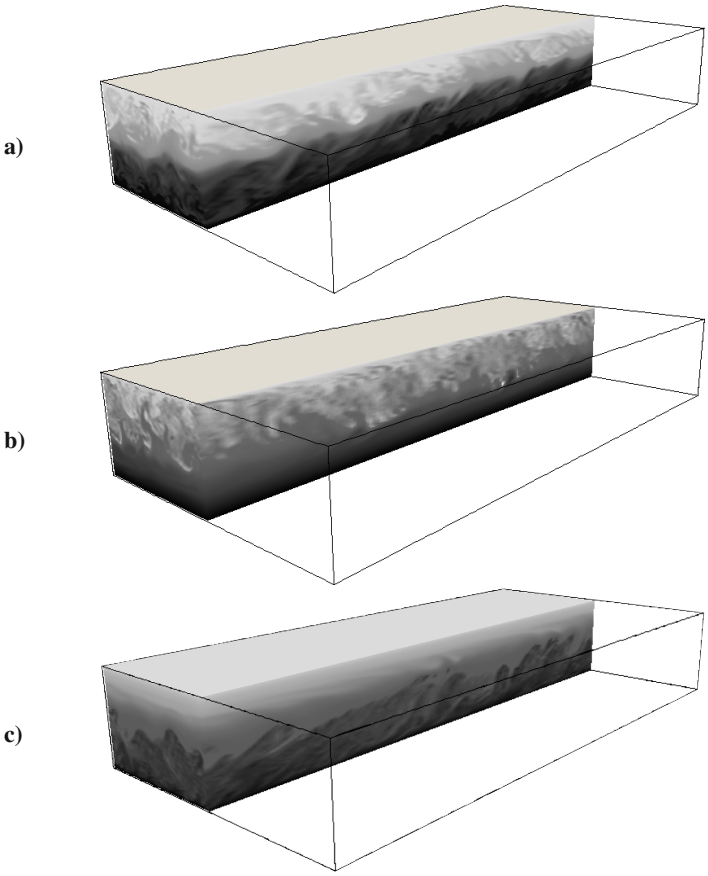

Fig. 2 Contour maps of the temperature field for simulations at $Ri_\tau = 498$ ($Re_\tau = 150$) after the steady-state condition has been reached. Three dimensional visualizations (false colour) of temperature distribution and associated two dimensional views ($x-z$ planes, black and white) are shown: **a)** uniform thermophysical properties; **b)** temperature-dependent viscosity; **c)** temperature-dependent thermal expansion coefficient.

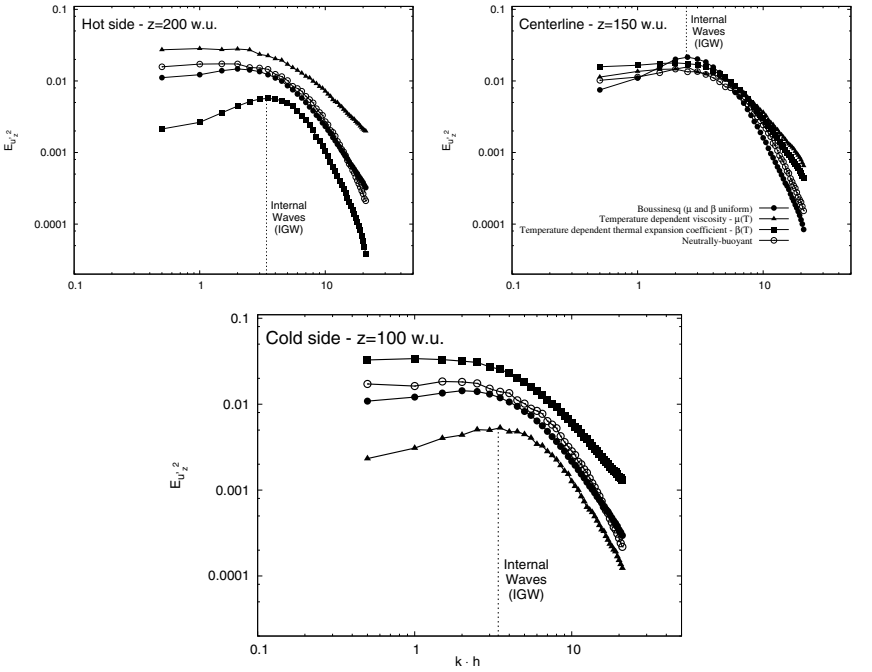

Fig. 3 Streamwise frequency spectra of wall-normal velocity fluctuations ($Ri_\tau = 498$) at three different positions along the wall normal direction: **a)** $z^+ = 200$ (hot side); **b)** $z^+ = 150$ (centerline); **c)** $z^+ = 100$ (cold side). Comparison between simulations with uniform thermophysical properties (filled circles) and simulations with temperature-dependent viscosity (filled triangles) and temperature-dependent thermal expansion coefficient (filled squares). Results from simulation of neutrally-buoyant turbulent channel flow (open circles) are also included.

Acknowledgements. CINECA supercomputing center (Bologna, Italy) and DEISA Extreme Computing Initiative are gratefully acknowledged for generous allowance of computer resources. Support from PRIN (under Grant 2006098584_004) and from HPC Europa Transnational Access Program (under Grants 466 and 708) are gratefully acknowledged. F.Z. gratefully acknowledge Department of Physics, University of Torino, for financial support under Grant 234175.

References

1. Iida, O., Kasagi, N., Nagano, Y.: Direct numerical simulation of turbulent channel flow under stable density stratification. Int. J. Heat Mass Transfer. 45, 1693 (2002)
2. Incropera, F.P., Dewitt, D.P.: Fundamentals of heat and mass transfer. John Wiley and Sons Inc., New York (1985)
3. Lessani, B., Zainali, A.: Numerical Investigation of stably-stratified turbulent channel flow under non-Boussinesq conditions. J. Turbulence 10, 1 (2009)
4. Turner, J.S.: Buoyancy effects in fluids. Cambridge University Press, Cambridge (1973)

5. Yeo, K., Kim, B.G., Lee, C.: Eulerian and Lagrangian statistics in stably stratified turbulent channel flows. J. Turbulence 10, 1 (2009)
6. Zonta, F., Marchioli, C., Soldati, A.: Modulation of turbulence in forced convection by temperature-dependent viscosity. J. Fluid Mech. 697, 150 (2012)
7. Zonta, F., Onorato, M., Soldati, A.: Turbulence and internal waves in stably-stratified channel flow with temperature-dependent fluid properties. J. Fluid Mech. 697, 175 (2012)

Author Index